Summer 9-1-2014

Shape and Structure of Neutron-Rich from Cf-252 Fission Fragments

Jason Benjamin Snyder
Washington University in St. Louis

WASHINGTON UNIVERSITY IN ST. LOUIS

Department of Physics

Dissertation Examination Committee:
Demetrios G. Sarantites, Chair
Robert J. Charity
Willem H. Dickhoff
Henric Krawczynski
Walter Reviol
Lee G. Sobotka

Shape and Structure of Neutron-Rich Nuclei from ^{252}Cf Fission Fragments

by

Jason Benjamin Snyder

A dissertation presented to the
Graduate School of Arts and Sciences
of Washington University in
partial fulfillment of the
requirements for the degree
of Doctor of Philosophy

August 2014

Saint Louis, Missouri

CONTENTS

LIST OF TABLES

LIST OF FIGURES

ACKNOWLEDGMENTS

I would like to acknowledge and deeply thank all of those fine teachers that have guided my education.

First, I would like to express my gratitude to my advisor, Dr. Demetrios Sarantites, for providing a supportive research environment and for sharing his knowledge. Special thanks are also due to the man who served as my mentor, Dr. Walter Reviol. I am a better scientist and a better man for having known him. I would also like to thank the members of my committee for the insight and feedback they provided towards the improvement of this work.

Many collaborators contributed to this work, including an exceptional group at Argonne National Lab. Thank you, Dr. Robert Janssens, Dr. Michael Carpenter, Dr. Christopher Chiara, John Greene, Dr. Torben Lauritsen, Dr. Elizabeth McCutchan, John Rohrer, Dr. Dariusz Seweryniak, and Dr. Shaofei Zhu for many insightful discussions and experimental support. I am also grateful to Dr. Anatoli Afanasjev and Dr. Hazem Abusara, who provided the theoretical interpretation of this work and checked the discussion chapter of the thesis (Afanasjev). Additional thanks are due to Jon Elson for his technical expertise. I would also like to thank my officemate, Dr. Xinfeng Chen, for his positive attitude, advice, and for bringing in mooncakes to keep me motivated. Special thanks are also due to Dr. Olga Pechnaya for showing me the ropes when I first joined the research group.

Finally, I would like to thank my family and friends for their continual encouragement, and especially my lovely wife for keeping me focused.

ABSTRACT OF THE DISSERTATION

Shape and Structure of Neutron-Rich Nuclei from ^{252}Cf Fission Fragments

by

Jason Benjamin Snyder

Doctor of Philosophy in Physics

Washington University in St. Louis, 2014

Professor Demetrios G. Sarantites, Chair

The transition quadrupole moments, Q_t, of rotational bands in the neutron-rich, even-mass $^{102\text{-}108}$Mo and $^{108\text{-}112}$Ru nuclei were measured with the Doppler-shift attenuation method. The nuclei were populated as fission fragments from ^{252}Cf fission. The detector setup consisted of the Gammasphere spectrometer and the Hercules fast-plastic array. This allowed the measurement of asymmetric DSAM lineshapes at different Gammasphere detector angles with respect to the fission axis. The measurements typically covered the 6 to 16ħ spin range of the ground-state band and at least a strong transition in the γ band. At moderate spin, the Q_t moments are found to be reduced with respect to the values near the ground states, the latter being reported in the literature.

An attempt has been made (by Afanasjev) to describe the data in the framework of cranked relativistic Hartree-Bogolyubov theory, and the results are reported in the present work as well as in a Physics Letters paper by Snyder et al. For ^{104}Mo reliable predictions can be made. Here an oblate shape and a low-spin triaxial shape (deformation parameter γ~-44°), predicted to be favored in other theoretical calculations, are ruled out by the data. There is some indication for a gradual change, at higher spin, from an initially prolate shape to a triaxial shape in ^{104}Mo. The Q_t data for ^{106}Mo and

^{110,112}Ru support this picture. The challenge of theory to describe the Q_t data is addressed, which has to do with the very γ-soft potential-energy surfaces.

As a byproduct of the Q_t analysis (which requires the determination of the intensities of the feeding transitions), the transition intensities of many weak high-spin or non-yrast states have been determined. These previously unknown intensity data are also reported.

In the appendix, the results of an attenuation-coefficient analysis for γ-ray angular distributions (due to recoil-in-vacuum) in heavy Ba isotopes are reported. These results are from a separate project, though from the same data set.

Chapter 1: Introduction

The nucleus is a quantum mechanical system of protons and neutrons; bound together by the strong interaction within a radius of ~$5x10^{-15}$m [1]. The current best direct observation option, a scanning tunneling microscope, can observe individual atoms (10^{-10}m) [2], but is still a factor of 10^4 away from resolving the nucleus. To gain an understanding of the nucleus requires the use of "other" observation methods. Often, this involves placing the nucleus in an excited state and detecting the particle and γ emissions released by the nucleus as it returns to stability (the ground-state properties are, of course, also important). The measurement of experimental quantities from an excited-state emission, specifically spin, parity, and lifetime of the state, combined with their interpretation through theoretical models, allows for the reconstruction of the nuclear shape and the underlying nuclear structure.

For the present work, the shape is an important feature of the nucleus to be considered. Specifically deviations of the atomic nucleus from a spherical shape, i.e., nuclear deformation, are a point of concern. A quantity that describes such deformation is the nuclear quadrupole moment. Earth is said to have a quadrupole moment, reflecting the "flatness" of the poles, where the difference in the major and minor axes is of the order of 1.003:1. A typical quadrupole moment of a deformed nucleus corresponds to a 1.2:1 axis ratio, while in exceptional cases, so called superdeformed nuclei, 2:1 axis ratios have been observed. In the case of the positively charged atomic nucleus, one often uses the charge quadrupole moment. One way to determine the charge quadrupole moment is through the so-called transition quadrupole moment, which is related to the lifetime of certain excited nuclear states.

The discovery of the nuclear quadrupole moment dates back to the mid 1930s and is described in Reference [3]. On the experimental side, the discovery is associated with the names of Schüler and Schmidt, who found an unusual line splitting in the optical hyperfine spectroscopy of rare-earth probes. That splitting suggested an electric interaction between the nucleus and its atomic environment. Notably, the so-called magnetic hyperfine interaction was already known at this point. On the theoretical side, Pauli, Racah, and Casimir were involved. They defined the problem as due to an elongation or compression of the nucleus along a certain orientation axis (the spin axis), and they solved the problem by providing the first calculations of nuclear quadrupole moments. For example, the value of 560 efm^2 for ^{175}Lu is a value that is certainly in the right "ballpark". Using present-day terminology, this was the first determination of the so-called static quadrupole moment, which is another method of determining the degree of nuclear deformation, in addition to the aforementioned transition quadrupole moment.

Another milestone of this type of nuclear research was the discovery of nuclear rotation that, in turn, implies that the nuclear shape is deformed. This dates back to the early 1950s and is associated with the names of Huus and Zupancic, and Asaro and Perlman on the experimental side, and N. Bohr, A. Bohr, and B. Mottelson, on the theoretical side; see the Nobel lecture of A. Bohr [4].

As indicated in the previous paragraphs, there was always a close interaction between experimental observation and nuclear modeling. A brief introduction of various nuclear models is in order.

One of the earliest attempts to "model" a more global observation of nuclear science, namely the nuclear binding energy, is the so-called liquid-drop model. The nuclear binding energy is the difference between the actual nuclear mass and the mass of all the individual nucleons, i.e. protons and neutrons that makes up the nucleus. It is often normalized by the mass number to give

the binding energy per nucleon. The larger the binding energy per nucleon, the more stable the nucleus is, i.e. the more work it would take to remove a nucleon from the nucleus. Bethe and von Weizsäcker pioneered the liquid-drop model in the mid 1930s, with the development of the semi-empirical mass equation [5] [6] to describe the nuclear binding energy. The model essentially treats the nucleus as an incompressible, uniformly charged, drop of liquid.

A plot of the binding energy per nucleon as a function of mass number reveals that nuclei with proton or neutron numbers equal to 2, 8, 20, 28, 50, 82, or 126 are significantly more stable than predicted by the mass equation. These numbers are known as "magic" numbers and their existence motivated the development of the shell model in the early 1950s [7]. Among the shell-model pioneers are Goeppert-Maier, Jensen, and Feenberg.

The traditional shell model, also called the spherical shell model, assumes that each nucleon moves independently in the average potential created by all the other nucleons in the nucleus. This assumption is based upon the long mean free path of the nucleons. Justified in part by the Pauli Exclusion Principle which requires that no two fermions, i.e. protons or neutrons, may occupy the same state. The average potential has been modeled in a variety of ways ranging from harmonic oscillator and square well potentials, to the more realistic, yet difficult to solve, Wood-Saxon potential [7]. These potentials led to certain energy gaps (shell gaps), which only matched the first three "magic" numbers. The inclusion of the spin-orbit interaction is still required. The spin-orbit interaction couples the orbital (L) and spin (S) angular momentum of each nucleon into total angular momentum (J), where $J=L\pm S$ ($S=1/2$). That is, the nucleonic motion may be visualized as moving in certain J orbitals.

This arrangement of levels correctly reproduces all the "magic" numbers. The spin-orbit interaction is of strong-interaction origin (nuclear force). A spin-orbit term in the Hamiltonian of

electromagnetic origin (like in the atomic case), would be an order of magnitude too weak to be of help explaining the "magic" numbers.

The spherical shell model works well at predicting nuclear properties near closed shells, i.e. near the "magic" numbers. However, it is inappropriate when it comes to describing nuclear deformation and the excitation modes that are based on a deformed nuclear shape: rotation and surface vibration. These considerations are related to the "mid-shell" regions and to the outskirts of the nuclear chart (a representation of all known nuclei in terms of atomic number and isotopic chain for a given atomic number). The vast majority of nuclei are located in these regions.

To account for these nuclei additional models have been developed that are in a sense extrapolations of the previously discussed models. There is the Nilsson model that describes single nucleonic motion in a deformed mean field hereby representing the effect of deformation. There is the so-called cranking model that describes the effect rotational motion has on nucleonic orbitals. And there is the so-called Nilsson-Strutinsky method that leads to "multi-dimensional" potential energy surfaces, i.e., the total energy as a function of nuclear shape parameters and angular momentum. These models (together with the concept of nuclear "pairing") are relegated to a later chapter.

To elaborate somewhat on shape parameters, the following considerations are in order. The deformation of the nucleus may or may not preserve axial and reflection symmetry. If axial symmetry is broken, the nucleus takes on a triaxial shape. If reflection symmetry breaks down, it leads to pear-like shapes. This is directly related to present research activities in nuclear spectroscopy. Specifically, as stated in Reference 8, it is still disputed in which way permanent triaxial or reflection-asymmetric shapes are realized in atomic nuclei. The present work addresses this question and contributes in particular to the study of triaxial nuclear shapes.

The nuclei of interest are located in the hard to access neutron-rich region of the nuclear chart, where isotopes with a relative excess of neutrons compared to the stable nuclei in a given isotopic chain are located. One main method to produce neutron-rich nuclei, particularly at states with high angular momentum, is the spontaneous fission of ^{252}Cf. A ^{252}Cf source has been used, in this work, however, unlike in most previous source experiments, the emphasis is on measuring lifetimes and subsequently extracting transition quadrupole moments (previous work focused on constructing level schemes). This primarily requires extracting information from γ rays deexciting the states of interest. However, to obtain high experimental sensitivity, the principle of the measurement combines the γ-ray detector array with a particle detector that identifies the fission fragments and the fission axis. This has been achieved by using the Gammasphere-Hercules detector combination.

In Chapter 2 of this work, background information on the fission of ^{252}Cf, shape parameters, methods for measuring excited-state lifetimes, and how the fission fragments and their γ rays interact with the detectors is provided. Chapter 3 provides a description of the detectors themselves (Hercules and Gammasphere) and how the experiment is conducted. In Chapter 4, the analysis methods used to identify one fragment from another and extract excited-state lifetimes from this data set are covered. In Chapter 5 the results are presented, which comprise transition quadrupole moments in a series of heavy Mo and Ru isotopes and previously unavailable intensity fits of higher lying, weak transitions in these nuclei. In Chapter 6, a discussion of the measured transition quadrupole moments based on theoretical considerations is presented. Chapter 7 provides a summary of this work. There are also extensive appendices including one on a recoil-in-vacuum angular distribution measurement that was carried out as a second, independent project.

Chapter 2: Background

2.1 The Nuclear Landscape

Figure 2-1 shows the part of the nuclear chart that is relevant for the nuclei produced by the spontaneous fission of ^{252}Cf. Every nucleus in the chart is represented by a neutron number (N) along the x axis and a proton number (Z) along the y axis. Both protons and neutrons contribute to the nuclear interaction, but there is also Coulomb repulsion by the protons. The black squares in Figure 2-1 identify the nuclei that are stable against β decay (see Section 2.2). These are the nuclei where the binding energy has reached a maximum for a given mass number. The maximum is determined within the liquid drop model by those terms that are explicitly Z and/or N dependent (Coulomb and assymetry terms). At low mass number (e.g. ^{20}Ne) stable nuclei have an N/Z ratio at or near 1.0. As the mass number increases, balancing out the Coulomb repulsion requires an increasing neutron excess. In Figure 2-1, the N/Z ratio for stable nuclei has increased to ~1.3.

The β-stability line divides, in a sense, the chart. Those nuclei "west" and "east" of the line are called proton rich and neutron rich, respectively. The proton-rich side is accessible, for example, by fusion-evaporation reactions using a heavy-ion accelerator. In this case, two stable nuclei with small N/Z ratios (compared to heavier stable nuclei) are fused together to produce a proton-rich nucleus. The fusion process leaves the product compound nucleus in an excited state that will reduce its energy by evaporating particles. If only the Coulomb barrier for the evaporated particle is considered, the emission of a neutron is in general preferred over proton or α emission. This process leads to an evaporation residue, where the N/Z ratio is small (proton rich) compared to stable nuclei of the same mass number. In fission, a parent nucleus with a large N/Z ratio (compared to lighter nuclei) produces two neutron-rich "daughters" (notice the separation into two

mass peaks in Figure 2-1). The ratio for ^{252}Cf is 1.57. For the production of neutron-rich nuclei, there are several options: neutron-transfer reactions, spallation, fragmentation, and various types of fission (see next section).

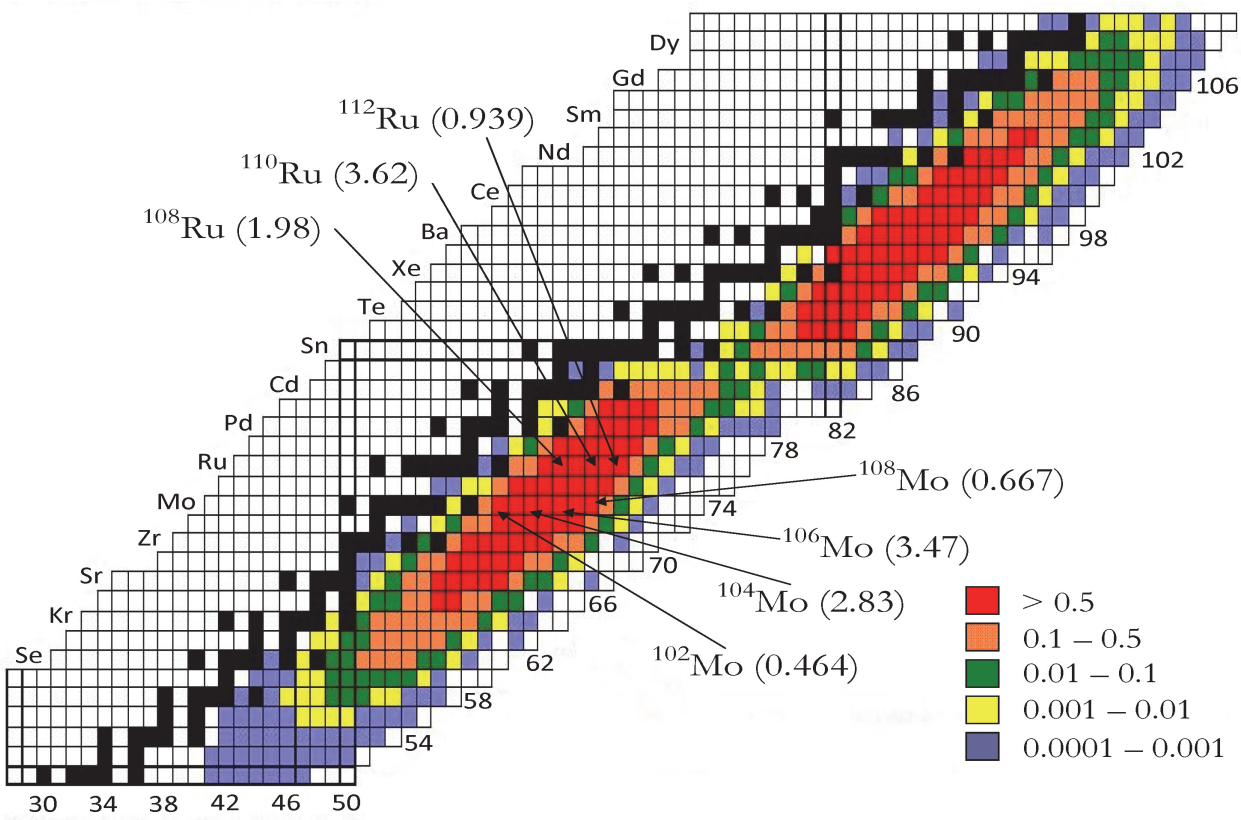

Figure 2-1: Part of the chart of the nuclides, color-coded with the ^{252}Cf spontaneous-fission independent yields (IN values). The IN value is a measure for the direct population yield of the fission products (see Section 2.2). Examples of such products are ^{102,104,106,108}Mo and ^{108,110,112}Ru, the nuclei studied in this work. These are identified and their IN values are reported.

2.2 The Fission Process

The different types of radioactive decay are briefly mentioned hereafter. Alpha (α) decay is the emission of an α particle, ^{4}He. There are three types of beta (β) decay: β^- where an electron and electron antineutrino are emitted, β^+ where a positron and electron neutrino are emitted, and electron capture where a proton captures an atomic electron to form a neutron and emit an electron neutrino. The nuclei studied are neutron rich, so the β decays will exclusively be β^-. Proton decay is the emission of a proton, ^{1}H. Neutron decay is the emission of a neutron, ^{1}n. In spontaneous fission, a nucleus splits into two smaller fragments which release evaporation neutrons (see below) without the influence of an outside force. In induced fission, in principle, the same result occurs, but the process is facilitated by bombarding the nucleus with neutrons or charge particles. Gamma (γ) decay is an electromagnetic emission from the nucleus.

The process by which fission occurs is illustrated in Fig. 2-2 [9]. The nucleus starts with an initial configuration and then begins elongating and pinching into two separate pieces of nuclear matter, a process known as necking. This process continues until the elongated nucleus reaches the scission point and breaks into two separate fragments. These fragments are known as primary fragments. They are excited and cool predominantly through neutron evaporation, a process comparable with the evaporation following a fusion reaction. On average 3.75 neutrons are emitted during a ^{252}Cf fission event [10]. Once the fragments no longer emit neutrons, they are referred to as secondary fragments and are abbreviated FF hereafter. The FFs continue to cool down to the ground state by γ emission. Initially there is statistical γ emission and the density of states is comparatively high. As the ground state is approached and the density of states decreases the γ

transitions can more easily be resolved and the levels are often called discrete states. Those with the lowest excitation energy for a given spin are termed yrast states. Accordingly, they are more strongly populated than other states at the same spin. On average each FF emits 3-4 γ rays, however 5% of all FFs formed emit as many as 10 γ rays [9]. Finally, the FFs will undergo β decay until a stable nucleus is reached. The present work focuses on the FF discrete states.

The spontaneous fission of ^{252}Cf produces a light fragment (LF) and a heavy fragment (HF), centered around A=110 and 140, respectively [9]. A symmetric distribution would be centered at A=122. The nuclear shell closures at Z=50 and N=82 combine to preferentially form a FF with A>132, the HF. The remaining nucleons combine into the LF. Symmetric distributions occur when the shell effects are minimized. This situation is obtained in induced fission, where the excitation energy of the system is initially higher.

Conservation of angular momentum requires that the net angular momentum of the FFs after fission be equal to that of the combined system before (i.e. 0^+, the ground state of ^{252}Cf). The angular-momentum conservation in fission is satisfied by adding the spins of the FF and the orbital angular momentum to a total spin of 0. This is accomplished in the three angular momentum bearing modes described by Nix and Swiatecki [11] and summarized in Figure 2-3. The dominant mode is the bending mode. The bending and wriggling modes align the spins of the FF perpendicular to the fission axis, while the twisting mode aligns them parallel to it. In the twisting mode there is considerable friction between the separating fragments and this makes this mode less likely. This was first suggested by Hoffman and supported by Sarantites and it is the basis for the present work [12] [13].

For completeness, it should be mentioned that the FFs also inherit the kinetic energy of the primary fragments. This has the effect that the FFs are recoiling, which in turn can be used in certain measurements such as Doppler-shift lifetime measurements (see Section 2.4).

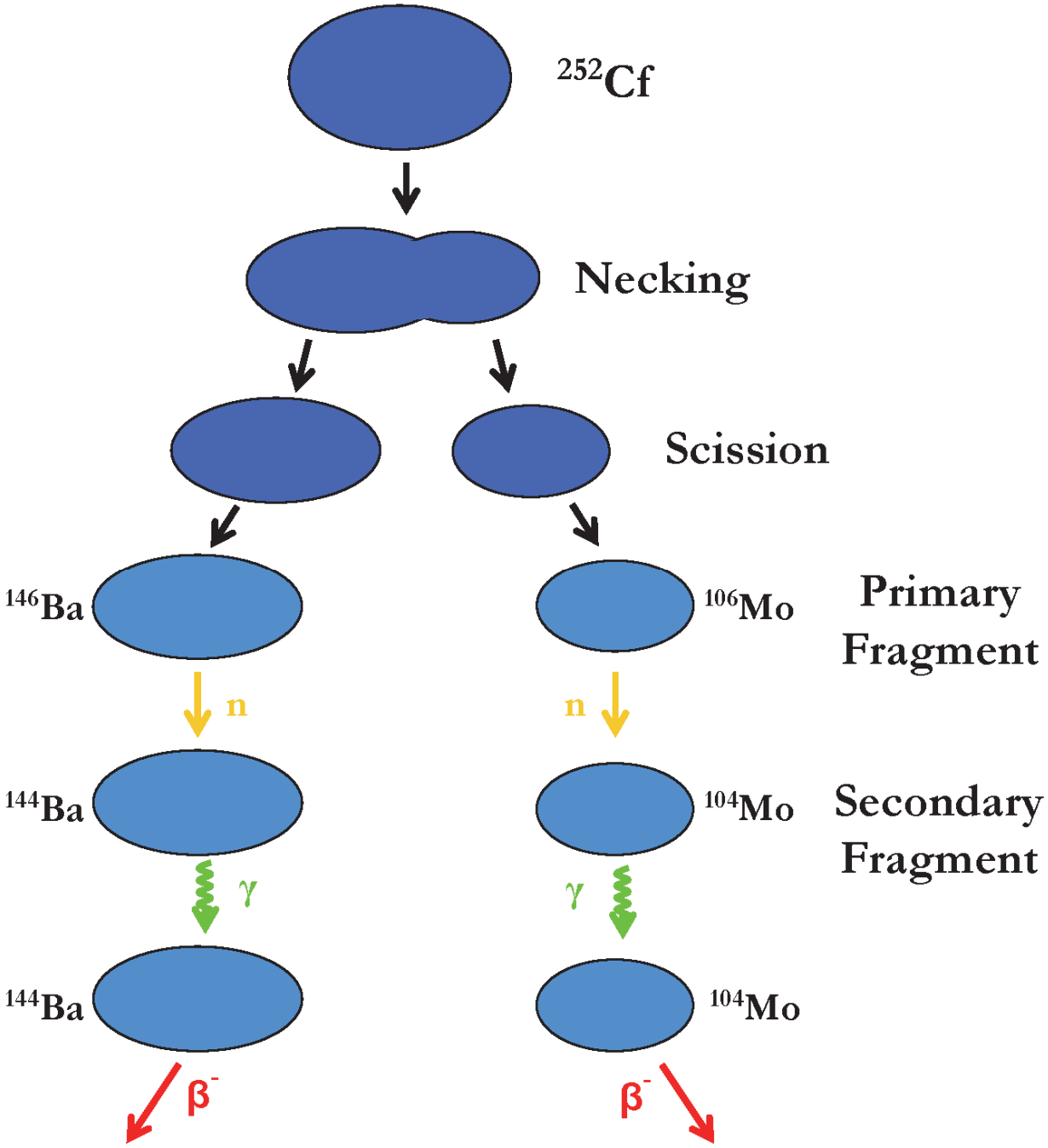

Figure 2-2: Schematic representation of the formation of primary and secondary fragments from the spontaneous fission of ^{252}Cf. The letters n, γ, and β^- represent neutron evaporation, γ decay, and β^- decay respectively.

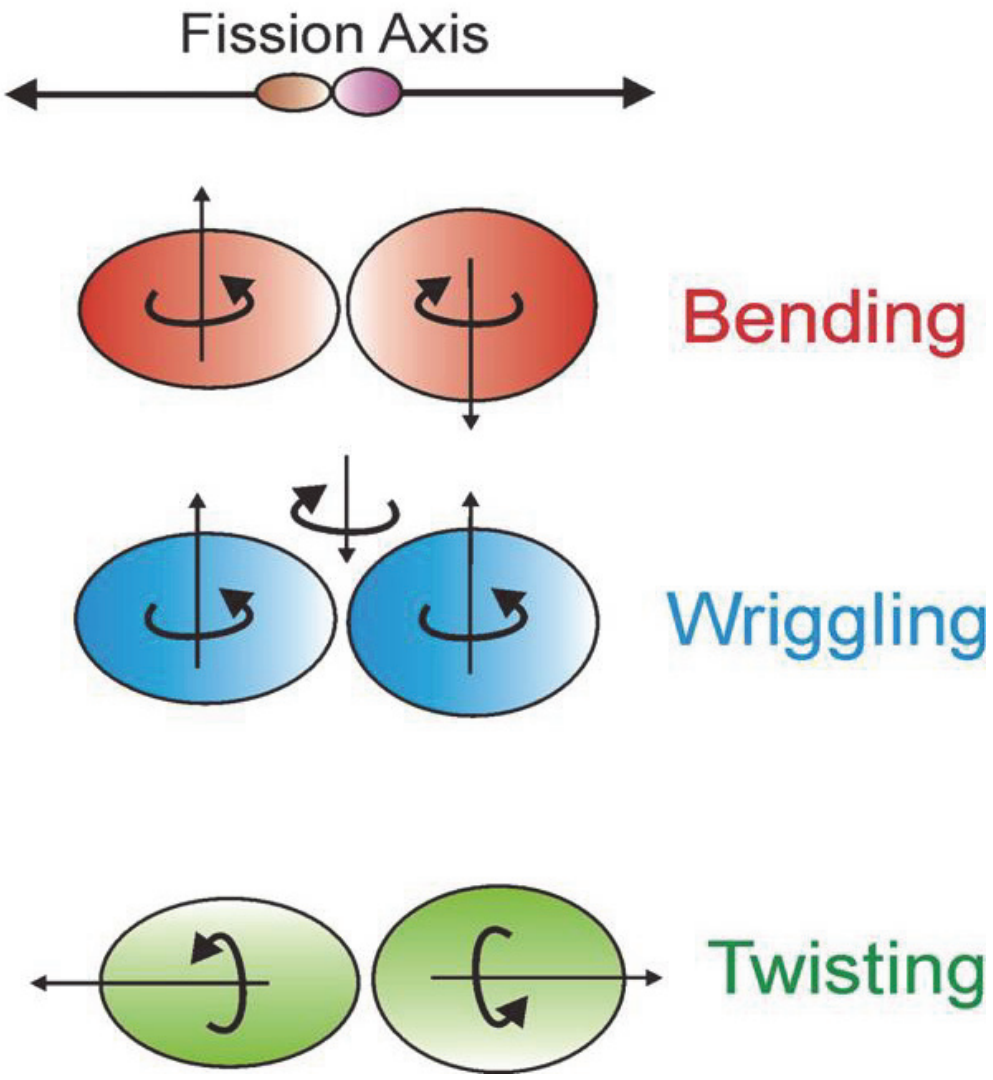

Figure 2-3: Modes by which the nascent fragments can bear angular momentum while the entire scission-point complex conserves angular momentum. The bending and wriggling modes are dominant, since twisting involves more friction. Figure from Reference [14].

The fission yield is the percent of a fission events that produce a given nucleus, with two fragments per event, the yields are normalized to 200%. There are two types of yields used in the literature (e.g. in Reference [15]): independent, where the yield is determined before β decay, and cumulative, where the yield is determined after β decay. The independent yield (abbreviated IN) is

the quantity used in Figure 2-1 and the later chapters of this work. In Figure 2-1, the ^{102,104,106,108}Mo and ^{108,110,112}Ru nuclei studied in this work are identified, and their IN values are reported. According to the color code of Figure 2-1, these IN values are among the largest for the fission of ^{252}Cf. There are 62 FF with IN values greater than 1% and ~200 FF with values greater than 0.1% [16].

2.3 Theoretical and Empirical Concepts

2.3.1 Shape Deformations

The following presentation on the deformation of the nucleus is based upon Reference [8]. The radius of the nuclear surface (R), with respect to the origin, is described as an expansion of spherical harmonics ($Y_{\lambda\mu}$) as shown in Equation (2-1).

$$R(\theta,\varphi) = r_0 A^{1/3}\left[1 + \sum_{\lambda=0}^{\lambda_{max}} \sum_{\mu=-\lambda}^{\lambda} \alpha^*_{\lambda\mu} Y_{\lambda\mu}(\theta,\varphi)\right] \quad (2\text{-}1)$$

The $\alpha^*_{\lambda\mu}$ coefficients describe the magnitude of each $Y_{\lambda\mu}$ component, ($r_0A^{1/3}$) is the empirical nuclear radius where r_0=1.2 fm, and A is the mass number for a given nucleus. The α_{00} term ensures volume conservation. The three $\alpha_{1\mu}$ terms describe a shift in the center of mass. The $\alpha_{1\mu}$ terms can be ignored if the center of mass is chosen to coincide with the origin of the body fixed frame. The $\alpha_{2\mu}$ terms are the lowest order of interest here. They represent the quadrupole deformation. The next higher order terms ($\alpha_{3\mu}$) represent the octupole deformation. Sketches of these two shapes are shown in Figure 2-4.

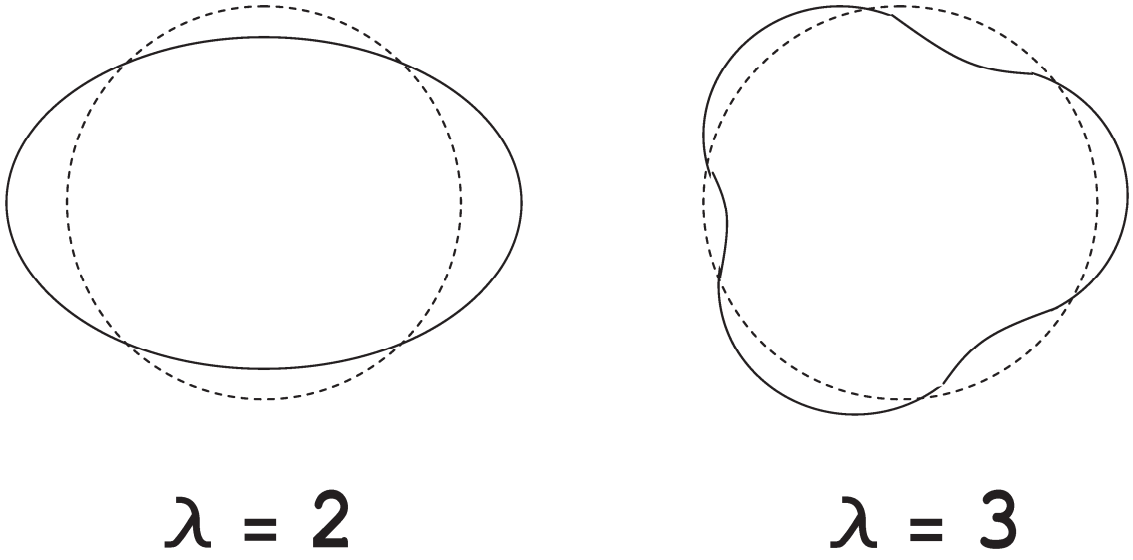

Figure 2-4: Sketches of quadrupole (λ=2) and octupole (λ=3) shapes. The former is cigar like, the latter pear like. The dashed lines indicate a spherical shape.

The $\alpha_{\lambda\mu}$ coefficients can be simplified by the requirement that the radius be real and that the shape be invariant with respect to the three symmetry planes. Enforcing the former condition real imposes the requirement that $\alpha^*_{\lambda\mu} = (-)^{\mu}\alpha_{\lambda-\mu}$. The latter condition imposes that $\alpha_{\lambda\mu} = \alpha_{\lambda-\mu}$ and that $\alpha_{\lambda\mu} = 0$ for odd λ or μ. Applying the latter condition to the quadrupole deformation leads to $\alpha_{22} = \alpha_{2-2}$ and $\alpha_{21} = \alpha_{2-1} = 0$. If the additional requirement is placed that the shape be axially symmetric, then those coefficients with μ≠0 are also zero. The quadrupole deformation can now be described by just the α_{20} coefficient. This remaining parameter is called β_2. The parameters for the higher-order multipoles are not considered in the present context. However, it is important to consider that the axial symmetry of a quadrupole shape may be broken (e.g. squeezed cigar). It is helpful to reparameterize the quadrupole deformation in terms of β_2, the magnitude of the deformation, and γ, the deviation from an axially symmetric shape. These parameters were

introduced in Reference [17], and are known as Hill-Wheeler coordinates. In Equation (2-2), the α_{20} and α_{22} coefficients are written in terms of this polar representation:

$$\alpha_{20} = \beta_2 \cos\gamma, \quad \alpha_{22} = \alpha_{2-2} = \frac{-1}{\sqrt{2}} \beta_2 \sin\gamma \tag{2-2}$$

The value of the γ parameter covers, in principle, a range from 0 to 2π. However, in order to give the principal axes of the ellipsoidal shape a physical meaning, rotation of the shape is required. The accepted convention is the Lund convention [18], which is illustrated in Figure 2-5.

Here the term "collective" is used for a rotation perpendicular to the symmetry axis; angular momentum is created by cranking the nuclear shape and all nucleons are thought to follow the cranking motion. A distinction is made between "collective prolate" (γ=0°) and "collective oblate" (γ=-60°). The term "single particle" is reserved for an excitation mode where angular momentum is created by the spin(s) of a (several) valence nucleon(s). This spin may coincide with a symmetry axis and is then called "single-particle prolate" and "single-particle oblate" for γ=-120° and 60°, respectively. The region described by -60°<γ<0° allows for cranking about an axis perpendicular to a symmetry axis where the nuclear shape can be triaxial. Rotational-like motion near this region is conceivable as well, for example, a shape with a small, positive value of γ.

The following expressions relate the intrinsic quadrupole moment to the deformation parameters. For an axially symmetric nucleus, the quadrupole moment is described, in the simplest way, by Equation (2-3):

$$Q_{20}(\gamma = 0^\circ) = \frac{3}{\sqrt{5\pi}} Z r_0^2 A^{2/3} \beta_2 . \tag{2-3}$$

Equation (2-4) builds on the previous expression to include the effect of γ upon Q_{20}:

$$Q_{20} = Q_{20}(\gamma = 0^\circ)\frac{\cos(\gamma + 30^\circ)}{\cos(30^\circ)}. \quad (2\text{-}4)$$

Notably, the expression with the cosines is equal to 1 for γ=0° (collective prolate) and γ=-60° (collective oblate).

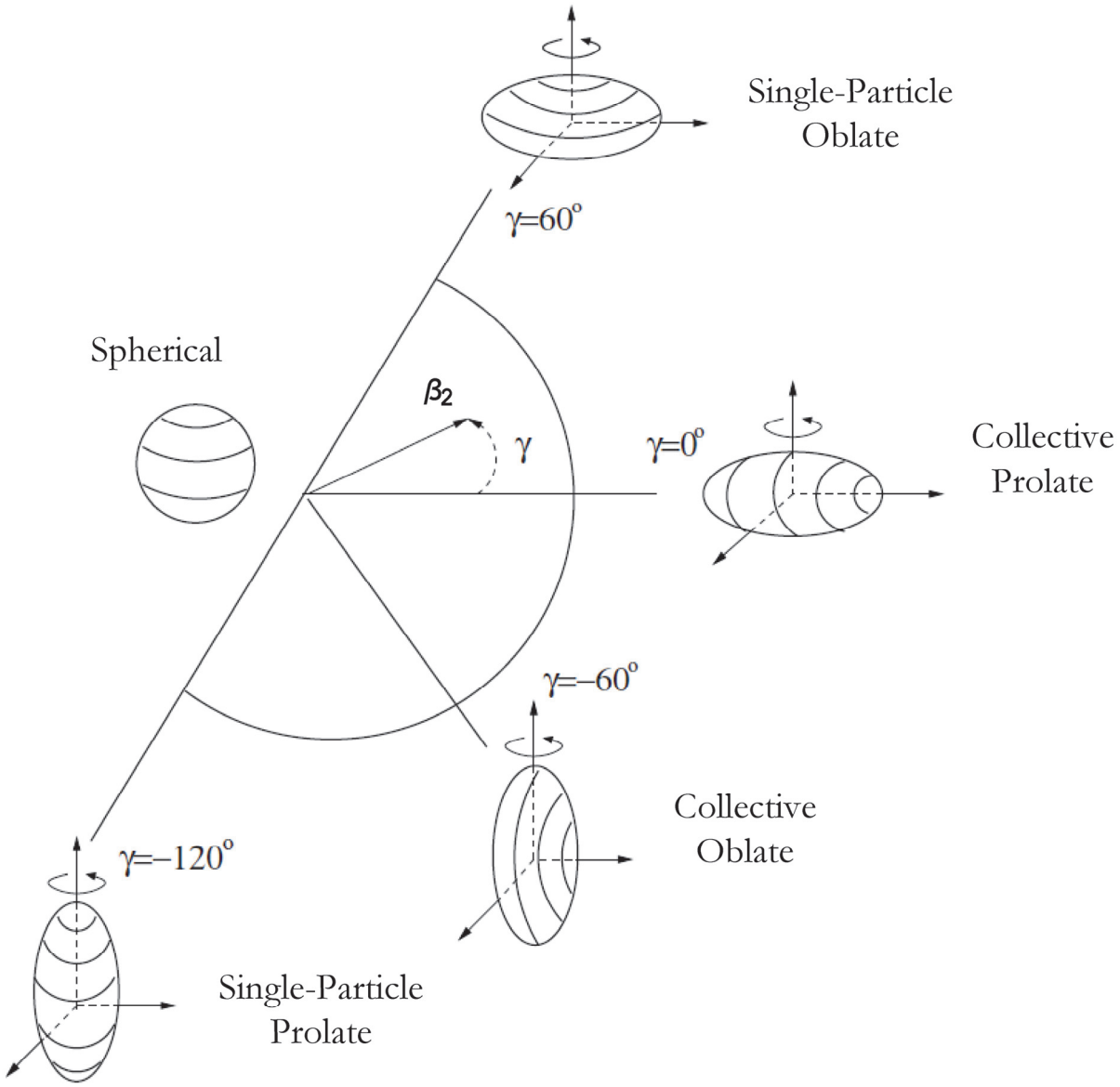

Figure 2-5: The quadrupole deformation described in terms of β_2 and γ, the polar coordinates, is shown. The type of deformation (prolate or football-like and oblate or doorknob-like) and its association with collective rotation or single-particle motion, as used by the Lund convention, is indicated. The spherical shape (β_2=0) should be viewed just as a reference point. This figure is adapted from Reference [19].

2.3.2 Level Schemes

Upon completion of particle emission, an excited nucleus releases its remaining energy through electromagnetic transitions and in the process decays to lower states. An electromagnetic transition can be either a γ decay or internal conversion. In the latter case, the energy of a transition is given to an electron that is eventually knocked out. Internal conversion and γ decay are, in principle competing processes. However, in the present work, where the nuclei have "medium" Z (Z=42,44) and the transitions of interest have energies that are quite large (Eγ ≥ 600 keV) and are not of ΔI=0 type (see below), γ decay is the prime process.

The level energies and spin-parities (I^{π}) of excited states establish the level structure of the nucleus, called the level scheme (e.g. Figure 5-5). An additional property of an excited state is its lifetime (see Section 2.3.3).

The multipolarity of a γ-ray transition describes the electromagnetic character and angular momentum (λ) carried by the field. It is related to the spins and parities of the initial and final states that it connects. Angular momentum is conserved, the λ carried by the γ ray is constrained to

$$\left|J_i - J_f\right| \leq \lambda \leq J_i + J_f . \tag{2-5}$$

Parity is also conserved, the character of the transition will be electric (Eλ) if

$$\pi_i \pi_f = (-1)^{\lambda} \tag{2-6}$$

or magnetic (Mλ) if

$$\pi_i \pi_f = (-1)^{\lambda+1}. \tag{2-7}$$

These are the so-called spin-parity selection rules; i and f stand for the initial and final states respectively [7].

Only the λ of a γ-ray transition can be determined by measuring its angular distribution. To distinguish, for example, between M1 and E1 transitions requires additional information. An angular distribution is the observed γ-ray intensity as a function of angle relative to a chosen quantization axis. Typical choices for the quantization axis are the spin, beam direction, or fission axes. The shape of the distribution is given by the function:

$$Z_{\lambda\mu}(\theta,\phi) = \frac{1}{2}\left[1 - \frac{\mu(\mu+1)}{\lambda(\lambda+1)}\right]\left|Y_{\lambda,\mu+1}\right|^2 + \frac{1}{2}\left[1 - \frac{\mu(\mu-1)}{\lambda(\lambda+1)}\right]\left|Y_{\lambda,\mu-1}\right|^2 + \frac{\mu^2}{\lambda(\lambda+1)}\left|Y_{\lambda\mu}\right|^2, \quad (2\text{-}8)$$

where $Y_{\lambda\mu}(\theta,\phi)$ are the spherical harmonics, λ is the multipolarity, μ is its component, and θ,ϕ are the polar angles with respect to the quantization axis [20]. These distributions are anisotropic and differences between distributions are often enough to distinguish the multipolarity of the transition. Figure 2-6 shows a representation of the angular distribution for a stretched quadrupole (ΔI=2, λ=2, μ=2) and a stretched dipole (ΔI=1, λ=1, μ=1) where the spin axis has been chosen as the quantization axis.

Transitions can also have mixed multipolarity, this is described by the mixing ratio (δ) shown in Equation (2-9).

$$\delta = \sqrt{\frac{Intensity\ of\ \lambda'}{Intensity\ of\ \lambda}} = \frac{\langle f | E\lambda' | i \rangle}{\langle f | M\lambda | i \rangle} \quad (2\text{-}9)$$

λ' and λ are the two "mixed" multipolarities. This typically occurs for an unstretched E2 (ΔI=1, λ=2, μ=1) and a stretched M1 (ΔI=1, λ=1, μ=1). As a general rule, an electric transition will have a higher transition probability than a magnetic transition of the same λ. The transition rates also tend to decrease with increasing multipolarity [21].

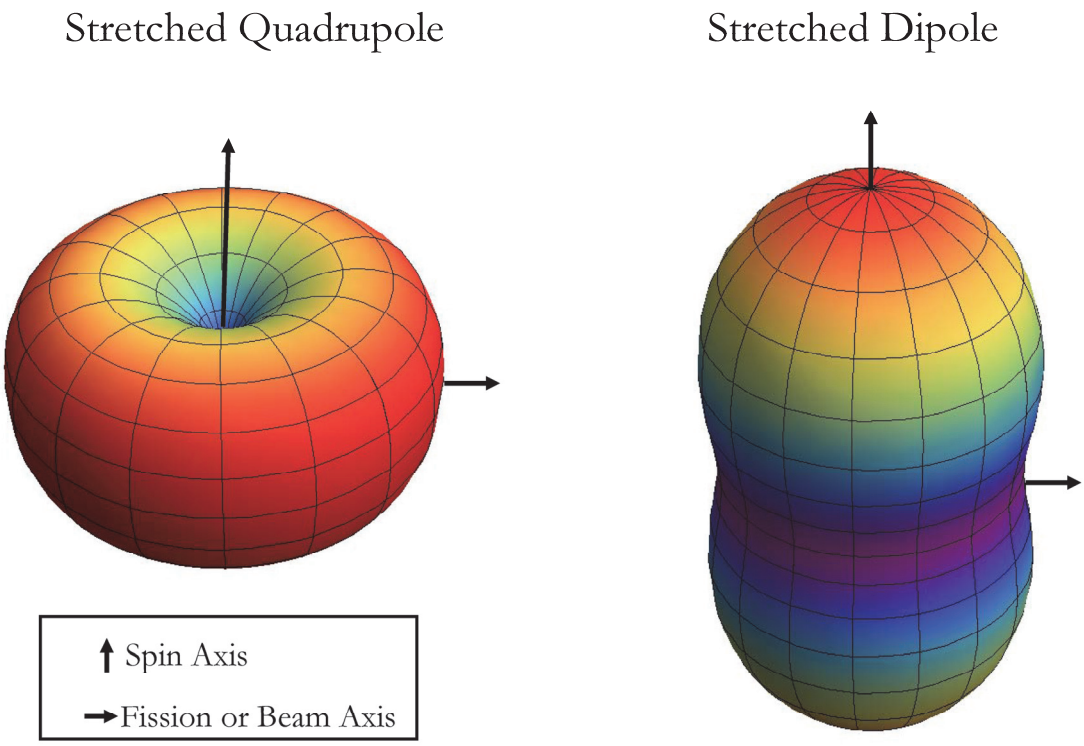

Figure 2-6: A three dimensional representation of the angular distribution function $Z_{\lambda\mu}$ for a stretched quadrupole and a stretched dipole. The spin axis has been chosen as the quantization axis. This figure is adapted from Reference [22].

There are 2I+1 possible orientations, m, for each nuclear spin state. The population of these substates are described statistically by the population parameter P(m), which is normalized such that $\sum_m P(m) = 1$. The measured angular distribution function, $W(\theta,\phi)$, is the shape of the distribution weighted by the particular population of states.

$$W(\theta,\phi) = \sum_{m_i,\mu} \left| \left\langle I_i m_i \lambda\mu \left| I_f m_f \right\rangle \right|^2 P(m_i) Z_{\lambda\mu}(\theta,\phi) \tag{2-10}$$

The population parameter can be reformulated into a statistical tensor $[\rho_k(I)]$ to describe the orientation of nuclear substates, see Reference [23] for further details. The effect of this reformulation upon $W(\theta,\phi)$ is shown in Equation (2-11).

$$W(\theta,\phi) = \sum_k \rho_k(I)\sqrt{2k+1}A_k(\delta,\lambda,\lambda',I_f,I_i)Q_k(E_\gamma)P_k(\cos\theta) \qquad (2\text{-}11)$$

Here, A_k are the angular distribution coefficients, the Q_k coefficients correct for the non-zero opening angle of the detector [24], and $P_k(\cos\theta)$ are Legendre polynomials. Only even values of k occur in Equation (2-11) due to parity conservation.

The pattern of the energy levels may provide a first important insight into the behavior of the nucleons, and sometimes even the shape of the nucleus. This pattern may also point to the model description which is most appropriate for the experimental observation.

When interpreting the level scheme, both non-collective and collective excitation modes have to be considered. Non-collective or single-particle like excitations involve the successive alignment of the nucleonic spins in individual orbitals. In the case of a deformed nucleus this alignment is along one of its symmetry axes. This mode of generating spin is, in principle, also valid for a spherical nucleus. The collective excitations include the rotation of the nucleus about an axis perpendicular to a symmetry axis and the oscillation of the nuclear shape (vibration). The former is always based on a static shape deformation. The latter is often based on a shape deformation, however, of "dynamic" type (see below). Non-collective excitations are associated with an irregular behavior of the level energies as a function of spin. In contrast, the rotational-like excitations are associated with a regular behavior where $E \propto I(I+1)$ [25].

A schematic of an angular momentum coupling scheme, sometimes called "deformation aligned", is shown in Figure 2-7. Here the individual nucleon has a spin labeled J. The other quantum numbers are those for the core angular momentum labeled R, and total angular momentum labeled I. The latter is the vector sum of the two former quantities. The symmetry axis (Z), the rotation axis (X), and an arbitrary laboratory-frame axis (Z_{lab}) of the nucleus are labeled as

well. The nucleus rotates about X with a rotational frequency ω. The projection of I onto the symmetry and rotation axes is given respectively by K and I_x. The expression for the latter is

$$I_x = \sqrt{I(I+1)^2 - K^2}\,. \tag{2-12}$$

P is the projection of I into the laboratory frame Z_{lab}.

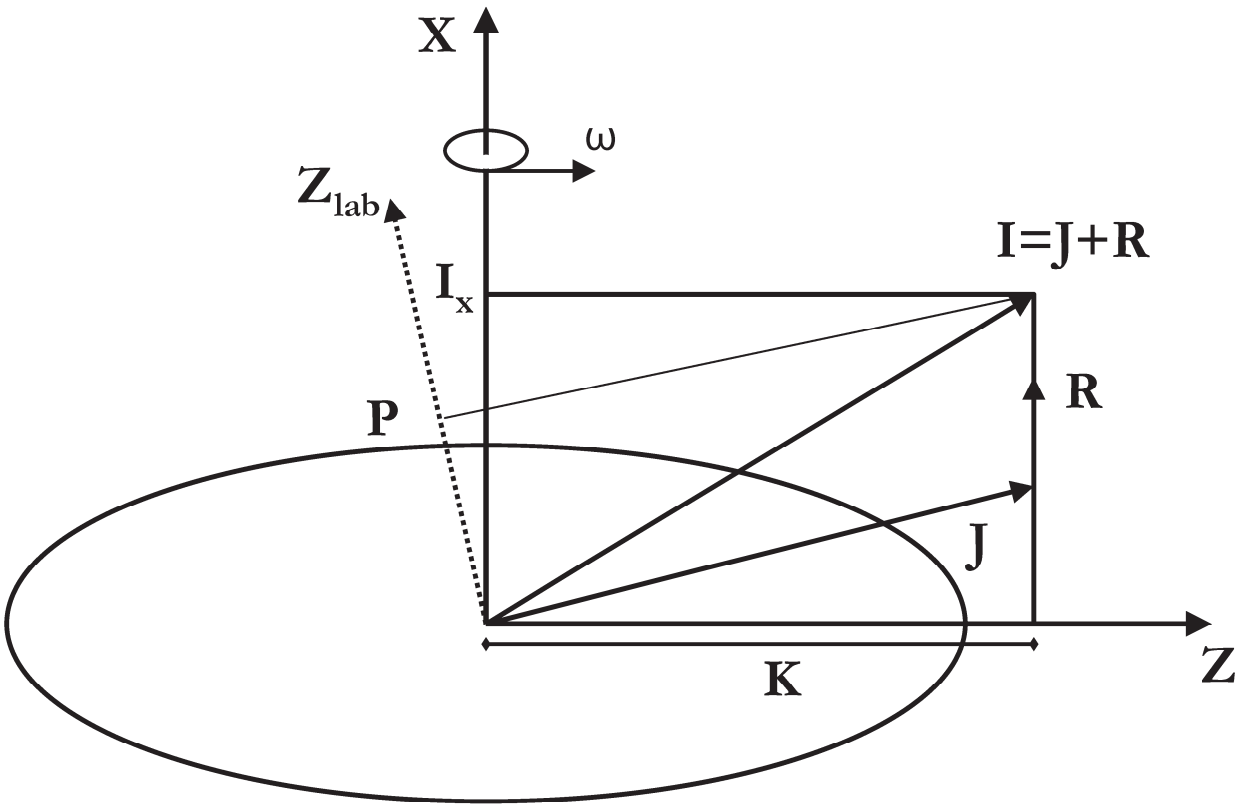

Figure 2-7: The vectors indicate the angular momentum coupling for a nucleus treated as a deformed core plus particle. I is the total spin, it is comprised of contributions from J, the sum of the single nucleon spins, and R, the rotation of the core. They are oriented on the symmetry axis (Z), the rotation axis (X), and an arbitrary laboratory frame axis (Z_{lab}) of the nucleus. Imagine that J precesses around Z. This figure is adapted from Reference [21].

Regularly behaving level sequences, where subsequent states are connected by E2 transitions are called rotational bands. If the rotational band is built upon a single-particle state, for example in an odd-mass nucleus, or a vibrational excitation, for example in an even-even nucleus, then K is not equal to zero (c.f. Figure 2-7). This is accounted for in the more general expression of Equation (2-13).

$$E = \frac{\hbar^2 \left[I(I+1) - K^2 \right]}{2\Im^{(0)}} \tag{2-13}$$

Here $\Im^0$ is the moment of inertia and it is considered as a constant. However, a realistic description usually requires treating the moment of inertia as a function of I or ω. Specifically, the moment of inertia for a rotational band tends to smoothly increase with spin. This is sometimes called centrifugal stretching which is analogous to the stretching of the bonds in a rotating diatomic molecules in molecular spectroscopy.

The rotational frequency can be defined as shown in Equation (2-14). The approximation assumes that I is large compared to K and that ΔI=2.

$$\hbar\omega = \frac{dE}{dI_x} \approx \frac{E_\gamma}{2} \tag{2-14}$$

For a comparison with theory, the experimental data, for example on excitation energy and spin, are transformed to the intrinsic frame by plotting these quantities as a function of ħω. The prescription for the latter is

$$\hbar\omega(I) = \frac{E_i - E_f}{I_x(I_i) - I_x(I_f)} \tag{2-15}$$

where i and f denote initial and final states respectively.

In the present context, it is also helpful to introduce the kinematic ($\Im^{(1)}$) and dynamic ($\Im^{(2)}$) moments of inertia, shown respectively in Equations (2-16) and (2-17) [21].

$$\Im^{(1)} = I_x \frac{dI_x}{dE} \approx \frac{(2I-1)\hbar^2}{E_\gamma} \tag{2-16}$$

$$\Im^{(2)} = \frac{d^2 I_x}{dE^2} \approx \frac{4\hbar^2}{\Delta E_\gamma} \tag{2-17}$$

In the limit of a "rigid rotor", $\Im^{(1)} = \Im^{(2)} = \Im^{(0)}$. In the case of a rotational band, $\Im^{(1)}$ contains information on the static properties of the nucleus, particularly deformation and pairing (a term that is explained in Chapter 6). $\Im^{(2)}$, on the other hand, expresses the response of the nucleus to a force. An example here is the so-called upbend or backbend of the moment of inertia that is amplified in the $\Im^{(2)}$ representation, see Figure 2-8. The upbend or backbend is attributed to the Coriolis force: If this force reaches a critical value it may dominate the behavior of certain valence nucleons, which are then not in coherent motion with the bulk of the nucleons.

The moments of inertia shown in Figure 2-8 are those for two rotational-like bands in ^{104}Mo: the ground-state E2 sequence and the positive-parity near-yrast sequence of the so-called γ-band are shown on the left and the right, respectively. The peak of $\Im^{(2)}$ for the ground-state band at $\hbar\omega \simeq 0.4$ MeV is thought to represent a set (pair) of two decoupled neutrons in the $h_{11/2}$ orbital. The first peak for the γ band occurs at a similar frequency and is likely associated with the same $h_{11/2}$ neutron excitations. The slight shift in frequency may be due to subtle differences in pairing between the two level structures. There is the onset of a second, high-frequency peak in the γ band that likely indicates the decoupling of another neutron pair or a proton pair.

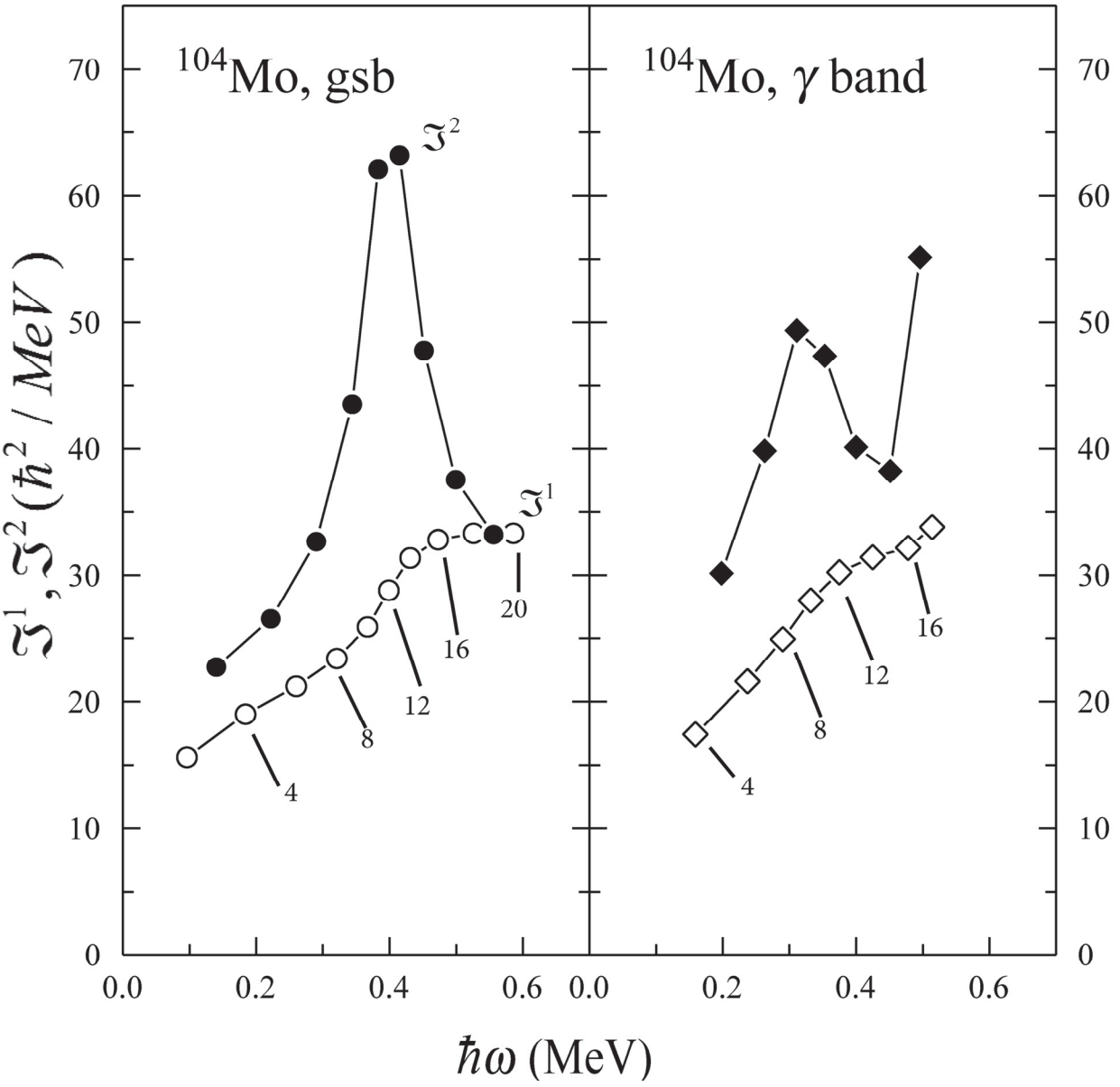

Figure 2-8: Kinematic ($\mathfrak{I}^{(1)}$, open symbols) and dynamic ($\mathfrak{I}^{(2)}$, closed symbols) moments of inertia, as a function of rotational frequency (ω), for the ground state band (left) and the γ band (right) in ^{104}Mo based on the level scheme [26]. Every other data point of the $\mathfrak{I}^{(1)}$ plot is labeled by its spin.

Vibrational excitations correspond to a dynamic effect, i.e., an oscillating shape that has on average the shape of the ground state of the nucleus. In some cases this is a spherical shape, in many cases this is a deformed shape and the vibration enhances the deformation effect. The

description of vibrational excitations is, in principle, based upon the same spherical harmonic expansion as given in Equation (2-1). A quantum of vibrational energy or a phonon, carries $\lambda\hbar$ units of angular momentum. The different types of phonons (λ) correspond to different multipole excitations ($\hbar\omega_\lambda$). The monopole excitation ($\lambda=0$) is an expansion and contraction of the entire nucleus, a "breathing" mode. The dipole excitation ($\lambda=1$) is the shifting of excess neutron density from one side of the nucleus to the other. The quadrupole excitation ($\lambda=2$) is relevant for this work; qualitative depictions of the two forms, β and γ, can be found in Figure 2-9 and are discussed hereafter. There are also octupole excitations ($\lambda=3$) and multiphonon excitations of the $\lambda=2$ type that can occur [27].

For deformed nuclei (deformed ground state), so-called β and γ vibration need to be considered. The β vibration is an oscillation along the nucleus's symmetry axis and has projection $K=0$. The γ vibration is an oscillation perpendicular to the nucleus's symmetry axis and has projection $K=2$. These vibrations can couple with rotations. Specifically a rotational band built on the β vibration is possible and has an initial 0^+ state (band head). A rotational band built on the γ vibration has an initial 2^+ state. Usually the γ band appears at lower energy than the β band. An example for a γ band is the near-yrast positive-parity sequence in ^{104}Mo. The moments of inertia of this band are shown on the right of Figure 2-8.

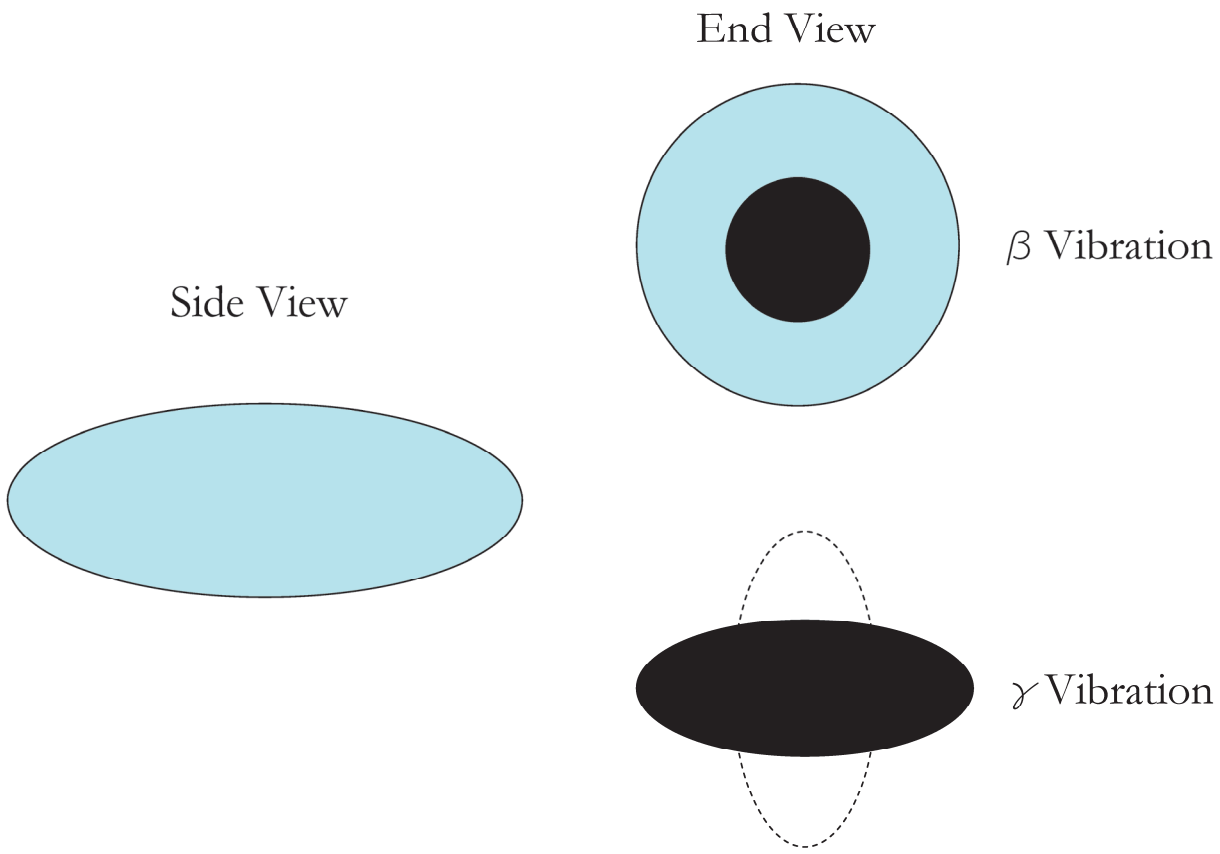

Figure 2-9: A schematic of certain quadrupole vibration modes is shown. The β vibration is an oscillation of the nucleus along the symmetry axis. The γ vibration is an oscillation upon an axis perpendicular to the symmetry axis. Notice that this axis changes with time.

The ratio of the energy of the 4^+ level over the 2^+ level of the ground state band (4/2 ratio) provides qualitative evidence as to the collective nature of a nucleus. A survey of this ratio is plotted as a function of neutron number for Mo, Ru, and Zr isotopes in Figure 2-10. Those isotopes studied in the present work are highlighted in green. For a perfect rotor, the ratio should be 3.33, as can be derived from Equation (2-13). The ratio for a perfectly vibrational nucleus is 2.0, as the energy levels are proportional to I. Those nuclei with a ratio <2.0 have non-collective excitations; sometimes they are also called shell model nuclei. Those nuclei with a ratio of ~2.7 are sometimes

referred to as transitional nuclei. These nuclei may have more complicated structural features often pointing to a softness to β or γ deformation [27]. However, the 4/2 ratio has its limitations; higher spin states need to be considered as faster rotation tends to stabilize deformation within certain ranges of spin (centrifugal stretching).

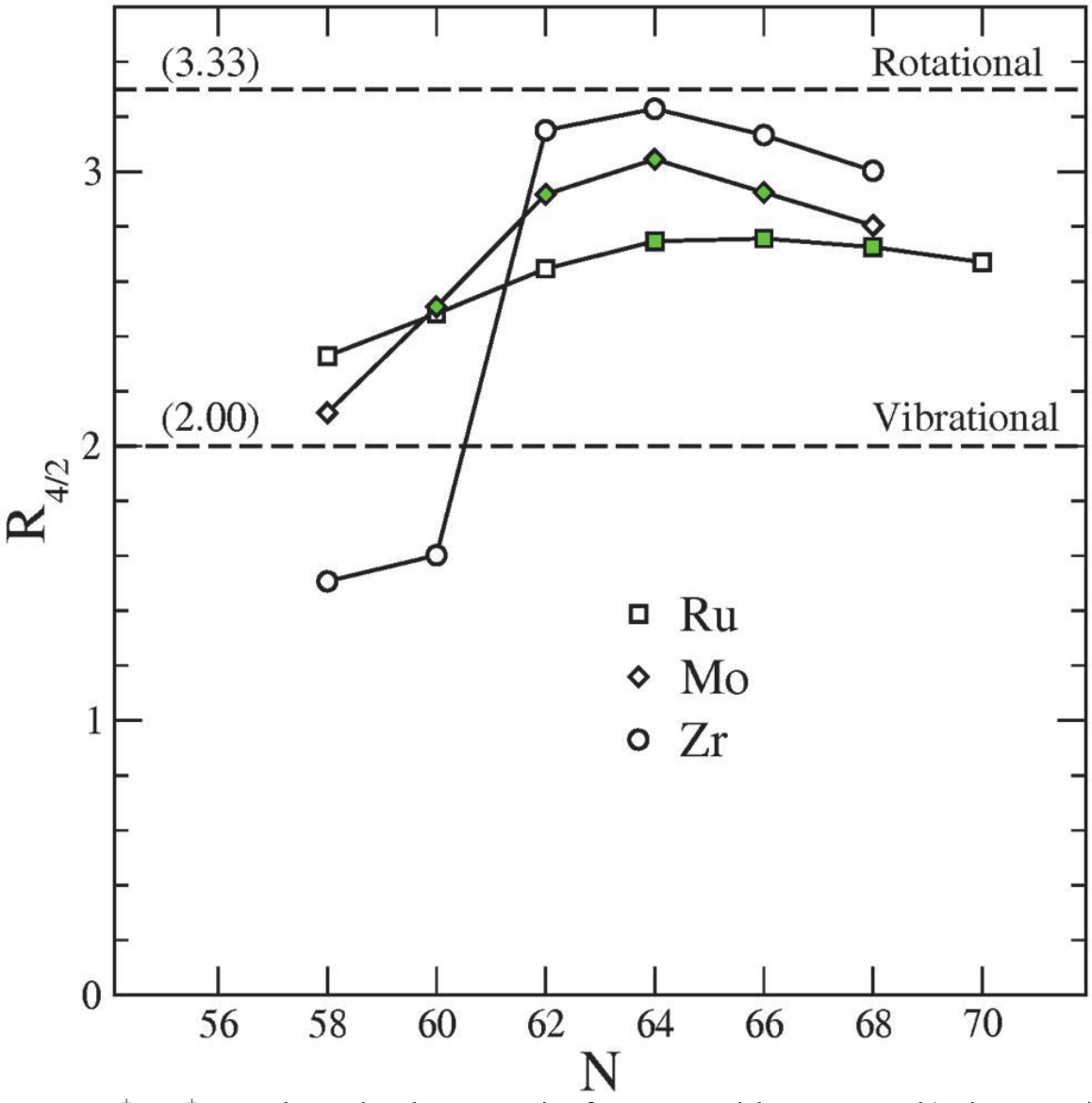

Figure 2-10: 4^+ to 2^+ ground-state band energy ratios for neutron-rich Ru, Mo, and Zr isotopes. The rotational and vibrational limits are displayed. For reference, shell-model nuclei often have ratios approaching 1.1. The nuclei studied are highlighted in green. On this level of comparison they are not clearly vibrational or rotational (see text).

2.3.3 Lifetime and Decay Laws

The measured observable in this research is the mean lifetime (referred to hereafter as just the lifetime) of the excited FF states. The lifetime (τ) is the average time that a nucleus is likely to

survive before it decays. The inverse of the lifetime is the transition probability ($T=1/\tau$), the probability per unit time that the nucleus will decay. The transition probability is often referred to as the decay constant. A related term not applied in this work is the half-life ($t_{1/2}$), the time necessary for half of the nuclei to decay ($t_{1/2} = \ln 2 \cdot \tau$). This section is based upon the presentation of the topic in Reference [1].

The definition of the transition probability, under the assumption that no additional nuclei are added and that T is constant regardless of the age of the nuclei, yields the expression

$$T = -\frac{(dN/dt)}{N}, \tag{2-18}$$

where N is the number of nuclei in the sample. Integrating Equation (2-18) gives the exponential law of radioactive decay, Equation (2-19). Notice that τ has been substituted for T in the expression and that N_0 is the initial number of nuclei.

$$N(t) = N_0 e^{-t/\tau} \tag{2-19}$$

By differentiating Equation (2-19), an expression for the activity [A(t)], the number of decays that occur per unit time, can be derived.

$$A(t) = \left|\frac{dN(t)}{dt}\right| = \frac{N_0}{\tau} \cdot e^{-t/\tau} \tag{2-20}$$

When measuring excited-state lifetimes the situation can arise where the state can decay by two or more different routes. Consider the case where there are two different states, a and b, that the initial state can decay to. The rate of decay to state a is determined by the partial lifetime τ_a and into state b by τ_b.

$$\frac{1}{\tau_a} = \frac{-(dN/dt)_a}{N} \quad and \quad \frac{1}{\tau_b} = \frac{-(dN/dt)_b}{N} \tag{2-21}$$

The total decay rate ($[dN/dt]_t$) is given in Equation (2-22), where $1/\tau_t=1/\tau_a+1/\tau_b$.

$$-\left(\frac{dN}{dt}\right)_t = -\left(\frac{dN}{dt}\right)_a - \left(\frac{dN}{dt}\right)_b = N\left(\frac{1}{\tau_a}+\frac{1}{\tau_b}\right) = \frac{N}{\tau_t} \qquad (2\text{-}22)$$

The initial excited state therefore decays according to Equation (2-19) with lifetime τ_t. This result is important; it shows that regardless of whether the lifetime is measured using the transition to state a or state b, the measured lifetime will always be the total lifetime. The partial lifetimes only describe the fraction of nuclei that decay through each route. This can be seen explicitly by inspecting Equation (2-23), which shows the growth of states a and b.

$$N_a(t) = \left(\frac{\tau_t}{\tau_a}\right)N_0(1-e^{-t/\tau_t}) \quad and \quad N_b(t) = \left(\frac{\tau_t}{\tau_b}\right)N_0(1-e^{-t/\tau_t}) \qquad (2\text{-}23)$$

2.3.4 Reduced Transition Probability and Quadrupole Moments

Once the excited-state lifetime has been measured, the reduced transition probability, and from there the transition quadrupole moment can be determined.

The lifetime of a state depends on the underlying nuclear structure, the availability of states to transition to, and the energy and angular momentum requirements of the photon making the transition. By removing the latter contributions, the reduced transition probability [$B(\lambda)$] is obtained. Here, λ designates the multipolarity of the associated γ emission (or internal conversion process). $B(\lambda)$ provides a measure of the underlying nuclear structure of a state.

The $B(\lambda)$ value can be extracted from experimental lifetime values using Equation (2-24) and accounting for the electric or magnetic character of the associated electromagnetic transition as well as the branching ratio [28].

$$\frac{1}{\tau_{E\lambda}} = T(E\lambda) = \frac{B(E\lambda)\downarrow}{1.819\cdot 10^{-23}\cdot BR}\cdot\frac{\lambda+1}{\lambda[(2\lambda+1)!!]^2}\cdot\left(\frac{E_\gamma}{\hbar c}\right)^{2\lambda+1}$$
$$\frac{1}{\tau_{M\lambda}} = T(M\lambda) = \frac{B(M\lambda)\downarrow}{1.648\cdot 10^{-21}\cdot BR}\cdot\frac{\lambda+1}{\lambda[(2\lambda+1)!!]^2}\cdot\left(\frac{E_\gamma}{\hbar c}\right)^{2\lambda+1} \quad (2\text{-}24)$$

The B(Eλ) and B(Mλ) are in units of $e^2fm^{2\lambda}$ and $\mu_N^2fm^{2\lambda}$ respectively, τ is in sec, T in sec^{-1}, BR is the branching ratio ($0<BR\leq 100$), and E_γ is in MeV. The constant μ_N^2 is defined as $(e\hbar/2m_pc)^2$ which equals 0.01589 MeV fm^3. The downward arrow (↓) indicates deexcitation $I_i \rightarrow I_f$. All the measured transitions in the present data are deexcitations. It is noteworthy to mention the relationship between excitation and deexcitation, which is

$$B\uparrow = \frac{2I_i+1}{2I_f+1}B\downarrow. \quad (2\text{-}25)$$

This relationship is useful if a result of a direct lifetime measurement is to be compared with lifetime information obtained from a Coulomb-excitation cross-section measurement.

The reported excited-state lifetimes are all measured from E2 γ transitions. Equation (2-26) is the application of Equation (2-24) for the case of an E2 γ transition.

$$\frac{1}{\tau_{E2}} = \frac{B(E2)\downarrow E_\gamma^5}{8.1617\cdot BR} \quad (2\text{-}26)$$

The units are the same as those for Equation (2-24).

The transition quadrupole moment (Q_t) can be constructed from the B(E2) value and provides a measure of the nuclear charge distribution's deviation from sphericity. The concept of shape deformation is introduced in Section 2.3.1, the Q_t values are presented in Chapter 5, and the

nuclear structure implications of changes in Q_t as a function of N, Z, and I are discussed in Chapter 6.

The B(E2) and Q_t values are related as shown in Equation (2-27) [8].

$$B(E2;K_iI_i \rightarrow K_fI_f) = \frac{5}{16\pi} \cdot \left\langle I_iK_i 2\Delta K \middle| I_fK_f \right\rangle^2 \cdot Q_t^2 \qquad (2\text{-}27)$$

The subscripts i and f denote the initial and final states of the transitions. The expression is brackets is a Clebsch-Gordan coefficient. See Appendix B for a list of commonly used Clebsch-Gordan coefficients. Q_t is in units of efm^2.

The transition quadrupole moment is an experimentally derived quantity which is identical to the intrinsic quadrupole moment Q_{20} [8, 29]. Hence the strength of the B(E2) value or the related quantity Q_t is an indication of the size of the quadrupole deformation. Due to the $B(E2) \propto Q_t^2$ relation, the constructed Q_t is not sensitive to the "sign" of the quadrupole deformation (prolate or oblate). Both Q_t and Q_{20} are defined in the body-fixed (intrinsic) frame of the nucleus.

There are other experimental techniques by which the size and "sign" of the quadrupole deformation can be measured. These techniques provide the static quadrupole moment Q_s, where Q_{20} has been averaged over the rotation of the nucleus. Q_s is sometimes called the spectroscopic quadrupole moment. Assuming axial symmetry, this quantity is related to Q_{20} as shown in Equation (2-28) [8].

$$Q_s = \left(\frac{3K^2 - I(I+1)}{(I+1)(2I+3)} \right) Q_{20} \qquad (2\text{-}28)$$

Some of these techniques take advantage of certain hyperfine effects. A popular example is the hyperfine splitting, due to the electric hyperfine interaction, in muonic Lu atoms (^{175}Lu is its most abundant isotope), see the discussion in Reference [8]. Another technique is the so-called

reorientation effect in Coulomb excitation, i.e. the reorientation of the nuclear axis caused by the electric field of the projectile after the nucleus has been excited, see the discussion in Reference 29. However, these techniques do not have the broad applicability the Q_t measurement has. For example, they are limited to rather low spin (Coulomb excitation) or to stable nuclei ("muonic" technique).

According to Reference 30, theory can use nuclear model wavefunctions to calculate a value for B(λ). Let $\left|\Psi_{IKP}\right\rangle$ represent the wavefunction of a state with spin I, where K is the projection of I onto the symmetry axis and P is the projection in the laboratory frame (see Figure 2-7 for a diagram of the angular momentum coupling of the nucleus). The matrix elements $\left\langle \Psi_{I_f K_f P_f} \left| \mathrm{M}(\lambda\mu) \right| \Psi_{I_i K_i P_i} \right\rangle$ make use of the electromagnetic multipole operator [M(λμ)] to describe the magnitude of a γ transition from an initial state (i) to a final state (f) (μ is the projection of the of λ). The matrix elements can be expressed in terms of reduced matrix elements, $\left\langle I_f K_f \| M(\lambda\mu) \| I_i K_i \right\rangle$, by using Clebsch-Gordan coefficients to remove the orientation dependence of P and μ as shown in Equation (2-29).

$$\left\langle \Psi_{I_f K_f P_f} \left| \mathrm{M}(\lambda\mu) \right| \Psi_{I_i K_i P_i} \right\rangle = \frac{\left\langle I_i P_i \lambda\mu \left| I_f P_f \right.\right\rangle}{2(I_f + 1)^{1/2}} \left\langle I_f K_f \| M(\lambda) \| I_i K_i \right\rangle \qquad (2\text{-}29)$$

The B(λ) is then the sum of the squared matrix elements averaged over the $(2I_i+1)$ substates of the initial level. It becomes:

$$B(\lambda) = \frac{1}{2I_i + 1} \left| \left\langle I_f K_f \| M(\lambda) \| I_i K_i \right\rangle \right|^2 \qquad (2\text{-}30)$$

The comparison of the experimental and theoretical values is often used to improve our understanding of the underlying nuclear structure. (Alternatively, theory may calculate the quadrupole moment directly.)

Weisskopf developed an approximation for the reduced matrix elements of Equation (2-30) [31]. The estimates imply that the excitation is single-particle in nature. By dividing a measured B(λ) by the estimate $B_{sp}(\lambda)$, the B(λ) is expressed in Weisskopf units [$B_{WU}(\lambda)$]. The expressions for the single-particle estimates are given in Equation (2-31) [32].

$$B_{sp}(EL) = \frac{1}{4\pi}\left(\frac{3}{3+L}\right)^2 (r_0 A^{1/3})^{2L}$$
$$B_{sp}(ML) = \frac{10}{\pi}\left(\frac{3}{3+L}\right)^2 (r_0 A^{1/3})^{2L-2} \qquad (2\text{-}31)$$

All quantities and constants have already been defined, a Weisskopf unit is dimensionless. If the value in terms of $B_{WU}(\lambda)$ is significantly larger than one, the excited state is said to be collective. In particular B(E2) values of tens to hundreds of Weisskopf units have been observed.

2.4 Concepts of Lifetime Measurements

Lifetimes of nuclear states cover a large time range. In the μs to s range, the lifetimes are usually measured with electronic-timing techniques, see e.g. [28] [33]. For very short lifetimes, i.e. $\tau \lesssim 1$ μs, Doppler-shift methods are commonly used, see e.g. [34]. For "ultra-short" lifetimes, i.e. $\tau \lesssim 1$ fs, the so-called crystal blocking technique can be applied [34]. It takes advantage of a comparison of the time scale of the nuclear process and that of the time of the nucleus to traverse an atomic spacing in a crystal.

Among the Doppler-shift methods, one distinguishes between the Doppler-shift attenuation method (DSAM) and the recoil-distance Doppler-shift method, also referred to as the "plunger" method. DSAM covers lifetimes in the range 10 fs $\lesssim \tau \lesssim$ 5 ps, whereas with a "plunger", a range of 1 ps $\lesssim \tau \lesssim$ 1 μs can be reached. In this work, the DSAM approach has been used; the ^{252}Cf source has a backing, in which the FFs are immediately stopped, i.e. within about 1 ps. The

various aspects of the DSAM approach are discussed hereafter. A brief discussion of the "plunger" method is also included. These methods are relevant for experiments where the recoil is a FF from a fission source or a product of a reaction initiated by an accelerated beam (of sufficient energy) hitting a target. The former case is relevant for this work, but the terms recoil or nucleus will be used to write this section in a more general fashion. This section is written based upon the presentation of the topic in Reference [28] and additional details specific to DSAM from References [35] and [36].

The frequency of an emitted wave becomes Doppler shifted when an observer and the wave source are in relative motion. The classic example given for the Doppler effect involves an ambulance emitting a siren. As the ambulance approaches an observer, the siren is shifted to a higher frequency because the waves are emitted closer together due to the relative motion. As it departs the relative motion has the opposite effect and the siren is shifted to a lower frequency. In this work, the Doppler Effect is relevant as a FF emits γ rays while "in flight", i.e. it is in relative motion with the γ-ray detectors.

The detected energy (E_γ) of a γ ray emitted by a recoiling nucleus is described by Equation (2-32), the relativistic Doppler shift formula:

$$E_\gamma = \frac{E_\gamma^0[1-\beta^2]^{1/2}}{1-\beta\cos\theta}. \qquad (2\text{-}32)$$

Here E_γ^o is the energy of the γ ray in the moving rest frame, β is the (constant) recoil velocity expressed as a fraction of the speed of light, and θ is the γ-ray emission angle relative to the recoil direction (fission axis). The angular dependence of the Doppler correction has no effect at θ=±90° and reaches a maximum at θ=0°, 180°.

Further inspection of Equation (2-32) leads to a concept known as Doppler broadening. The accuracy of the Doppler correction is dependent upon "knowing" both β and θ. There are several effects to be considered: the material-thickness effect, the finite opening-angle effect, and the aberration effect. The latter two considerations are discussed in Section 3.3. The material thickness effect, here the intended effect of the backing, adds a time dependence to β [$\beta \rightarrow \beta(t)$]. The moving nucleus of interest is slowing down in the backing; the effect due to the thickness of the ^{252}Cf source is negligible. During the slowing-down process, the velocity of the recoil reduces from the initial value $\beta=\beta_0$ to $\beta=0$ (nucleus completely stopped). Accordingly, the Doppler shift $\left|E_\gamma - E_\gamma^0\right|$ is a function of time. If the excited states of the recoiling nuclei decay during the slowing-down process the γ-ray lines are Doppler broadened, and the broadening is sensitive to the lifetime of the decaying state.

The DSAM measurement requires that the excited-state lifetimes being measured are of the same order as the stopping time of the recoil in the backing. If the lifetime is long compared to that time then the nucleus will be stopped and is seen to emit a γ ray with E_γ^0. If the lifetime is short compared to that time then the γ ray will be fully shifted since $\beta=\beta_0$. In these situations, there is no lineshape information and they represent the limits of the DSAM method. For excited-state lifetimes between the limits, the lineshape obtained is sensitive to the lifetime. The lineshape inherits an angular dependence from Equation (2-32) and sketched examples of lineshapes are shown in Figure 2-11.

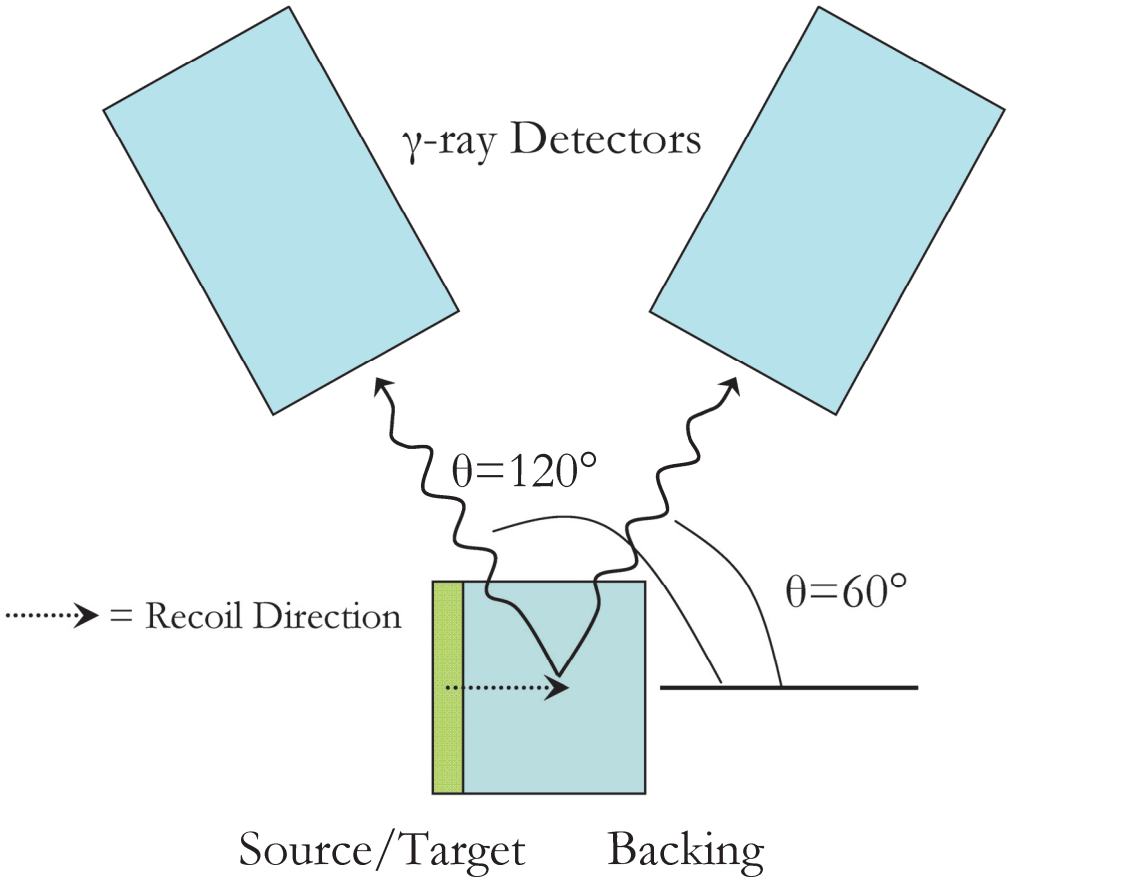

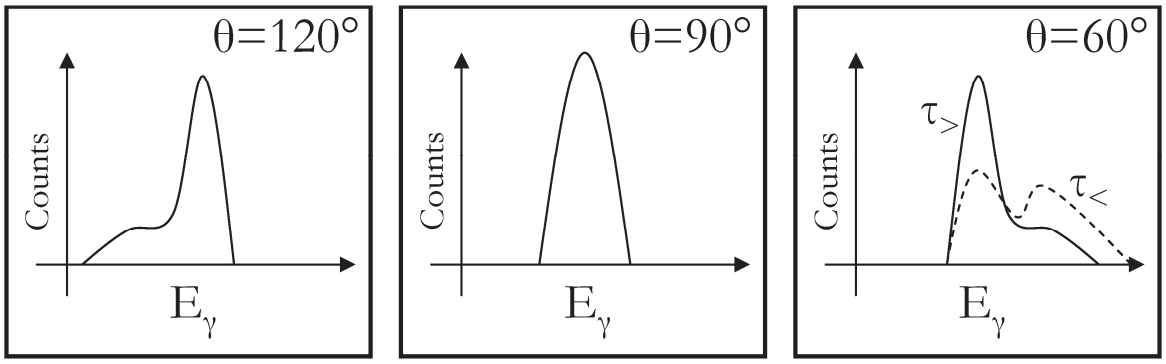

Figure 2-11: Principle of a DSAM setup and schematic display of γ-ray lineshapes at representative forward (θ=60°), backward (θ=120°), and 90° angles of detectors with respect to the direction of the moving γ-ray emitter. For the spectrum at θ=60°, the lineshapes for a lifetime $\tau=\tau_>$ and a lifetime $\tau_<<\tau_>$ are sketched.

Extracting lifetime information from a lineshape requires an understanding of how the recoil stops in the backing. $\beta(t)$ is dependent upon the initial velocity β_0 and the stopping power of the backing. The link between the stopping power and the nuclear velocity is made through use of the force equation

$$\frac{dE}{dx} = -M\frac{dv}{dt}, \tag{2-33}$$

where dE/dx is the stopping power of the backing material, M is the mass of the recoiling nucleus, and dv/dt is the change in velocity of the recoiling nucleus as a function of time. It is illustrative to integrate Equation (2-33) and reformulate it in terms of β as seen in Equation (2-34).

$$\beta(t) = \beta_0 - \frac{1}{Mc}\int \frac{dE(t)}{dx}dt \tag{2-34}$$

The time dependence of the stopping power has been made explicit, i.e. it changes as the recoil slows.

The number of recoils that decay at each $\beta(t)$ is determined by solving the Bateman equations, a procedure that has been widely discussed in the literature e.g. in Reference [35]. Bateman developed a method for setting up differential equations to determine the population of a state as a function of time from the initial population of states and the lifetimes of those states. The method is designed to handle more complicated growth and decay problems than the simple case of an initial state decaying to a "daughter" state introduced in Equation (2-18) of Section 2.3.3. The general solution to the Bateman equations [37] [38] is given in Equation (2-35).

$$N_k(t) = N_0 \prod_{i=1}^{k-1} \frac{1}{\tau_i} \cdot \sum_{j=1}^{k} \frac{e^{-t/\tau_i}}{\prod_{l \neq j}^{k} \left(\frac{1}{\tau_l} - \frac{1}{\tau_j} \right)} \tag{2-35}$$

$N_k(t)$ is the number of recoils that populate state k, N_0 is the number of recoils that populate the initial state [$N_0=N_1(t=0)$] , and τ_i is the lifetime of a state i. The initial population of states that feed the state of interest is constructed through a model. Additional considerations such as side feeding, branching ratios, and internal conversion are included to obtain a more precise solution. The correction for internal conversion in the case of a Mo or Ru nucleus a typical E2 transition of 600 keV as analyzed in this work is negligible (of the order of 0.2%).

A lineshape represents the number of recoils that decay as a function of the γ-ray energy. Translating the lineshape into an excited-state lifetime requires simulating the convolution of β(t) with the number of recoils that decay during each time step. A code developed by Wells and Johnson was used to accomplish this [36]. For further details on the simulation, see Section 4.3.

Details on the determination of the stopping power follow. There are two types of stopping: electronic and nuclear. Electronic stopping results from the Coulomb interaction between the recoiling ion and electrons in the backing. Nuclear stopping results from the collision of a recoiling nucleus with other nuclei in the backing. The stopping power for heavy ions can be roughly divided into three velocity regions: "low" (β<0.005) where nuclear stopping dominates, "high" (β>0.02) where electronic stopping dominates, and "intermediate" (β~0.005-0.02) where there is competition between the two. The recoiling ion has a large number of collisions with electrons and this number only increases with increasing β. There are many times fewer nucleus-

nucleus collisions. The higher energy loss associated with such collisions results in larger deflections to the recoil's trajectory.

At "low" to "intermediate" velocity direct measurement of the stopping power is difficult so there is a strong reliance on theory, specifically Lindhard theory [39] and its later refinements by Blaugrund [40]. Lindhard theory defines the stopping power in terms of the dimensionless energy and range parameters ε and p [28]. The stopping power is separated into nuclear and electronic components as described by Equation (2-36).

$$\frac{d\varepsilon}{d\rho} = \left(\frac{d\varepsilon}{d\rho}\right)_n + \left(\frac{d\varepsilon}{d\rho}\right)_e \tag{2-36}$$

with

$$\varepsilon = E\frac{aM_2}{Z_1 Z_2 e^2 (M_1 + M_2)} \text{ and } p = RNM_2 4\pi a^2 \frac{M_1}{(M_1 + M_2)^2}$$

where kinetic energy, atomic number, and mass of the stopping recoil are respectively E, Z_1, and M_1. The density (atoms/cm^3), atomic number, and mass of the backing are respectively N, Z_2, and M_2. The range of the ion, the Bohr radius, and the screening parameter are respectively R, a_0, and a, where $a=[0.8853a_0(Z_1^{2/3}+Z_2^{2/3})^{-1/2}]$. For further details on determining the nuclear and electronic components see Reference [28].

At "high" velocity, where electronic stopping is dominant, direct measurements can be made and empirical models based on experiment can be used. Much of the original work developing the stopping power tables in the "high" velocity region was done by Northcliffe and Schilling [41] and Ziegler and Chu [42]. The code for Stopping and Range of Ions in Matter (SRIM)[43] has widespread use. It calculates a nuclear stopping component based upon theory and an electronic component based upon refinements to the work of Reference [42].

A schematic for the setup of a plunger experiment can be found in Figure 2-12. A plunger apparatus essentially consists of a target or source and a stopper or degrader that can be moved with respect to each other. A recoil nucleus travels through vacuum from the source/target to the stopper/degrader. The lower-limit to a lifetime measured with this method is determined by the smallest measurable distance (d) between the stopper/degrader and the source/target.

Unlike in a DSAM experiment, the nuclei of interest travel in vacuum before they are brought to rest in the stopper. Accordingly, two peaks are obtained from the decay: a fully Doppler-shifted peak and a "stopped" peak. In the case of a degrader, the position of the corresponding peak is also considerably different from the position of the shifted peak. In the following discussion only a stopper is considered.

The method relies upon measuring, for a particular state, the ratio of the number of recoiling nuclei that decay in the stopper/degrader versus the total number of nuclei as a function of d. The total is found by determining the number that decay in flight and summing it with those that decay in the stopper/degrader.

If a nuclear level is populated instantaneously and has a lifetime (τ), then the number of nuclei decaying before hitting the plunger (I_s) is given by Equation (2-37).

$$I_s = \int_0^{t_f} \left(\frac{-dN}{dt} \right) dt = N_0 (1 - e^{-t_f/\tau}) \tag{2-37}$$

The flight time (t_f), equals d divided by the absolute velocity of the recoil (βc) and N_0 is the total number of decaying nuclei. The number of nuclei that decay in the stopper/degrader (I_0) is given by Equation (2-38) and rearranging to express I_0 as a fraction of N_0 yields Equation (2-39).

$$I_0 = \int_{t_f}^{\infty} \left(\frac{-dN}{dt} \right) dt = N_0 e^{-t_f/\tau} \tag{2-38}$$

$$I_0 / N_0 = I_0 / (I_0 + I_s) = e^{-t_f/\tau} = e^{-d/\beta c \cdot \tau} \tag{2-39}$$

The slope of the line produced by plotting the intensity ratio according to Equation (2-39) as a function of d on a log(y)/linear(x) scale will give the lifetime.

The overlap between the upper-limit lifetime for the DSAM approach (a few ps) and the lower-limit lifetime of the "plunger" method can be justified as follows. Consider a recoil velocity β=0.045 and a corresponding absolute velocity of 13.5 μm/ps. Limiting the closest distance, d_{min}, to 13.5 μm, which is realistic, translates into a lower-limit lifetime of 1 ps. If such a short distance cannot be measured, the sensitivity limit shifts towards longer lifetimes. In conclusion, the distance measurement is crucial for the sensitivity of the "plunger" method at this limit (no shifted peak). The upper-limit lifetime of the "plunger" method corresponds, in principle, to an absence of an unshifted peak or the need of a ridiculously large value for d. Then, however, electronic-timing methods become available.

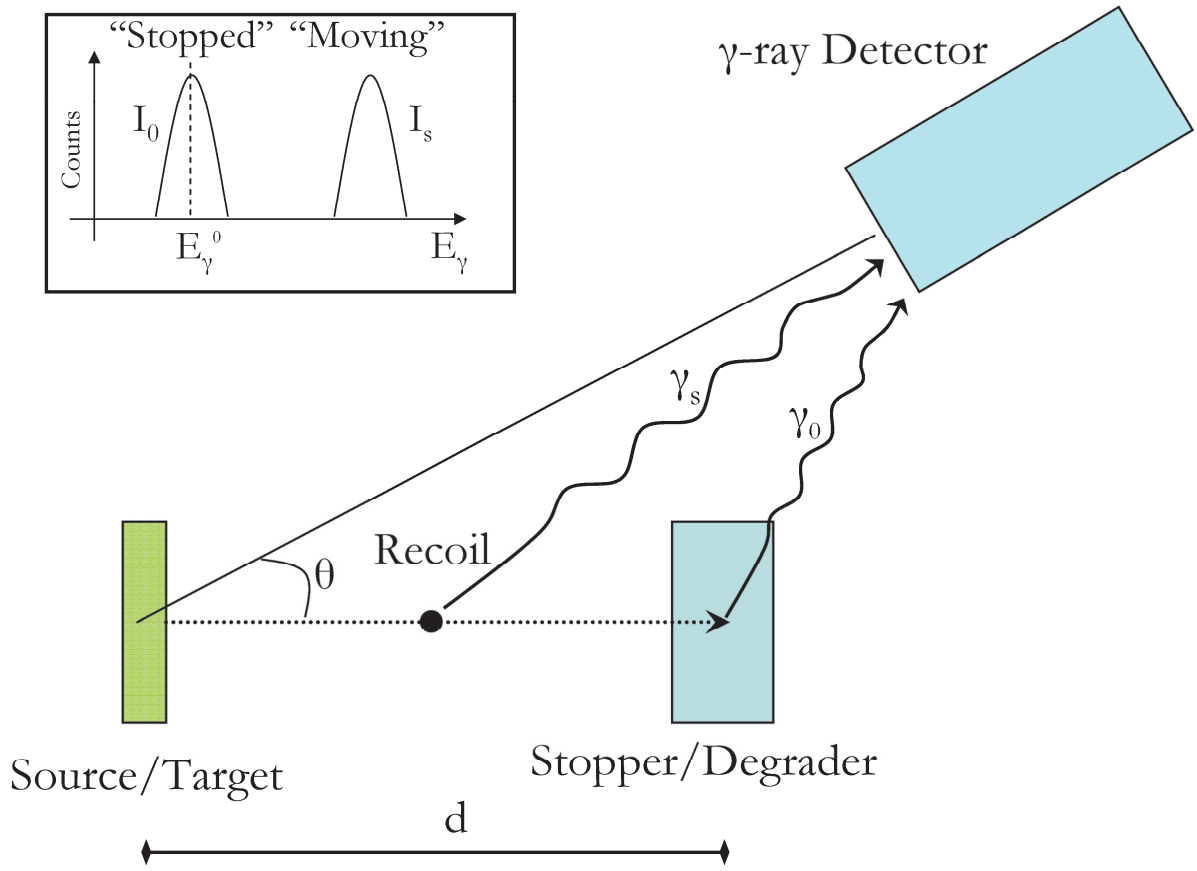

Figure 2-12: Schematic of a plunger setup for a recoil-distance Doppler-shift measurement. For the sake of the argument, only a "forward" detector is considered. The distance d between source/target and stopper/degrader must be varied. The recoil can be either a FF from a fission source or a residue from a reaction using an accelerator beam and a target.

2.5 Interaction of Radiation with Matter

As discussed in Section 2.2, the fission of ^{252}Cf releases FF's which are ionized, γ rays, and neutrons. The neutrons are not detected in the present experiment. The interactions discussed are those relevant for the detection of γ rays and charged particles. The former are detected in the HPGe crystals of Gammasphere, the latter in a fast-plastic scintillator array, called Hercules, which is described in Chapter 3. The combination of these detectors provides an efficient way to select a FF (a nucleus) and perform DSAM lifetime measurements for the nucleus of interest.

2.5.1 Photon Interactions with HPGe Crystals

A γ ray can interact with matter such as a HPGe crystal through three different processes: the photoelectric absorption, Compton scattering, and pair production. In the photoelectric process, an atomic electron absorbs the entire energy of the photon and an electron is jettisoned from the atom. In the case of Compton scattering, the electron only absorbs part of the photon's energy and this results in a lower-energy outgoing photon that may or may not be observed, and a scattered electron. Pair production requires that the photon's energy is at least twice the rest mass of an electron (1.022 MeV), and means that a photon interacts with the nucleus and produces an electron-positron pair. The positron typically annihilates within a few hundred picoseconds [44], producing two 511 keV photons. If all of a photon's energy is deposited in the HPGe the photopeak energy is recovered. If the photon interacts with the HPGe and then scatters out of the crystal, an incomplete energy is recovered that increases the background. To reduce this background it is prudent to veto the γ-ray hit recorded in the HPGe crystal that scatters out of the crystal. This leads to the concepts of a Compton-suppression shield.

The cross sections for the photoelectric, Compton scattering, and pair production processes within a HPGe crystal are shown in Figure 2-13. The interaction cross section is a function of the photon energy and the atomic number (Z) of the absorber (HPGe crystal). The photoelectric process dominates below ~100 keV, Compton scattering around ~800 keV, and pair production above 3 MeV. The γ-ray transitions studied in this work cover a range of 180 to 1100 keV. Pair production is negligible in the present context.

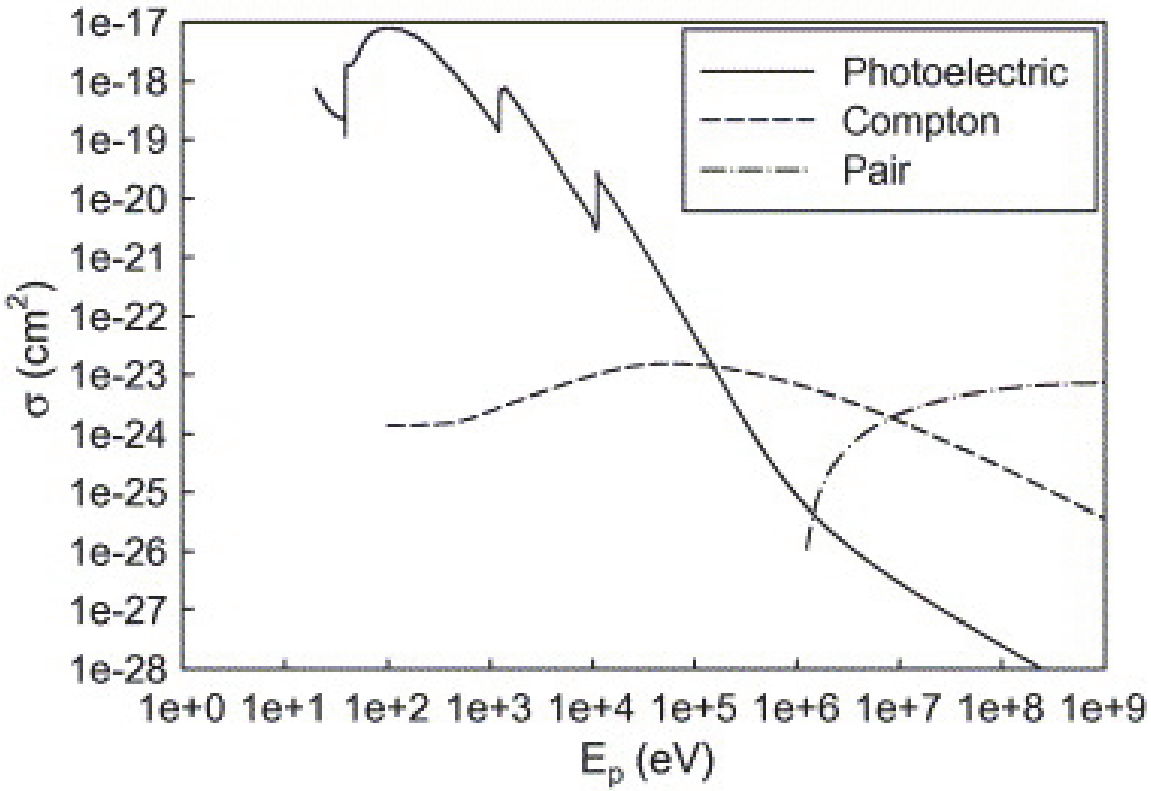

Figure 2-13: The interaction cross sections for the photoelectric, Compton scattering, and pair production processes as a function of γ-ray energy in a HPGe crystal. The figure is reproduced from Reference [45].

The total photopeak efficiency of a detector array is expressed as the product of the number of detectors (N), the solid angle covered by each detector (Ω), and the fraction of γ rays that deposit their entire energy in the detector (ϵ_p). Gammasphere has a total photopeak efficiency ($N\Omega\epsilon_p$) of ~10% for a 1.3 MeV γ ray.

The quality of the a γ-ray spectrum can be described by the peak to total (P/T) ratio, the number of counts in the peak divided by the total counts in the spectrum. The P/T ratio can be expressed in terms of the following equation:

$$P\Big/T = \frac{\varepsilon_P}{\varepsilon_P + \varepsilon_C/R} \tag{2-40}$$

Here ϵ_P once again is the fraction of γ rays hitting the detector that deposit their full energy. The quantity ϵ_C is the fraction that Compton scatter and deposit only part of their energy. The quantity R is the so-called background reduction factor determined by a Compton-suppression shield. In the present work the Gammasphere array has been used (see Sec. 3-3). In an effort to maximize the ϵ_P fraction, the Gammasphere detectors were made with the largest HPGe crystals available at the time of construction, i.e. 8.0 cm x 7.1 cm diameter cylinders. As much of the remaining space as possible was given to the Compton-suppression shield to maximize the R factor. The use of a bismuth germanate suppression shield leads to a P/T of 0.6 as compared to 0.25 without suppression for a 1.3 MeV γ ray [46].

The resolution of the photopeak is also of importance when discussing the quality of a γ-ray spectrum. The resolution is expressed as the full width of the peak at half its maximum height (FWHM). A HPGe detector typically has a resolution (FWHM) of 2.1 keV at 1.3 MeV [47].

2.5.2 Charged Particle Interactions with Plastic Scintillators

As a charged particle moves through a plastic scintillator atomic and molecular excitations occur which cause the subsequent emission of visible light. The transfer of energy from the kinetic energy of the moving particle to these atomic and molecular excitations is responsible for the energy loss. A photo-multiplier tube coupled to the scintillator converts this light to an electrical signal and then amplifies it. The resultant electrical pulse is proportional to the kinetic energy of the charged particle. It also carries timing information.

The plastic scintillator used for the charged particle identification is polyvinyltoluene. Its typical elemental composition is according to Saint Gobain-Bicron: 4.73 x 10^{22} C atoms/cc, 5.24 x

10^{22} H atoms/cc, 3.50 x 10^{19} N atoms/cc, and 1.70 x 10^{9} O atoms/cc (scintillator BC-498) [48]. The peak wavelength is in the 410-440 nm range. The scintillator light output is reasonably high (typically 25-30% NaI), and the scintillator has a short, 2.4 ns decay constant. The fast timing allows for the measurement of an accurate time of flight (ToF) measurement. The low density and relatively small atomic number lead to poor energy resolution. This resolution is still sufficient to separate the light fragment (LF) from the heavy fragment (HF) on a map of the ToF versus the pulse height, see Section 4.2. An example of the pulse height separation for a thin (0.97 mg/cm^2) fast plastic scintillator when commissioning Hercules is shown in Figure 2-14.

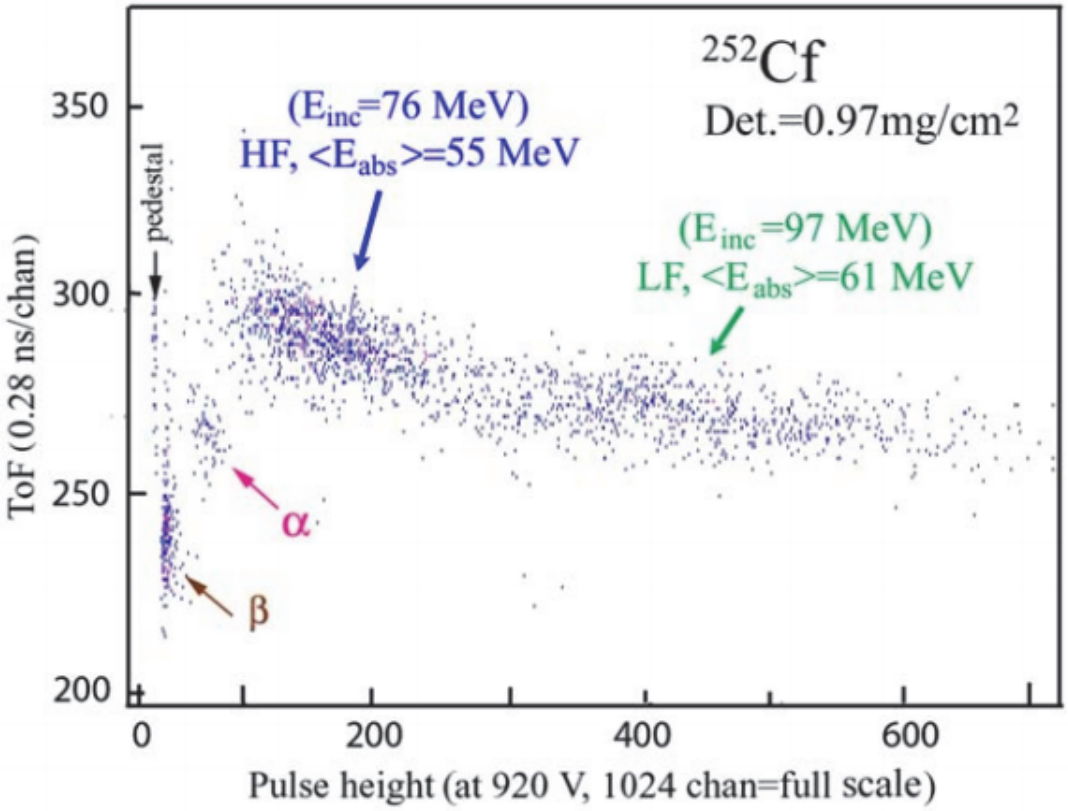

Figure 2-14: ToF vs. pulse height of LF and HF from a ^{252}Cf fission source. The fast plastic scintillator had a thickness of 0.97 mg/cm^2. The different dE/dx between the LF and HF was enough to separate the groups. E_{inc} and <E_{abs}> represent the incident and average absorbed energies. The figure is reproduced from Reference [49].

Chapter 3: Experimental Setup

3.1 Overview

The experiment, upon which this work is based, was performed at the Gammasphere location at the ATLAS accelerator site at Argonne National Laboratory (ANL). The nuclei studied are FFs of a ^{252}Cf fission source. The ^{252}Cf source described in Section 3.2 was positioned in the center of Gammasphere. This 4π array of nominally 108 Compton-suppressed high purity germanium (HPGe) γ-ray detectors [46], [47] is described in Section 3.3. The Gammasphere detectors are arranged into has 17 rings. The numbering for the rings starts at what would be considered the most forward position in an experiment using an accelerator beam. The first two rings of Gammasphere, which contain 10 detectors total were removed to make room for Hercules. Hercules is a 64 element fast-plastic detection device, see Section 3.4. Hercules was designed to detect residue nuclei from fusion-evaporation reactions [49], where a target foil is hit by an accelerator beam of projectiles with sufficiently high energy (to overcome the Coulomb barrier). Due to the kinematics in such reactions the residue nuclei are "forward peaked", i.e., they are spread out in a cone around the beam axis with a rather narrow angular range. As suggested in Sec. 2.4 of Reference [49], Hercules can also be used as a FF detector. It is particularly useful in a DSAM experiment, like the present one, as it helps to define the fission axis. Figure 3-1 illustrates the arrangement of the ^{252}Cf source, Hercules, and Gammasphere during the experiment.

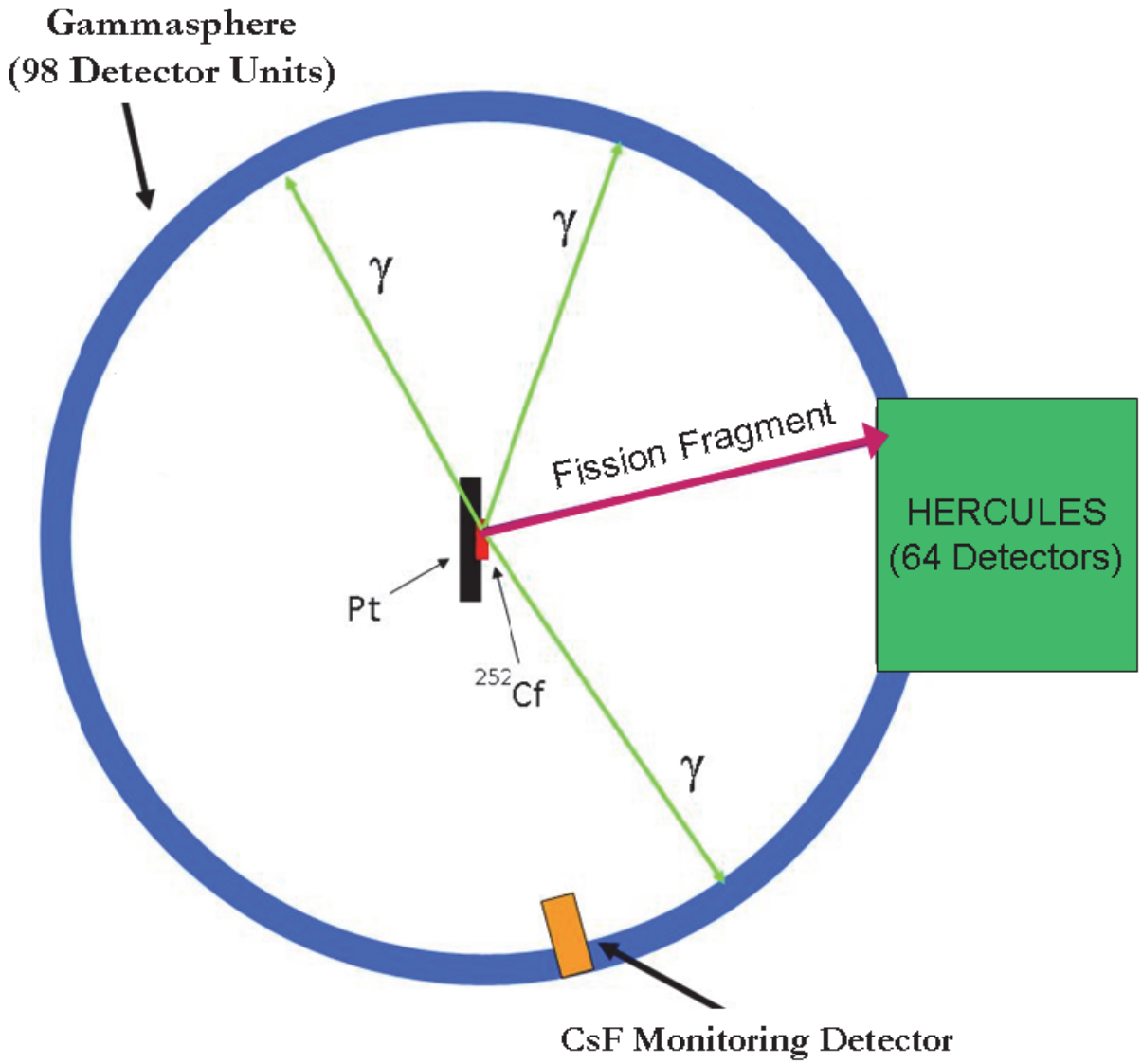

Figure 3-1: Schematic representation of the experimental setup. The ^{252}Cf source is mounted on the Pt backing placed in the center of Gammasphere and oriented to face Hercules. Only the fragment hitting Hercules is indicated, the partner fragment is stopping in the Pt backing. The CsF detector is for monitoring purposes (see Section 4.1.1).

3.2 ^{252}Cf Source Arrangement

The ^{252}Cf source used in the experiment was fabricated at the High Flux Isotope Reactor at Oak Ridge National Laboratory and then shipped to ANL. The source material was made in the reactor by starting with ^{239}Pu and using the neutron-capture and beta-decay processes to finally

produce a sufficient quantity of ^{252}Cf. Figure 3-2 shows the scheme by which this is accomplished [50].

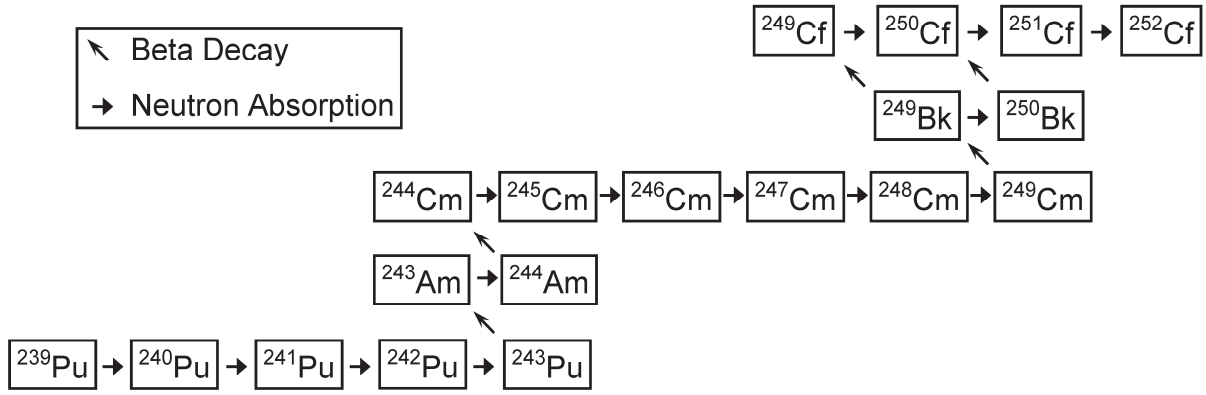

Figure 3-2: The production of ^{252}Cf according to Reference [50]. The arrows indicate the capture and decay processes explained in the legend. The intermediate products differ in the vertical direction by one unit of atomic number and in the horizontal by one unit of neutron number.

Table 3-1: The initial isotopic mass distribution for the ^{252}Cf source used in this experiment (labeled 10R13Cf Electrodeposition). The atomic and weight percentage values have decayed six months by the start of the experiment.

Isotope	$t_{1/2}$ (yrs)	Atom %	Weight %
^{249}Cf	351	12.78	12.68
^{250}Cf	13.08	23.04	22.94
^{251}Cf	898	9.83	9.83
^{252}Cf	2.654	54.35	54.55

The ^{252}Cf source had an α activity of 228μCi at the start of the experiment. ^{252}Cf has a half-life of 2.646 years and is unstable to both α emission and spontaneous fission: 96.9% of the decays result in α emission (6.217 MeV) and 3.1% spontaneous fission [51]. The short half life, combined with the strength of the fission branch, gives ^{252}Cf a specific activity of 536 Ci/g for spontaneous fission. Other spontaneous fission sources, most notably ^{248}Cm ($t_{1/2}$=3.5·10^5 yr), could be used, but of the sources available none have as high a specific activity for spontaneous fission as ^{252}Cf. This

allows ^{252}Cf sources to be thinner and therefore minimize collisions between FFs and the source material.

As indicated in Table 3-1, the source is not a pure one. The source will continue to be referred to as a ^{252}Cf source, since the contaminants are longer lived than ^{252}Cf.

Figure 3-3 illustrates the source arrangement. The ^{252}Cf material was electro-deposited on a 0.204 mm thick platinum disk of 16 mm diameter. The active spot of the material has a diameter of 6 mm. The source is covered with a thin Au foil (243 $\mu g/cm^2$). This prevents ^{252}Cf atoms, which have not yet decayed, from migrating into the surrounding vacuum chamber if they receive enough energy from a collision with a FF or α particle to leave the surface of the source. The spacing between the Pt disk and the Au foil was ~2 mm. The Pt disk was mounted in an Al frame. The frame was part of a source holder, which was then mounted inside a vacuum chamber, in the center of Gammasphere, with the Au-foil side facing the Hercules detectors.

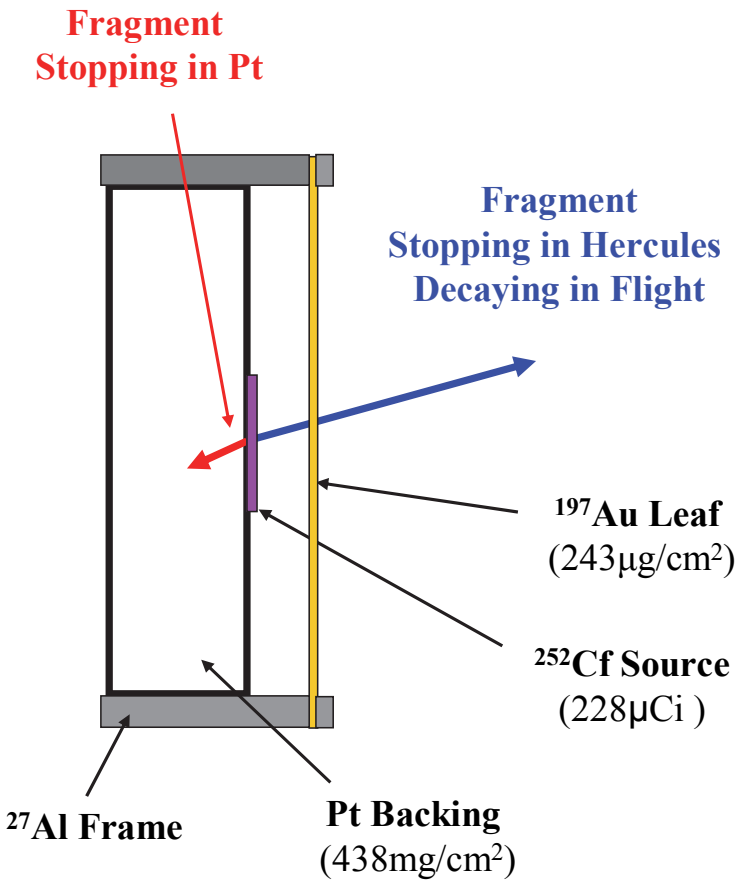

Figure 3-3: Sketch of the ^{252}Cf source arrangement. The source is mounted on a Pt disk. The source is facing towards Hercules. The Au foil stops only loose ^{252}Cf atoms. DSAM analysis is performed on the FFs stopping in the Pt backing. RIV g-factor analysis is performed on the FFs recoiling into vacuum to be detected by Hercules.

3.3 Gammasphere

Gammasphere is an array of 108 Compton-suppressed HPGe detectors for γ detection; see Figure 3-4. The cylindrical HPGe crystals are approximately 7.1 cm in diameter and 8 cm in length. Their front faces are located 25.4 cm from the target position (in this case the source position); giving them an opening angle of 7.4° (half angle). Of the 7 bismuth germanate (BGO) crystals surrounding each HPGe crystal and acting as a Compton-suppression shield, 6 are arranged in a hexagonal structure around the HPGe crystal and the seventh is located behind it (see Figure 3-5). For a detailed discussion of the performance and characteristics of this device, see References [46] and

47. In the present experiment the face of each HPGe detector was covered with 0.05 mm of Ta and 0.25 mm of Cu to absorb low-energy x-rays (<50 keV) and dedicate the detector to counting the higher-energy γ-transitions of interest. In the Gammasphere array about one half of the solid angle is taken up by the HPGe detectors and the other half by the BGO shields. As mentioned in Sec. 3.1, two rings of Gammasphere were removed (10 detectors).

The concept of a Compton-suppression shield has been introduced is Section 2.5.1. To prevent false vetoes for such a suppression, the BGO detectors are shielded from direct γ rays by a tungsten alloy known as hevimet (93 wt % W, 4 wt % Ni, and 3 wt % Cu).

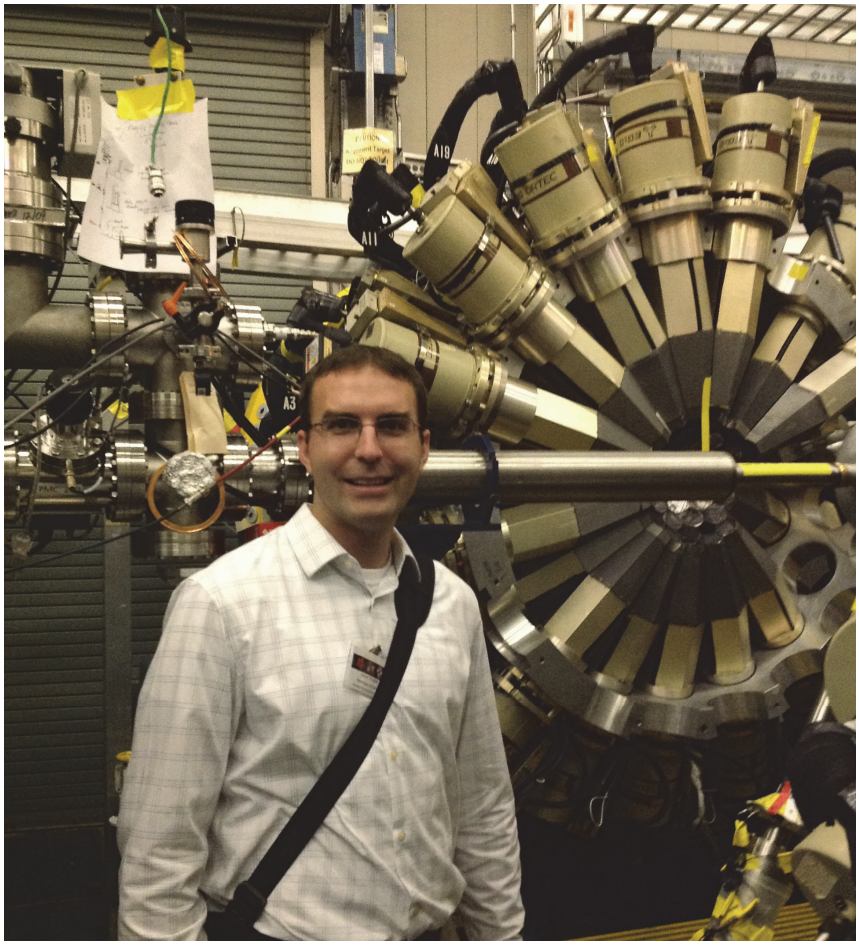

Figure 3-4: Photograph of Gammasphere with the author. Gammasphere has two hemispheres. These are open here to allow access to the detectors and the target position. The BGO Compton suppressors and the liquid-nitrogen filled dewars for cooling the HPGe detectors are recognizable.

Figure 3-5: The modus operandi of Gammasphere. The HPGe detectors, their surrounding BGO Compton-suppression shields, hevimet shields, electronics, liquid nitrogen cooling system, and the support structure for a so-called hemisphere are all displayed. The γ rays illustrate a photoelectric interaction where all of the γ-ray's energy is deposited in the HPGe crystal and two Compton-scattering interactions where the BGO shield acts as a suppressor.

The observed energies (E_γ) of the γ rays emitted by the moving FFs are Doppler shifted [see Equation (2-32)]. The LFs and HFs have average β values of 0.0461 and 0.0346 respectively [55]. Due to their greater velocity, the LFs require a larger Doppler correction than the HFs. The angular dependence of the Doppler correction has minimal impact at θ=90° and then increases as θ approaches 0° or 180°.

The Doppler effect does also degrade the γ-ray detector's energy resolution. This effect is due to the fact that the opening angle of a γ-ray detector is non-zero. The γ rays that strike the detector will have slightly different Doppler shifts depending upon where the strike occurs. A schematic of the situation is provided in Figure 3-6. The opening angle of the detector is Δθ. The effect this has on the energy resolution (ΔE) of a detector is expressed by Equation (3-1) [52].

$$\Delta E = E_\gamma^0 \left(\frac{\beta \sin\theta}{1 - \beta \cos\theta} \right) \Delta\theta \qquad (3\text{-}1)$$

To minimize the Doppler broadening effect more than 1/2 of the Gammasphere detectors have longitudinally segmented outer electrodes. By means of a position signal the detector opening angle (7.4° half angle) can be essentially reduced by a factor of two [53] (3.7° half angle). The effect is largest at 90° with respect to the beam axis. Hence preference for segmentation was given to those detectors.

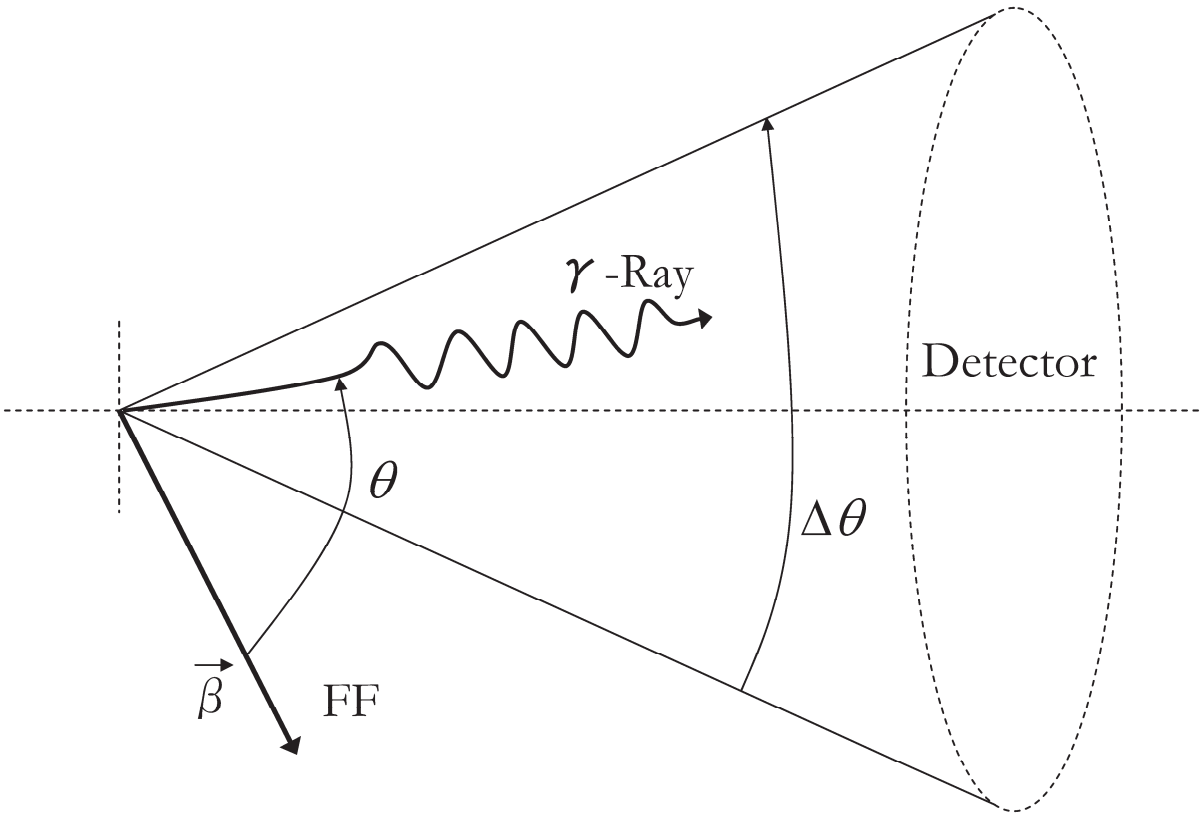

Figure 3-6: Schematic of the Doppler broadening scenario. The opening angle and angle of γ emission relative to the fission axis, are labeled by Δθ and θ respectively.

The Lorentz transformation between the laboratory system (θ_{lab}) and the recoil's moving system (θ_r) gives rise to what is known as the aberration effect. The relationship between the systems is described by Equation (3-2) [28].

$$\cos\theta_{lab} = \frac{\cos\theta_r + \beta}{1 + \beta\cos\theta_r} \tag{3-2}$$

This results in a small change in the angle itself, but more importantly, it changes the effective solid angle subtended by the γ-ray detectors. Expressing the effect as it relates to solid angle (dΩ) leads to

Equation (3-3) [28]. Essentially, as β increases, those detectors forward of the direction of motion become "larger" and any measured angular distribution will be forward focused.

$$\frac{d\Omega_r}{d\Omega_{lab}} = \frac{1-\beta^2}{(1-\beta\cos\theta_{lab})^2} \tag{3-3}$$

3.4 Hercules

The 64 elements of the Hercules device are arranged in 4 rings, see Table 3-2. Each element is located 23.2 cm from the ^{252}Cf source and has an arc-type shape. They cover angles θ =4.1°-26.8° and φ=0°-360°. Figure 3-7 shows a photograph of the array.

Table 3-2: The geometry of Hercules. Listed are the number of detectors in each ring, the angles subtended by each ring, and the solid angle coverage of the Hercules array. The distance between the source and the detector array is 23.2 cm.

Ring	Detectors	θ° in	θ° out	msr/det.	msr/ring	θ° avg
1	8	4.1	9.6	8.99	71.9	6.85
2	14	9.7	15.3	9.49	132.9	12.50
3	18	15.5	21.2	10.80	194.4	18.35
4	24	21.3	26.8	10.20	245.0	24.05

The fast-plastic scintillator foils are produced at Washington University using a product from Saint Gobain called Beta Paint (BC-498). The plastic scintillator (polyvinyltoluene, see Section 2.5.2) is initially dissolved in xylene. The scintillator material can then be spun as the solvent is evaporated to produce foils of various thicknesses [54]. In the present experiment, the surface density of the scintillators varies between 1.5 and 2.5 mg/cm^2. This corresponds to thicknesses of 13.5 to 22.5 μm. The average kinetic energy of a LF (e.g. ^{104}Mo) is 103.77 MeV and that of a HF (e.g. ^{144}Ba) is 79.37 MeV [55]. The fragments will penetrate to a depth of 21.7 and 19.4 μm, respectively, in a scintillator foil. The 6.217 MeV α particle deposits 1.2-2.0 MeV in the 1.5-2.5 mg/cm^2 fast plastic.

The scintillator thicknesses were chosen to be rather thin, in order to have a small pulse-height signal for the α particle (ΔE signal). In the thinner plastic, the FF pulse height is also a ΔE signal, in the thicker plastic, the pulse height represents the total energy of the FF. Even a ΔE signal for the FFs is sufficient to identify them. In order to increase their pulse height somewhat, the scintillators were covered with 150 μg/cm Al leaf. This reflected the light towards the light guides (see below) and increased the pulse height.

The fast plastic scintillator emits light mainly in the visible range. The scintillators are coupled to 1.42-cm-thick UV-transparent Lucite light guides (arc-type shape). The light guides are coupled to photomultiplier tubes (Hamamatsu R1450) that are potted in 0.5-mm-thick μ-metal magnetic shields with an outside diameter of 2.012 cm. The tubes are then connected to voltage dividers encased in 1.0-mm-thick Al cylinders with an outside diameter of 1.91 cm. The light guides pass through an Al vacuum-sealed plate. This allows the heat from the divider chains to be dissipated by an air-cooling system.

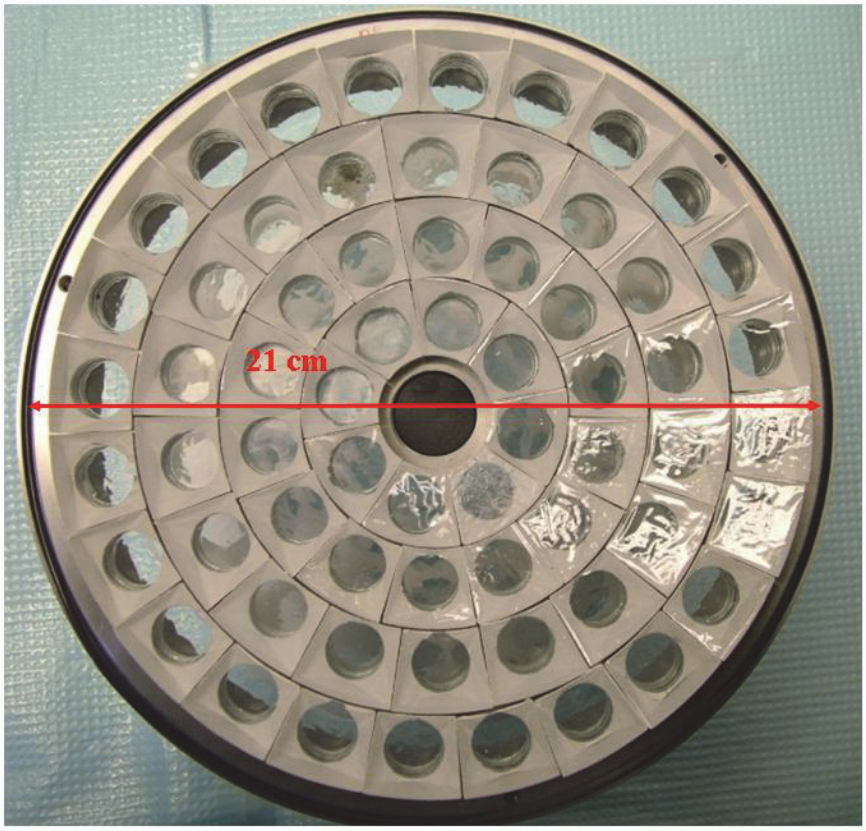

Figure 3-7: Photograph of the Hercules array as seen from the ^{252}Cf source position. Note that during the experiment the plastic scintillators were covered with Al leaf (see text).

At 23.2 cm from the source, Hercules has solid angle coverage of 4.9% of 4π. Conservation of momentum demands that the LF and HF are emitted in opposite directions. This boosts the number of fission events detected by Hercules to 9.8%. Fission is isotropic. The FF do not have a forward peaked angular distribution like the residues in a beam-induced reaction have. The value of Hercules for a source experiment is the ability to determine the fission axis on an event-by-event basis, and to distinguish between LF and HF.

3.5 Experimental Conditions

The purpose of this section is to describe the conditions for taking data and the parameters measured with Gammasphere and Hercules. The trigger for an event, i.e. a minimum coincidence requirement to be satisfied, was Hercules detecting a FF and Gammasphere detecting four "clean" γ rays. A "clean" γ ray deposits its entire energy into the HPGe crystal whereas a "dirty" γ ray Compton scatters some of its energy into the surrounding BGO. A "clean" BGO γ ray deposits energy in the BGO, but not the HPGe crystal. Before going into details, the following terms have to be introduced.

Gammasphere Pre-Trigger: This is the first level of triggering this array, where a minimum coincidence requirement of "dirty" HPGe detectors is examined. The time window is 200-800 μsec. In the present experiment the number of "dirty" HPGe detectors required was 4.

Gammasphere Master Trigger: This is the second level of triggering this array, where a minimum coincidence requirement of "clean" HPGe detectors is examined. The time window was chosen to be 1 μsec and, as already mentioned, the minimum number of "clean" HPGe detectors was 4.

Gammasphere Late Trigger: This is the third level of triggering this array, where the pileup status of each HPGe detector is checked and the possibility that more than one γ ray was absorbed by a single detector can be excluded. For this check, 6 μsec are spent. A pileup of 6% is considered to be acceptable which is obtained for a count rate of 10kHz per detector.

Prompt (or delayed) External Trigger for Gammasphere: This is an additional option for triggering Gammasphere. In the present experiment an external trigger was created based on an overlap

coincidence between the Gammasphere Master Trigger (narrower logic signal) and a so-called Hercules OR signal (wider signal). This overlap signal is called the AND signal for further reference. The AND signal served several purposes, including the need of a reference for the HPGe trigger-time parameter (so-called TAC1 spectrum) and the Hercules time of flight (ToF) parameter (see below).

If all these conditions are met, the event is accepted and the parameters will be read out. Otherwise, the acquisition is reset. A detail of the present experiment is the use of a CsF detector, a fast-timing detector for γ rays. This detector was used as a replacement for the accelerator radio-frequency signal in an "in-beam" experiment in the following sense. It helped to monitor and adjust the HPGe timing measurement in case of a drift (so-called TAC2 spectrum).

Gammasphere was pushed to its limit, with each HPGe detector counting at ~10 kHz. At the correspondingly high event rates, data losses from computer dead time become a concern. To mediate this, the trigger condition for Gammasphere was the aforementioned four "clean" γ rays. In addition, HERUCLES was part of the trigger requirement. The typical triggering rates during the experiment follow: 25 kHz were pre-triggers (i.e. 4 or more "dirty" γ rays + Hercules), an additional 1.9 kHz pre-triggers were lost to dead time and pileup, and 6.3 kHz of the pre-triggers meet the stricter requirement of the master trigger (i.e. 4 or more "clean" γ rays).

An energy threshold was set for each Hercules detector element to reduce those events where an α particle hits the detector and not a FF. Rates of 22 kHz (FF) and 368 kHz (α particles) were expected. Notice that the number of pre-triggers was higher than the expected number of FF; this was from a small fraction of the α particles overcoming the energy threshold and triggering Hercules. Additionally, there can be random coincidences between α particles and the FF.

The measured parameters are described hereafter. Gammasphere measures/records the times and energies of all the γ rays passing the coincidence overlap with the trigger (1 μs) and the detectors that are hit. The single CsF detector provides a standard reference point to align the times of the individual Gammasphere HPGe detectors; its timing signal is read out as well. Hercules measures/records the ToF and energy, for each FF (and α particle) it detects. These parameters, along with the position information from the Gammasphere detector and Hercules element hit, can be combined to ultimately yield high quality angle sorted spectra (primarily for DSAM lifetime measurements). A map of how the parameters are combined is provided in Figure 3-8.

The ToF of the FF detected in Hercules is measured. The start for the ToF measurement is the AND signal. The resolution of the start is improved in the offline analysis by taking a weighted average of the times of all the γ rays detected in an event (see Chapter 4). The stop for the ToF measurement is the detection of the FF in Hercules. Based on the distance between Hercules and the fission source the ToF can be translated into fragment velocity.

The fission axis is constructed from the line between the Hercules element hit and the source location. The γ-ray angular position is determined with respect to the direction the FF is traveling along the fission axis (see Chapter 4), for the DSAM analysis that direction points into the Pt backing.

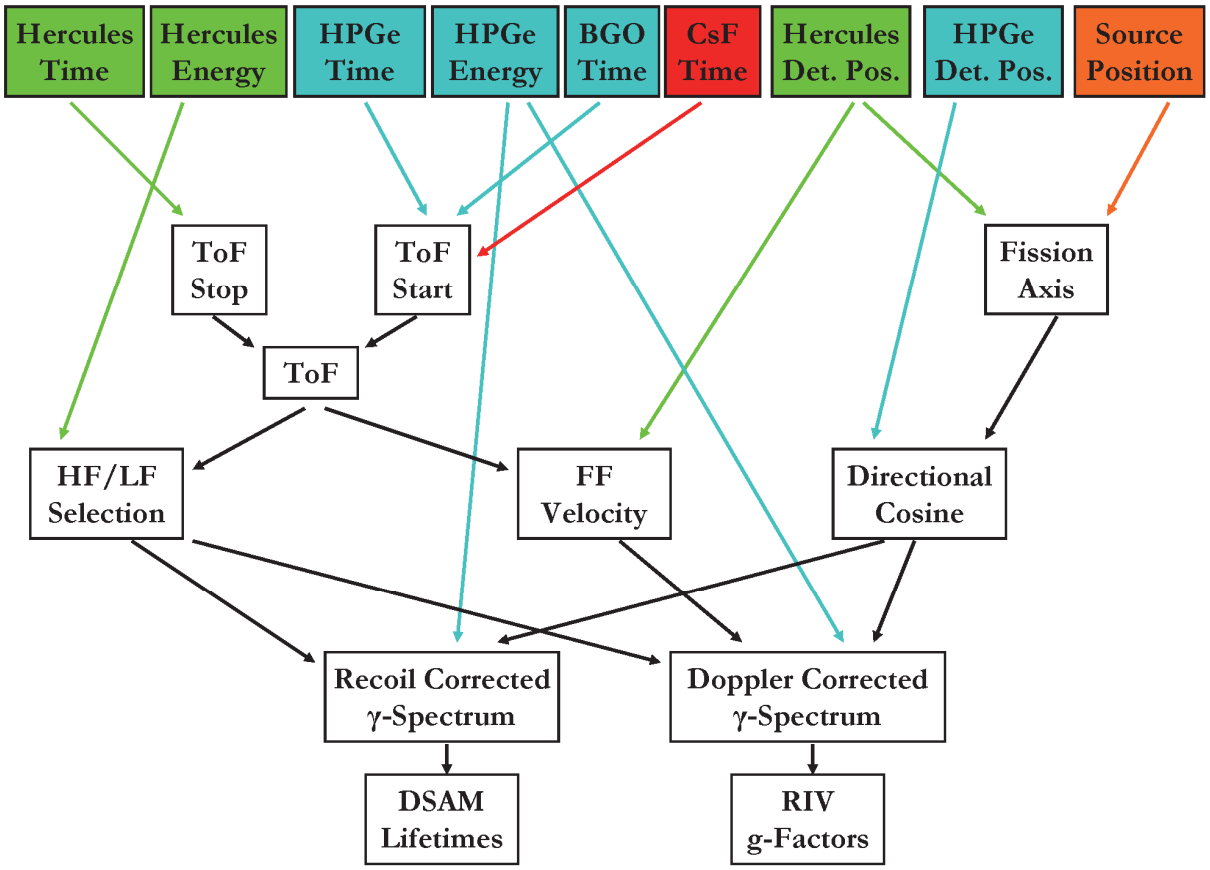

Figure 3-8: The top row contains the parameters entering the data stream (except the right most). The parameters in blue boxes are from Gammasphere, the green from Hercules, the red from the CsF (through the TAC2 output). The remaining one in the orange box is the source position (needed for the analysis). The arrows illustrate how the different parameters are combined to ultimately measure a DSAM lifetime (see Chapter 4) or a RIV g-factor (see Appendix C).

The statistics of the experiment are discussed hereafter. A precursor experiment to the experiment upon which this work is based was conducted about 4 years earlier (called 2006 data). For the DSAM analysis the current and the 2006 data are combined. The current experiment ran for a period of 18 days. During this period a total of $2.1 \cdot 10^9$ events were recorded. The 2006 experiment ran for a period of 12 days with a 110 μCi ^{252}Cf source. During this period a total of $6.2 \cdot 10^8$ events were recorded but with different trigger requirements. At that time, the detection of a

FF in Hercules and a γ-event in an array of CsF detectors (used to provide the start for the ToF measurement), and three "clean" γ rays in Gammasphere was required.

The current experiment recorded 3.4 times more events than the 2006 experiment. The required fourfold γ-event, is equivalent to four times the statistics of a threefold γ-event. Hence, the current experiment contains 13.6 times the statistics of the 2006 experiment.

Chapter 4: Data Analysis

4.1 Data Handling

After the trigger conditions have been met (see Sec. 3.5), the signals from both Gammasphere and Hercules are digitized and output into the data stream (see Appendix C). Only 95 of the 98 Gammasphere detectors were used in the analysis. Three malfunctioned and were not recoverable. Of the 64 detectors of Hercules only 59 were used in the analysis, 2 were damaged during assembly, and the other 3 malfunctioned.

4.1.1 γ-Ray Calibrations

Time Alignment: First, an initial alignment was produced from a fraction of the data. Here the centroids of the time spectra of the individual HPGe detectors were measured and aligned to channel 2000. Then a dynamic self-correction was applied to each HPGe detector while the data were being scanned. Blocks of 10,000 "clean" γ rays that hit a detector were added together and an average time value was produced. That value was subtracted from 2000 to determine the dynamic self-correction for that detector. This correction was applied to the next 10,000 "clean" γ rays to re-center the spectrum on channel 2000. To avoid overcompensating with the correction, the actual correction applied was half the dynamic shift correction value. This process of averaging and re-centering continued for the remainder of the data.

The self-correction ensures that every HPGe detector stays constant in time, but all 95 detectors also need to be lined up relative to each other. To accomplish this, the experiment included a CsF detector that provides a reference timing signal when a coincidence between any HPGe detector and the CsF detector is recorded. Due to the small solid angle covered by the CsF,

this correction is made less than 2% of the time. When a CsF-HPGe coincidence does occur, the two times are properly gain matched with their offsets removed and the correction needed to align the HPGe time with the CsF is determined. This provides a final shift to line up the HPGe times relative to each other. Again, to avoid overcompensating, the actual correction applied is half the final shift value.

Timing Resolution: The trigger requires four "clean" HPGe hits. The timing information for both the "clean" and "dirty" HPGe hits are recorded at the detector's timing resolution (FWHM) of 4-5 ns [56]. If a "clean" BGO hit occurs it is written out at the BGO timing resolution (FWHM) of ~10 ns (literature values range from 7.2 to 12.7 ns [57]). The CsF detector has a timing resolution (FWHM) of <1 ns [58]. Each of the "clean" HPGe, "dirty" HPGe, and "clean" BGO hits provide an independent start signal for the Hercules ToF measurement. By averaging the γ-ray times the resolution can be improved by the square root of the number n of the γ rays recorded; the standard error is equal to $\sigma/\sqrt{n}$. The worst case is that only four "clean" γ rays are recorded, and the resolution (FWHM) improves from 5 ns to 2.5 ns. There are better cases, however.

To account for the different timing resolutions of the HPGe, BGO, and CsF detector, each γ-ray time in the average is assigned a weight factor reported in Table 4-1. The choices of the weight factors are motivated by the timing-resolution values reported in the literature, except for the item "dirty" HPGe. Here it is assumed that the hit of the Ge crystal is on average more peripheral than in the case of "clean" HPGe hits and, thus, the travelling distance of the charge carriers to the central (charge collecting) electrode is longer. The timing resolution is therefore somewhat less than in the "clean" case and the weight factor has been chosen accordingly. In an attempt to prevent outliers from shifting the weighted average, the times of the γ rays were filtered to remove such γ

rays. Table 4-2 reports the limits applied in the filter. The time gates are asymmetric around channel 2000 because of the shape of the peak.

Table 4-1: The timing resolution (FWHM) according to the literature or an argument presented in the text and the weight factors used for the HPGe, BGO, and CsF timing measurements.

	Timing Resolution (FWHM)		Weight Factor
CsF	<1ns		x4
"Clean" HPGe	4-5ns		x2
"Dirty" HPGe	>5ns		x1
"Clean" BGO	~10ns		x1

Table 4-2: The conditions to prevent outliers from skewing the weighted average of the timing measurements.

	Min Time (chan)	Max Time (chan)
"Clean" HPGe	1985	2012
"Dirty" HPGe	1985	2012
"Clean" BGO	1985	2012

Energy Calibration: The Gammasphere detectors were calibrated with two γ-ray sources: ^{152}Eu and ^{243}Am. The energy and relative intensity of their γ rays are listed in Table 4-3. The ^{152}Eu source provides calibration from 122 to 1408 keV, the ^{243}Am source from 75 to 334 keV. Data was collected for several hours with each of the calibration sources in the center of Gammasphere. The calibration data were sorted into one-dimensional histograms, one for each Gammasphere detector. A Gaussian fit was applied to the peaks to determine their centroids. The energy calibration was then generated from a comparison of the measured centroids to the known energies of the calibration sources. The relative intensities in the table were considered for the efficiency calibration, see Section 4.1.3.

Table 4-3: The transition energies (E_γ), relative intensities (I), and respective errors (ΔE_γ and ΔI) of the ^{152}Eu and ^{243}Am calibration sources. The values of the calibration standards are taken from a library of the Radware software [59].

^{152}Eu					**^{243}Am**			
Eγ	ΔEγ	I	ΔI		Eγ	ΔEγ	I	ΔI
121.7817	0.0003	13607	62		74.6600	0.0200	6800	200
244.6975	0.0008	3612	19		99.5300	0.0200	1280	40
295.9390	0.0080	211	5		103.7400	0.0200	2040	60
344.2785	0.0013	12743	53		106.1200	.0200	2640	80
367.7890	0.0050	405	8		209.7400	.0200	330	10
411.1165	0.0013	1073	5		228.1600	.0200	1120	30
443.9760	0.0050	1480	20		277.5800	.0200	1450	40
488.6610	0.0390	195	2		315.8600	.0200	160	5
564.0210	0.0080	236	5		334.2900	.0200	206	6
688.6780	0.0060	400	8					
778.9045	0.0024	6221	29					
867.3680	0.0040	2021	12					
964.1310	0.0090	6920	90					
1005.2790	0.0170	310	7					
1085.8360	0.0090	4859	24					
1089.7370	0.0050	830	4					
1112.0740	0.0040	6494	29					
1212.9480	0.0110	677	4					
1299.1400	0.0090	780	5					
1408.0110	0.0040	10000	30					

4.1.2 Fission Fragment Calibrations

Hercules Time Alignment: A 2D contour map, plotting corrected values of Hercules ToF versus pulse height is shown in Figure 4-1. Two groups are labeled in the figure, one for the HF and one for the LF.

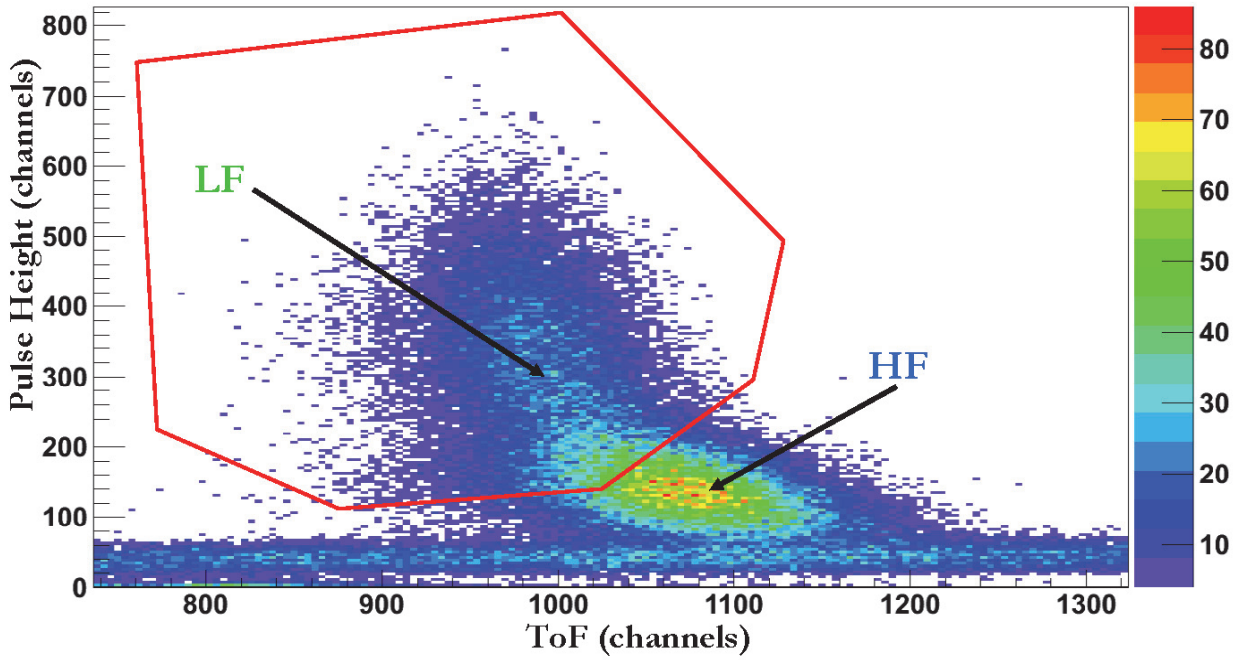

Figure 4-1: Example map ToF versus pulse height for Hercules (detector 6). The gating mask for the LF is shown in red and discussed in Section 4.2.

At the flight distance and timing resolution used in this experiment the peaks in the ToF spectrum overlap. This overlap can be seen in the raw ToF spectrum of Figure 4-2. The approximate LF and HF peak positions are labeled. The α-particle background forms a band across the spectrum at pulse height <60 channels. This random background indicates that the α particles are not associated with γ-ray transitions.

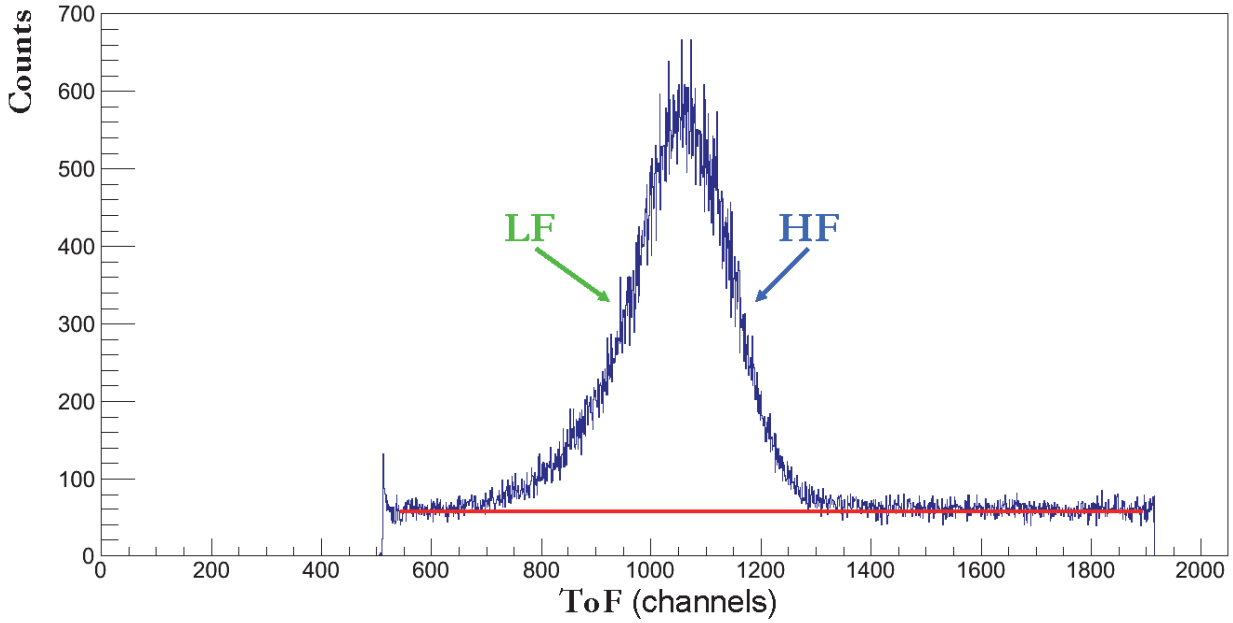

Figure 4-2: Sample raw ToF spectrum (Hercules detector number 6). The approximate LF and HF positions are indicated. The background indicated by a red line is due to α particles.

The ToF spectrum was corrected to prevent detectors from drifting. An initial alignment was made for every Hercules element, and the centroid of the time distribution was put at channel 500. Then a dynamic timing correction was performed. The correction required 8000 counts in a detector element before calculating a centroid value. Hercules times above channel 750 and below channel 250 were filtered out to avoid biasing the centroid calculation. Once the centroid was calculated the appropriate shift to return the time peak to channel 500 in that element was determined. To avoid overcorrection, that shift was divided in half. The procedure was repeated, every time a Hercules element received 8000 counts.

Hercules Pulse Height Alignment: The Hercules pulse-height distribution contains an α, a HF, and a LF peak, an example is shown in Figure 4-3. The α peak is used for an initial detector alignment (see

below) and then such events are filtered out of the data. The fission of ^{252}Cf makes ~200 MeV available to the HF and the LF. The average HF energy is 79.37 MeV. Due to conservation of momentum, the LF receives ~30% more energy than the HF. The average LF energy is 103.77 MeV [55]. In Hercules, the LF peak is broader and at higher pulse height than the HF peak.

The pulse-height spectrum was corrected to prevent detectors drifting. An initial alignment is performed to place the α peak on channel 80. The gain is also adjusted, by placing the centroid of the entire distribution at channel 400, and maintaining it with a dynamic correction. Every time a Hercules element receives 10000 counts, the appropriate shift and gain modification to return the α peak and the centroid of the distribution to their appropriate channels is calculated. Only half of the calculated dynamic correction is applied to avoid overcorrection.

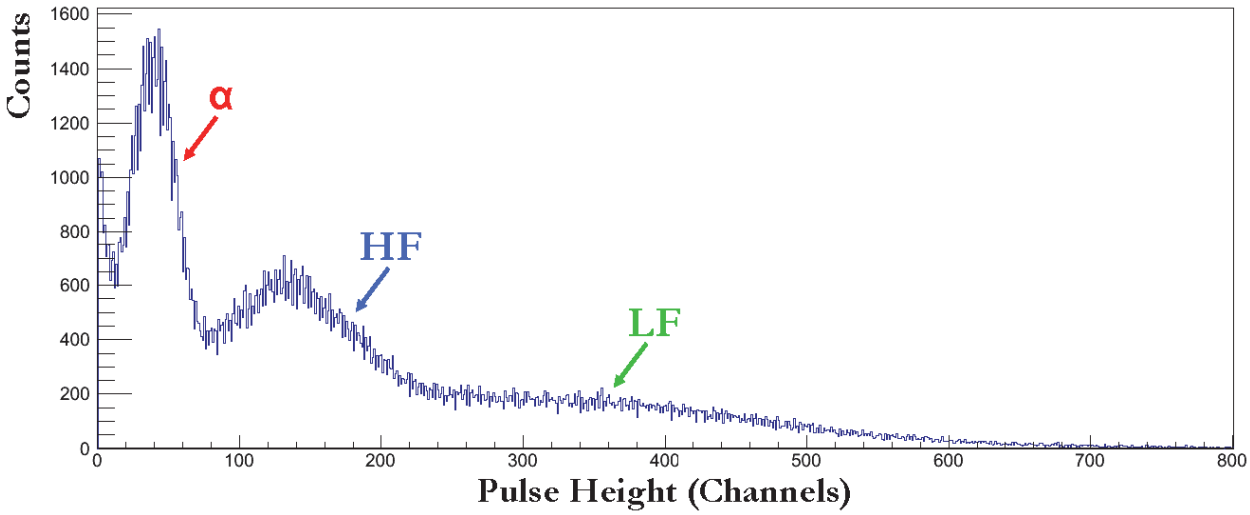

Figure 4-3: A sample pulse-height spectrum for Hercules: detector number 6 is displayed. The locations of the LF, HF, and α peak are labeled.

Improving the Time of Flight Measurement: As discussed in Section 3.5, the AND signal is determined by the narrow logic signal of the master trigger (MT). The start signal, whether it be from the AND

signal or an average of the detected γ rays (see below), needs to be corrected for the time it takes a γ ray to travel from the source to the detector (~0.85 ns).

An energy scale for the pulse height measurement can be obtained by assuming 103.77 MeV and 79.37 MeV for the LF and HF peak, respectively. A small correction of <0.5% is needed to account for the energy lost by the FF as it passes through the Au foil. When the FF emits γ rays (promptly) it is traveling somewhat faster than it is when it hits Hercules. The Au foil thickness will vary with the cosine of the angle between the fission axis and the normal on the Pt disk. The dE/dx (stopping powers) for a representative LF (^{104}Mo) and HF (^{144}Ba) in Au are calculated using the code SRIM [43]. The dE/dx multiplied by the foil thickness gives the energy lost in the Au foil. The effect of this correction is to lengthen the ToF.

Performing a time measurement means determining the time interval between two "events". The start time has been adjusted by using the time difference between the master trigger (MT) and the weighted average of the individual HPGe, BGO, and CsF time measurements. Using the weight factors from Table 4-1, the start time is then

$$\frac{2\cdot\left(\sum_{i}^{\#CleanGe} MT - CleanGe_i\right) + \left(\sum_{j}^{\#DirtyGe} MT - DirtyGe_j\right) + \left(\sum_{k}^{\#CleanBGO} MT - BGO_k\right) + 4\cdot\left(\sum_{n}^{\#CsF} MT - CsF_n\right)}{2\cdot(\#CleanGe) + (\#DirtyGe) + (\#CleanBGO) + 4\cdot(\#CsF)} \quad (4\text{-}1)$$

where the i, j, and k represent the number of "clean" HPGe, "dirty" HPGe, and "clean" BGO γ rays detected respectively. Depending upon whether the CsF detector is present, n is either 0 or 1. The expression (4-1) will be symbolically expressed as (MT - AveT). The initial ToF measurement is the time difference between Hercules (Stop) and the MT signal: (Stop - MT). The improved ToF is the difference between the Stop signal and the averaged start time (Stop - AveT) and is constructed by summing the averaged start time to the initial ToF measurement:

$$ToF = (MT - AveT) + (Stop - MT) = (Stop - AveT). \quad (4\text{-}2)$$

Since every detector has a different gain (ns/ch), the recorded time values are to be converted from channels to ns before the ToF is calculated. This is done by subtracting the offset and then multiplying by the corresponding gain listed in column 2 of Table 4-4. The HPGe and BGO time gains were adopted from the preceding Gammasphere in-beam experiment. The pulsed beam from the ATLAS accelerator has a well defined time structure of 82.5 ns (or a multiple of it), which provides a time calibration. The time gain for the TAC2 data channel (here representing the CsF) was based on the previous in-beam run as well. The Hercules time gains are determined from data taken with a certain amount of cable delay added to the start signal of the ToF measurement. The time peaks in this data set and in the "normal" data set (no cable delay) are offset, and the difference (in channels) divided by the known delay (in ns) provides the Hercules gains.

Table 4-4: Time and energy gains for the HPGe, BGO, CsF, and Hercules detectors where applicable. The starred values are averages of the measured individual detector gains.

	Time Gains (ns/ch)		Energy Gains (keV/ch)
HPGe	0.56*	HPGe	1/3
BGO	0.56*	BGO	3
CsF	0.5		
Hercules	0.1*		

It is also necessary to know the offset to subtract. The dynamic corrections place the centroid of the Hercules ToF spectrum at channel 500 and the Gammasphere time spectra at channel 2000. The offset for the Hercules ToF spectrum was 0 and for the averaged start time 2000. These offsets produced a ToF spectrum that better separated the LF and HF, due to the improved resolution, and placed the centroid on channel 500 (~50 ns). The average velocities for

the LF and HF from the literature [55], 1.383 and 1.036 cm/ns respectively, were used to calibrate the offset. The velocities were averaged and converted to ToF; the offset was adjusted to place the centroid at 19.2 ns.

4.1.3 Gammasphere Efficiency Calibration

The efficiency calibration helps to normalize every detector's response to an incident γ ray. Differences in the response are possible and can be due to variations in detector size, counting rate, amount of radiation damage accrued, and mass of the material blocking the detector's line of sight to the source of emission. This response is described by the relative efficiency, the ratio of the measured relative intensity to the known relative intensity. The energy dependence can be included by determining the relative efficiency of a detector at several γ-ray energies and fitting those values with a smooth function. These efficiency curves are then used to correct the data.

Two different efficiency calibrations have been used. The first calibration is based on data taken at the end of the run with ^{243}Am and ^{152}Eu sources (Table 4-3). Notably, these sources were mounted on Pt disks to mirror the arrangement of the ^{252}Cf source. The second calibration is a sort of internal calibration using the ^{252}Cf source. This calibration is necessary because the efficiency of Gammasphere changed throughout the run. Reasons for the change include variations in detector behavior at high count rates, gradual changes in detector response due to radiation damage, and temporary reductions of the detector efficiency (e.g. the detector is offline for brief periods due to maintenance).

The internal calibration provides the example efficiency curve shown in Figure 4-4. It is produced, by summing the counts from the total γ-ray spectrum according to 20 keV wide bins and normalizing to the integrated bin with the most counts (most efficient detector). The efficiency

curve correctly accounts for all the conditions present during the experiment. It cannot be used to correct measurements involving γ rays of different energies. However, when analyzing angle-sorted spectra, where a certain energy is considered and the measurement is a comparison of strength at different angles, the internal calibration is useful. Figure 4-5 shows the number of counts detected as a function of detector number (i.e. a hit pattern) within a specified γ-energy range. The left block of channels 11-108 represent Gammasphere detectors without an efficiency correction applied, the right one with the correction applied.

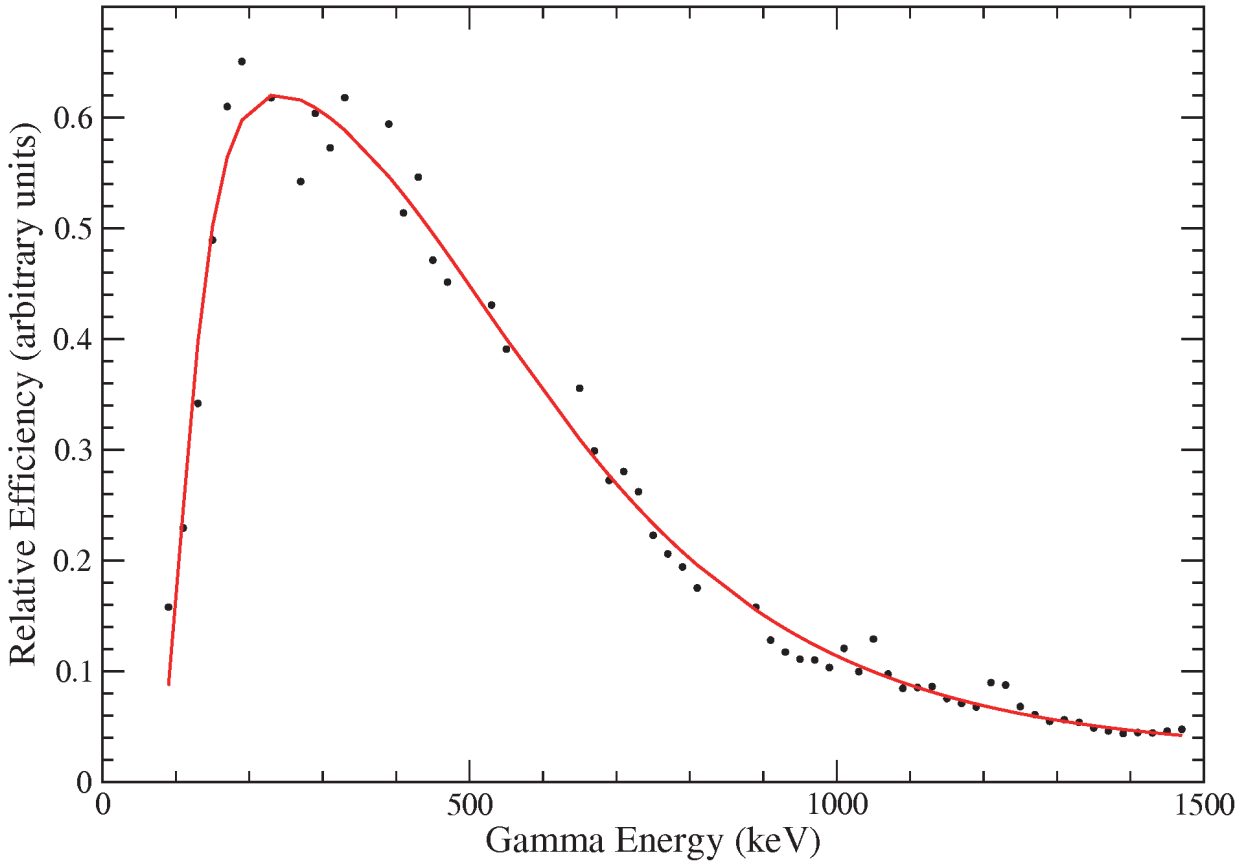

Figure 4-4: An example efficiency curve for a Gammasphere detector (detector number 11). This calibration is from the ^{252}Cf source, see text. Gaps in the data represent areas where excessive counts from neutron peaks or high yield FF have been removed to improve the overall fit. The statistical error bars are within the data points.

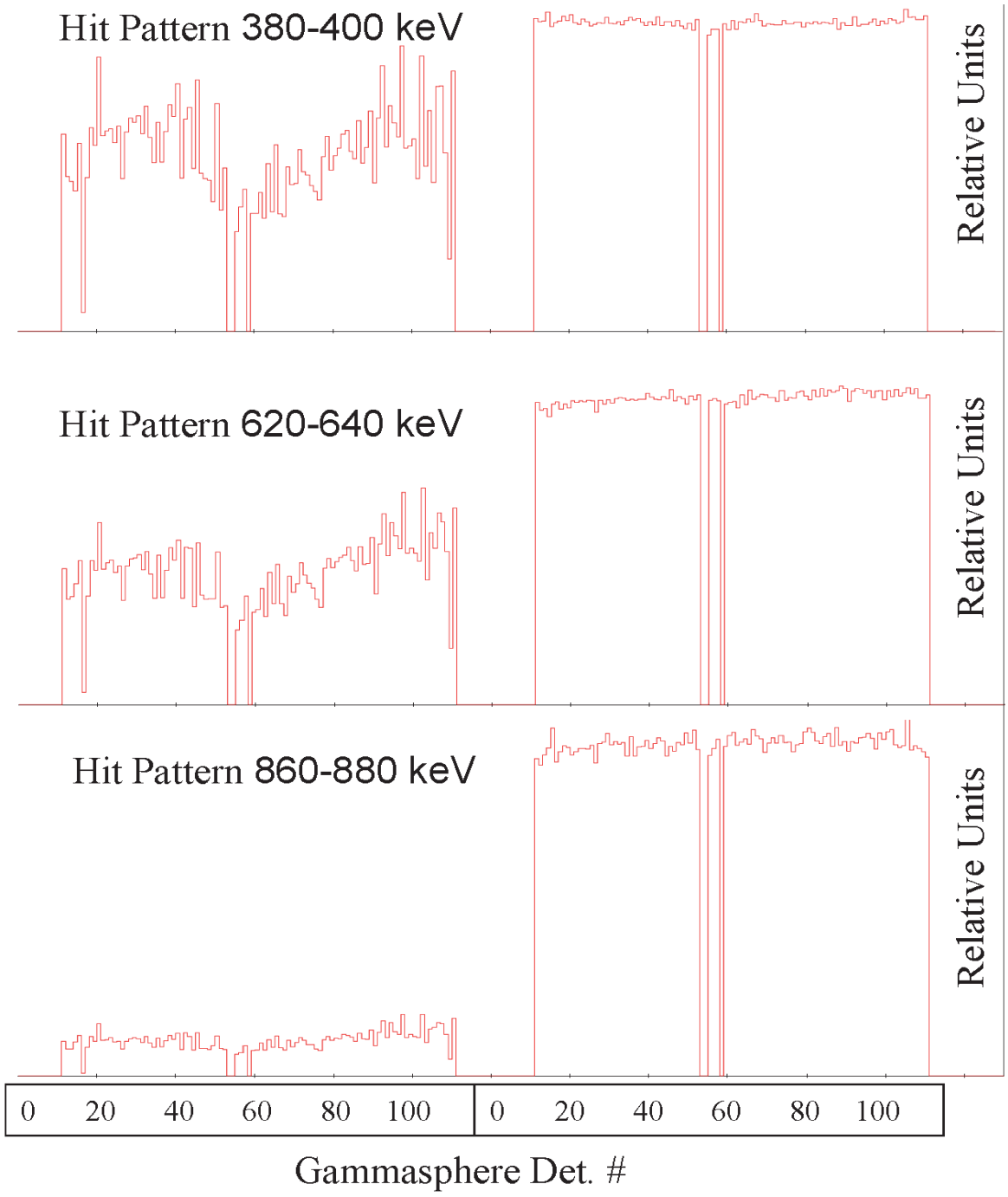

Figure 4-5: Number of counts in each Gammasphere detector (11-108) within a specified energy range. The left and right blocks represent the hit pattern without and with an efficiency correction applied.

When producing angle-sorted γ-ray energy spectra, angular bins (15° wide) relative to the fission axis are used. Each bin is assigned an efficiency generated from the sum of the efficiencies of the detectors of which it is comprised, weighted by the frequency with which counts from that detector are actually included in the bin. The efficiency as a function of bin number will be referred to as the Gammasphere response function. This function is generated by a Monte Carlo simulation.

The simulation requires the input of a γ-ray energy. The simulation then picks a Hercules detector (to define the fission axis), and a HPGe detector (and adjusts its angle according to the side-channel information if present). Then the angle of the HPGe detector with respect the fission axis is calculated [using the directional cosine – see Equation (4-3)]. Finally the appropriate bin in which to add an efficiency weighted count at a given energy is selected. After fifty million cycles, the simulation normalizes the result by five million (more counts than the strongest bin) and outputs the response function.

The detectors in each of the four rings of Hercules are different in size. The simulation weights each Hercules detector picked by its surface area to account for this. The Gammasphere detectors are all the same size and, thus, are equally weighted. If the selected HPGe detector has side channel information, there are five ways to proceed: no correction, or an adjustment of the theta angle by +2.4°, -2.4°, +2.9°, or -2.9°. Every detector has its own side-channel distribution. In the simulation, an average distribution is used with the no correction option occurring for 12% of the events and the other four options each present in 22% of the events. The simulation randomly selects a correction based on the preceding percentages. This is done by picking a random number between 0 and 1, if that number is between (0 and 0.12) no correction is applied, between (0.12 and 0.34) plus 2.4° is applied, between (0.34 and 0.56) minus 2.4° is applied, (0.56 and 0.78) plus 2.9° is applied, and finally between (0.78 and 1.00) minus 2.9° is applied.

The angle (Ψ) of the Gammasphere detector relative to the Hercules segment hit is calculated according to (Eq. 4-5). This requires the transformation of the angles θ_G and φ_G, defining each Gammasphere detector, into Cartesian coordinates G_x, G_y, and G_z, and the angles θ_H and φ_H, defining each Hercules detector, into H_x, H_y, and H_z.

$$\cos(\Psi) = H_X G_X + H_Y G_Y + H_Z G_Z \tag{4-3}$$

The transformation to Cartesian coordinates is done by means of Equations 4-6 and 4-7.

$$H_X = \sin(\theta_H)\cdot\cos(\varphi_H) \quad H_Y = \sin(\theta_H)\cdot\sin(\varphi_H) \quad H_Z = \cos(\theta_H) \tag{4-4}$$

$$G_X = \sin(\theta_H)\cdot\cos(\varphi_G + 180°) \quad G_Y = \sin(\theta_G)\cdot\sin(\varphi_G + 180°) \quad G_Z = \cos(\theta_G) \tag{4-5}$$

The angle convention for Gammasphere is that $\varphi_G = 0^\circ$ is at 6 o'clock while in the convention for Hercules $\varphi_H = 0^\circ$ is at 12 o'clock. This can be accounted for by adding 180° to φ_G. For the DSAM analysis, the angle relative to the fission axis is ξ, the supplement of Ψ.

Figure 4-6 shows examples of the response function for the $2^+ \rightarrow 0^+$ (171.5 keV), $6^+ \rightarrow 4^+$ (511.0 keV), and $12^+ \rightarrow 10^+$ (896.7 keV) transitions of ^{106}Mo. At lower γ-ray energies the function is peaked at ξ>90°. This is due to the reduced efficiency of the HPGe detectors for which the line of sight to the source is intercepted by the Pt backing. The reduced efficiency for ξ>135° is due to the removal of detectors when making room for Hercules.

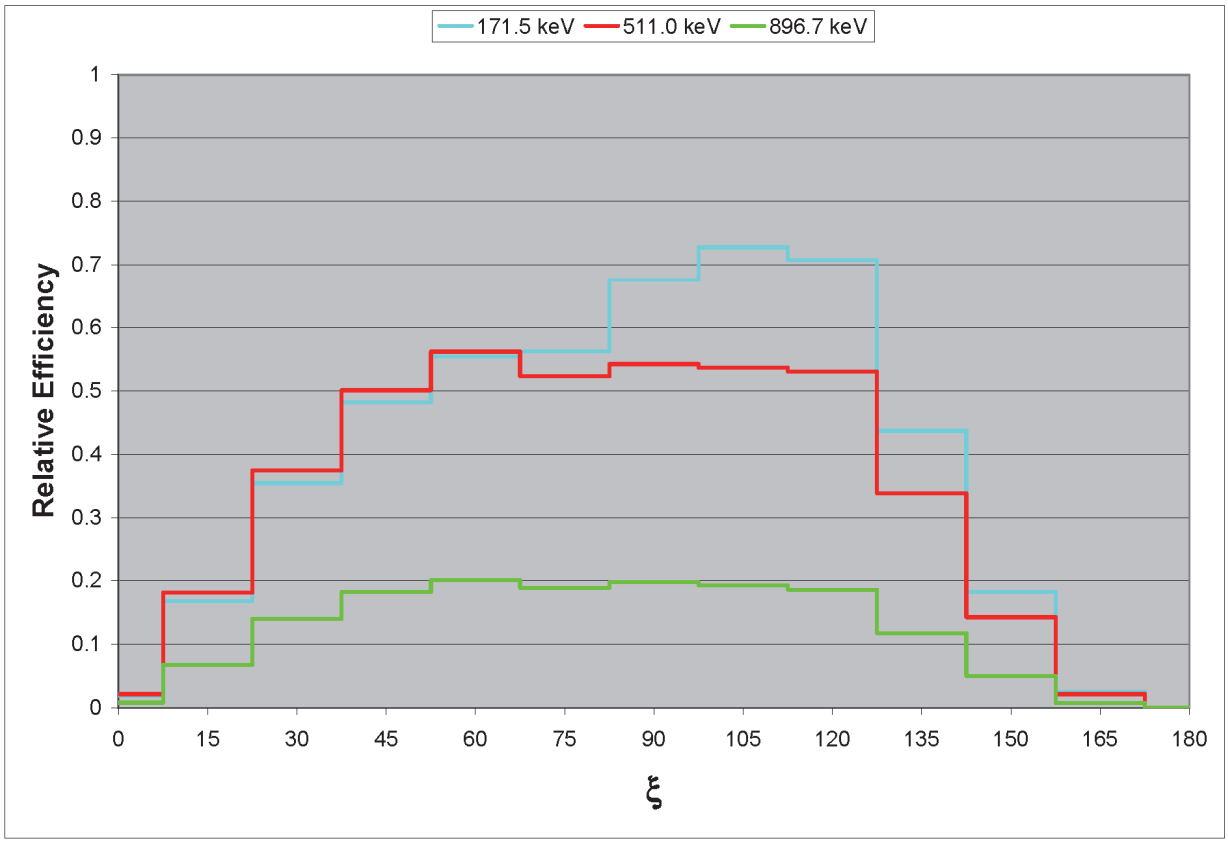

Figure 4-6: Examples of the Gammasphere response function in ^{106}Mo. The functions that apply for E_γ=171.5 keV (the $2^+ \rightarrow 0^+$ transition, blue), 511.0 keV (the $6^+ \rightarrow 4^+$ transition, red), and 896.7 keV (the $12^+ \rightarrow 10^+$ transition, green) are shown.

4.2 Gating Considerations

The fission of ^{252}Cf produces over 200 species of FFs with independent yields greater than 0.1% [16]. The challenge is to suppress/reduce the data from the other FFs so that the γ-ray spectrum of the FF of interest can be studied. This is accomplished by appropriate gating.

Gating on FFs: 2D maps of ToF vs. pulse height are used to gate on either one of the FFs, see the example in Figure 4-1. The color code, where "maximum" is red and "minimum" is purple,

represents the number of counts at a particular ToF vs. pulse height combination. Masks are drawn, for the subsequent selection of the LF or HF.

The γ rays from both fragments are present in the same event. The γ rays from the FF that hits Hercules require a Doppler correction, while the partner fragment that went into the Pt backing does not, see Table 4-5. When the Doppler correction sharpens the lines of one fragment, it blurs the lines of the other. This is exemplified by the LF spectrum of Figure 4-7. Here a gate is applied on the HF and no Doppler correction is performed: this makes the γ-ray spectrum of the LF sharp and the HF blurred. The issues of the gating procedure are discussed hereafter.

Table 4-5: The LF/HF gating and Doppler correction combinations used for the DSAM and RIV measurements. The latter are reported in Appendix C.

Gate	Doppler Cor.	Used For	Comment
LF	No	HF DSAM	The lines of the HF stopping in Pt are sharp.
HF	No	LF DSAM	The lines of the LF stopping in Pt are sharp.
LF	Yes	LF RIV	The lines of the LF recoiling in vacuum are sharp.
HF	Yes	HF RIV	The lines of the HF recoiling in vacuum are sharp.

Figure 4-7 compares the γ-ray spectra obtained when the same γ-ray gates, but different FF gates are applied to the data. For the purpose of comparison, no Doppler correction is applied in any case (this also applies to the lines used as gating transitions). The so-called LF spectrum is representative of a γ-ray spectrum used in the analysis. The so-called HF-background spectrum displays the counts removed from the LF spectrum by the FF gate. The so-called combined spectrum shows the resultant γ-ray spectrum if no FF gate is applied, it is the sum of the LF and HF-background spectra. Clearly, the LF spectrum is cleaner than the so-called combined one: the peak to background ratio is larger for the former than for the latter. By gating on the HF to produce the LF spectrum shown, random background coincidences are obviously removed. The set of spectra in Figure 4.8 is in a sense the best-case example. If weaker transitions are used as gating

transitions, the LF peaks are less intense and the peaks in the HF-background spectrum become comparatively stronger.

Gating on γ Rays: Isolating a specific FF for study requires γ-ray gating. Gating on γ rays has been introduced above, especially in Figure 4-7. Considerations of gate width, gating from "above" or "below", and choosing the "fold" of the gate are discussed hereafter. When gating from "above", the gating transition is higher in the level scheme than the transition being measured. When gating from "below", the gating transitions are lower in the level scheme than the transition being measured. Notably, a ^{252}Cf fission produces a broad distribution with an average of ~9 γ rays split between the LF and HF [60].

In a compromise between collecting statistics and minimizing background, the typical gate width is slightly wider than the FWHM of the peak being gated upon (i.e. ±2.0 keV for an 800 keV γ ray with a 3 keV FWHM). Variations are made to optimize, for example, a narrow gate is appropriate for a strong peak in a high-background region. On the other hand, a weak peak in low background region would receive a wider gate.

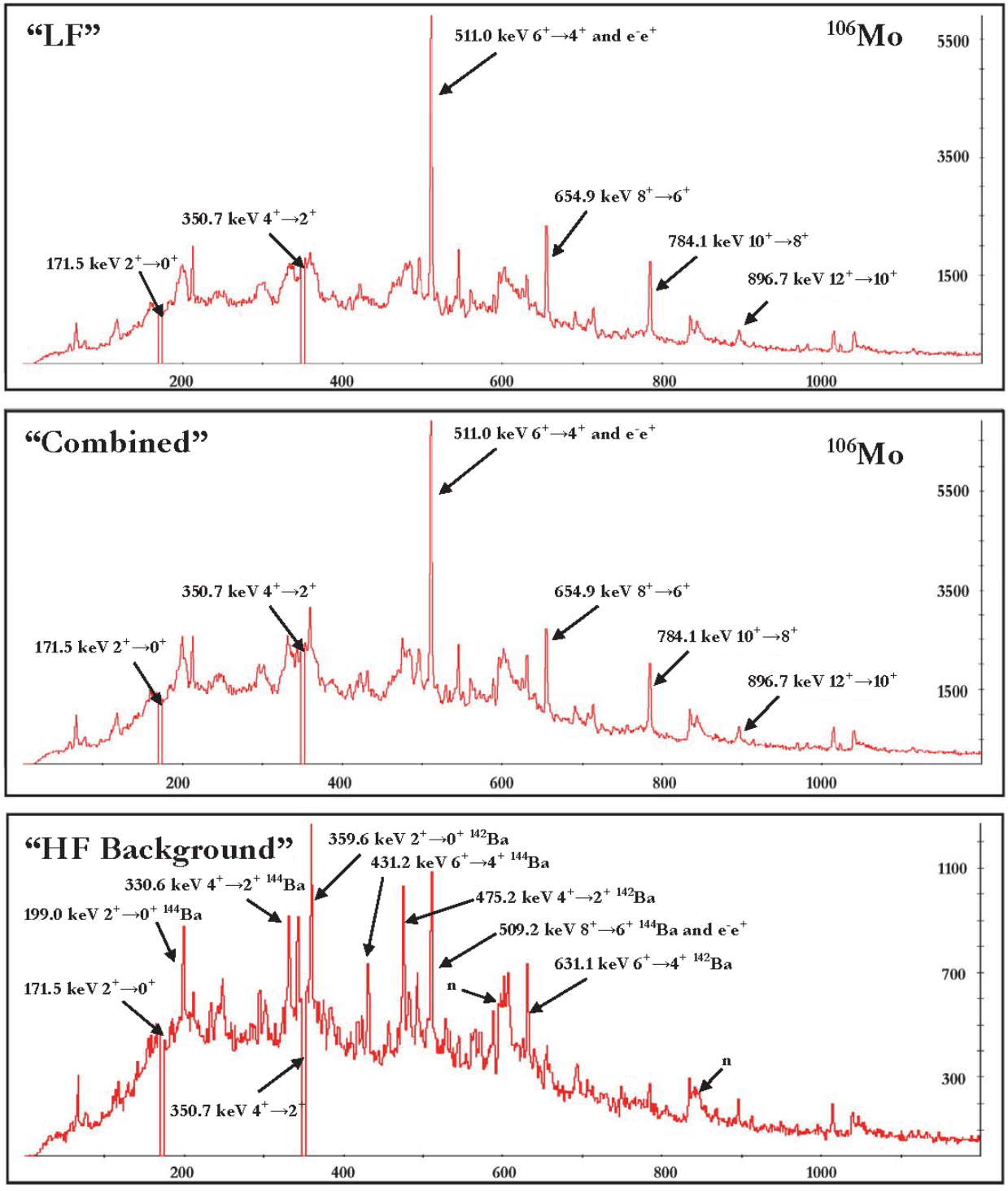

Figure 4-7: Set of spectra made by double gating on the $2^+ \rightarrow 0^+$ (171.5 keV) and $4^+ \rightarrow 2^+$ (350.7 keV) transitions in the ground-state band of ^{106}Mo. No Doppler correction is applied. The top spectrum is the result of a gate on the HF. The middle spectrum is the result of not applying a FF gate. The bottom is the result of a gate on the LF and represents a background spectrum.

Figure 4-8 shows γ spectra for the $8^+ \rightarrow 6^+$ (641.8 keV) transition in the ground-state band of ^{104}Mo gated under different conditions. The γ rays of the LF stopping in the Pt are sharp, as all spectra have been gated by a HF mask and no Doppler correction has been applied. The spectra are "binned" at the ξ=120°. The spectrum of panel A has the gating conditions: 192.2 keV ± 1.5 keV, $2^+ \rightarrow 0^+$ ground-state transition (^{104}Mo), and 368.5 keV ± 1.5 keV, $4^+ \rightarrow 2^+$ transition (^{104}Mo). The effect of the lifetime on the lineshape is visible on the low-energy side of the peak. Two background peaks are present at higher energy. This is the gating combination used in the DSAM analysis, the gates are narrow and from "below". This combination provides sufficient statistics and low enough background to perform lifetime measurements even for weak transitions.

Panel B illustrates the effect a gate from "above" with a narrow width has on the lineshape. The condition is: gating by 192.2 keV ± 1.5 keV, $2^+ \rightarrow 0^+$ ground-state transition (^{104}Mo), and 733.6 keV ± 1.5 keV, $10^+ \rightarrow 8^+$ transition (^{104}Mo). Gating from "above" forces the transition of interest to inherit the FF velocity distribution of the gating transition. Gating from "below" makes no such restriction. If the gate from "above" is narrow, it will preferentially select γ rays from mostly stopped FF over those that are still moving.

Panel C illustrates an option for gating from "above" without biasing the lineshape. The condition for the spectrum is: double gating by 192.2 keV ± 1.5 keV, $2^+ \rightarrow 0^+$ ground-state transition (^{104}Mo), and 733.6 keV ± 15 keV, $10^+ \rightarrow 8^+$ transition (^{104}Mo). By making such a gate wide enough the lineshape is restored, but more difficult to distinguish as the peak to background ratio is much lower.

A γ-ray double gate is found to be optimum for the gating procedure. A triple gate drastically reduces the background, but costs roughly a factor of 10 in statistics. If a single gate is used it can be readily assumed that one or more of the other FFs will share that same gate. Panel D

shows the γ-ray spectrum created by a single gate of width 1.5 keV on the 192.2 keV, $2^+ \rightarrow 0^+$ ground-state transition of ^{104}Mo. Here the background is in general higher: with a single gate it is more likely that transitions in other FFs overlap with the gate and contaminate the spectrum. For rather strong transitions (e.g. $10^+ \rightarrow 8^+$), one may consider using a γ-ray triple gate. This proved unnecessary; the double-gated spectra were clean enough to produce satisfactory fits.

Other groups performing FF lifetime measurements used γ-ray triple gating [61], but did not have an orientation axis. They had to sum over all angles, imbedding the contaminant peaks from the complementary fragments into their spectra. In addition, when gating from "above" the gate must be made "wide" and include the entire tail of the Doppler shifted lineshape; otherwise the gate or the gate will bias the measurement. The advantage of the present method is the ability to push up to higher-spin states inaccessible to other groups. In the spin region where both methods overlap the results are consistent (see Chapter 5).

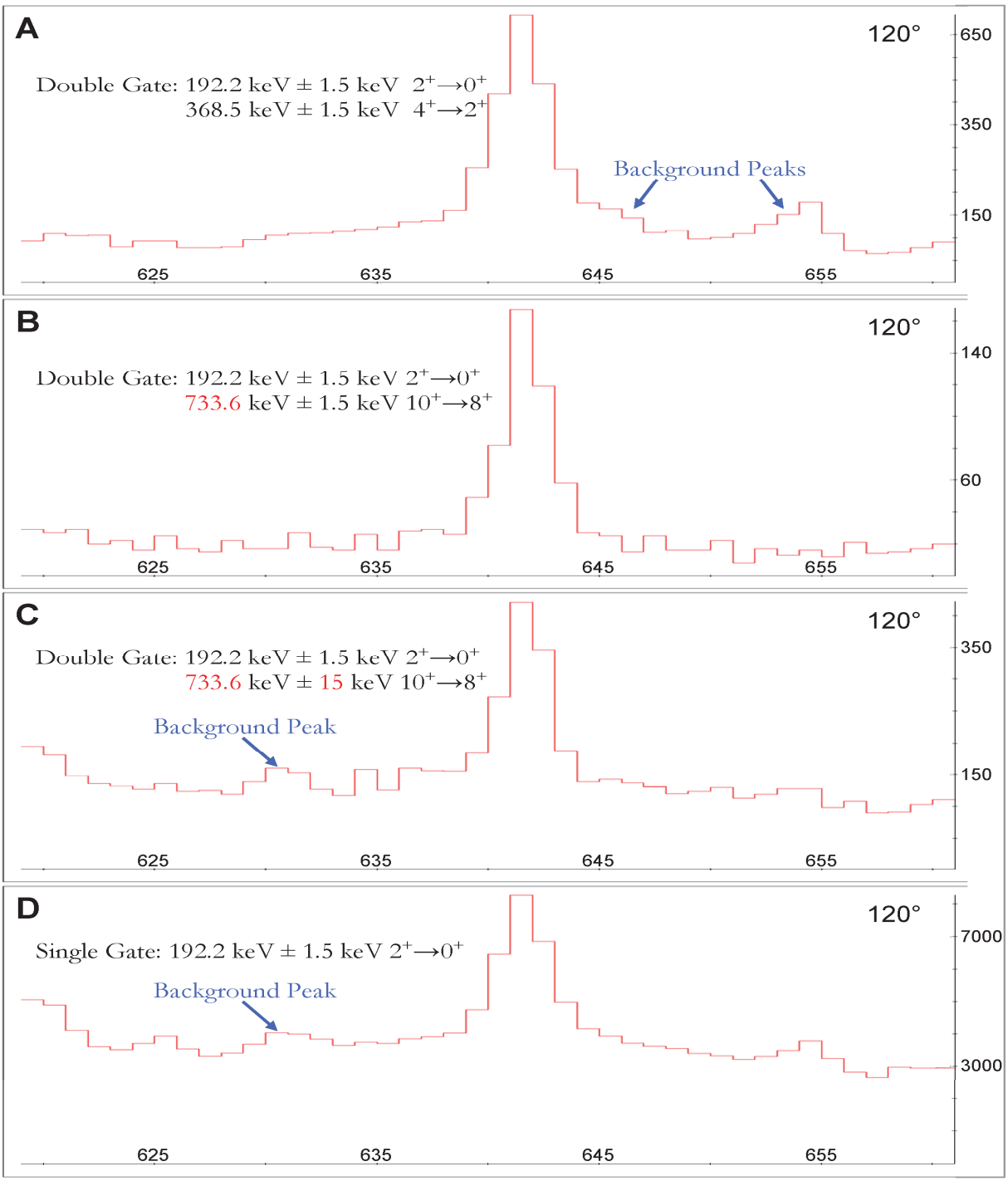

Figure 4-8: Blow-up of spectra produced by different gating options focusing on the $8^+ \rightarrow 6^+$ (641.8 keV) transition in the ground-state band of ^{104}Mo. Panel A: double gated from "below" (in the manner used for the analysis). Panel B: double gated from "above". Panel C: double gated from "above" with a wide gate. Panel D: single gated from "below".

4.3 DSAM Lineshapes

4.3.1 General Considerations

The DSAM is applicable to lifetimes comparable to the stopping time of the γ-ray emitter. The stopping time is simulated using the DECHIST routine of the analysis code, see Section 4.3.3. LF/HF particle gates and γ double gates are applied. If several double gated spectra (gating from "below") are available, they are summed to produce the input spectrum for the analysis code.

The 15° wide bins chosen to produce the γ-ray spectra for the analysis are centered around the ξ=90° position. The decision to use 15° bins was made to balance having enough statistics for a precise measurement, with having narrow enough bins that the Doppler-shifted lineshapes do not blend and sacrifice the accuracy. Only the bins around 45°, 60°, 75°, 90°, 105°, 120°, and 135° are considered. With 59 Hercules and 96 Gammasphere detectors measurements at 5664 different angles were possible. Table 4-6 shows the bin numbering convention, the number of angular combinations in each bin, and the mean angle for each bin. Each bin is described by the median bin angles, but in the analysis the median angle is corrected to the mean value.

In the present analysis the lifetimes are extracted from the lineshapes of three different angular bins. Exceptions are made in a few cases where background peaks (see Section 4.3.4) obscure the lineshape for a majority of available angles. The 90° bin (symmetric lineshape) aids in the identification of background peaks and provides a correct normalization for the spectra from the other bins (asymmetric lineshapes).

Figure 4-9 compares traditional DSAM analysis, as performed in this work, with a previous DSAM analysis where the fission axis is not determined. Without the fission axis all angles are summed over and background peaks get averaged into the measurement.

Table 4-6: The angular combinations obtained when combining the 59 Hercules and 96 Gammasphere detectors.

Median Bin Angle	Bin Number	Combinations Per Bin	Mean Bin Angle
3.75	1	0	NA
15	2	31	18.195
30	3	187	31.646
45	4	436	45.689
60	5	686	60.273
75	6	766	75.066
90	7	798	90.000
105	8	769	104.926
120	9	722	119.931
135	10	596	134.883
150	11	435	149.364
165	12	212	163.894
176.25	13	26	174.845
	Total Combinations:	5664	

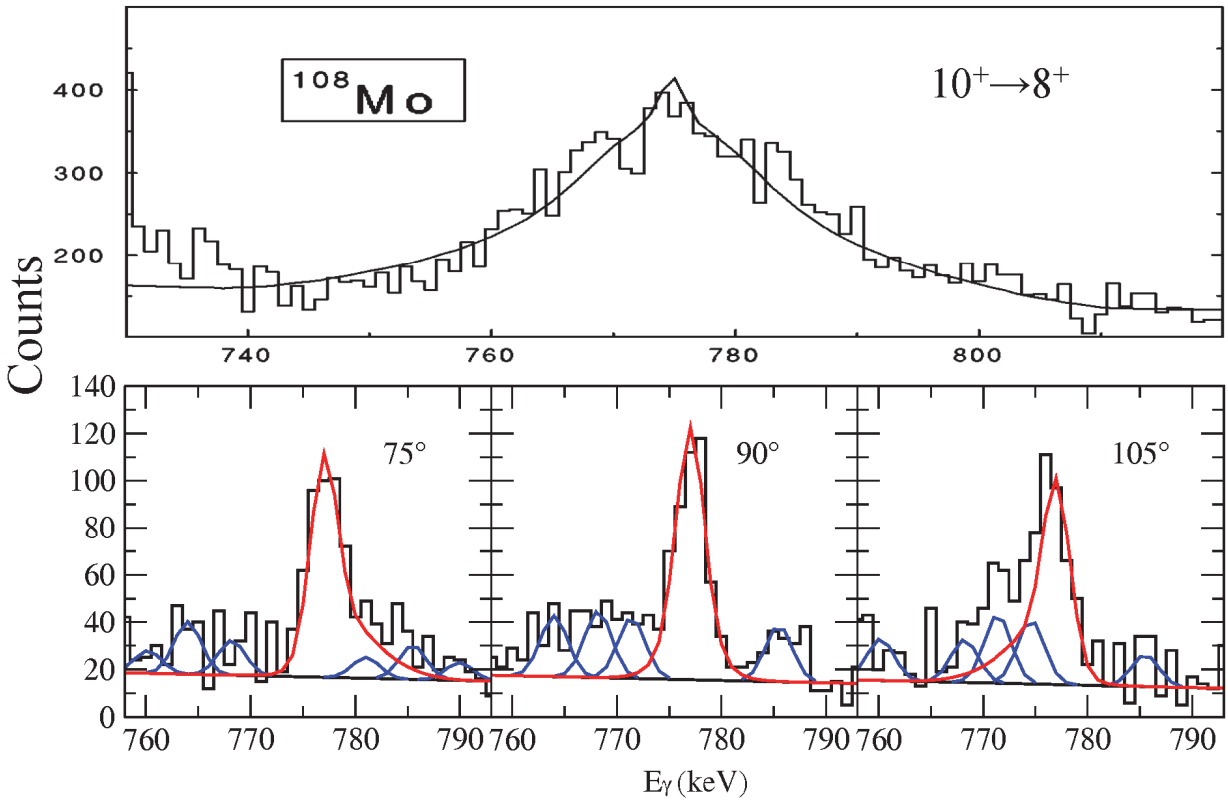

Figure 4-9: Illustration of two different methods for a DSAM analysis of the $10^+ \rightarrow 8^+$ transition in the ground-state band of ^{108}Mo. In the upper figure [61], the fission axis is not known and all angles are summed over. Thus, γ spectra that would contain angular information are not available. In the lower figure (this work) the fission axis is known and angle dependent lineshapes are fit. The red line represents the lineshape fit, the blue lines represent the fits to background peaks, and the black line represents a linear fitted background. Like in Figure 4-7, no Doppler correction is applied.

4.3.2 Side Feeding

To maximize statistics and measure the weakest transitions possible, the decision was made to gate from below, and estimate the side feeding with a model, depicted in Figure 4-10. The side feeding is the contribution to the intensity of the transition that does not come from the in-band feeding transition. The apparent or effective lifetime has contributions from both the intrinsic lifetime, the quantity of interest, and the cumulative feeding time from all the preceding states, see

the dotted lines in Figure 4-10. The relationship between the lifetime, moment of inertia, and quadrupole moment for E2 transitions are described in Section 2.3.

For the in-band feeding intensity the program generates a set of rotational transitions with the same moment of inertia as the state of interest. The in-band feeding lifetime and the intrinsic lifetime are both calculated from the transition quadrupole moment provided by a fit.

The side-feeding intensity, roughly 40% of the intensity of the analyzed transition, was determined in the following way: gating from "below" and taking the difference in intensity between the in-band feeding and analyzed transitions. The side-feeding model assumes a five-transition rotational cascade. A dynamic moment of inertia for this cascade must be provided and should be comparable to that of the in-band cascade. For example, the side-feeding cascades for the ground-state band of ^{106}Mo are given moment of inertia values comparable to the ground-state-band values before the band crossing (values of 23 - 40 $\hbar^2$ /MeV as spin increases). This treatment of the moment of inertia values is consistent with the literature, e.g. Reference [62]. The moment of inertia was then combined with the fitted quadrupole moment of the side feeding to produce an effective lifetime for the side feeding. Table 5-1 in the next chapter, contains the transition and side-feeding intensities for every reported transition, measured with the RADWARE software package [59],

The side-feeding transitions measured in this work are typically faster than the in-band transitions. The Bateman equations are solved to generate the γ-ray yield as a function of time and then combined with so-called "shape vs. time" matrices (see Section 4.3) to produce the lineshapes. Side feeding represents a time delay in the solution to the Bateman equations [38]. Fast side-feeding represents little to no delay and minimizes errors (i.e. errors in the side feeding lifetime are small compared to the lifetime of the state of interest). If the side feeding lifetime is slow (i.e. of the order of the lifetime of the state of interest or slower), then the Bateman solutions are delayed and any

errors in the side-feeding parameters (i.e. side-feeding intensity or moment of inertia) should be scrutinized.

If enough statistics are available, the side feeding can, in principle, be removed by gating from above. Such a gate forces the nucleus to have followed a decay path through the in-band transition above the state of interest. However, the state of interest has now inherited the feeding history of the gating transition. This history needs to be accounted for; the effective lifetime of the gating transition needs to be known. By measuring the effective lifetime of the in-band feeding transition from below and then gating with a wide gate from above through that feeding transition, a measurement of the lifetime of the transition of interest can be made free from any interference by the side feeding. However, as discussed in Section 4.2, there are implications to such a gating procedure.

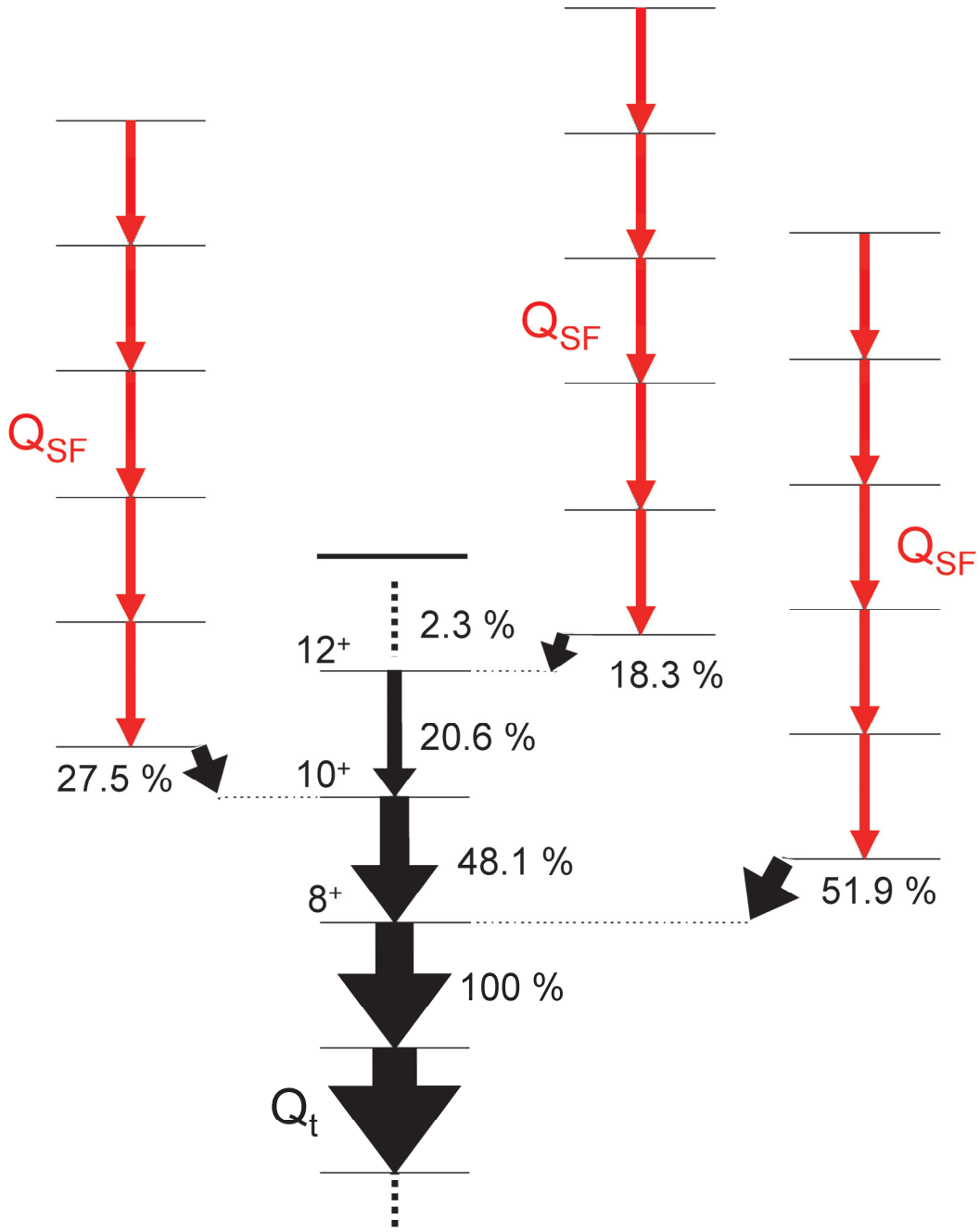

Figure 4-10: A schematic of the side-feeding model used in the analysis. Each transition in the band of interest (black) is fed by a five-transition rotational cascade (red), with a constant dynamic moment of inertia comparable to that of the band. The quadrupole moment of the side feeding (Q_{SF}) and the transition (Q_t) are free parameters. The percentages indicate example feeding intensities from ^{102}Mo.

4.3.3 LINESHAPE Analysis Code

The computer program LINESHAPE by Wells and Johnson [36], was used for the DSAM analysis. It is based on the program DSAMFT written by Gascon [63]. It incorporates several routines described hereafter.

The DECHIST routine, written by Bacelar [64] [65], uses Monte Carlo techniques [66] to simulate both the scattering direction and changes in velocity of a series of slowing down nuclei. Both the electronic and nuclear stopping powers have to be taken into account when calculating the slowing down process. The DECHIST routine treats the electronic stopping as a continuous process, and the nuclear stopping as a discrete one, occurring at a rate given by the Lindhart cross section [67].

The DECHIST routine formally deals with an in-beam experiment, but it can be adapted for a fission experiment. For that purpose, the Z and A parameters for the "projectile", "target", and "recoil" nuclei are made equal to those of the "recoil" nucleus of interest, i.e. the FF. The "beam" energy parameter is used to match the average initial velocity of the FF in the simulation to the measured value. The "target" thickness is set to zero to ensure that the only interactions that occur are the collisions of the FF in the Pt backing.

The stopping powers are generated by the routine STOPO, written by Milner [35]. The tabulated values of Northcliffe and Schilling with atomic shell corrections are used for the electronic stopping [41] [42]. For the nuclear stopping, a multiple Coulomb scattering formalism is used [67] [39] [40].

The HISTAVER routine uses the velocity history from the DECHIST routine to create "shape vs. time" matrices. These matrices store the lineshapes ranging from "fully shifted" to "completely stopped". The routine accounts for γ-ray transition energy, detector opening angle, and

bin angle relative to the orientation axis (here the fission axis). Each matrix is 250 channels wide and contains about 500 time steps; the exact number is determined internally as the number of steps to reduce the kinetic energy of the fragment to 0.1% of its initial value.

The LINESHAPE code accepts the above matrices as input, converts them into lineshapes, and produces the fit to the data. That is, the lineshapes produced represent a sum over all of the "shape vs. time" matrices, with each time interval weighted by the γ-ray yield. The γ-ray yield as a function of time is calculated using the solution of the Bateman equations [Equation (2-35)] [38] [62]. Every new lifetime value input into the Bateman equations will be solved as a new γ-ray yield and thus a new lineshape. The lifetime value is adjusted until a best fit is obtained. The routines of the program MINUIT [68] aid in finding the best fit.

The MINUIT program performs a least-squares minimization of the varied parameters: (1) the in-band transition quadrupole moment (Q_t), (2) the modeled side-feeding transition quadrupole moment (Q_{SF}), and for each angle, (3) a factor to normalize the intensity of the fit, (4) the peak width (FWHM), (5) the intercept and (6) slope of a linear background, and (7) contaminant peak intensities. Parameters (1) and (2) are always freely varied, the other parameters can be fixed when necessary. The routine MINOS [67] performs the χ^2-minimization by which the uncertainty in the quadrupole moment is determined. This routine assumes that the χ^2_{min} represents the best-fit parameter values and that the region where the χ^2 is less that $\chi^2_{min}+1$ corresponds to a confidence interval of 68.2% (one standard deviation). By varying the quadrupole moment above/below its minimum, the error limits are determined. At each step, the quadrupole moment is fixed and the other parameters are varied to minimize the χ^2. This procedure often leads to asymmetric errors.

For every nucleus being studied, the DECHIST routine was used to generate 10000 simulations of the FF stopping in the Pt backing with a time step of 0.004 ps (per the

recommendation of Reference [36], 0.01 times the shortest expected lifetime). The average initial kinetic energy of the fragment was determined by double gating on the appropriate γ-transition energies and projecting out the Hercules velocity distribution. The HISTAVER routine generated "shape vs. time" matrices for detectors at selected angles ξ.

Fits were made in LINESHAPE by starting with the uppermost transition and then fixing the transition above as the subsequent transitions lower in the band were measured. Examples of the lineshape fits are shown in Figure 4-11 and Figure 4-12 in Section 4.3.4. By gating from "below" the state of interest, the lineshape contains a contribution from both in-band feeding and side feeding. This situation is resolved by using the side-feeding model discussed in Section 4.3.2. The standard arrangement was for three angles to be included in the χ^2 minimization of the fit. This helps to compensate for any irregularities in the lineshape from any one angle. It also leads to a more conservative estimate of the error compared to the possible alternative of reporting a weighted average of the lifetimes from each angle-sorted spectrum. However, the conservative approach is here the better choice.

Notably, the spectra being fitted have not had any background subtracted. Two methods for background subtraction were considered. The first involved placing gates above and below the peak of interest to generate a representative spectrum for the underlying background (mainly Compton scattering due to imperfect escape suppression). However, in a fission experiment, the gating conditions for the background spectrum tend to overlap with those for a different FF, creating holes in the resultant spectrum. The second method involved tracing a background underneath the peaks and subtracting it. However, this seemed redundant as a linear background was included in parameters (5) and (6) of the fit. Hence, background subtraction was discarded.

4.3.4 Background and Contaminant Peaks

The γ rays of both the FF of interest and its partner are in coincidence and cannot be separated from each another by gating. These partner-fragment lines are the source of moving background peaks in the γ-ray spectra. For example, when measuring a LF lineshape the moving peaks are from the partner HF. Assuming those moving γ-peaks are 700 keV, their centroids will move ~6 keV for every 15° increase in binning angle; this estimate is made by assuming the average HF β and applying the relativistic Doppler-shift formula. The challenge associated with the background peaks is tracking the peaks as they move, and accounting for them when they interfere with the peak of interest. The following figures demonstrate how the background peaks are accounted for in the lineshape fits.

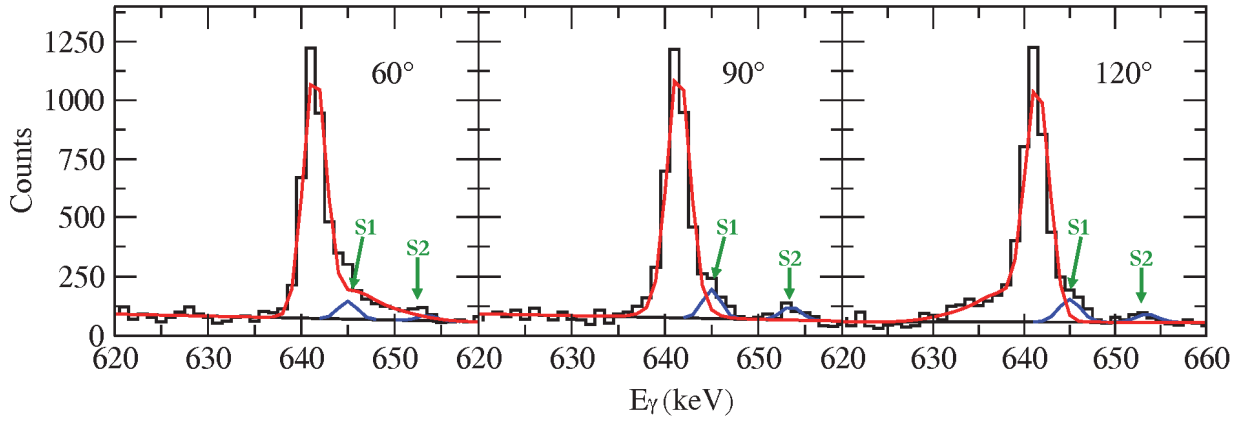

Figure 4-11: The lineshape fits for the $8^+ \rightarrow 6^+$ (641.7 keV) transition in the ground-state band of ^{104}Mo. Two stationary peaks, S1 and S2, needed to be included in the fit. The S1 peak is from the $9^+ \rightarrow 7^+$ (646.5 keV) transition in the γ band of ^{104}Mo. The S2 peak is from the $4^+ \rightarrow 4^+$ (654.1 keV) γ-band to ground-state-band decay-out transition (see Chapter 5).

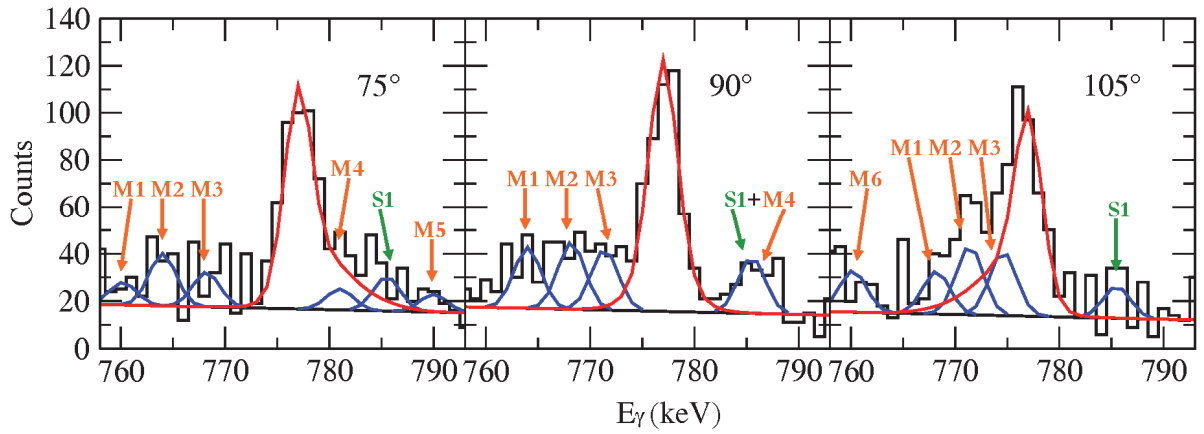

Figure 4-12: The lineshape fit for the $10^{+} \rightarrow 8^{+}$ ground-state-band transition of ^{108}Mo. One stationary peak, S1, needed to be fit. The S1 peak does not correspond to any ground-state-band or γ-band transition of ^{108}Mo. It is from another stopped FF that satisfied the ^{108}Mo gating conditions. The positions of the moving peaks, M1 - M6, change toward higher energies as the binning angle increases (i.e. ~6 keV per 15° increase in binning angle).

Other sources of background or contaminant peaks in the γ-ray energy spectrum are: γ rays of other FF that can satisfy the γ-ray gating conditions, "β-delayed" γ rays from excited states in daughter nuclei, and so-called, neutron peaks produced by exciting Ge through inelastic neutron scattering. These sources of background produce stationary peaks. Often the spectra from several gates are summed and used as the spectrum to be analyzed. The summing tends to reduce the intensity of a background peak relative to the peak of interest; the former is not correlated with all of the gates. The "β-delayed" γ rays can arise from any location where FFs are implanted (Hercules detectors, Pt backing, vacuum-chamber wall). By tightening the timing gate for the individual HPGe detectors to reduce random coincidences the "β-delayed" peaks can largely be reduced. The neutron peaks are due to the neutron flux from the ^{252}Cf source. As in the case of the "β-delayed" peaks tightening of the timing gate will also help to suppress these random peaks.

4.3.5 Estimated Systematic Error

In this experiment there are three sources of systematic error that need to be accounted for: uncertainties in the stopping powers, in β, and in the γ-ray transition energy. For $\beta > 0.02$, electronic stopping is dominant [34]. In the original code the electronic stopping is from the semi-empirical tabulation of Northcliffe and Schilling [41], modified to include shell corrections. For $\beta < 0.005$, nuclear stopping dominates, and Lindhard's theoretical cross sections [39] along with Blaugrund's correction [40] for large angle scattering is used to calculate it. Literature studies estimate errors in the lifetime of less than 15% when Blaugrund's theory is used for the stopping powers of $\beta=0.02$ Al stopping in Au [34]. The error in the stopping powers in this work is far less. The Mo and Ru fragments measured have a β of 0.0456-0.0461, i.e. more of the stopping (than in the Al case) occurs in the better understood electronic-stopping regime. In addition, the mismatch in the mass of the stopper versus the mass of the recoil is less for ^{104}Mo in ^{195}Pt than for ^{27}Al in ^{197}Au.

A comparison was made with the stopping powers from the SRIM package [43] to better characterize the uncertainty in the stopping powers. The differences in the stopping powers were on the order of 11%. When translated into lifetime and transition quadrupole moments the variations were of the order of 8.8% and 4.4% respectively. The measurement of the FF velocity had an uncertainty of 3% which translated into an uncertainty in the lifetime of 2.2%. Uncertainties in the γ-ray transition energies are very small and represent an uncertainty in the lifetime of 0.6%. Combining these systematic relative errors yields a systematic error of 9.1% for τ and 4.55% for Q_t. These errors were rounded up to 10% and 5% respectively.

Chapter 5: DSAM Results for $^{102\text{-}108}$Mo and $^{108\text{-}112}$Ru

5.1 Overview

The Q_t and B(E2) values extracted from the lineshape fits are compiled into a table in Section 5.2. The lineshape fits are shown and discussed in the same section. The Q_t values are plotted as a function of I for each nucleus in Section 5.3 and trends of Q_t with I, Z, and N are discussed. The feeding intensities of levels used in the lineshape fits are discussed separately, in Section 5.4, as they represent a supplemental result of the present analysis. Some experimental features relevant for the assignment and the collective features of the γ bands are presented in Section 5.5. Specifically, observations relevant to the K=2 assignment for these bands (based on the Alaga rule) are discussed here.

5.2 DSAM Lineshape Fits

The DSAM results for the even-mass $^{102\text{-}108}$Mo and $^{108\text{-}112}$Ru nuclei are listed in Table 5-1. The table is arranged by nucleus and further divided into transitions of the ground-state-band, the γ-band, and so-called decay-out transitions. The latter transitions link the γ band with the ground-state band and are also called interband transitions. Extensive level-scheme work has been done in this region [26], and the evaluated level and transition energies, spins, and parities have consistently been used for the lineshape fits and the calculation of transition quadrupole moments.

The transition and side-feeding intensities, I_γ and I_{SF}, are measured in this work, in relative units. All reported intensities are normalized to the corresponding $8_1^+ \rightarrow 6_1^+$ transition, which is set to $I_\gamma \equiv 100$. The τ, Q_t, and Q_{SF} values are extracted from the fits with the method described in Section 4.3. The B(E2) values are calculated from the lifetimes using Equation (2-26) from Section

2.3.4. The statistical and systematic errors have been combined leading to the error that is listed. According to Section 4.3.5, the systematic error is 10% for τ and B(E2) and 5% for Q_t and Q_{SF}. If needed the Q_{SF} is limited to values of 1100 efm^2. At this limit the effective side-feeding lifetime is very fast ($\sim 0.01 \cdot \tau$), i.e., has little to no affect upon the lineshape fits. The θ_{Meas} column lists the angles relative to the fission direction that the lifetimes were extracted from. The "items" 2, 3, 4, 5, and 6 represent angles ξ=60°, 75°, 90°, 105°, and 120° (see Section 4.3.1).

The limits of DSAM applicability are discussed in Section 2.4. When such a limit is reached (e.g. for the $6_1^+ \rightarrow 4_1^+$ transition in ^{104}Mo) a lower limit for τ is reported. This value is the measured lifetime minus one standard deviation. A lower limit on τ corresponds to an upper limit on the Q_t and B(E2) values.

A selection of the individual lineshape fits, arranged by nucleus, follows. A partial level scheme is included for each nucleus, where the transitions that have been measured are highlighted. As discussed in Section 2.3.2, the level schemes of the present nuclei are organized in bands where the ground-state band and the γ-band are the most strongly populated structures. The fits are discussed according to these bands and intensity considerations are made. These include the independent yields from Section 2.1. Secondly, it should be noted that the ground-state-band intensities are at least twice as strong as the corresponding transition in the γ band, see also Section 5.4. All of the γ-ray spectra used for the lineshape fits had a gate on the HF and no Doppler correction applied. The majority of the γ-ray gating is done by making "narrow" double gates from "below", see Sections 4.2 and 4.3.4. The spectra displayed below represent the sum of all available gating combinations. Variations in gating are noted in the figure captions.

Table 5-1: Properties of transitions in even-mass $^{102\text{-}108}$Mo and $^{108\text{-}112}$Ru for which τ, B(E2), Q_t, and Q_{SF} values are obtained. Uncertainties contain both statistical and systematic errors. Spin-parity assignments and transition energies are adopted from Reference [26]. Intensities are from the present work and are given relative to $I_\gamma \equiv 100$ for the corresponding $8_1^+ \rightarrow 6_1^+$ transition. θ_{Meas} identifies the angles used for the lineshape fit, see text.

E_γ (keV)	$I_i^\pi \rightarrow I_f^\pi$ [a]	I_γ	I_{SF}	τ (ps)	B(E2) (e^2fm^4)	Q_t (efm^2)	Q_{SF} (efm^2)	θ_{Meas}
^{102}Mo	**g.s. band**							
879.2	$14_1^+ \rightarrow 12_1^+$	2.3 ±0.8	1.8	0.74 $^{+0.16}_{-0.16}$	2099 $^{+592}_{-368}$	245 $^{+27}_{-26}$	391 ±44	2,3,5,6
834.9	$12_1^+ \rightarrow 10_1^+$	20.6 ±3.4	18.3	0.82 $^{+0.21}_{-0.13}$	2454 $^{+454}_{-495}$	267 $^{+21}_{-34}$	258 ±29	2,5,6
771.5	$10_1^+ \rightarrow 8_1^+$	48.1 ±6.3	27.5	1.20 $^{+0.18}_{-0.27}$	2488 $^{+711}_{-322}$	272 $^{+30}_{-20}$	439 ±54	2,5,6
690.9	$8_1^+ \rightarrow 6_1^+$	≡100 ±8.0	51.9	1.59 $^{+0.23}_{-0.32}$	3261 $^{+836}_{-418}$	315 $^{+32}_{-23}$	424 ±45	2,5,6
^{104}Mo	**g.s. band**							
945.0	$16_1^+ \rightarrow 14_1^+$	2.6 ±0.4	2.4	0.55 $^{+0.11}_{-0.10}$	1969 $^{+417}_{-323}$	237 $^{+21}_{-23}$	1099 ±63	4,5,6
861.3	$14_1^+ \rightarrow 12_1^+$	10.0 ±1.3	7.4	0.63 $^{+0.10}_{-0.09}$	2733 $^{+431}_{-382}$	281 $^{+19}_{-23}$	1048 ±120	2,4,6
798.0	$12_1^+ \rightarrow 10_1^+$	19.7 ±1.2	9.7	0.96 $^{+0.11}_{-0.11}$	2627 $^{+344}_{-272}$	275 $^{+16}_{-16}$	1098 ±122	2,4,6
733.6	$10_1^+ \rightarrow 8_1^+$	40.8 ±1.3	21.1	1.93 $^{+0.24}_{-0.24}$	1990 $^{+283}_{-220}$	243 $^{+15}_{-15}$	1099 ±123	2,4,6
641.7	$8_1^+ \rightarrow 6_1^+$	≡100 ±2.0	59.2	2.44 $^{+0.29}_{-0.30}$	3074 $^{+432}_{-328}$	305 $^{+19}_{-18}$	1093 ±123	2,4,6
519.2	$6_1^+ \rightarrow 4_1^+$	184 ±3.1	84.0	>4.78 [b]	<4526	<380	1000 ±89	3,4,5
	γ band							
712.9	$11^+ \rightarrow 9_1^+$	5.1 ±2.2	3.0	1.96 $^{+0.44}_{-0.44}$	2261 $^{+655}_{-415}$	267 $^{+30}_{-30}$	939 ±105	2,3,4
678.4	$10_2^+ \rightarrow 8_2^+$	6.2 ±0.9	3.7	1.88 $^{+0.51}_{-0.59}$	3021 $^{+1382}_{-645}$	312 $^{+49}_{-42}$	721 ±89	2,4,6
646.5	$9_1^+ \rightarrow 7_1^+$	14.0 ±2.8	8.9	2.24 $^{+0.64}_{-0.73}$	1613 $^{+928}_{-436}$	233 $^{+59}_{-34}$	1100 ±121	2,3,4
601.7	$8_2^+ \rightarrow 6_2^+$	24.9 ±2.1	18.7	3.4 $^{+1.5}_{-1.4}$	2496 $^{+2073}_{-897}$	300 $^{+100}_{-60}$	1100 ±123	2,4,5
^{106}Mo	**g.s. band**							
1087.6	$18_1^+ \rightarrow 16_1^+$	1.9 ±0.9	1.3	0.57 $^{+0.21}_{-0.15}$	941 $^{+322}_{-249}$	162 $^{+21}_{-29}$	1089 ±122	3,4,5
1051.5	$16_1^+ \rightarrow 14_1^+$	5.2 ±0.9	3.3	0.63 $^{+0.12}_{-0.12}$	1008 $^{+242}_{-156}$	169 $^{+16}_{-16}$	1099 ±123	3,4,5
992.9	$14_1^+ \rightarrow 12_1^+$	8.9 ±1.9	3.7	0.54 $^{+0.08}_{-0.10}$	1566 $^{+348}_{-198}$	211 $^{+19}_{-15}$	1095 ±123	2,4,6
896.7	$12_1^+ \rightarrow 10_1^+$	17.9 ±1.9	9.0	1.02 $^{+0.12}_{-0.12}$	1380 $^{+182}_{-144}$	200 $^{+12}_{-12}$	1100 ±123	2,4,6
784.1	$10_1^+ \rightarrow 8_1^+$	42.9 ±2.5	25.0	1.52 $^{+0.17}_{-0.17}$	1812 $^{+230}_{-183}$	231 $^{+13}_{-13}$	1100 ±123	2,4,6
654.9	$8_1^+ \rightarrow 6_1^+$	≡100 ±3.7	57.1	2.43 $^{+0.29}_{-0.29}$	2788 $^{+372}_{-293}$	291 $^{+17}_{-17}$	873 ±97	2,4,6
511.2	$6_1^+ \rightarrow 4_1^+$	252 ±8.6	152	>3.80 [b]	<6152	<443	806 ±112	3,4,5
	γ band							
756.4	$10_2^+ \rightarrow 8_2^+$	3.6 ±0.9	1.9	1.77 $^{+0.52}_{-0.52}$	1862 $^{+775}_{-423}$	246 $^{+36}_{-36}$	1081 ±97	3,4,6
690.9	$9_1^+ \rightarrow 7_1^+$	9.1 ±0.8	6.4	1.81 $^{+0.54}_{-0.47}$	2864 $^{+996}_{-661}$	311 $^{+40}_{-47}$	487 ±53	4,5,6
631.0	$8_2^+ \rightarrow 6_2^+$	12.1 ±2.5	8.5	3.46 $^{+0.71}_{-0.69}$	1344 $^{+718}_{-483}$	218 $^{+51}_{-44}$	1081 ±121	2,3,4
	decay out							
896.2	$4_2^+ \rightarrow 2_1^+$	55.9 ±16.5	9.3	2.33 $^{+0.27}_{-0.29}$	158 $^{+57}_{-44}$	115 $^{+19}_{-17}$	1060 ±122	5
^{108}Mo	**g.s. band**							
945.6	$14_1^+ \rightarrow 12_1^+$	8.2 ±2.5	4.4	0.61 $^{+0.14}_{-0.18}$	1770 $^{+734}_{-328}$	225 $^{+33}_{-26}$	555 ±62	3,4,5
872.0	$12_1^+ \rightarrow 10_1^+$	19.6 ±6.8	11.4	1.08 $^{+0.22}_{-0.30}$	1499 $^{+578}_{-258}$	208 $^{+29}_{-22}$	580 ±73	3,4,5
776.6	$10_1^+ \rightarrow 8_1^+$	57.7 ±6.2	38.1	2.02 $^{+0.39}_{-0.44}$	1430 $^{+402}_{-232}$	205 $^{+22}_{-20}$	1075 ±97	3,4,5
662.1	$8_1^+ \rightarrow 6_1^+$	≡100 ±8.8	42.3	2.05 $^{+0.46}_{-0.32}$	3129 $^{+589}_{-573}$	309 $^{+24}_{-35}$	1100 ±123	3,4,5
	γ band							
707.0	$9_1^+ \rightarrow 7_1^+$	25.0 ±2.7	9.0	1.6 $^{+1.2}_{-0.6}$	2943 $^{+1632}_{-1275}$	310 $^{+80}_{-80}$	446 ±49	3,4,5

Table 5-1: (Continued.)

E_γ (keV)	$I_i^\pi \rightarrow I_f^\pi$ [a]	I_γ	I_{SF}	τ (ps)	B(E2) (e^2fm^4)	Q_t (efm^2)	Q_{SF} (efm^2)	θ_{Meas}
^{108}Ru	**g.s. band**							
863.6	$16^+_1 \rightarrow 14^+_1$	2.3 ±1.0	1.4	0.69 $^{+0.14}_{-0.15}$	2462 $^{+698}_{-412}$	264 $^{+29}_{-27}$	1100 ±123	3,4,5
762.2	$14^+_1 \rightarrow 12^+_1$	5.1 ±1.3	2.8	1.34 $^{+0.21}_{-0.25}$	2368 $^{+532}_{-324}$	260 $^{+24}_{-21}$	1100 ±123	4,5,6
788.1	$12^+_1 \rightarrow 10^+_1$	19.9 ±1.9	14.8	1.28 $^{+0.31}_{-0.36}$	2097 $^{+810}_{-408}$	246 $^{+34}_{-30}$	280 ±31	3,4,5
798.3	$10^+_1 \rightarrow 8^+_1$	41.6 ±2.0	21.7	1.20 $^{+0.17}_{-0.18}$	2098 $^{+372}_{-265}$	249 $^{+19}_{-18}$	371 ±41	3,4,5
701.6	$8^+_1 \rightarrow 6^+_1$	≡100 ±2.7	58.4	1.53 $^{+0.25}_{-0.34}$	3138 $^{+880}_{-442}$	308 $^{+34}_{-25}$	316 ±39	2,3,6
	γ band							
730.0	$10^+_2 \rightarrow 8^+_2$	11.5 ±4.3	6.1	1.25 $^{+0.44}_{-0.50}$	3150 $^{+2133}_{-815}$	317 $^{+64}_{-55}$	336 ±38	3,4,5
657.8	$8^+_2 \rightarrow 6^+_2$	20.8 ±3.8	9.3	2.1 $^{+1.3}_{-0.8}$	3111 $^{+1798}_{-1185}$	330 $^{+90}_{-70}$	1100 ±123	5
	decay out							
940.5	$4^+_2 \rightarrow 2^+_1$	32.2 ±4.4	21.3	1.87 $^{+0.30}_{-0.30}$	74 $^{+55}_{-40}$	78 $^{+26}_{-26}$	301 ±34	2,3,5
^{110}Ru	**g.s. band**							
799.7	$16^+_1 \rightarrow 14^+_1$	5.4 ±0.8	2.0	2.03 $^{+0.40}_{-0.40}$	1229 $^{+304}_{-203}$	187 $^{+19}_{-19}$	1036 ±119	3,4,5
703.9	$14^+_1 \rightarrow 12^+_1$	7.9 ±2.0	2.5	3.6 $^{+2.9}_{-1.2}$	1312 $^{+656}_{-585}$	190 $^{+40}_{-50}$	788 ±117	4,5,6
887.6	$12^+_1 \rightarrow 10^+_1$	12.5 ±1.1	4.6	1.54 $^{+0.25}_{-0.25}$	962 $^{+190}_{-136}$	168 $^{+14}_{-14}$	1100 ±120	2,4,6
815.0	$10^+_1 \rightarrow 8^+_1$	37.6 ±1.4	25.1	2.22 $^{+0.26}_{-0.27}$	1022 $^{+141}_{-106}$	174 $^{+11}_{-10}$	1100 ±123	2,4,6
705.3	$8^+_1 \rightarrow 6^+_1$	≡100 ±2.1	62.4	2.17 $^{+0.25}_{-0.25}$	2155 $^{+277}_{-220}$	256 $^{+15}_{-15}$	1098 ±123	4,5,6
	γ band							
756.0	$9^+ \rightarrow 7^+$	8.6 ±1.6	3.0	1.24 $^{+0.40}_{-0.57}$	2665 $^{+2268}_{-650}$	299 $^{+69}_{-48}$	377 ±42	3,4,5
712.7	$8^+_2 \rightarrow 6^+_2$	25.0 ±3.8	13.1	1.94 $^{+0.36}_{-0.38}$	2029 $^{+668}_{-435}$	268 $^{+40}_{-31}$	557 ±63	2,3,4
645.5	$7^+ \rightarrow 5^+_1$	20.8 ±1.3	12.2	3.03 $^{+0.50}_{-0.49}$	2243 $^{+616}_{-450}$	292 $^{+37}_{-31}$	1098 ±123	3,4,5
599.8	$6^+_2 \rightarrow 4^+_2$	62.5 ±2.6	37.5	4.12 $^{+0.94}_{-0.99}$	1799 $^{+730}_{-434}$	278 $^{+52}_{-37}$	1100 ±123	2,3,4
^{112}Ru	**g.s. band**							
836.0	$16^+_1 \rightarrow 14^+_1$	7.1 ±2.2	3.7	1.90 $^{+0.34}_{-0.27}$	1052 $^{+177}_{-161}$	173 $^{+12}_{-16}$	934 ±88	4,5,6
791.9	$14^+_1 \rightarrow 12^+_1$	12.3 ±4.9	5.2	2.31 $^{+0.43}_{-0.35}$	1135 $^{+199}_{-177}$	180 $^{+13}_{-17}$	1100 ±123	3,4,5
763.4	$12^+_1 \rightarrow 10^+_1$	31.3 ±4.1	19.0	1.61 $^{+0.21}_{-0.20}$	1955 $^{+280}_{-226}$	239 $^{+15}_{-16}$	1099 ±123	3,4,5
723.3	$10^+_1 \rightarrow 8^+_1$	55.9 ±5.3	24.6	2.06 $^{+0.37}_{-0.44}$	2001 $^{+543}_{-303}$	244 $^{+26}_{-22}$	647 ±74	2,4,6
649.5	$8^+_1 \rightarrow 6^+_1$	≡100 ±6.0	44.1	2.5 $^{+1.8}_{-0.7}$	2813 $^{+1154}_{-1179}$	290 $^{+60}_{-70}$	369 ±39	3,4,5
	γ band							
756.0	$11^+_1 \rightarrow 9^+_1$ [c]	10.2 ±2.0	5.2	1.32 $^{+0.65}_{-0.70}$	2504 $^{+2834}_{-830}$	280 $^{+74}_{-69}$	328 ±37	2,4,6
693.3	$9^+_1 \rightarrow 7^+_1$	26.5 ±3.0	16.3	1.84 $^{+1.01}_{-0.79}$	2769 $^{+2084}_{-981}$	305 $^{+98}_{-61}$	429 ±48	2,3,4
605.4	$7^+_1 \rightarrow 5^+_1$	44.5 ±3.6	18.0	3.10 $^{+0.96}_{-1.12}$	3237 $^{+1842}_{-763}$	350 $^{+63}_{-54}$	1098 ±123	2,3,4

[a] Subscripts 1 and 2 indicate the first and second excited state, respectively, if there are two states with the same spin-parity assignment.

[b] Lower-limit value due to limited DSAM applicability.

[C] Transition reported in Reference 69.

For display purposes in the weaker cases, a constant background has been subtracted. The reasons for not performing a background subtraction prior to the lineshapes being fit are discussed in Section 4.3.3. The fitting of peaks in the background is covered in Section 4.3.4.

Figure 5-1 displays a partial level scheme for ^{102}Mo. Figures 5.2 through 5.4 are fits for ground-state-band transitions. The spectrum for the $14_1^+ \rightarrow 12_1^+$ transition has many background peaks. To account for this situation, four angles were included in the fit and distortions that may affect the result were averaged out. Fits to γ-band and decay-out transitions were not possible due to limited statistics. This is due to the low independent yield of ^{102}Mo (IN value of 0.464), the lowest of all the nuclei considered in this work.

Figure 5-5 displays a partial level scheme for ^{104}Mo. Figures 5.6 through 5.9 are fits for ground-state-band transitions. The lifetimes for the ground-state-band transitions seem to decrease with increasing spin. This can be concluded from the increasing proportion of counts in the tail of the lineshape for some of the consecutive transitions (but the reliability of this observation depends also on the strength of the side feeding). Figure 5-10 is a fit for the $10_2^+ \rightarrow 8_2^+$ γ-band transition. In this fit there appears to be a "red" background peak at 663 keV. This indicates that a "blue" background peak is overlapping with a region that is being ignored by the fit.

Figure 5-11 displays a partial level scheme for ^{106}Mo. Figures 5.12 through 5.15 are fits for ground-state-band transitions. Figures 5.16 and 5.17 are fits for γ-band transitions. Particularly when working with weaker transitions, the goal is to find at least one angle where the lineshape is not obscured by the background. An example is the ξ=120° spectrum of Figure 5-16.

Figure 5-18 displays a partial level scheme for ^{108}Mo. Figures 5.19 and 5.20 are fits for ground-state-band transitions, Figure 5-21 is a fit for the $9_1^+ \rightarrow 7_1^+$ transition. ^{108}Mo is again one of

the weaker products (IN value of 0.667), thus, a lesser amount of lifetime information is reported compared to ^{104,106}Mo.

Figure 5-22 displays a partial level scheme for ^{108}Ru. Figures 5.23 and 5.24 are fits for ground-state-band transitions. In Figure 5-23 the lineshapes for the $12_1^+ \rightarrow 10_1^+$ and $10_1^+ \rightarrow 8_1^+$ transitions are presented in the same window. Figure 5-25 is a fit for a decay-out transition.

Figure 5-26 displays a partial level scheme for ^{110}Ru. Figures 5.27 through 5.30 are fits for ground-state-band transitions. ^{110}Ru has an independent yield of 3.62, the highest of all the nuclei in this work. Despite the high yield, for some of these transitions, gating is complicated; see the captions of Figures 5.27 and 5.30 for further details. Figures 5.31 and 5.32 are fits for γ-band transitions.

Figure 5-33 displays a partial level scheme for ^{112}Ru. Figures 5.34 through 5.36 are fits for ground-state-band transitions. In Figure 5-35 the lineshapes for the $14_1^+ \rightarrow 12_1^+$ and $12_1^+ \rightarrow 10_1^+$ transitions are presented in the same window. Figures 5.37 and 5.38 are fits to γ-band transitions. The even-spin and odd-spin γ-band transitions that are apart by $1\,\hbar$ have roughly the same intensity. Due to the lower independent yield of ^{112}Ru (IN value of 0.939), there is less lineshape information available for this nucleus than for ^{110}Ru.

5.2.1 ^{102}Mo

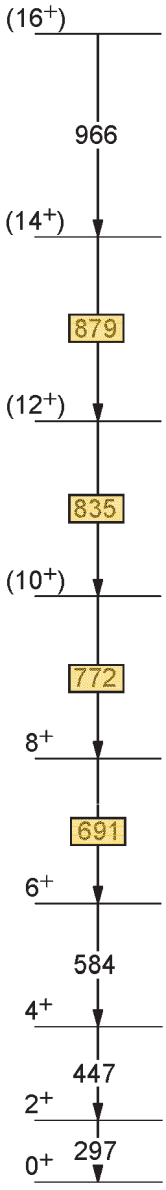

Figure 5-1: Partial level scheme of ^{102}Mo showing the ground-state band. The transitions subject to the DSAM measurement are highlighted.

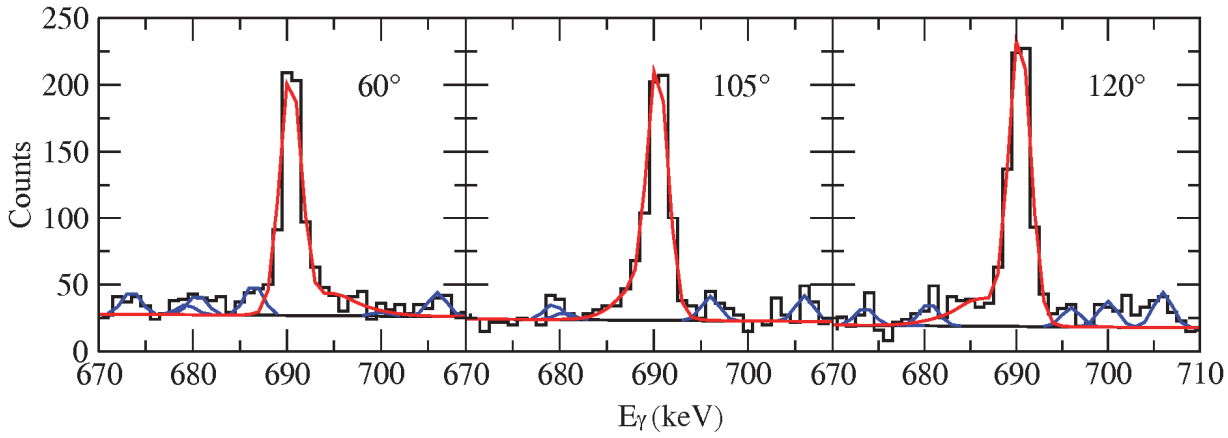

Figure 5-2: DSAM lineshapes for the $8_1^+ \rightarrow 6_1^+$ (690.9 keV) transition in ^{102}Mo. The angles ξ are given in the figure. The color code of the lines is the same as in Figure 4.10. Red, blue, and black respectively represent the lineshape, background peaks, and linear background.

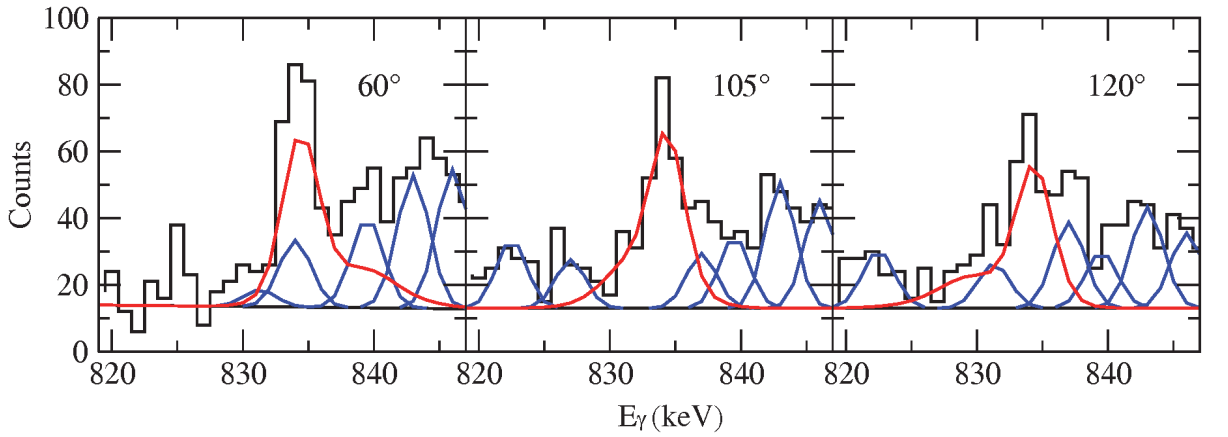

Figure 5-3: Same as Figure 5.2, but for the $12_1^+ \rightarrow 10_1^+$ (834.9 keV) transition.

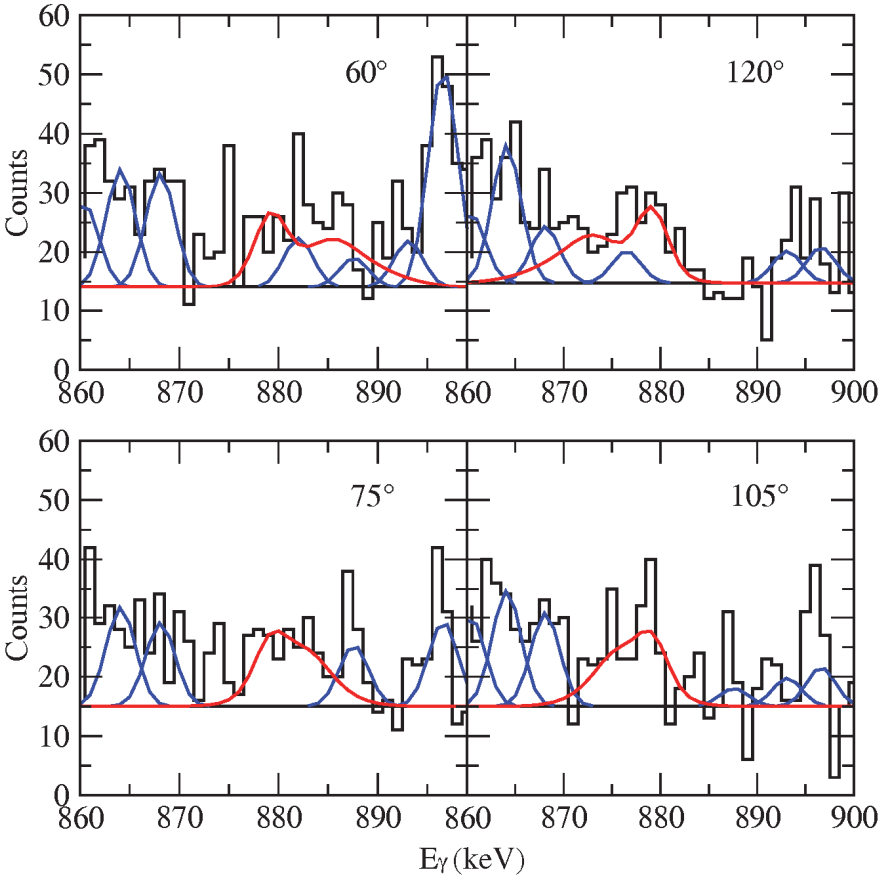

Figure 5-4: DSAM lineshapes for the $14_1^+ \rightarrow 12_1^+$ (879.2 keV) transition in ^{102}Mo. The meaning of the angle labels and the color code of the lines is the same as in Figures 4.11 and 5.2.

5.2.2 ^{104}Mo

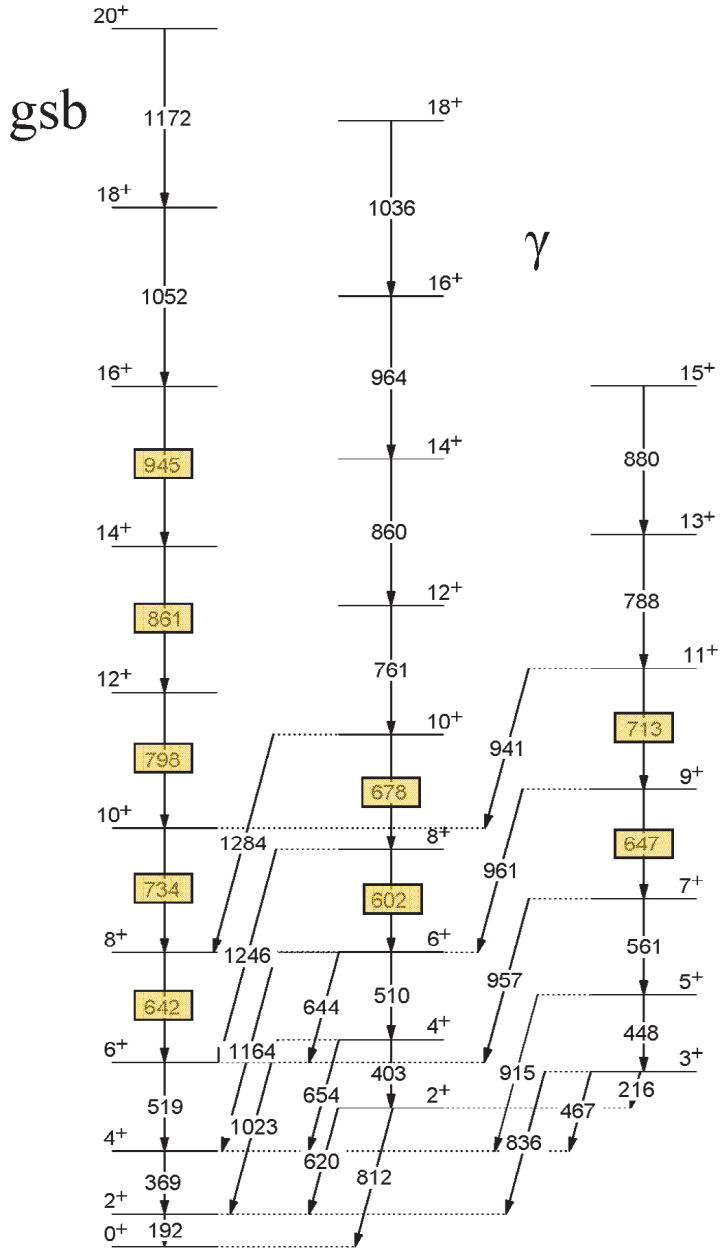

Figure 5-5: Partial level scheme of ^{104}Mo showing the ground-state band (gsb) and the γ band (γ). The transitions for which lineshapes are measured are highlighted.

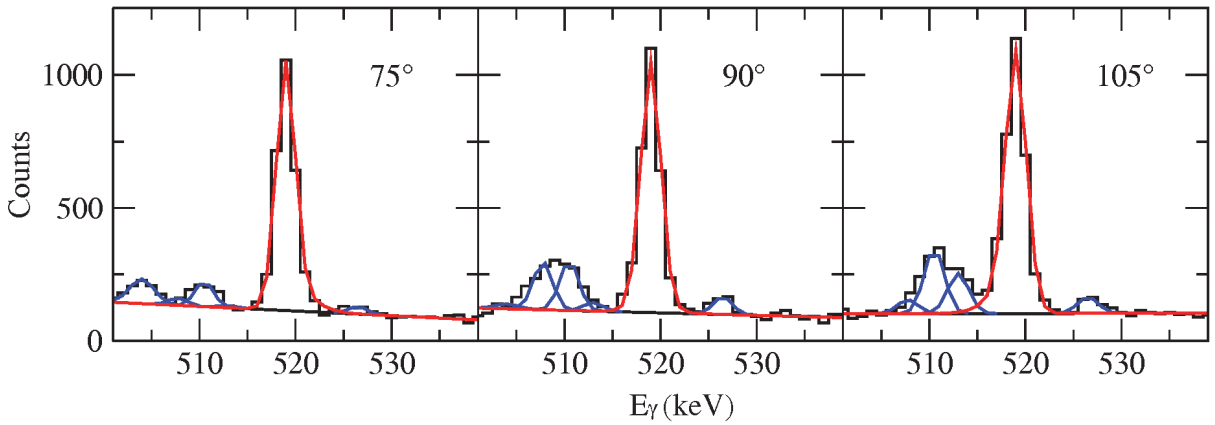

Figure 5-6: DSAM lineshapes for the $6_1^+ \rightarrow 4_1^+$ (519.2 keV) transition in ^{104}Mo. The angles ξ are given in the figure. The color code of the lines is the same as in Figures 4.11 and 5.2.

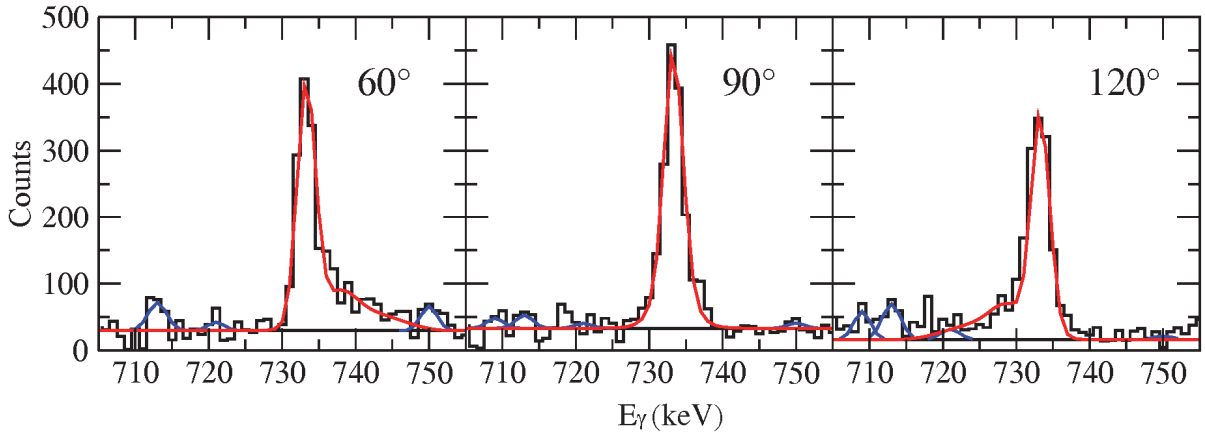

Figure 5-7: Same as Figure 5-6, but for the $10_1^+ \rightarrow 8_1^+$ (733.6 keV) transition.

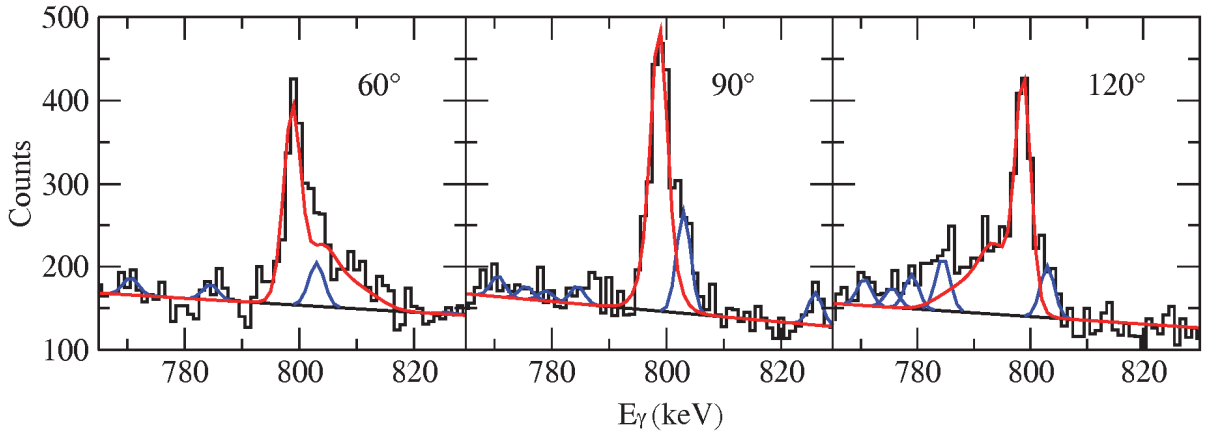

Figure 5-8: Same as Figure 5-6, but for the $12_1^+ \rightarrow 10_1^+$ (798.0 keV) transition.

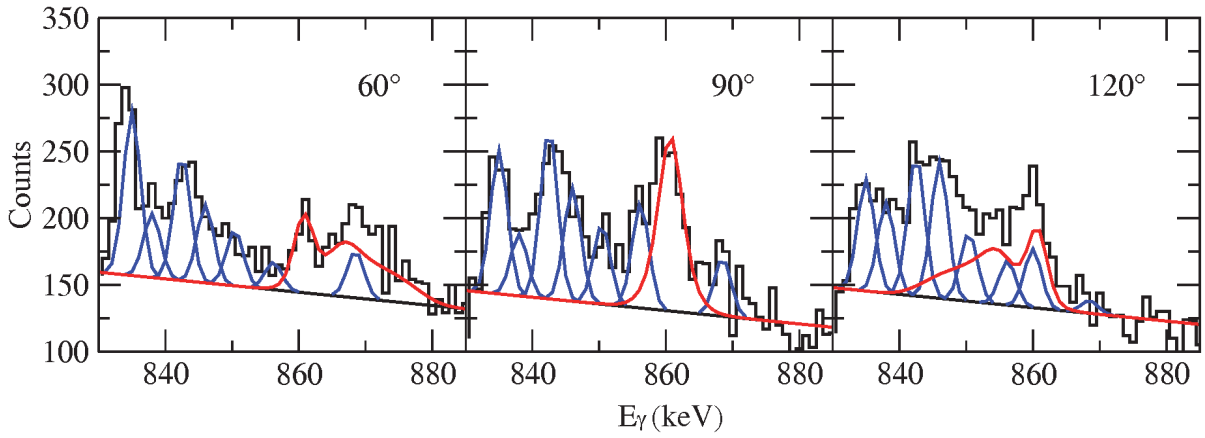

Figure 5-9: Same as Figure 5-6, but for the $14_1^+ \rightarrow 12_1^+$ (861.3 keV) transition.

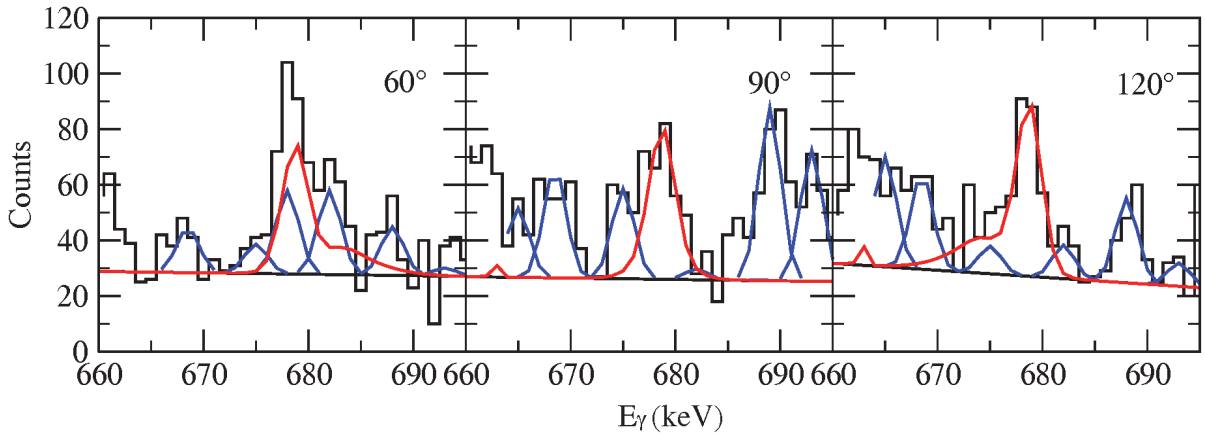

Figure 5-10: Same as Figure 5-6, but for the $10_2^+ \rightarrow 8_2^+$ (678.4 keV) transition.

5.2.3 ^{106}Mo

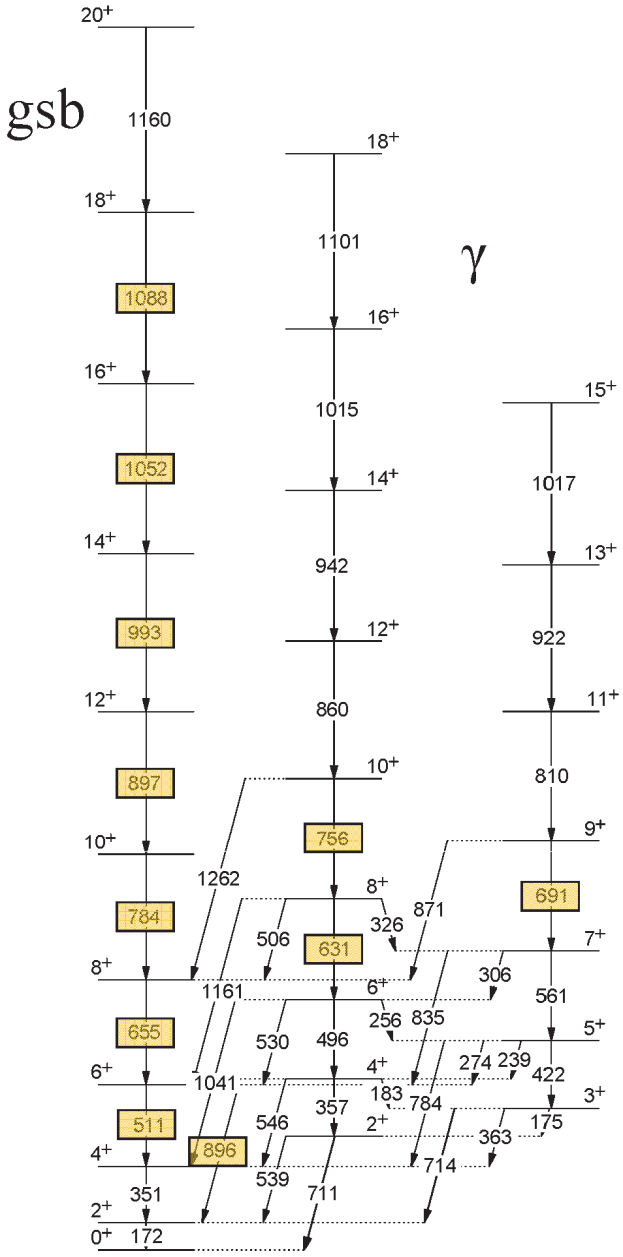

Figure 5-11: Partial level scheme of ^{106}Mo showing the ground-state band (gsb) and the γ band (γ). The transitions for which lineshapes are measured are highlighted.

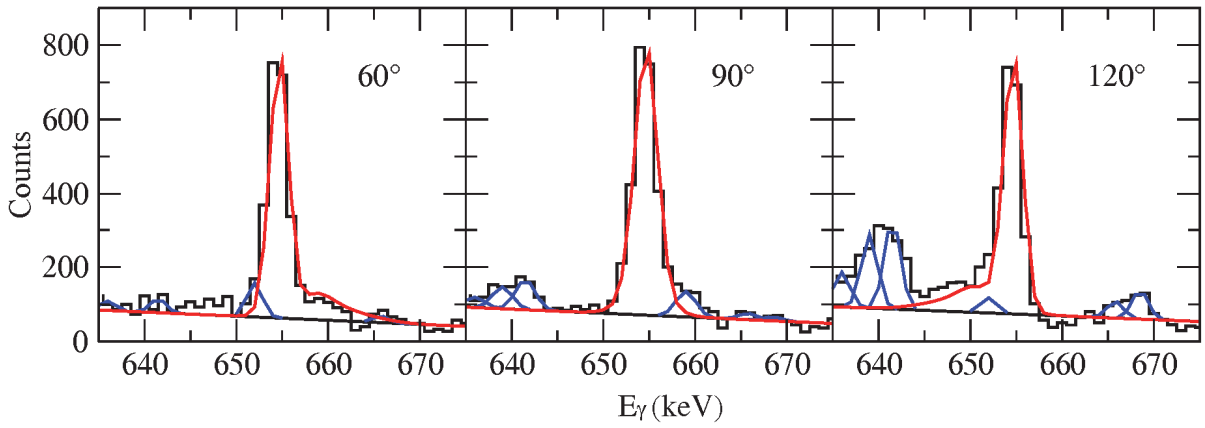

Figure 5-12: DSAM lineshapes for the $8_1^+ \rightarrow 6_1^+$ (654.9 keV) transition in ^{106}Mo. The angles ξ are given in the figure. The color code of the lines is the same as in Figures 4.11 and 5.2.

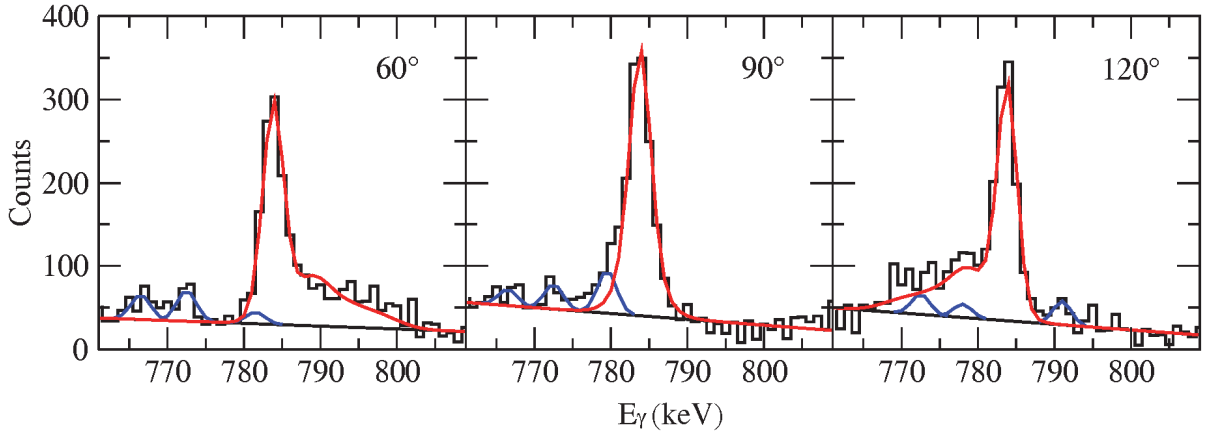

Figure 5-13: Same as Figure 5-12, but for the $10_1^+ \rightarrow 8_1^+$ (784.1 keV) transition.

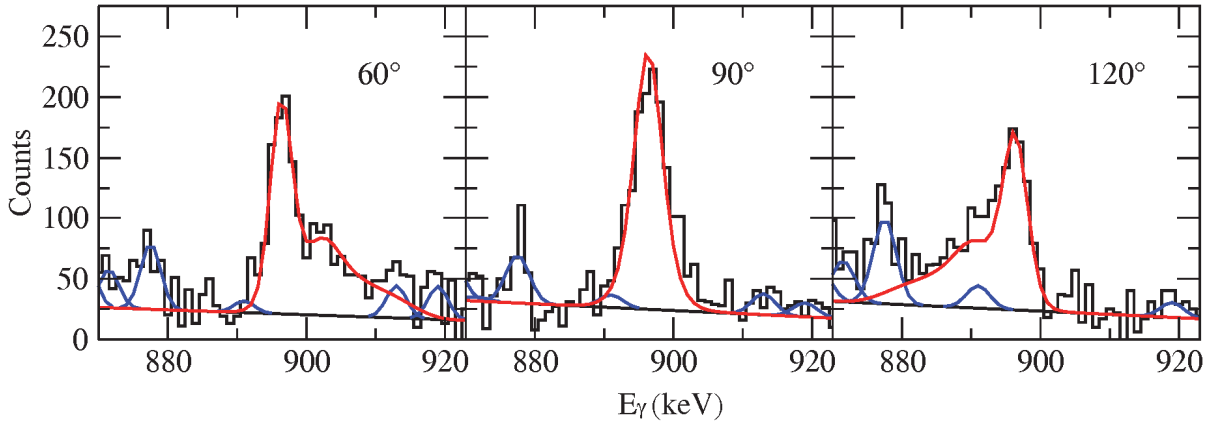

Figure 5-14: Same as Figure 5-12, but for the $12_1^+ \rightarrow 10_1^+$ (896.7 keV) transition.

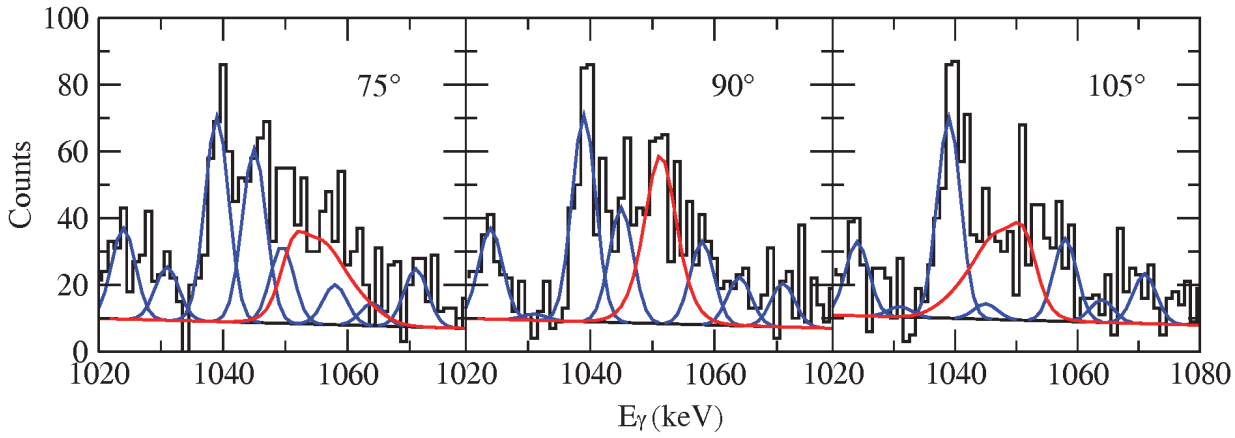

Figure 5-15: Same as Figure 5-12, but for the $16_1^+ \rightarrow 14_1^+$ (1051.5 keV) transition.

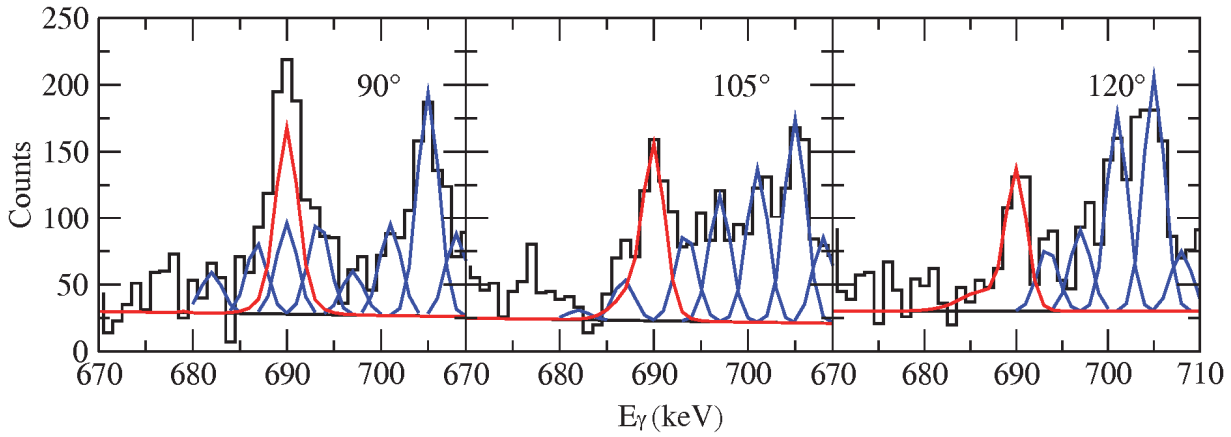

Figure 5-16: Same as Figure 5-12, but for the $9_1^+ \rightarrow 7_1^+$ (690.9 keV) transition.

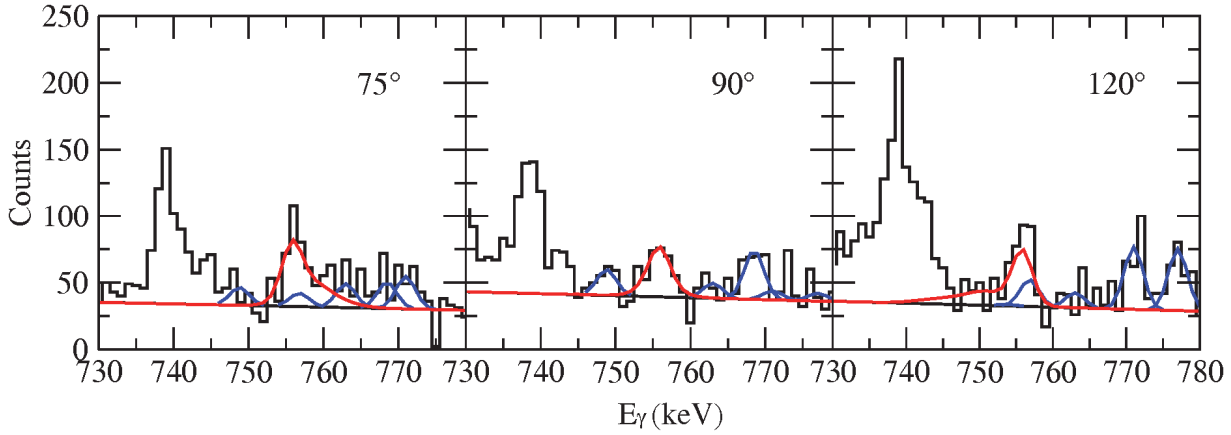

Figure 5-17: Same as Figure 5-12, but for the $10_2^+ \rightarrow 8_2^+$ (756.4 keV) transition.

5.2.4 ^{108}Mo

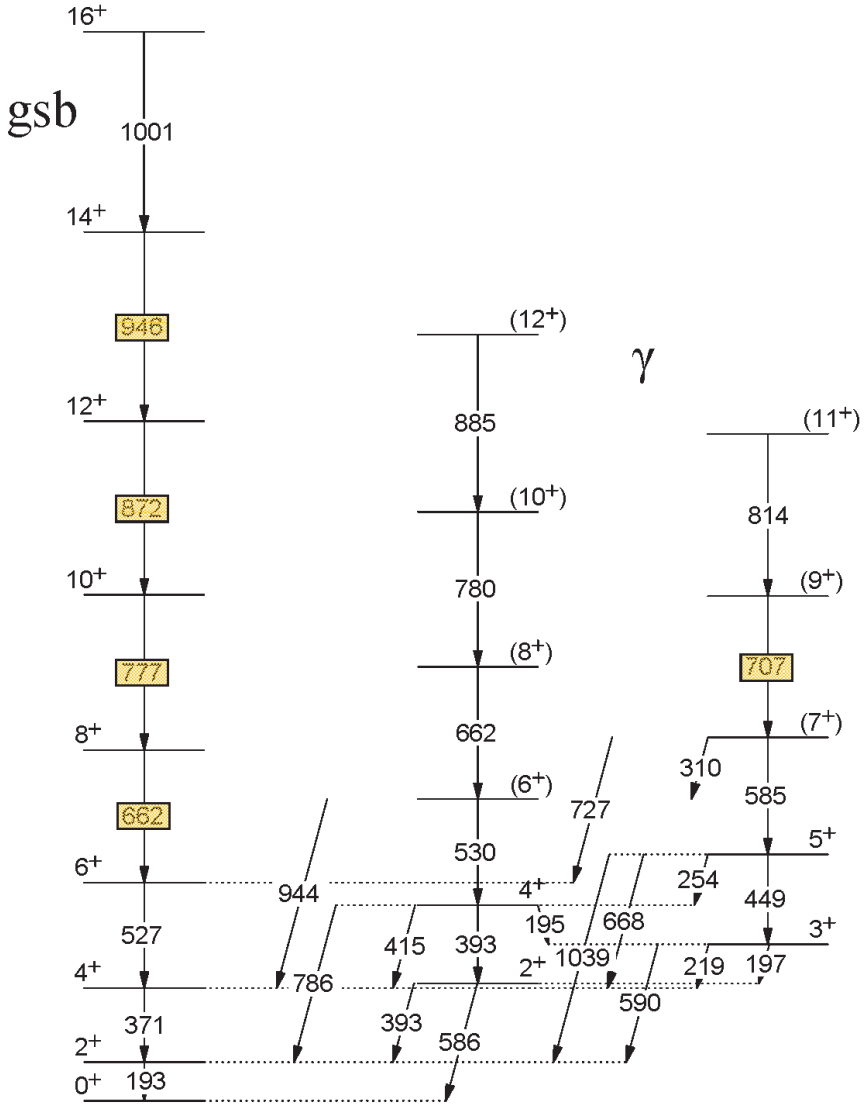

Figure 5-18: Partial level scheme of ^{108}Mo showing the ground-state band (gsb) and the γ band (γ). The transitions for which lineshapes are measured are highlighted.

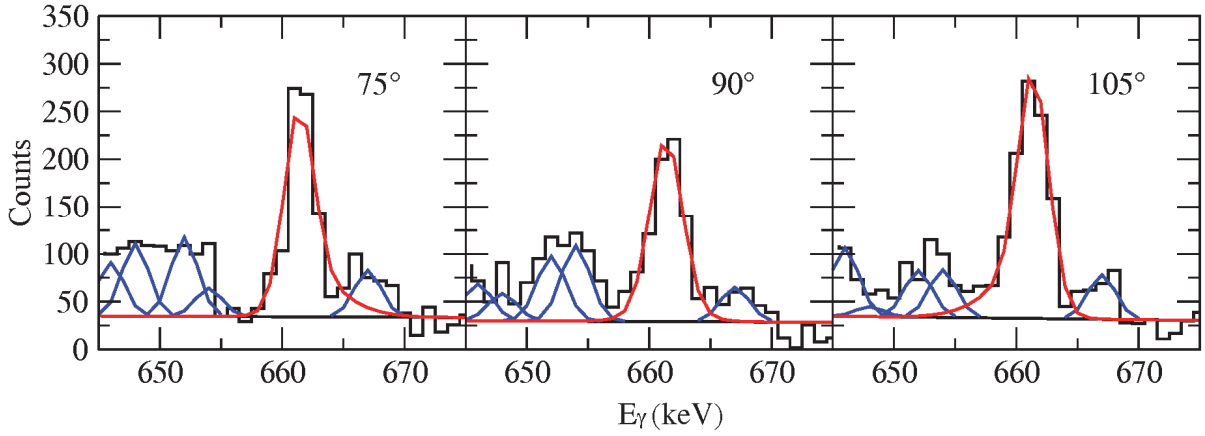

Figure 5-19: DSAM lineshapes for the $8_1^+ \rightarrow 6_1^+$ (662.1 keV) transition in ^{108}Mo. The angles ξ are given in the figure. The color code of the lines is the same as in Figures 4.11 and 5.2.

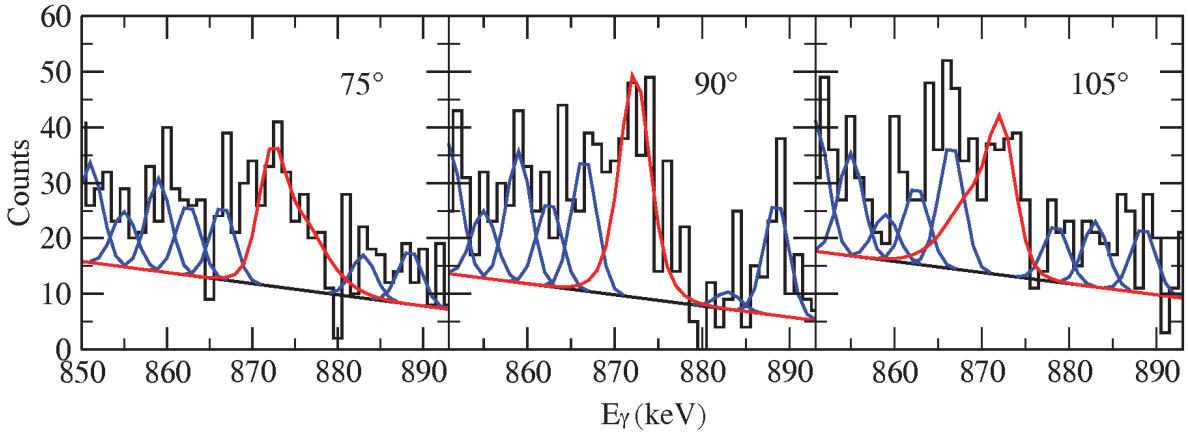

Figure 5-20: Same as Figure 5-19, but for the $12_1^+ \rightarrow 10_1^+$ (872.0 keV) transition.

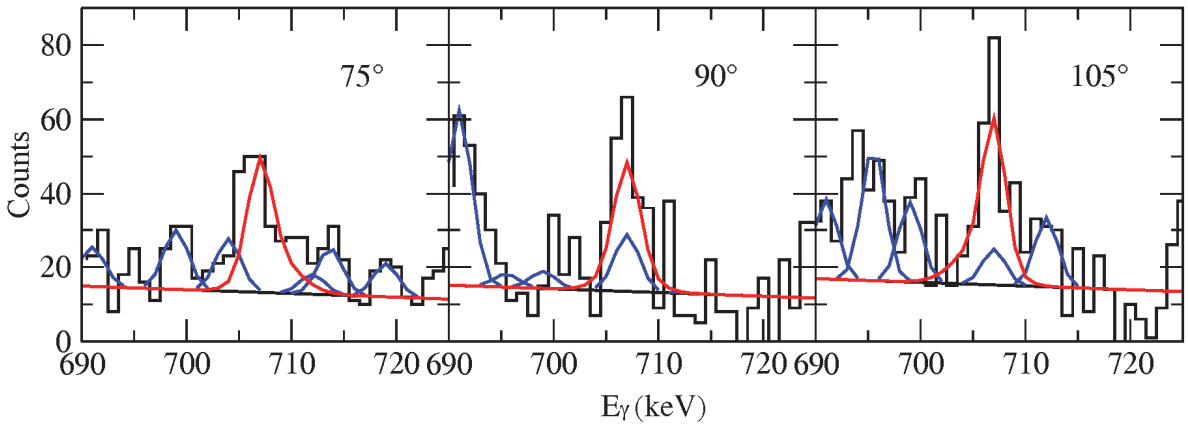

Figure 5-21: Same as Figure 5-19, but for the $9_1^+ \rightarrow 7_1^+$ (707.0 keV) transition.

5.2.5 ^{108}Ru

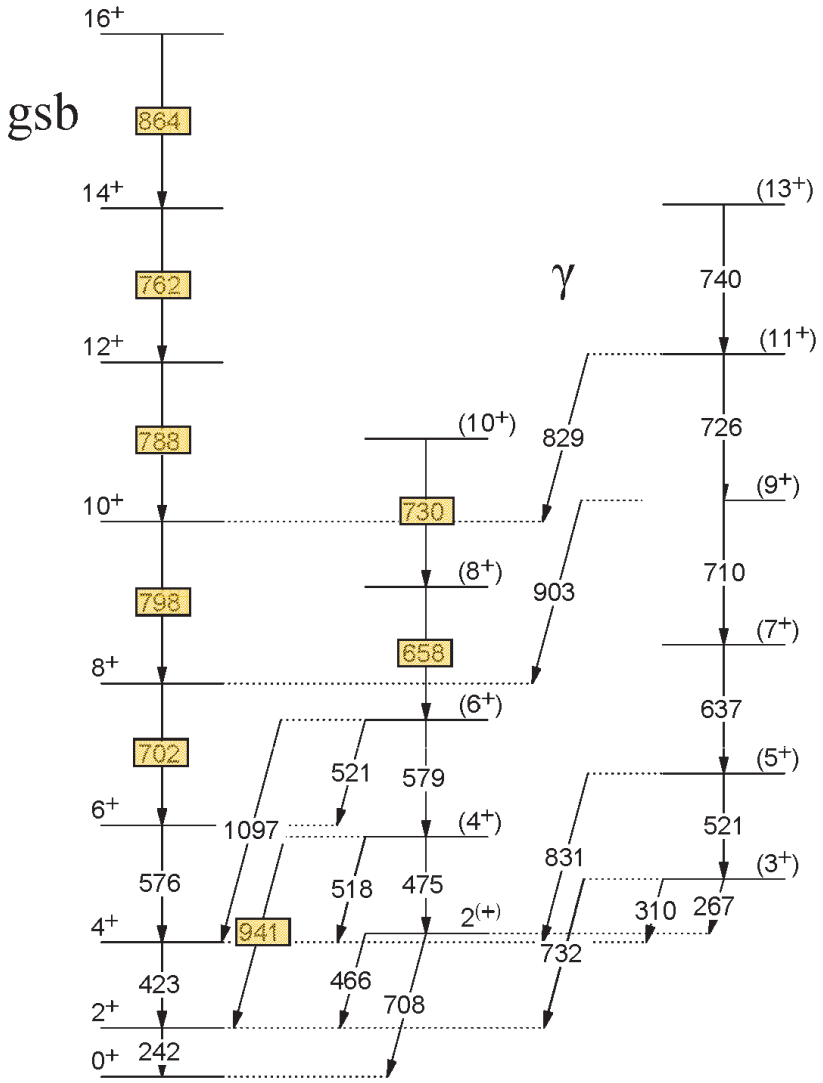

Figure 5-22: Partial level scheme of ^{108}Ru showing the ground-state band (gsb) and the γ band (γ). The transitions for which lineshapes are measured are highlighted.

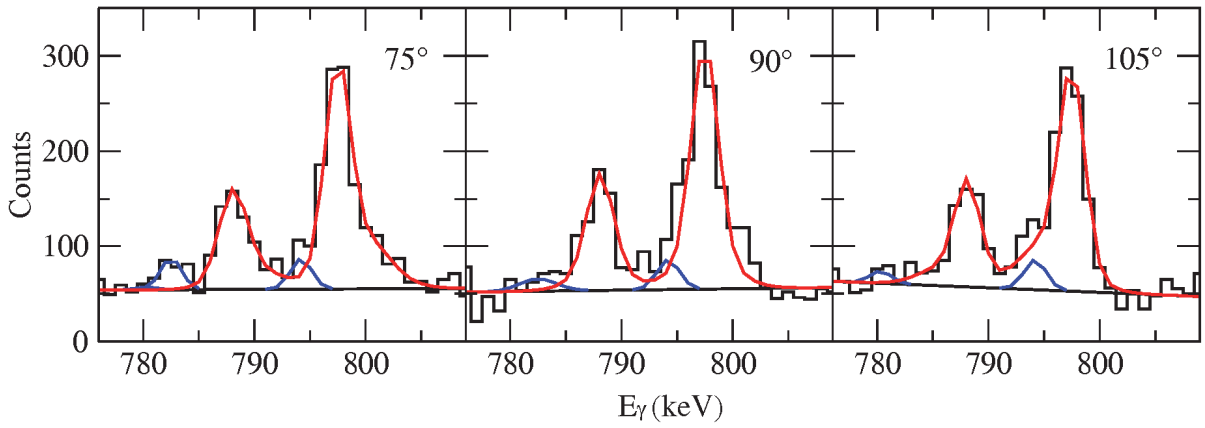

Figure 5-23: DSAM lineshapes for the $12_1^+ \rightarrow 10_1^+$ (788.1 keV) and $10_1^+ \rightarrow 8_1^+$ (798.3 keV) transitions in ^{108}Ru. The angles ξ are given in the figure. The color code of the lines is the same as in Figures 4.11 and 5.2. Every gate includes the $8_1^+ \rightarrow 6_1^+$ transition in ^{108}Ru to avoid overlap from the $16_1^+ \rightarrow 14_1^+$ (799.7 keV) transition in ^{110}Ru.

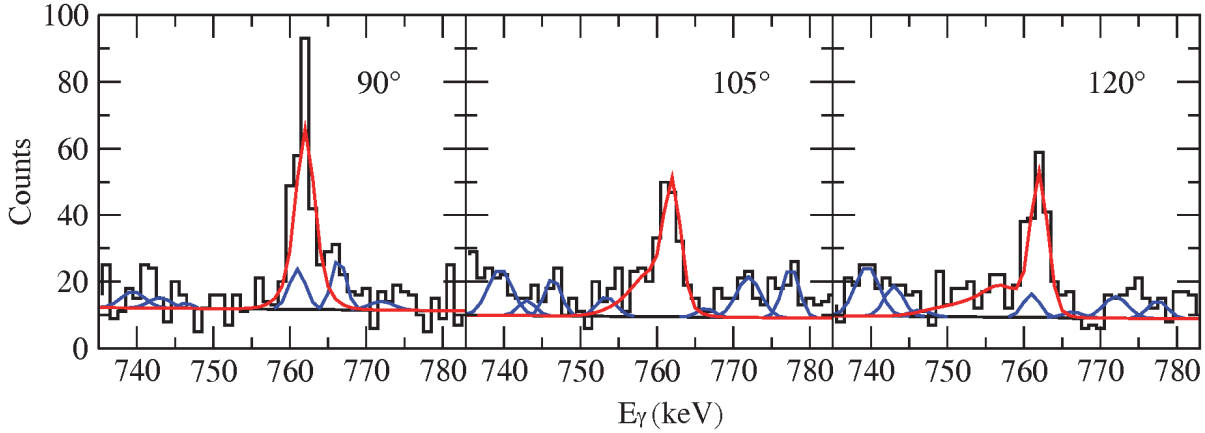

Figure 5-24: Same as Figure 5-23, but for the $14_1^+ \rightarrow 12_1^+$ (762.2 keV) transition.

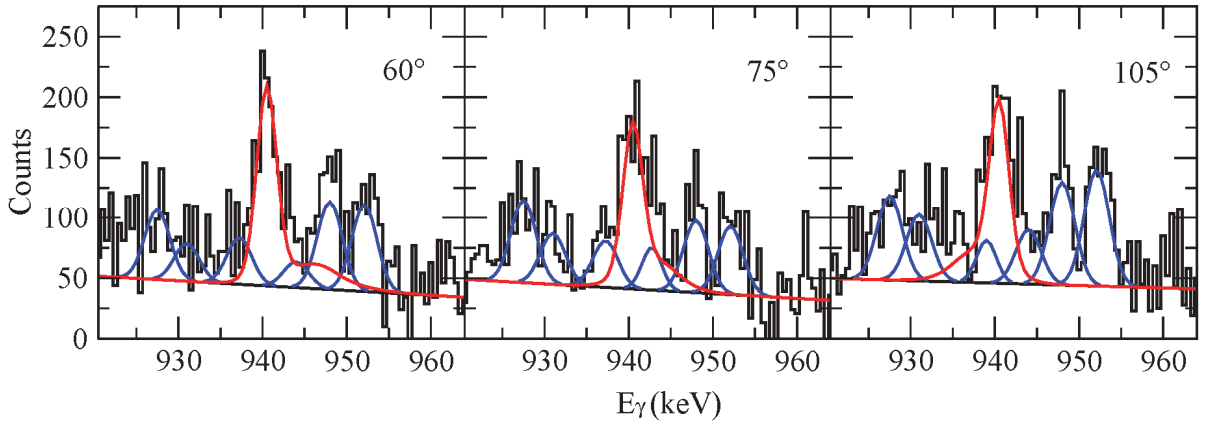

Figure 5-25: Same as Figure 5-23, but for the $4_2^+ \rightarrow 2_1^+$ (940.5 keV) transition. Gated by a single gate on the $2_1^+ \rightarrow 0_1^+$ (242.3 keV) transition.

5.2.6 ^{110}Ru

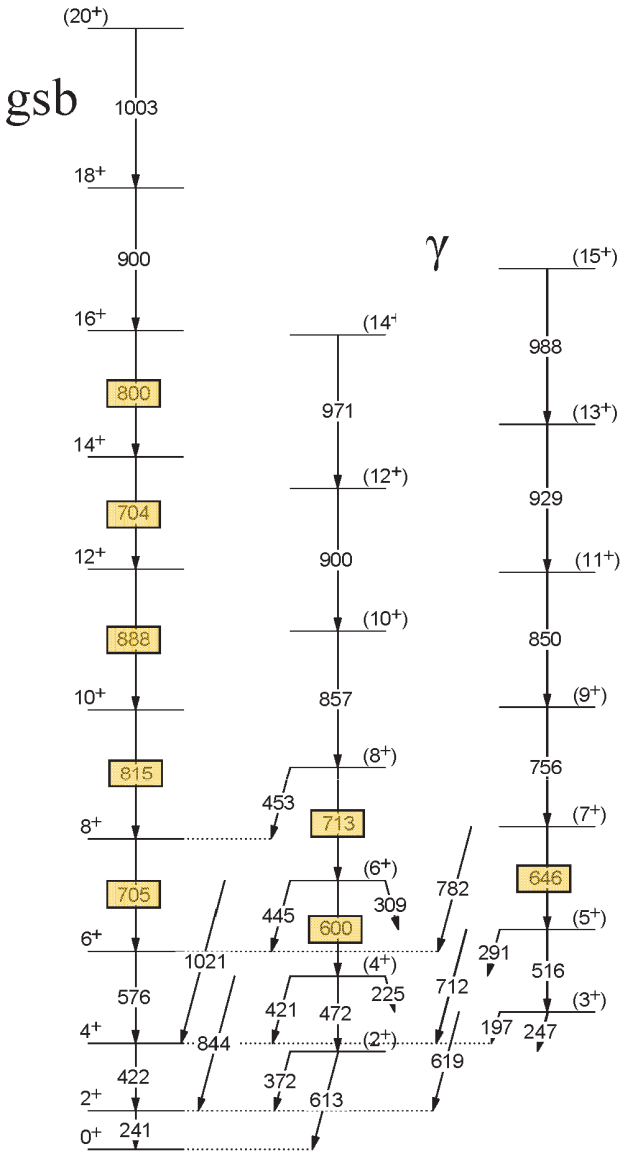

Figure 5-26: Partial level scheme of ^{110}Ru showing the ground-state band (gsb) and the γ band (γ). The transitions for which lineshapes are measured are highlighted.

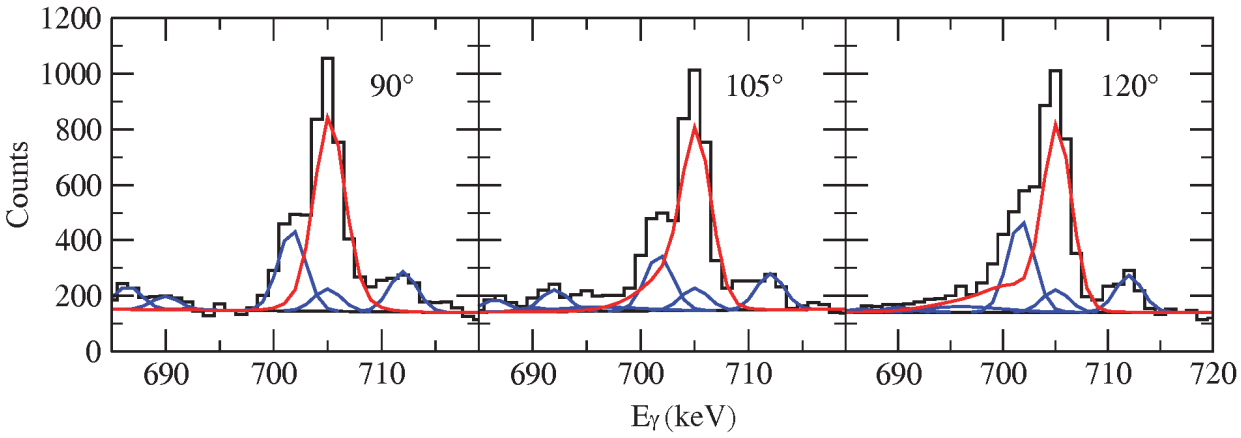

Figure 5-27: DSAM lineshapes for the $8_1^+ \rightarrow 6_1^+$ (705.3 keV) transition in ^{110}Ru. The angles ξ are given in the figure. The color code of the lines is the same as in Figures 4.11 and 5.2. The $14_1^+ \rightarrow 12_1^+$ (703.9 keV) and $8_2^+ \rightarrow 6_2^+$ (712.7 keV) transitions in ^{110}Ru and the $8_1^+ \rightarrow 6_1^+$ (701.6 keV) transition in ^{108}Ru cannot be removed by gating. They are accounted for in the fit.

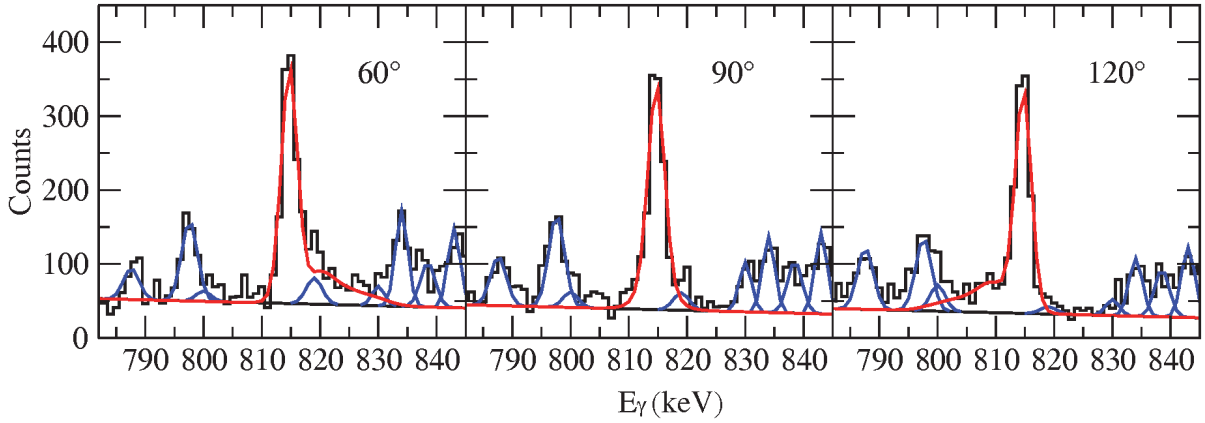

Figure 5-28: Same as Figure 5-27, but for the $10_1^+ \rightarrow 8_1^+$ (815.0 keV) transition.

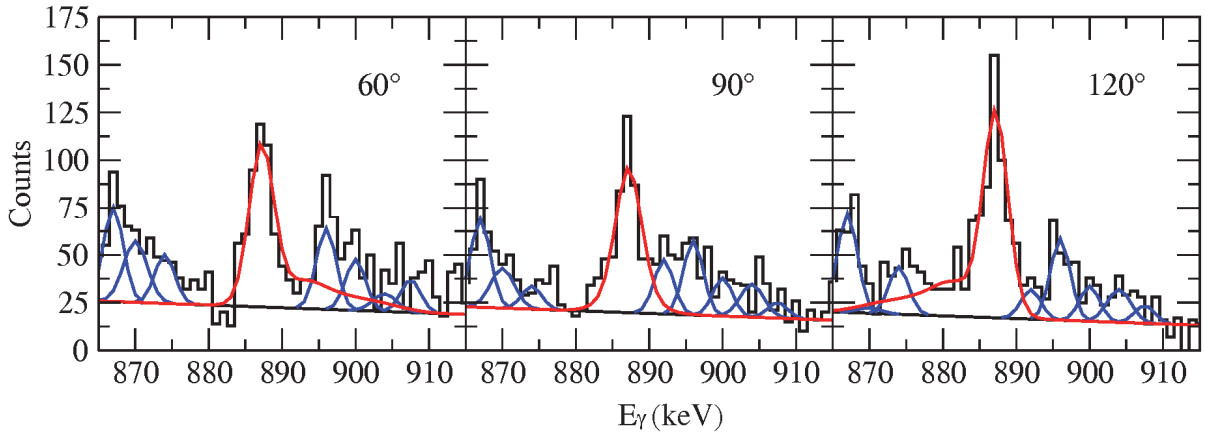

Figure 5-29: Same as Figure 5-27, but for the $12_1^+ \rightarrow 10_1^+$ (887.6 keV) transition.

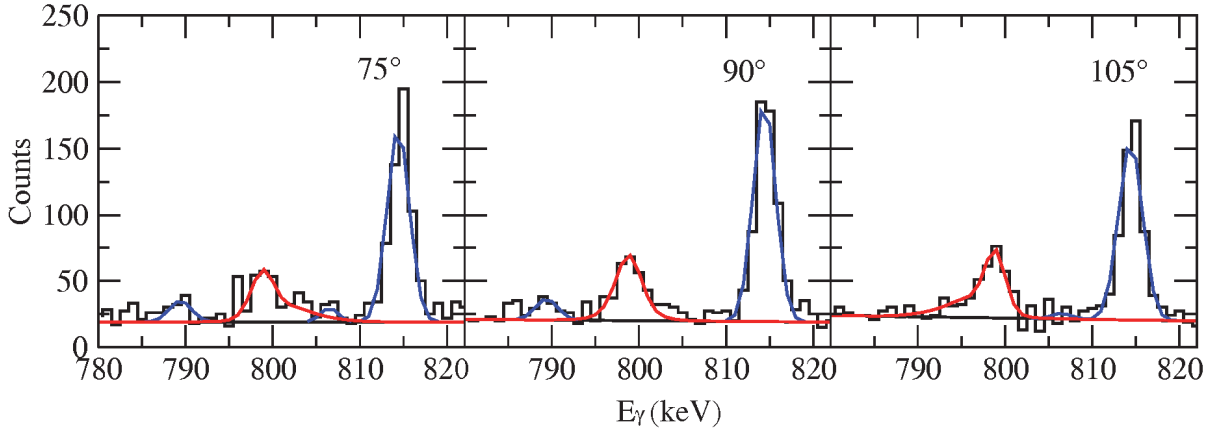

Figure 5-30: Same as Figure 5-27, but for the $16_1^+ \rightarrow 14_1^+$ (799.7 keV) transition ^{110}Ru. Every gate includes either the $10_1^+ \rightarrow 8_1^+$ or $12_1^+ \rightarrow 10_1^+$ transition in ^{110}Ru to avoid overlap from the $10_1^+ \rightarrow 8_1^+$ (798.3 keV) transition in ^{108}Ru.

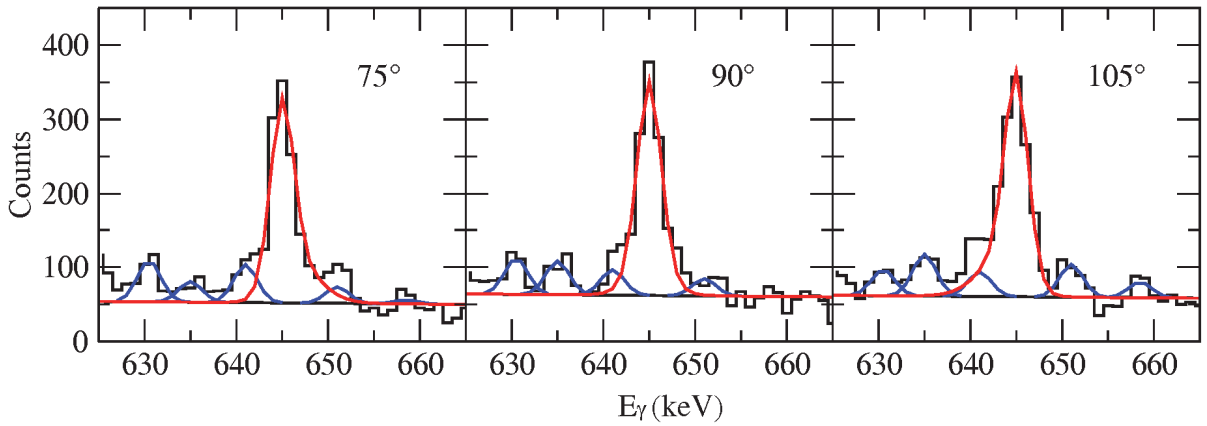

Figure 5-31: Same as Figure 5-27, but for the $7^+ \rightarrow 5_1^+$ (645.5 keV) transition.

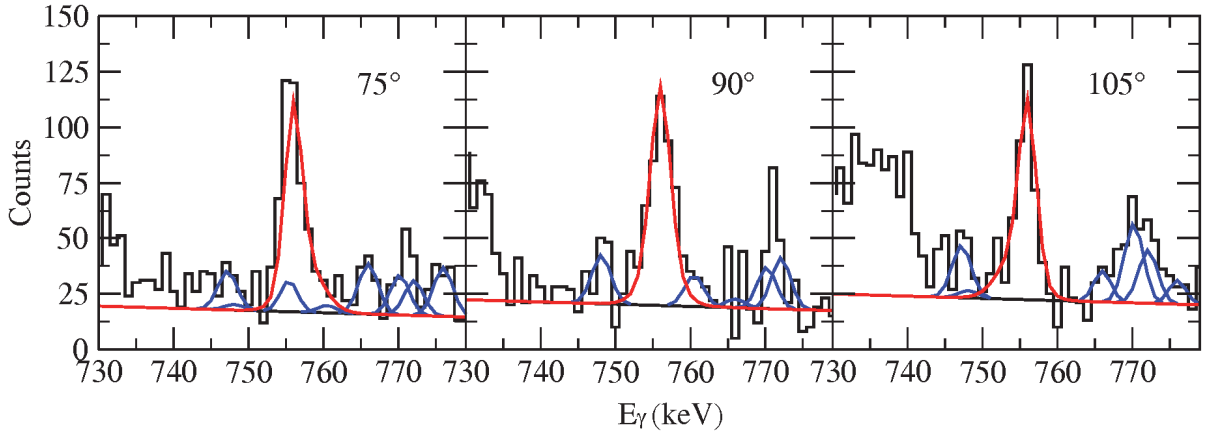

Figure 5-32: Same as Figure 5-27, but for the $9^+ \rightarrow 7^+$ (756.0 keV) transition.

5.2.7 ^{112}Ru

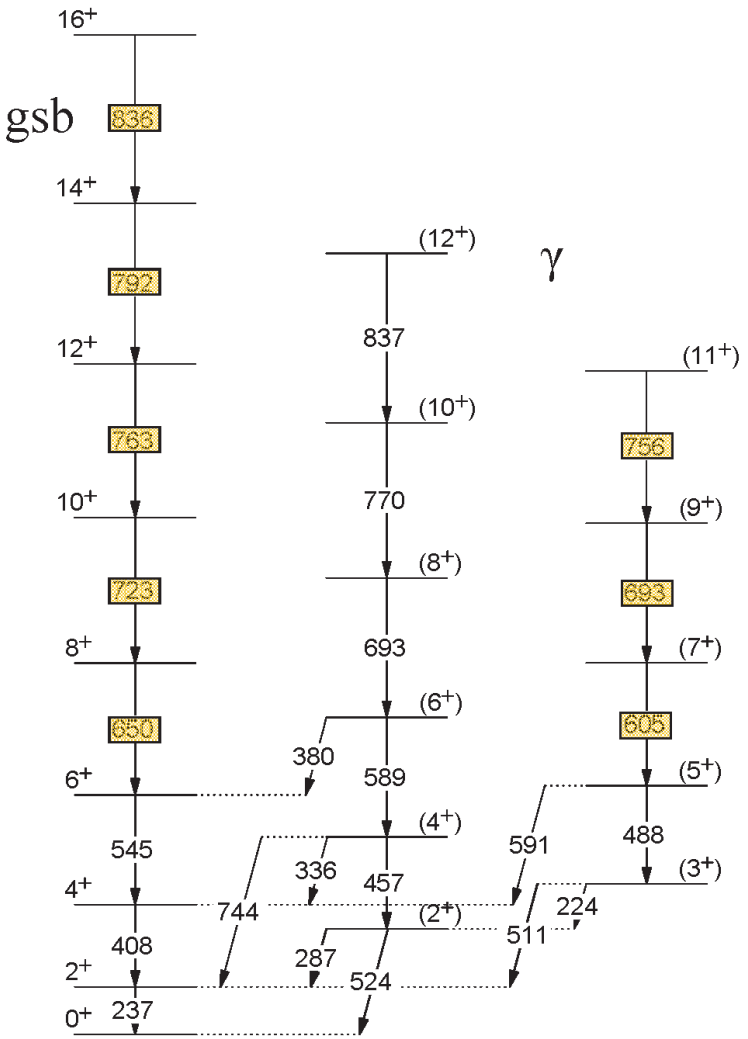

Figure 5-33: Partial level scheme of ^{112}Ru showing the ground-state band (gsb) and the γ band (γ). The transitions for which lineshapes are measured are highlighted.

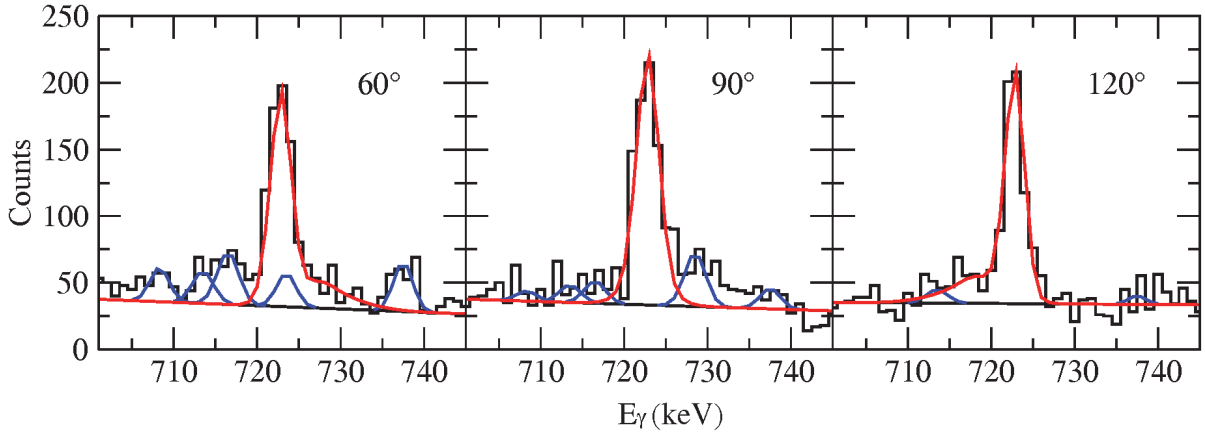

Figure 5-34: DSAM lineshapes for the $10_1^+ \rightarrow 8_1^+$ (723.3 keV) transition in ^{112}Ru. The angles ξ are given in the figure. The color code of the lines is the same as in Figures 4.11 and 5.2.

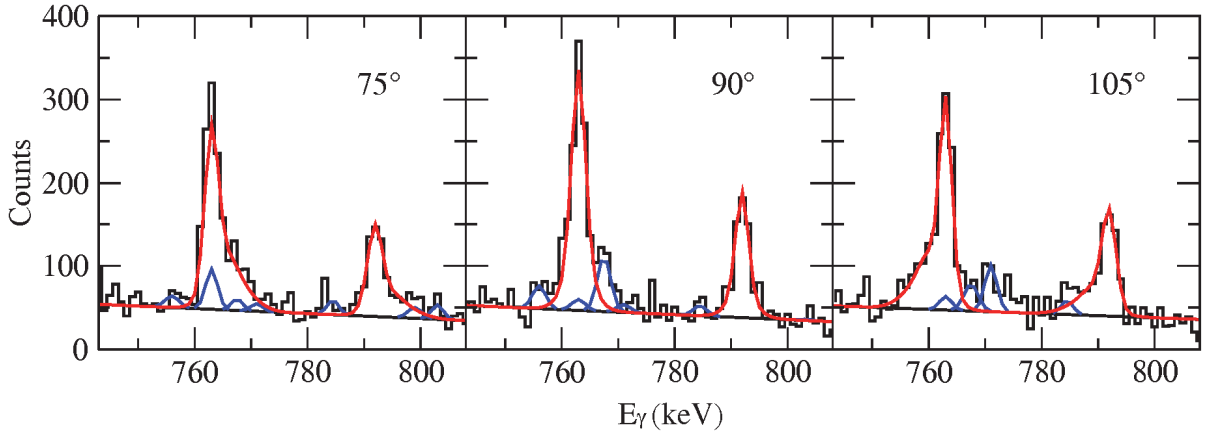

Figure 5-35: Same as Figure 5-34, but for the $14_1^+ \rightarrow 12_1^+$ (791.9 keV) and $12_1^+ \rightarrow 10_1^+$ (763.4 keV) transitions.

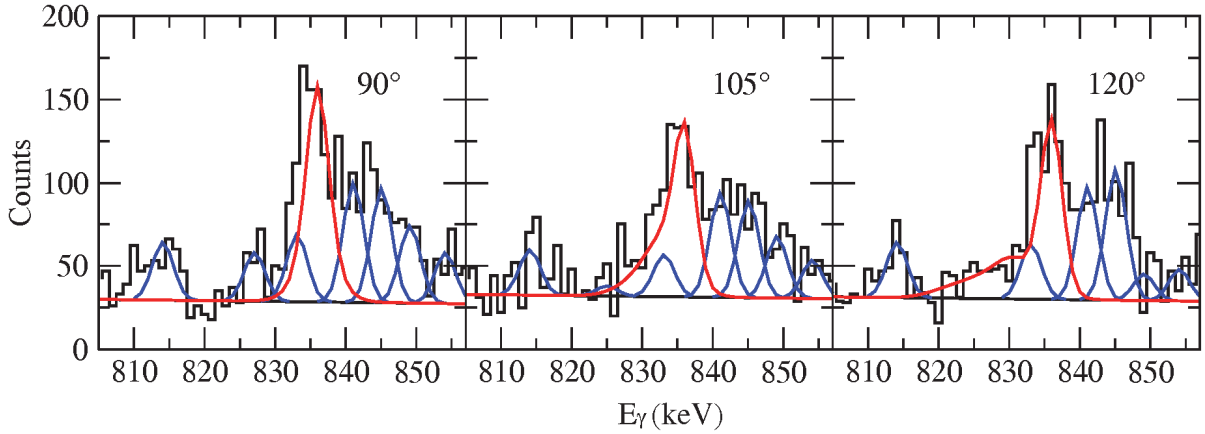

Figure 5-36: Same as Figure 5-34, but for the $16_1^+ \rightarrow 14_1^+$ (836.0 keV) transition.

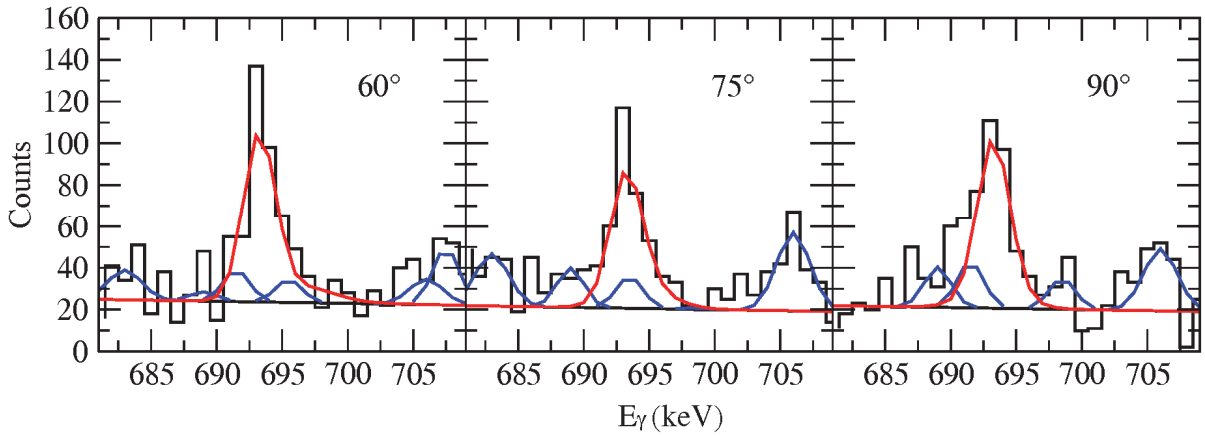

Figure 5-37: Same as Figure 5-34, but for the $9_1^+ \rightarrow 7_1^+$ (693.3 keV) transition.

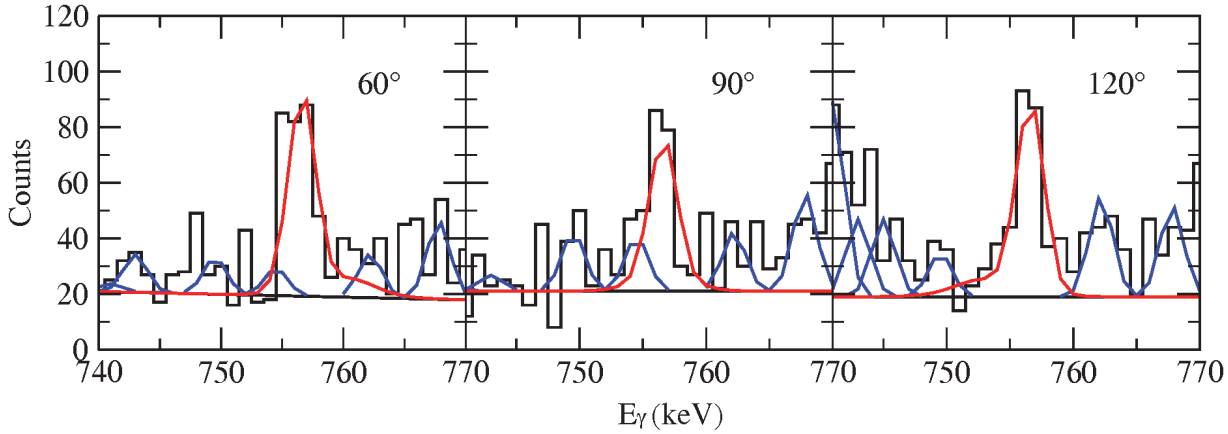

Figure 5-38: Same as Figure 5-34, but for the $11_1^+ \rightarrow 9_1^+$ (756.0 keV) transition.

5.3 Quadrupole Moments

As stated in Section 2.3.4, the Q_t value is calculated by converting the measured lifetime into a B(E2) value and subsequently the B(E2) value into the Q_t value. The Q_t values as a function of spin for the studied Mo and Ru nuclei are shown in Figure 5-39 and Figure 5-40 respectively. Circles and triangles respectively distinguish between the values for the ground-state band and γ band. The solid symbols represent the DSAM measurements of this work. The open symbols augment these measurements with those from the literature [26] [61], including lower-spin transitions accessible by the recoil-distance Doppler-shift method. For the $6_1^+ \rightarrow 4_1^+$ transitions of ^{104,106}Mo, the lineshape fits were only able to provide an upper limit to the Q_t (black arrow).

For some of the states in the γ band, an intensity branching ratio needs to be considered. Here, the partial lifetime of the corresponding transition is used to calculate the B(E2) value. The intensity branching ratios were taken from Reference [26], with two exceptions: the $8_2^+ \rightarrow 6_2^+$ (631.0 keV) and $4_2^+ \rightarrow 2_1^+$ (896.2 keV) transitions of ^{106}Mo. In three other γ-band cases, the reported branching was examined: the 11_1^+ state in ^{104}Mo and the 9_1^+ and 10_2^+ states in ^{106}Mo. Here only the in-band transition was observed with considerable intensity. The intensities of the reported, bypassing decay-out transitions were found to be negligible. This leads us to use a branching ratio of 100% (see Table 5-2).

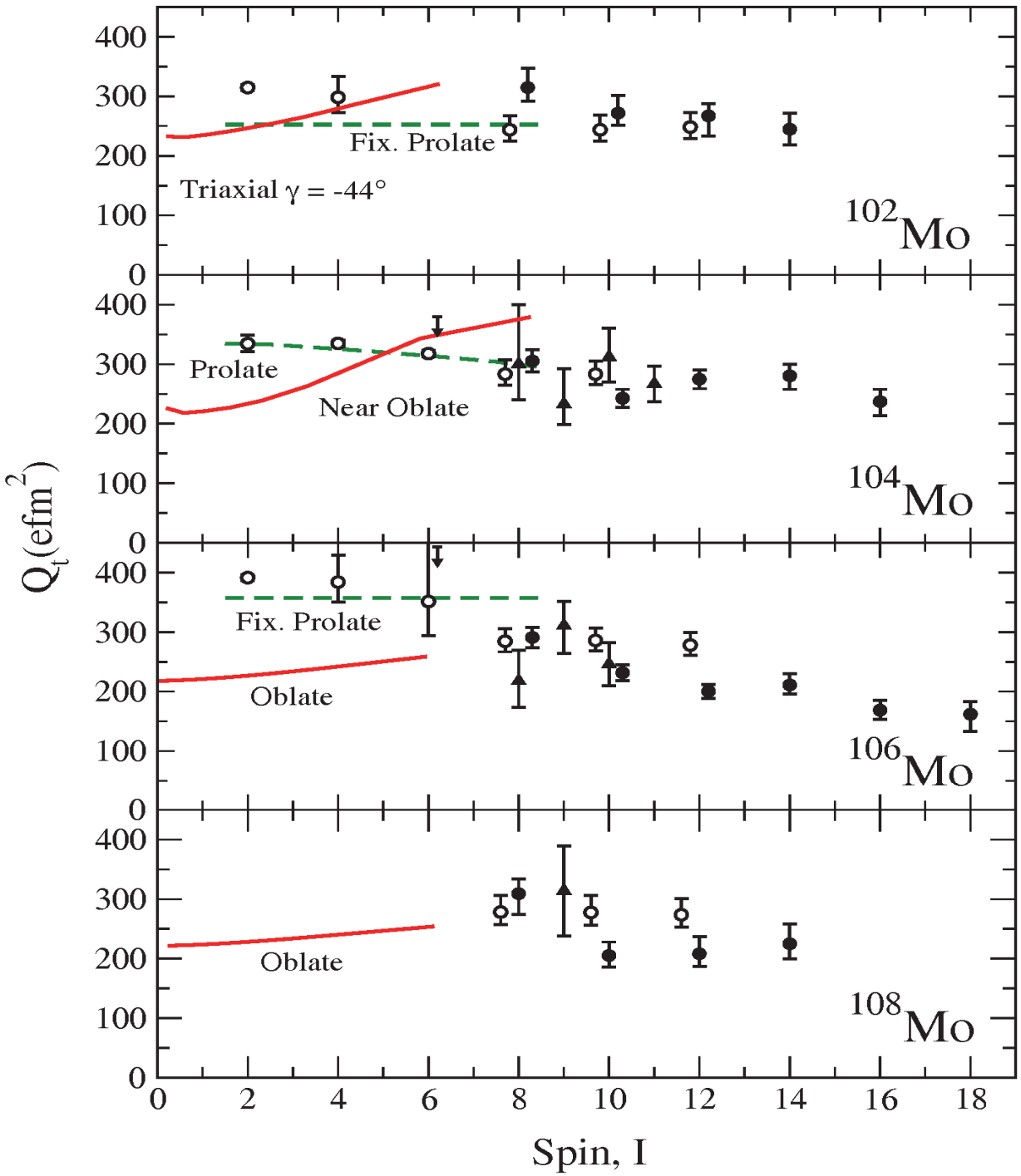

Figure 5-39: Transition quadrupole moments plotted as a function of spin for even-mass $^{102\text{-}108}$Mo. Circles represent data from ground-state-band transitions. Triangles up represent data from the γ-band transitions. The solid points represent the results of the present DSAM measurement, while the open points represent literature values. The curves are calculations discussed in Chapter 6.

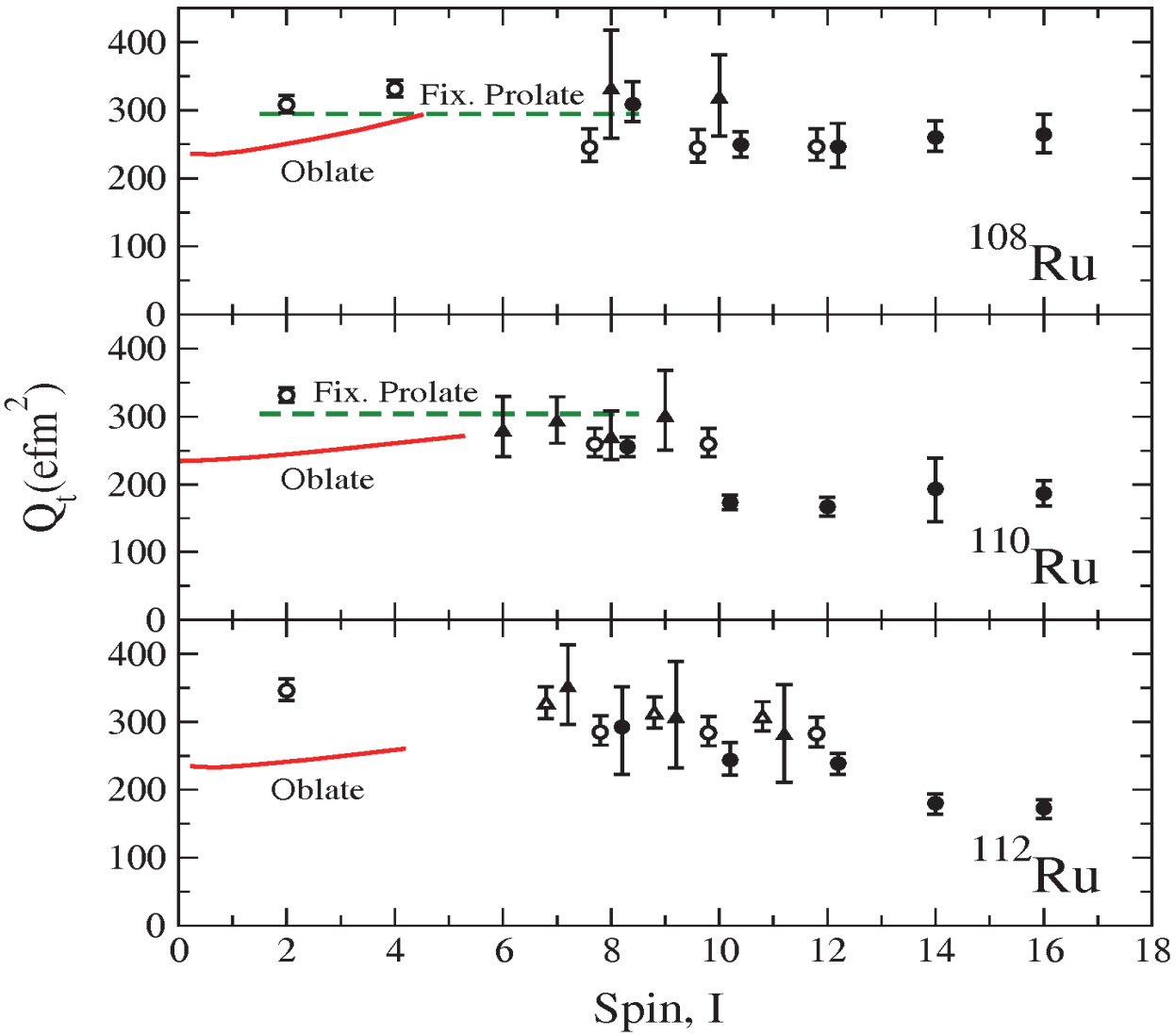

Figure 5-40: Transition quadrupole moments plotted as a function of spin for even-mass $^{108\text{-}112}$Ru. The meaning of the symbols and the curves is the same as in Figure 5-39.

Table 5-2: Properties of transitions relevant for branching ratios of γ-band in-band and decay-out transitions, level energies, spins, transition energies, lifetimes, are listed along with the branching ratios and a reference. This information leads to the B(E2) values. The references "Thesis" and "NNDC" represent this work and Reference [26] respectively. This aspect of the thesis supplements the database where branching ratios are unavailable. This table is a supplement to Table 5-1.

Nucleus	E (keV)	I_i^π	E_γ (keV)	τ (ps)	B.R.	Ref.	B(E2) (e^2fm^4)
^{104}Mo	3395.9	11^+_1	712.9	$1.96^{+0.44}_{-0.44}$	100 [a]	Thesis	2261^{+659}_{-416}
	3004.6	10^+_2	678.4	$1.88^{+0.51}_{-0.59}$	100	NNDC	3021^{+1366}_{-641}
	2683.0	9^+_1	646.5	$2.24^{+0.64}_{-0.73}$	50 (31)	NNDC	1613^{+928}_{-436}
	2326.2	8^+_2	601.7	$3.35^{+1.52}_{-1.42}$	82.0 (63)	NNDC	2533^{+2203}_{-924}
^{106}Mo	2950.7	10^+_2	756.4	$1.77^{+0.52}_{-0.52}$	100 [b]	Thesis	1862^{+775}_{-423}
	2559.2	9^+_1	690.9	$1.81^{+0.54}_{-0.47}$	100 [c]	Thesis	2864^{+996}_{-661}
	2194.3	8^+_2	631.0	$3.46^{+0.71}_{-0.69}$	57 (13)	Thesis	1344^{+719}_{-484}
	1067.8	4^+_2	896.2	$2.33^{+0.27}_{-0.29}$	26.1 (5)	Thesis	158^{+57}_{-44}
^{108}Mo	2524.3	9^+_1	707.0	$1.57^{+1.25}_{-0.56}$	100	NNDC	2943^{+1632}_{-1305}
^{108}Ru	3149.7	10^+_2	730.0	$1.25^{+0.44}_{-0.50}$	100	NNDC	3150^{+2133}_{-815}
	2419.7	8^+_2	657.8	$2.13^{+1.31}_{-0.78}$	100	NNDC	3111^{+1798}_{-1185}
	1183.0	4^+_2	940.5	$1.87^{+0.30}_{-0.30}$	12.4 (58)	NNDC	74^{+55}_{-40}
^{110}Ru	2776.9	9^+	756.0	$1.24^{+0.40}_{-0.57}$	100	NNDC	2665^{+2263}_{-652}
	2397.0	8^+_2	712.7	$1.94^{+0.36}_{-0.38}$	88.7 (61)	NNDC	2029^{+670}_{-434}
	2020.9	7^+	645.5	$3.03^{+0.50}_{-0.49}$	93.1 (64)	NNDC	2238^{+611}_{-450}
	1684.3	6^+_2	599.8	$4.12^{+0.94}_{-0.99}$	70.5 (48)	NNDC	1799^{+729}_{-435}
^{112}Ru	3290.2	11^+_1	756.0	$1.32^{+0.65}_{-0.70}$	100	NNDC	2504^{+2834}_{-830}
	2534.2	9^+_1	693.3	$1.84^{+1.01}_{-0.79}$	100	NNDC	2769^{+2084}_{-981}
	1840.9	7^+_1	605.4	$3.10^{+0.96}_{-1.12}$	100	NNDC	3237^{+1842}_{-763}

[a] The $11^+ \rightarrow 10^+_1$ (941.0 keV) transition reported in Reference [26] has negligible intensity.

[b] The $10^+_2 \rightarrow 8^+_1$ (1262.5 keV) transition reported in Reference [26] has negligible intensity.

[c] The $9^+_1 \rightarrow 8^+_1$ (871.0 keV) transition reported in Reference [26] has negligible intensity.

There is agreement between measured and literature Q_t values at the spins 8^+, 10^+, and 12^+ of the ground-state band. The Q_t values for the two types of bands from the present measurements are comparable in magnitude. The values for the γ bands have larger uncertainties, as expected. For

the γ band, comparison with literature is only available for the 7^+, 9^+, and 11^+ spin states of ^{112}Ru. The uncertainties of these values are surprisingly small.

The following observations can be made about the behavior of ground-state bands. The Q_t values decrease with increasing spin, this effect is accentuated in the heavier isotopes. Figure 5-41 displays the weighted average Q_t (efm^2) for $8 \leq I \leq 16$ of the ground-state bands (the I=16 state is not included for ^{102,108}Mo). The average Q_t decreases with increasing N, stepping "down" at N=66 and 64 for Ru and Mo respectively. This decrease seems more pronounced in the Ru isotopes than in the available Mo nuclei.

Z \ N	60	62	64	66	68
44			^{108}Ru 261±11	^{110}Ru 192±16	^{112}Ru 198±26
42	^{102}Mo 274±15	^{104}Mo 267±13	^{106}Mo 217±20	^{108}Mo 229±25	

Figure 5-41: Q_t (efm^2) trends as a function of Z and N.

5.4 Level Feeding Intensities

For the DSAM analysis the relative intensities of the transitions in a band are needed, in order to properly model the side feeding, see Section 4.3.2. Information on level-feeding intensities is in principle available in the NNDC database [26]. Unfortunately, many of the intensities reported there for the Mo and Ru isotopes under analysis here are useless (actually in many cases only branching ratios are reported in the database due to the scarce information in the literature). Hence, the transition intensities had to be measured. They are listed in Table 5-3. This is the complete account of the present intensity analysis, it partially overlaps with Table 5-1 and Table 5-2.

Only the side-feeding intensity of the $16_1^+ \rightarrow 14_1^+$ transition of ^{108}Ru, could not be determined in the way described above. A directly feeding $18_1^+ \rightarrow 16_1^+$ transition in this nucleus has not been reported. A candidate for the transition has been found at 986 keV (with an intensity of 0.12 and a >40% error). Here the predicted feeding intensity from the program (using a rotational model) has been adapted.

The feeding intensities, based on the values of Table 5-3, are plotted in Figures 5.42 and 5.43. The ground state and γ bands are represented with closed and open symbols respectively. The color code of the legend identifies the nucleus. As spin increases the feeding intensity within a band decreases. In some cases, for example ^{104}Mo, the difference in the intensity profiles of the two bands of the same nucleus also changes with spin. At low spin, the ground-state band is about a factor of ten stronger than the γ band. At high spin, this factor has been reduced to a factor of three to five. The feeding of the 2_2^+ state in the γ band of ^{106}Mo is found to be surprisingly strong; this cannot be explained at this point.

Table 5-3: Relative transition intensities (normalized such that $I_\gamma \equiv 100$ for the $8_1^+ \rightarrow 6_1^+$ transition) for $^{102, 104, 106, 108}$Mo and $^{108, 110, 112}$Ru. The transitions in the ground-state-band, the γ-band, and the decay-out transitions are grouped together. Subscripts a,b,c, and d denote those intensities taken from the literature. Subscript e denotes those determined from the branching ratio in Reference 26. The reference for the transition energies and spin assignments is the same as Table 5-1 except for the $18_1^+ \rightarrow 16_1^+$ state in ^{112}Ru 69.

^{102}Mo				^{104}Mo				^{106}Mo				^{108}Mo			
E_γ (keV)	I_i^π	I_f^π	I_γ (%)	E_γ (keV)	I_i^π	I_f^π	I_γ (%)	E_γ (keV)	I_i^π	I_f^π	I_γ (%)	E_γ (keV)	I_i^π	I_f^π	I_γ (%)
966.5	16_1^+	14_1^+	0.5 ±0.2	1172.0	18_1^+	16_1^+	0.2 ±0.1	1160.4	20_1^+	18_1^+	0.6 ±0.3	1000.5	16_1^+	14_1^+	3.8 ±1.7
879.2	14_1^+	12_1^+	2.3 ±0.8	945.0	16_1^+	14_1^+	2.6 ±0.4	1087.6	18_1^+	16_1^+	1.9 ±0.9	945.6	14_1^+	12_1^+	8.2 ±2.5
834.9	12_1^+	10_1^+	20.6 ±3.4	861.3	14_1^+	12_1^+	10.0 ±1.3	1051.5	16_1^+	14_1^+	5.2 ±0.9	872.0	12_1^+	10_1^+	19.6 ±6.8
771.5	10_1^+	8_1^+	48.1 ±6.3	798.0	12_1^+	10_1^+	19.7 ±1.2	992.9	14_1^+	12_1^+	8.9 ±1.9	776.6	10_1^+	8_1^+	57.7 ±6.2
690.9	8_1^+	6_1^+	=100 ±8.0	733.6	10_1^+	8_1^+	40.8 ±1.3	896.7	12_1^+	10_1^+	17.9 ±1.9	662.1	8_1^+	6_1^+	=100 ±8.8
584.2	6_1^+	4_1^+	209[a]	641.7	8_1^+	6_1^+	=100 ±2.0	784.1	10_1^+	8_1^+	42.9 ±2.5	527.0	6_1^+	4_1^+	190[b]
447.1	4_1^+	2_1^+	269 ±14	519.2	6_1^+	4_1^+	184 ±3.1	654.9	8_1^+	6_1^+	=100 ±3.7	370.9	4_1^+	2_1^+	300[b]
296.6	2_1^+	0_1^+	313 ±47	368.5	4_1^+	2_1^+	270[b]	511.2	6_1^+	4_1^+	252 ±8.6	192.7	2_1^+	0_1^+	490[b]
612.0	6_2^+	4_2^+	8.8 ±2.2	192.2	2_1^+	0_1^+	410[b]	350.8	4_1^+	2_1^+	390[c]	884.5	12_2^+	10_2^+	7.2 ±2.5
550.5	4_2^+	2_2^+	32[e] ±6.1	760.8	12_2^+	10_2^+	2.5 ±0.9	171.5	2_1^+	0_1^+	560[c]	779.5	10_2^+	8_2^+	13.0 ±4.3
847.9	2_2^+	0_1^+	14[e] ±2.7	712.9	11^+	9_1^+	5.1 ±2.2	859.8	12_2^+	10_2^+	1.7 ±0.4	707.0	9_1^+	7_1^+	25.0 ±2.7
654.7	4_2^+	4_1^+	34 ±4.8	678.4	10_2^+	8_2^+	6.2 ±0.9	756.4	10_2^+	8_2^+	3.6 ±0.9	662.3	8_2^+	6_2^+	33.8 ±6.4
1102.4	4_2^+	2_1^+	15[e] ±2.9	646.5	9_1^+	7_1^+	14.0 ±2.8	690.9	9_1^+	7_1^+	9.1 ±0.8	529.5	6_2^+	4_2^+	70.2 ±6.7
551.3	2_2^+	2_1^+	25 ±3.8	601.7	8_2^+	6_2^+	24.9 ±2.1	631.0	8_2^+	6_2^+	12.1 ±2.5	392.4	4_2^+	2_2^+	96[be]
				509.6	6_2^+	4_2^+	20.4 ±1.4	495.5	6_2^+	4_2^+	15.2 ±1.8	586.1	2_2^+	0_1^+	46[be]
				402.5	4_2^+	2_2^+	3.2[e] ±0.5	357.3	4_2^+	2_2^+	116 ±23	944.1	6_2^+	4_1^+	11.7 ±3.7
				812.4	2_2^+	0_1^+	21.8[be]	710.5	2_2^+	0_1^+	54[ce]	414.6	4_2^+	4_1^+	105[b]
				1246.2	8_2^+	6_1^+	5.5[e] ±1.4	506.2	8_2^+	8_1^+	4.2 ±2.1	785.5	4_2^+	2_1^+	84[be]
				644.4	6_2^+	6_1^+	15.5[e] ±4.2	1160.9	8_2^+	6_1^+	2.0 ±0.8	393.2	2_2^+	2_1^+	85[b]
				1163.7	6_2^+	4_1^+	9.6[e] ±2.6	326.1	8_2^+	7_1^+	3.1 ±1.1				
				654.1	4_2^+	4_1^+	9.6 ±0.8	529.9	6_2^+	6_1^+	8.2[b]				
				1022.6	4_2^+	2_1^+	10.1[e] ±1.3	1040.9	6_2^+	4_1^+	4.8[b]				
				620.2	2_2^+	2_1^+	27.9[b]	545.5	4_2^+	4_1^+	24.0 ±5.6				
								896.2	4_2^+	2_1^+	55.9 ±17				
								538.9	2_2^+	2_1^+	74[c]				

Table 5-3: (Continued.)

^{108}Ru				^{110}Ru				^{112}Ru			
E_γ (keV)	I_i^π	$\rightarrow$ I_f^π	I_γ (%)	E_γ (keV)	I_i^π	$\rightarrow$ I_f^π	I_γ (%)	E_γ (keV)	I_i^π	$\rightarrow$ I_f^π	I_γ (%)
863.6	16^+_1	$\rightarrow 14^+_1$	2.3 ±1.0	900.1	18^+_1	$\rightarrow 16^+_1$	3.4 ±1.5	875.0	18^+_1	$\rightarrow 16^+_1$	3.4 ±1.5
762.2	14^+_1	$\rightarrow 12^+_1$	5.1 ±1.3	799.7	16^+_1	$\rightarrow 14^+_1$	5.4 ±0.8	836.0	16^+_1	$\rightarrow 14^+_1$	7.1 ±2.2
788.1	12^+_1	$\rightarrow 10^+_1$	19.9 ±1.9	703.9	14^+_1	$\rightarrow 12^+_1$	7.9 ±2.0	791.9	14^+_1	$\rightarrow 12^+_1$	12.3 ±4.9
798.3	10^+_1	$\rightarrow 8^+_1$	41.6 ±2.0	887.6	12^+_1	$\rightarrow 10^+_1$	12.5 ±1.1	763.4	12^+_1	$\rightarrow 10^+_1$	31.3 ±4.1
701.6	8^+_1	$\rightarrow 6^+_1$	=100 ±2.7	815.0	10^+_1	$\rightarrow 8^+_1$	37.6 ±1.4	723.3	10^+_1	$\rightarrow 8^+_1$	55.9 ±5.3
575.5	6^+_1	$\rightarrow 4^+_1$	382[d]	705.3	8^+_1	$\rightarrow 6^+_1$	=100 ±2.1	649.5	8^+_1	$\rightarrow 6^+_1$	=100 ±6.0
422.9	4^+_1	$\rightarrow 2^+_1$	614[d]	575.6	6^+_1	$\rightarrow 4^+_1$	275[d]	544.9	6^+_1	$\rightarrow 4^+_1$	312[d]
242.3	2^+_1	$\rightarrow 0^+_1$	830[d]	422.3	4^+_1	$\rightarrow 2^+_1$	463[d]	408.4	4^+_1	$\rightarrow 2^+_1$	453[d]
730.0	10^+_2	$\rightarrow 8^+_2$	11.5 ±4.3	240.8	2^+_1	$\rightarrow 0^+_1$	625[d]	236.6	2^+_1	$\rightarrow 0^+_1$	588[d]
657.8	8^+_2	$\rightarrow 6^+_2$	20.8 ±3.8	857.3	10^+_2	$\rightarrow 8^+_2$	13.1 ±2.3	756.0	11^+_1	$\rightarrow 9^+_1$	10.2 ±2.0
578.8	6^+_2	$\rightarrow 4^+_2$	49.8[d]	756.0	9^+	$\rightarrow 7^+$	8.6 ±1.6	693.3	9^+_1	$\rightarrow 7^+_1$	26.5 ±3.0
475.4	4^+_2	$\rightarrow 2^+_2$	74.7[e] ±10	712.7	8^+_2	$\rightarrow 6^+_2$	25.0 ±3.8	693.0	8^+_2	$\rightarrow 6^+_2$	11.8[d]
707.8	2^+_2	$\rightarrow 0^+_1$	66.4[de]	645.5	7^+	$\rightarrow 5^+_1$	20.8 ±1.3	605.4	7^+_1	$\rightarrow 5^+_1$	44.5 ±3.6
521.3	6^+_2	$\rightarrow 6^+_1$	8.5[de]	599.8	6^+_2	$\rightarrow 4^+_2$	62.5[d]	589.3	6^+_2	$\rightarrow 4^+_2$	41.1[d]
518.0	4^+_2	$\rightarrow 4^+_1$	72.3[e] ±6.4	471.5	4^+_2	$\rightarrow 2^+_2$	75.0[d]	457.2	4^+_2	$\rightarrow 2^+_2$	76.4[d]
940.5	4^+_2	$\rightarrow 2^+_1$	32.2 ±4.8	612.9	2^+_2	$\rightarrow 0^+_1$	70.2[de]	523.6	2^+_2	$\rightarrow 0^+_1$	72.3[de]
465.6	2^+_2	$\rightarrow 2^+_1$	83[d]	445.2	6^+_2	$\rightarrow 6^+_1$	6.9[de]	380.2	6^+_2	$\rightarrow 6^+_1$	6.2[de]
				1020.9	6^+_2	$\rightarrow 4^+_1$	14.4[de]	335.9	4^+_2	$\rightarrow 4^+_1$	15.3[de]
				421.2	4^+_2	$\rightarrow 4^+_1$	38.0[de]	744.1	4^+_2	$\rightarrow 2^+_1$	5.3[de]
				843.6	4^+_2	$\rightarrow 2^+_1$	46.5[de]	286.9	2^+_2	$\rightarrow 2^+_1$	88.2[d]
				372.2	2^+_2	$\rightarrow 2^+_1$	87.5[d]				

[a] Reference 70 [b] Reference 71 [c] Reference 72 [d] Reference 73 [e] Reference 26

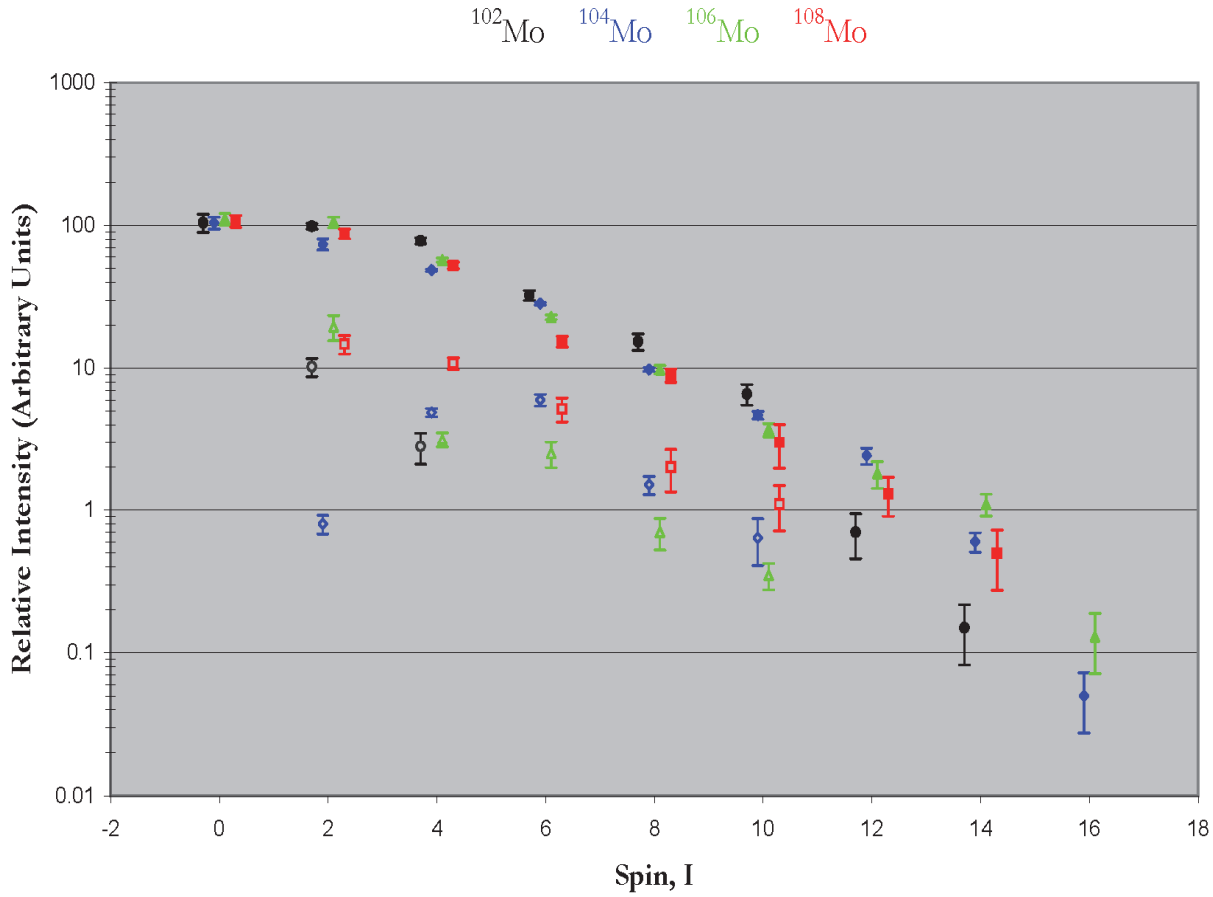

Figure 5-42: Level feeding intensities as a function of spin for $^{102, 104, 106, 108}$Mo (black, blue, green, and red). Closed and open symbols represent the ground-state and γ bands respectively.

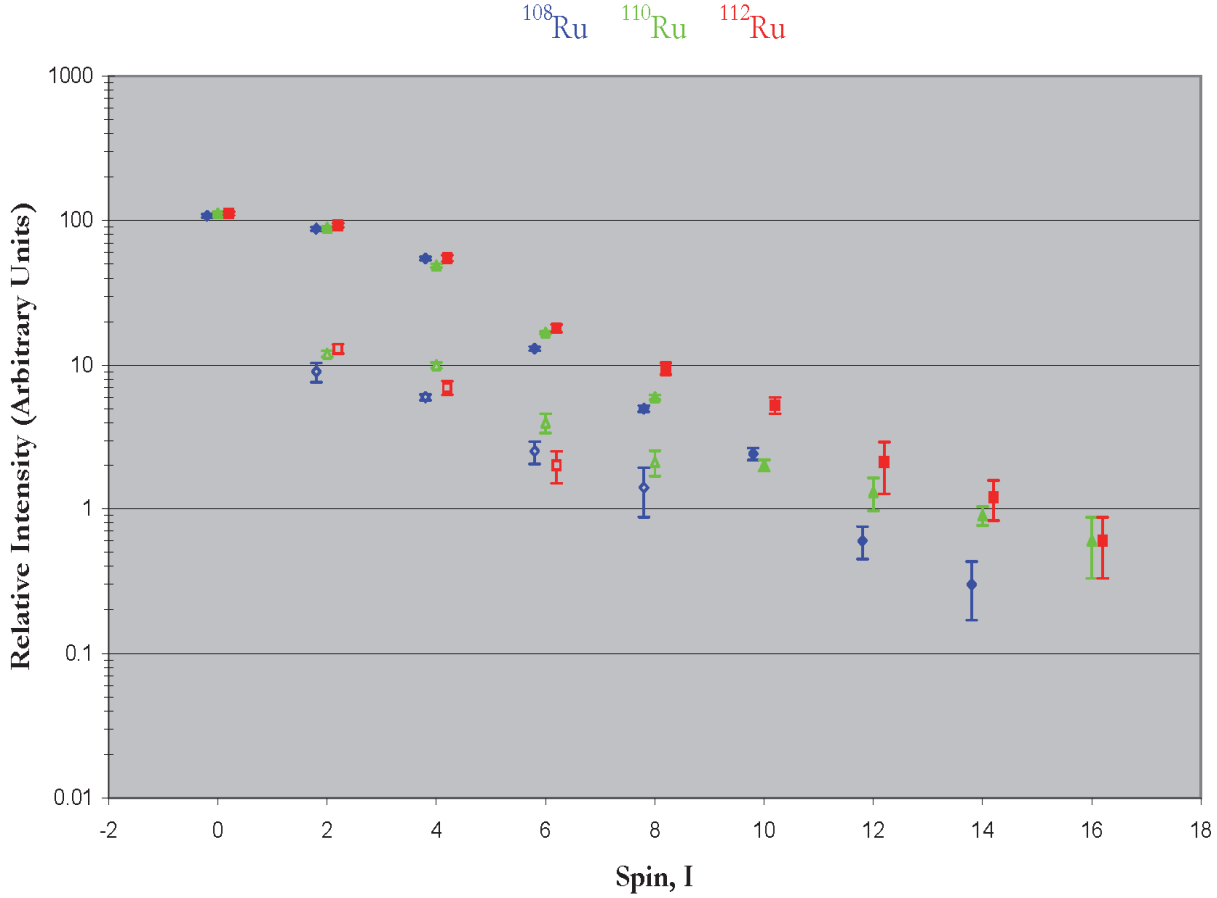

Figure 5-43: Same as Figure 5-42, but for $^{108, 110, 112}$Ru (blue, green, and red).

5.5 B(E2) Analysis for the γ Band

The side band is built on a 2^+ excitation and is thought to be associated with a principal quantum number K=2. This notion is tested hereafter by using the Alaga rule [74]. Equation (5-1) gives the relation used in the Alaga analysis.

$$\frac{B(E2:I_i \to I_f)}{B(E2:I_i \to I'_f)} = \frac{\left\langle I_i K_i 2 \ \Delta K \middle| I_f K_f \right\rangle^2}{\left\langle I_i K_i 2 \ \Delta K \middle| I'_f K_f \right\rangle^2} \tag{5-1}$$

As stated in Casten's book, the analyzed transitions can be either both intraband or both interband transitions with the same initial and final bands. Then the intrinsic matrix element will be identical for both transitions and will cancel in their ratio [27] [75]. The crucial parameter in Equation (5-1) is ΔK, that is, in case of a set of interband transitions, the change in K by these transitions. The different final states are denoted I_f and I'_f.

The B(E2) ratios depend only on the set of Clebsch-Gordan coefficients. The task is now to identify such combinations of B(E2) values that discriminate between the cases ΔK=0 and ΔK=2 (the ground-state band is always assigned K=0). In the present analysis the following ratios were available for discerning between these two cases:

$$\frac{B(E2:4_2^+ \rightarrow 2_1^+)}{B(E2:4_2^+ \rightarrow 4_1^+)} = 1.1 \text{ (ΔK=0), } 0.34 \text{ (ΔK=2) ("black label" Figures 5-44 and 5-45),}$$

$$\frac{B(E2:6_2^+ \rightarrow 4_1^+)}{B(E2:6_2^+ \rightarrow 6_1^+)} = 1.23 \text{ (ΔK=0), } 0.27 \text{ (ΔK=2) ("red label" Figures 5-44 and 5-45).}$$

By comparing the cases to the measured B(E2) ratio, either the ΔK=0 or ΔK=2 solution should be ruled out.

In this analysis the initial state is the same for both B(E2) values, i.e. both values originate from the same lifetime. This leads to a cancelation of the τ value in the B(E2) ratio [see Equation (2-26)] and the final expression:

$$\frac{B(E2;\gamma_1)}{B(E2;\gamma_2)} = \frac{BR_1 \cdot E_{\gamma 2}^5}{BR_2 \cdot E_{\gamma 1}^5} \tag{5-2}$$

Table 5-4 shows the relevant quantities to evaluate Equation (5-2), in particular the branching ratios and transition energies for the transitions with a 4_2^+ or a 6_2^+ initial state. It should be pointed out that the sets of transitions being analyzed contain a stretched and an unstretched E2

transition. The latter is assumed to be pure, an assumption that is made in the literature [76] and that is further discussed below.

Figure 5-44 and Figure 5-45 show the B(E2) ratios constructed for the transitions out of the 6_2^+ or 4_2^+ levels and into states in the ground-state band. The ratio data-points and the ΔK solutions to be considered are drawn in black (4_2^+ initial state) or red (6_2^+ initial state) as indicated in the legend. The measured ratios are much closer to the ΔK=2 lines, than to the ΔK=0 lines, so the latter solution is proposed to be ruled out.

Table 5-4: Similar to Table 5-2 but for transitions relevant to the Alaga analysis.

Nucleus	E_{lev}	I_i^π	τ (ps)		E_γ	I_f	B.R.	ΔBR	Ref.
^{102}Mo	1398.4	4_2^+			550.3	2_2	39.5%	2.9%	NNDC
					654.6	4_1	42.0%	3.6%	NNDC
					1102.4	2_1	18.5%	4.7%	NNDC
^{104}Mo	1214.8	4_2^+			402.3	2_2	14.1%	1.9%	NNDC
					654.1	4_1	41.9%	4.5%	NNDC
					1022.7	2_1	44.1%	4.9%	NNDC
	1724.4	6_2^+			509.8	4_2	44.8%	3.9%	NNDC
					644.2	6_1	34.1%	3.6%	NNDC
					1163.6	4_1	21.1%	2.1%	NNDC
^{106}Mo	1067.8	4_2^+	2.33	0.27	182.6	3	8.6%	1.7%	Thesis
				0.29	357.4	2_2	54.0%	8.5%	Thesis
					545.5	4_1[a]	11.3%	6.0%	Thesis
					896.2	2_1	26.1%	4.5%	Thesis
	1563.3	6_2^+			256.4	5	-	-	Thesis
					495.6	4_2	48.1%	9.4%	Thesis
					529.9	6_1	21.2%	6.3%	Thesis
					1041.2	4_1	30.8%	7.8%	Thesis
^{108}Mo	978.3	4_2^+			195.2	3	4.9%	2.1%	NNDC
					392.4	2_2	31.9%	4.2%	NNDC
					414.6	4_1	35.1%	4.2%	NNDC
					785.5	2_1	28.1%	3.5%	NNDC
^{108}Ru	1183.0	4_2^+	1.87	0.30	475.4	2_2	53.8%	13.2%	NNDC
				0.30	518.0	4_1[b]	33.9%	8.8%	NNDC
					940.5	2_1	12.4%	5.4%	NNDC
	1761.9	6_2^+			578.8	4_2	76.3%	8.5%	NNDC
					521.3	6_1	13.0%	1.5%	NNDC
					1097.1	4_1	10.7%	1.2%	NNDC
^{110}Ru	1084.4	4_2^+			224.5	3	1.3%	0.7%	NNDC
					471.5	2_2	46.4%	6.5%	NNDC
					421.0	4_1	23.5%	6.6%	NNDC
					843.6	2_1	28.8%	4.0%	NNDC
	1684.3	6_2^+	4.12	0.94	308.7	5	5.4%	0.4%	NNDC
				0.99	599.8	4_2	70.5%	7.9%	NNDC
					445.2	6_1[c]	7.8%	0.6%	NNDC
					1021.0	4_1	16.2%	2.9%	NNDC
^{112}Ru	980.8	4_2^+			457.2	2_2	78.8%	15.5%	NNDC
					335.8	4_1	15.8%	3.2%	NNDC
					744.2	2_1	5.4%	1.1%	NNDC

[a] B(E2) = 820 e^2fm^2 assuming transition is pure.
[b] B(E2) = 3900 e^2fm^2 assuming transition is pure.
[c] B(E2) = 880 e^2fm^2 assuming transition is pure.

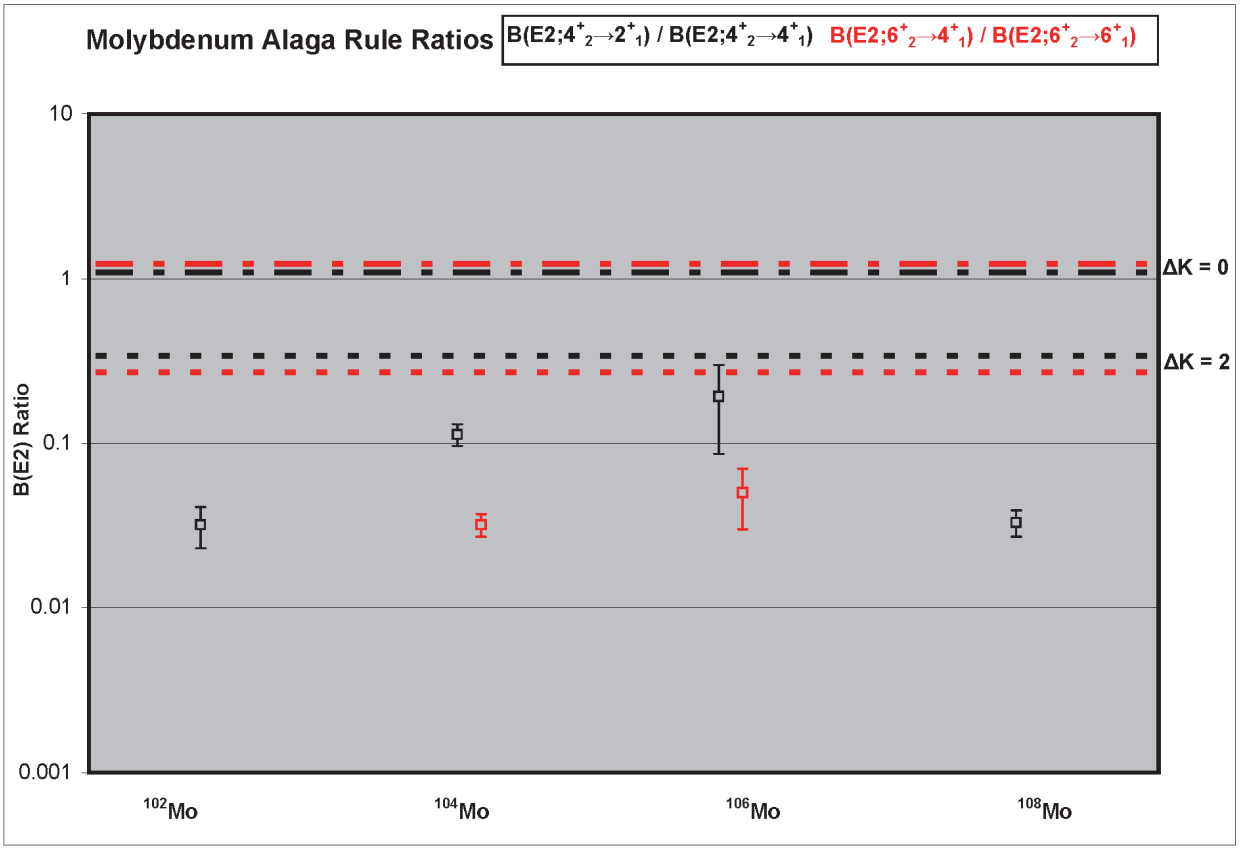

Figure 5-44: B(E2) ratios according to Equation (5-2) for even-mass $^{102\text{-}108}$Mo. Each ratio should be matched with the data points and the ΔK= 0 or 2 solutions according to the color code. The values for ^{106}Mo are from the thesis, the other values are based on the information in Reference 26 (see Table 5-4).

Figure 5-45: Same as Figure 5-44, but for the even-mass $^{108\text{-}112}$Ru.

The assumption that the unstretched E2 transitions are pure (E2/M1 mixing ratio $|\delta| >> 1$) is a good approximation, at least for the Ru nuclei. In Reference [77] the reported values of δ for such transitions measured in ^{106,108}Ru are typically $\delta \sim 4$ to 7. An M1 admixture would, in principle, lower the denominator in Equation (5-2) and increase the ratio. Focusing in on the largest value in Figure 5-44, the 0.30 upper-limit value for ^{106}Mo, the line for $\Delta K=0$ is a factor of 3.6 larger than that value. To merge this line with a corrected ratio, a value $\delta=0.53$ is required according to the relation:

$$\frac{T(E2)}{T(M1)} = \delta^2 \qquad (5\text{-}3)$$

Such a small value for δ is deemed unreasonable since the typical δ values are a factor of ten larger than this assumed value. In conclusion the ΔK=0 solution can be ruled out.

It is also pointed out in Reference [75], that the experimental ratios are empirically smaller than the Alaga-rule predictions (for $I_i > I_f$) and that this discrepancy increases with spin. This may reflect the onset of K mixing, an effect that is not included in the Alaga rule (constant K is assumed).

Finally, the lifetime information was also used for a B(E2) analysis of the transitions near the bandhead of the γ band. In Section 2.3.4 the Weisskopf estimate was introduced. Expressing the B(E2) in terms of Weisskopf units (B_{WU}[E2]) provides a qualitative measure of the collective behavior of a band. If the B_{WU}(E2) is near unity, the band is single particle in nature; if it deviates, it indicates a likelihood for collective excitations. Figure 5-46 shows the B_{WU}(E2) values for the $2_1^+ \rightarrow 0_1^+$ and the $2_2^+ \rightarrow 0_1^+$ transitions.

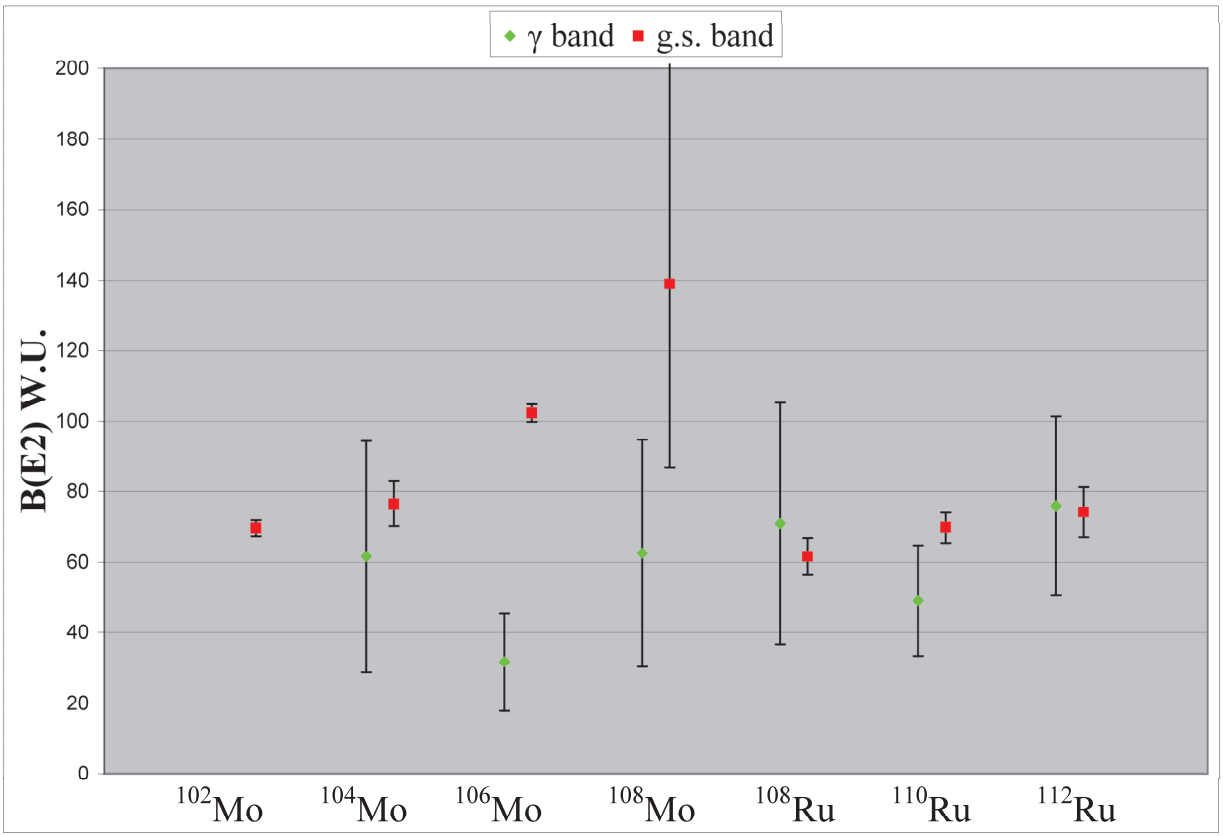

Figure 5-46: B(E2) values for the $2^+ \rightarrow 0^+$ transitions of the ground-state band (red squares) and γ band (green diamonds) expressed in Weisskopf units.

In the present analysis the B(E2) values for the ground-state transition were calculated from lifetime values in the literature [26]. The B(E2) values for the $2_2^+ \rightarrow 0_1^+$ transition were estimated by assuming that its Q_t is the same as the lowest measured γ-band transition (e.g. the Q_t from the $8_2^+ \rightarrow 6_2^+$ transition was used for ^{104}Mo). That Q_t was then converted into a B(E2) by using the relation:

$$B(E2;\ 2_2^+ \rightarrow 0_1^+) = \frac{5}{16\pi}\langle 2\ 2\ 2\ -2 \mid 0\ 0\rangle^2 Q_t^2. \qquad (5\text{-}4)$$

All of the $B_{WU}(E2)$ values presented in this work are >30 W.u. This indicates the collective behavior of the nuclei studied in this work. For the ground-state band, the $B_{WU}(E2)$ values increase

with increasing N for both the Mo and Ru isotopes. A comparison the ground-state bands of nuclei with equal N, e.g. ^{106}Mo and ^{108}Ru with N=64, reveals that $B_{WU}(E2)$ values are more enhanced for the Mo nuclei. The $B_{WU}(E2)$ values for the γ band are enhanced, but the error bars obscure observation of the N and Z dependence.

As spin increases, the observed Q_t value can decrease by as much as 50 percent. This leads to a 70 percent reduction in the $B_{WU}(E2)$ values. Even with this reduction at higher spin, the Weisskopf estimate still indicates that collective behavior is likely.

Based upon the $B_{WU}(E2)$ values, it comes as no surprise that rotational bands built upon the shape deformation of the nucleus and additional vibrational excitations dominate the level structure for the nuclei studied in this work. The strength of the collective behavior in this region motivates searching for features that can be associated with triaxial deformation.

Chapter 6: Discussion

6.1 Introduction to Deformed Mean-Field Models

This section continues the discussion of nuclear models from Chapter 1: the liquid-drop and the traditional shell model. Both models predict all nuclei to be spherical. From here, it remains to allow for the deformation of the nuclear surface through the lens of the Nilsson model and the advancements made by the Strutinsky, and certain Hartree-Fock methods. However, additional factors are to be included in the present theoretical consideration: pairing correlations between like particles (proton-proton, neutron-neutron) and the effect nuclear rotation has on the orbital motion of the nucleons as described by the so-called cranking model. Ultimately, cranked relativistic mean-field theory with pairing is used to describe the data in this work [78]. All these concepts are usually summarized as nuclear mean-field theory. Here mean field means that the interaction of one nucleon with the remaining ones is described by an average potential that is created by the other particles. For a more complete treatment of these concepts see Reference [29].

6.1.1 Review of Conventional Approaches

Nilsson-Strutinsky Method: The so-called Nilsson-Strutinsky approach is perhaps the most transparent one among the approaches discussed here. Nilsson introduced a phenomenological average potential that is ellipsoidal and can be described as an anisotropic harmonic oscillator [29]:

$$V_{AHO} = \frac{m}{2}(\omega_x^2 x^2 + \omega_y^2 y^2 + \omega_z^2 z^2). \quad (6\text{-}1)$$

The frequencies (ω_x, ω_y, ω_z) are chosen to be proportional to the half axes (a_x, a_y, a_z) of the ellipsoid as shown in Equation (6-2).

$$\omega_\upsilon = \omega_0 \frac{R_0}{a_\upsilon}, \quad (\upsilon = x, y, z). \tag{6-2}$$

R_0 is the radius of a sphere of the same volume as the ellipsoid. Volume conservation is maintained by the condition,

$$\omega_x \omega_y \omega_z = const. = \omega_0^3. \tag{6-3}$$

Nilsson was then required to combine the anisotropic harmonic oscillator potential with a spin-orbit term $(l \bullet s)$ and a term $(l^2 - \langle l^2 \rangle_N)$ that shifts levels with higher *l*-values downward, such that the "magic" numbers are correctly reproduced. The Nilsson model potential is shown in Equation (6-4) [29]:

$$V_{NM} = V_{AHO} - \hbar\omega_0 \kappa \cdot [2(l \bullet s) + \mu(l^2 - \langle l^2 \rangle_N)], \tag{6-4}$$

where κ and μ are adjustable coupling parameters, N is the principal quantum number of the major shell and $\langle l^2 \rangle_N$ is the expectation value of l^2 averaged over N, i.e. $1/2 \cdot N(N+3)$. Assuming axially symmetry, N can be expressed in cylindrical coordinates as:

$$N = n_z + 2n_p + m_l, \tag{6-5}$$

where n_z is the number of nodes in the wave function along the symmetry axis, n_p is the number of nodes perpendicular to the symmetry axis, and m_l is the projection of the orbital angular momentum onto the symmetry axis. Notably, V_{AHO} can be replaced by a deformed Woods-Saxon potential without affecting the statements made below.

In the deformed potential the total orbital and total angular momentum ($J=L\pm S$) are not good quantum numbers, contrary to the spherical shell model. Instead the eigenstates are characterized by the so-called asymptotic quantum numbers, which apply to angular-momentum projections along the symmetry axis (z-axis). The complete set of quantum numbers is $[N\ n_z\ m_l\ \Omega^\pi]$, where n_z and m_l are defined above, Ω is the projection of J onto the symmetry axis, and π is the

parity. For axially symmetric nuclei, Ω is equal to the K quantum number introduced in Section 2.3.2. The numbers n_z, m_l, and Ω take the following values:

$$n_z = 0,1,2,...,N,$$

$$m_l = N - n_z, N - n_z - 2,...,0 \text{ or } 1,$$

$$\Omega = m_l \pm 1/2.$$

The parity of a state is given by

$$\pi = (-1)^N.$$

It is illustrative to construct the available states for a major shell using Equation (6-5) and the relation between Ω and m_l. Table 6-1 shows the six Nilsson states in the N=5 major shell. If there is no deformation, they recombine into the shell model $3p_{1/2}$, $3p_{3/2}$, $2f_{5/2}$, $2f_{7/2}$, $h_{9/2}$, and $h_{11/2}$ orbitals.

Table 6-1: Construction of the Nilsson quantum numbers for N=5.

n_z	n_p	m_l	Ω
0	0	5	11/2 9/2
	1	3	7/2 5/2
	2	1	3/2 1/2
1	0	4	9/2 7/2
	1	2	5/2 3/2
	2	0	1/2
2	0	3	7/2 5/2
	1	1	3/2 1/2
3	0	2	5/2 3/2
	1	0	1/2
4	0	1	3/2 1/2
5	0	0	1/2

Figure 6-1 shows a Nilsson diagram for neutrons and protons in the top and bottom panels respectively [79]. The following observations can be made. For prolate shape (β_2>0), the high-j, low-Ω orbitals drop in energy as β_2 increases. For oblate shapes (β_2 <0), the high-j, high-Ω orbitals have

large slopes. When this type of orbital is occupied, a large deformation (either prolate or oblate) is energetically favored. With respect to Figure 6-1, the following should be noticed. There is no Coulomb term in Equation (6-4), an appropriate choice of the coupling parameters accounts for its effect. In practice, different coupling parameters are used for each major shell to obtain the best fit. Each Nilsson orbital is labeled with the quantum numbers [N n_z m_l Ω^{π}] (described above), and full (dashed) lines designate positive (negative) parity states. The parameters used in these diagrams are tuned for the ^{100}Zr nucleus (Z=40, N=60). However, Nilsson diagrams for the neighboring neutron-rich Mo and Ru nuclei would be very similar. For the Mo and Ru nuclei studied in this work, the proton orbitals near the Fermi surface have $g_{9/2}$ parentage and the active neutron orbitals are $d_{5/2}$ - $g_{7/2}$ and $h_{11/2}$ in character. Notably Nilsson orbitals such as [422 $3/2^+$] and [411 $3/2^+$], representing $d_{5/2}$ and $g_{7/2}$ subshells, repel each other near β_2=0.2. These orbitals are said to be mixed.

Perhaps the most important message from Figure 6-1 is that certain orbitals are shape stabilizing. For example, the low-Ω orbitals of $h_{11/2}$ in the prolate sector tend to favor deformation due to their downsloping behavior. In other words, their occupation is energetically favorable for β_2>0.

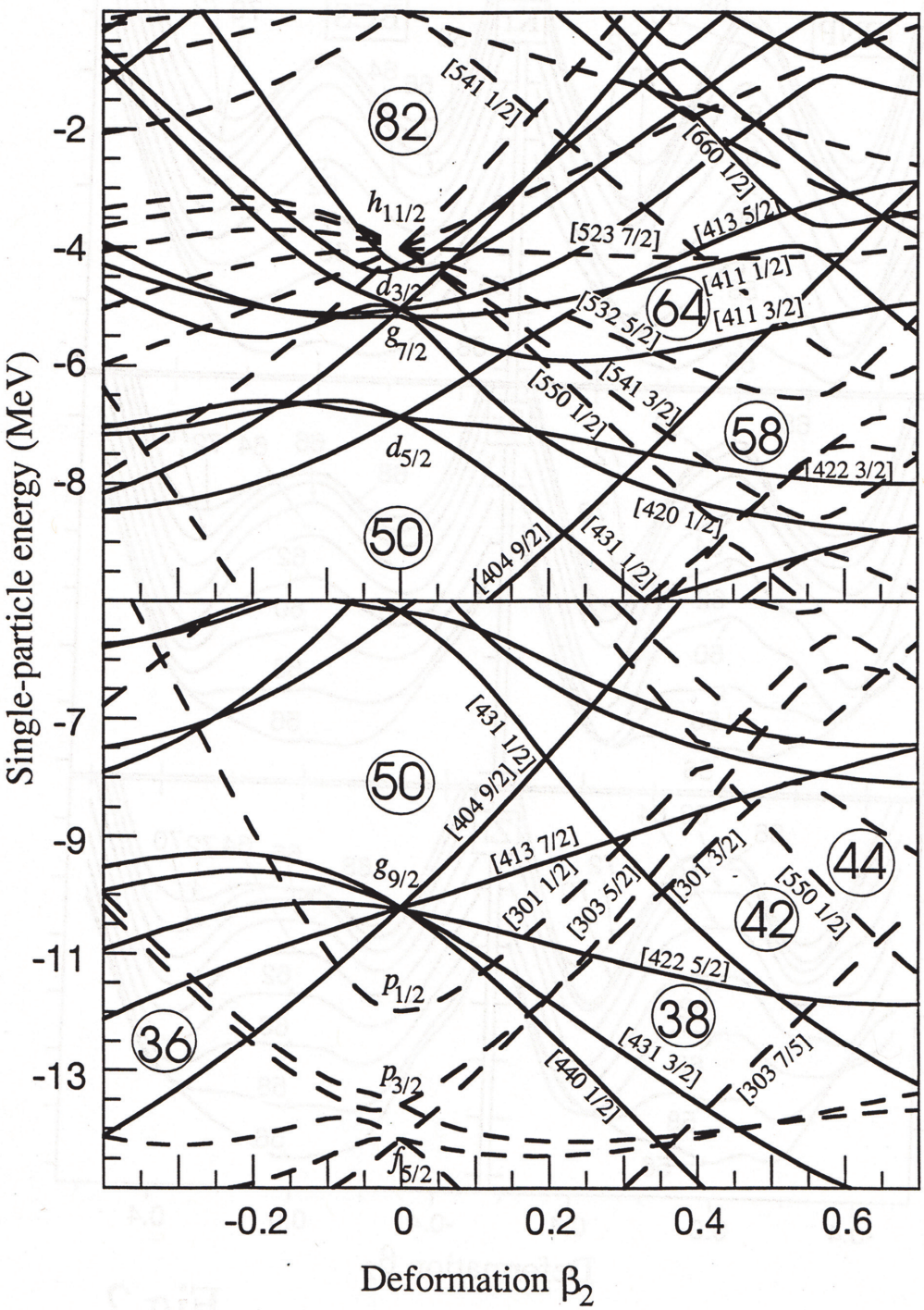

Figure 6-1: Nilsson diagram for the single-particle neutron (top) and proton (bottom) levels as a function of quadrupole deformation. Full (dashed) lines correspond to positive (negative) parity states. The spherical and deformed shell gaps, and subshell closures, are indicated. The diagram is based upon a deformed Woods-Saxon potential. This figure is from Reference [79].

The Nilsson model is successful in calculating nuclear deformation, but cannot be used to predict binding energies; another shortcoming of this model is its failure in explaining large-deformation effects in the fission process. The liquid-drop model, on the other hand, reproduces "bulk" properties of the nucleus, such as its binding energy. However, it cannot account for variations in the binding energy near the "magic" numbers. These shell effects are associated with nucleons at or near the Fermi surface and are described by the shell model. The Strutinsky method reconciles the two models by combining the best parts of both [80] [81]. For completeness, similar techniques were developed by Myers and Swiatecki [82].

The Strutinsky method constructs the "shell corrected" total energy (E_{TOT}) for the nucleus by taking the average value from the liquid drop model (E_{LDM}) and correcting for oscillations around that value (δE_{SHELL}) using the shell model.

$$E_{TOT} = E_{LDM} + \delta E_{SHELL} \tag{6-6}$$

E_{LDM} is the liquid-drop binding energy [5]. δE_{SHELL} is treated separately for proton and neutrons and is defined as the difference between the sum of the single-particle energies, e_ν, and an averaged value of this sum, $\widetilde{E}$.

$$\delta E_{SHELL} = \sum e_\nu - \widetilde{E} \tag{6-7}$$

$\widetilde{E}$ is calculated by replacing the distribution of e_ν, as a function of particle number, with a smooth distribution. For details on this level smearing see Reference [29] (where δE_{SHELL} is expressed as E_{OSC}). In principle, the effect of nuclear deformation enters Equation (6-6) through the shell-correction term. For example, $\delta E_{SHELL}<0$ when the level density is comparatively low. This occurs at the spherical and deformed shell gaps of Figure 6-1.

If the deformed shell model is used, it is called the Nilsson-Strutinsky method. The objective is then describing the total energy of the ground state as a function of deformation. There are other methods similar to the Strutinsky method; they are also called macroscopic-microscopic methods.

Hartree-Fock Method: The sum of the two-body nuclear interactions are used to derive an appropriate single-particle Hartree-Fock potential

$$V_{HF} = \sum_{i<j=1}^{A} V(i,j) \cong \sum_{i=1}^{A} V(i) \tag{6-8}$$

V_{HF} contains a local Hartree potential that accounts for the mean field. Further improvement comes from including a non-local exchange (Fock) potential in V_{HF}. A local potential has position dependence, whereas a nonlocal potential further depends on the characteristics of the region surrounding that position, e.g. the momentum distribution, which implies a velocity dependence. The descriptions for the strength of the interactions are phenomenological and there are many of them, two popular forms are Skyrme [83] and Gogny [84]. Skyrme makes use of delta functions to describe the interactions independent of the range associated with them (so-called zero-range). Gogny improves upon this by using a Gaussian form (so-called finite range).

The Hartree-Fock method makes use of the variational principle, by which it can be shown that the eigenvalue of the Hamiltonian, for any trial eigenfunction (Ψ_{TRIAL}), represents an upper bound to the ground state energy (E_{GS}) [29].

$$\left\langle \Psi_{TRIAL} \middle| H \middle| \Psi_{TRIAL} \right\rangle \geq E_{GS} \tag{6-9}$$

The bound becomes an equality if the correct eigenfunction is used. The variational principle can be extended to calculate the excited states as well.

Solving the Schrödinger equation with the Hartree-Fock potential is a non-linear problem typically solved by iterative methods. Such methods are self-consistent, i.e. an initial eigenfunction is chosen and then modified each iteration to minimize the eigenvalue and converge to the ground state energy. In practice a Slater determinant, a set of arbitrary but orthogonal single-particle wave functions for each nucleon, represents the initial eigenfunction [29]. See reference [85] for further details on iterative methods.

Pairing Correlations: These correlations between like nucleons are responsible for the 0^+ ground state of even-even nuclei, the weaker binding of an odd-even nucleus when compared to its even-even neighbors, and experimental moments of inertia deviating by about a factor of two compared to a pure rigid-body value [29]. There is also pairing between "unlike" nucleons, the so-called proton-neutron pairing, but it is not relevant for physics determined by valence nucleons.

The pairing correlations are residual interactions beyond the deformed mean field. They are short-range attractive forces, similar to the correlations between electrons in a super conductor, i.e., they lead to Cooper pairs of protons or neutrons. Such pairs couple to I=0. They can be visualized as a configuration where the two nucleons move in time reversed orbits. This guarantees two interactions per orbit period, and, thus a considerable spatial overlap of the two nucleons. Pairing increases the binding energy of the nucleus.

The theory of Barden, Cooper, and Schrieffer (BCS) [86] provides the basic understanding of superconductivity. Bohr, Mottelson, and Pines [87] and Belyaev [88] adapted the methods of BCS theory to describe pairing correlations in the nucleus. This also required the inclusion of the quasiparticle formalism (see below) of Bogolyubov.

To describe the BCS treatment, it is necessary to introduce the particle-hole representation of a quantal state. In principle, a particle or hole state can be created above or below the Fermi

surface, which is defined by filling a certain number of the lowest states. Adding (destroying) a particle in the particle picture is equivalent to removing (creating) a hole in the hole picture. To combine both operations, it is required that the particle and hole states be created simultaneously. For example, anytime when a particle is created in a state, a hole must be annihilated in the corresponding state. This can be simplified by introducing the concept of a quasiparticle, which is a hybrid of both particle and hole. The quasiparticle energy, E_ν, is given by

$$E_\nu = \sqrt{(\varepsilon_\nu - \lambda)^2 + \Delta^2}, \tag{6-10}$$

where ε_ν is the single-particle energy of the state ν, λ the Fermi level corresponding to the appropriate particle number, and Δ the so-called pairing gap.

In the present picture, pairing corresponds to scattering two correlated nucleons from one set of time-reversed orbitals to another set. Due to this fluctuation, the Fermi surface is diffuse, while it would be sharp for a state without pairing. However, only half of the energy space needs to be considered, as already stated above.

Cranking Model: The cranking model was suggested by Inglis, in the 1950s, but has mostly been used in the 1970s and thereafter. It links the independent-particle pictures discussed above and the rotational description of the nucleus.

As discussed in Section 2.3.2, treatment of nuclear rotation can be simplified by using an intrinsic frame that rotates with a frequency ω with respect to the lab frame. The initial assumption for the cranking model is the rotation of a nucleus about an axis (x) perpendicular to the symmetry axis. Then the motion of a particle is characterized by j_x, the projection of the total angular momentum onto the x-axis.

$$j_x = l_x + s_x, \tag{6-11}$$

where l_x is the orbital angular momentum projection onto the x-axis and s_x the intrinsic spin projection onto the x-axis of the particle. The cranking Hamiltonian is defined as

$$h_\omega = h - \hbar\omega j_x, \tag{6-12}$$

where h is the Hamiltonian of the intrinsic system. The total cranking Hamiltonian is obtained by summing the angular momentum contributions of individual nucleons as they are dragged around by a uniformly rotating potential:

$$H_\omega = H - \hbar\omega J_x. \tag{6-13}$$

Coriolis and centrifugal forces that act in the non-inertial system of the rotating frame can be derived from the term ωJ_x.

There are certain symmetries of the cranking Hamiltonian that help to group single-particle states differently and label them by certain quantum numbers. Time-reversal: invariance with respect to a reversal in time, is a symmetry that implies that the single-particle energy levels of an even-particle system are doubly degenerate. However, rotation ($\omega>0$) tends to mix particle states of different j. If states that are time-reversal counterparts are not occupied pairwise, then time-reversal symmetry is broken. Parity: invariance with respect to inversion through the origin, is a symmetry that remains in H_ω (provided that the shape of the potential can be expanded in terms of even multipoles). Signature: invariance of a state under a 180° rotation around the cranking axis, is also a conserved symmetry.

The signature is introduced as the eigenvalue of an $R_x(180°)$ operation:

$$r = e^{-i\pi\alpha}.$$

Rotational bands in even-even nuclei are said to have signatures of

$$r = 1 \quad (\alpha = 0) \quad I = 0,2,4,...$$

$$r = -1 \quad (\alpha = 1) \quad I = 1,3,5,...$$

The single-particle orbits are affected by nuclear rotation, in particular the high-j, low Ω orbitals (effect due to the Coriolis force). This effect tends to "stress" pair-correlated nucleons: the force has opposite signs based on whether the nucleon is moving in the direction of, or oppositely to the bulk rotation of the nucleus. This may finally lead to a decoupling of the pair as discussed in Section 2.3.2 (upbend of the moment of inertia).

6.1.2 Relativistic Mean Field Approach

The following discussion focuses on some of the basics for a relativistic mean field (RMF) description of excited states in nuclei. It is based on References 78 and 89, it also takes advantage of the literature references given therein.

The RMF theory replaces the Schrödinger equation with the Dirac equation. The nucleus is considered as a system of protons and neutrons that interact by the exchange of mesons and photons. The σ-meson is responsible for large scale attraction at intermediate distance, the ω-meson for short-range repulsion, and the ϱ-meson for variations caused by proton or neutron excess. Perhaps most appealing is that the spin-orbit splitting, which plays an important role in nuclear-structure physics, naturally emerges as a relativistic effect.

The RMF approach also makes use of the ideas of density functional theory developed by Kohn and Sham. Instead of starting with a two-body Hamiltonian, a density dependent Lagrangian is used. The variational principle is then applied to derive the equations of motion for the nuclear system, which are then solved in a self-consistent manner. The density-dependent Lagrangian includes parameters for the meson masses, their coupling constants and two additional nonlinear

terms. To describe rotational and deformation properties of nuclei, including pairing correlations, within the relativistic framework, Afanasjev, Ring, and others have developed the cranked relativistic Hartree-Bogoliubov (CRHB) theory. The concepts and steps involved are:

RMF Lagrangians. There are different parametrizations of the RMF Lagrangian. In the context of the present work, the so-called NL3 and NL3* parameter sets have been used. The latter represent more recent considerations (fits) to optimize the parameters mentioned above (meson masses etc.). There is also a so-called NL1 parameter set available; however, it is less suitable for nuclei far from stability.

Cranked relativistic mean field. The RMF Lagrangian, in the unpaired formalism, is transferred to the rotating frame within the framework of the cranking model. This leads to the cranked relativistic mean-field equations. The authors restrict themselves to one-dimensional cranking around the x axis.

CRHB theory. There are pairing correlations at work between the fermions. Incorporation of pairing into RMF calculations requires the application of the Bogoliubov transformation. Notice that in the present Hartree-Bogoliubov approach, a Fock exchange term is absent. However, pairing itself is a nonrelativistic phenomenon. It is included in a phenomenological manner, using a Gogny type interaction between like nucleons (so-called particle-particle, pp, channel). A so-called D1S parameter set is employed for the Gogny force. The details of how to treat pairing depend upon the choice of using either the BCS treatment for pairing or the Lipkin-Nogami method.

Lipkin-Nogami (LN) pairing treatment. The Bogoliubov transformation does not commute with the particle number operator and, thus, particle number is not conserved. The principle solution would be to perform an exact particle-number projection before variation of the density functional, but this solution is computationally "slow". This situation can be rescued by the LN method, which approximates the principle solution while remaining computationally "fast".

Charge Quadrupole moment. The charge quadrupole moment, Q, is a one of the physical observables calculated:

$$Q = e\sqrt{\frac{16\pi}{5}}\sqrt{\left\langle r^2 Y_{20}\right\rangle_p^2 + 2\left\langle r^2 Y_{22}\right\rangle_p^2}, \tag{6-14}$$

Y_{22} and Y_{20} are the diagonal and off-diagonal elements of the quadrupole tensor, respectively, e is the electric charge and the subscript p is a label for protons.

The transition quadrupole moment Q_t for a triaxially deformed nucleus is calculated by the expression:

$$Q_t = e\sqrt{\frac{16\pi}{5}}\left\langle r^2 Y_{20}\right\rangle_p \frac{\cos(\gamma + 30^\circ)}{\cos(30^\circ)}, \tag{6-15}$$

where the γ deformation of the proton system is defined by

$$\tan\gamma = \sqrt{2}\,\frac{\left\langle r^2 Y_{22}\right\rangle_p}{\left\langle r^2 Y_{20}\right\rangle_p}. \tag{6-16}$$

6.2 Components of and Signatures for Triaxiality

The nuclear shape has a threefold sensitivity: (i) to the nucleus' collective behavior, (ii) to the total angular momentum the nucleus carries, and (iii) to the single-particle structure of the nucleus. The aspects (i) and (ii) are covered by the discussions in Sections 2.3.1 and 2.3.2, while aspect (iii) is

perhaps best addressed by the discussion of the Nilsson model in Section 6.1. The parameters mentioned above, are interrelated. For example, as nuclear rotation increases it perturbs the microscopic structure and this can lead to shape changes with increasing spin. Factors relating to the presence of a triaxial shape are discussed hereafter.

γ Softness. In their theoretical study, Möller et al. [90] have called the presence of a γ band in a nucleus a necessary condition for searching for stable triaxial deformation. The characteristics of a γ band have been discussed in Section 2.3.2 and examples of γ bands can be found, for example, in the level schemes of ^{104}Mo or ^{108}Ru. Here the 2_2^+ bandhead states of the γ band have a low excitation energy: 466 keV relative to the 2_1^+ state (^{108}Ru). For comparison, γ bands in the rare-earth region are located at about 1 MeV relative to the ground-state band.

Figure 6-2 is adapted from the study mentioned above. It displays the chart of the nuclides, overlaid with the predicted ground-state energy correction when axial symmetry is broken. The theoretical calculations use a macroscopic-microscopic model and predict a triaxial ground state for ^{108}Ru and the surrounding region [90]. The macroscopic-microscopic approach taken by Skalski, Mizutori, and Nazarewicz, predicts that $^{104\text{-}108}$Mo have a shallow potential energy surface (PES) that tends to favor a triaxial shape and that $^{108\text{-}112}$Ru also favor triaxial shapes [79]. RMF calculations performed by Li et al., predict for ^{100}Mo an oblate shape with a soft PES; neighboring isotopes gradually become triaxial as N increases [91]. Not all calculations predict stable triaxiality [92], but they all predict an instability of the PES to γ deformation.

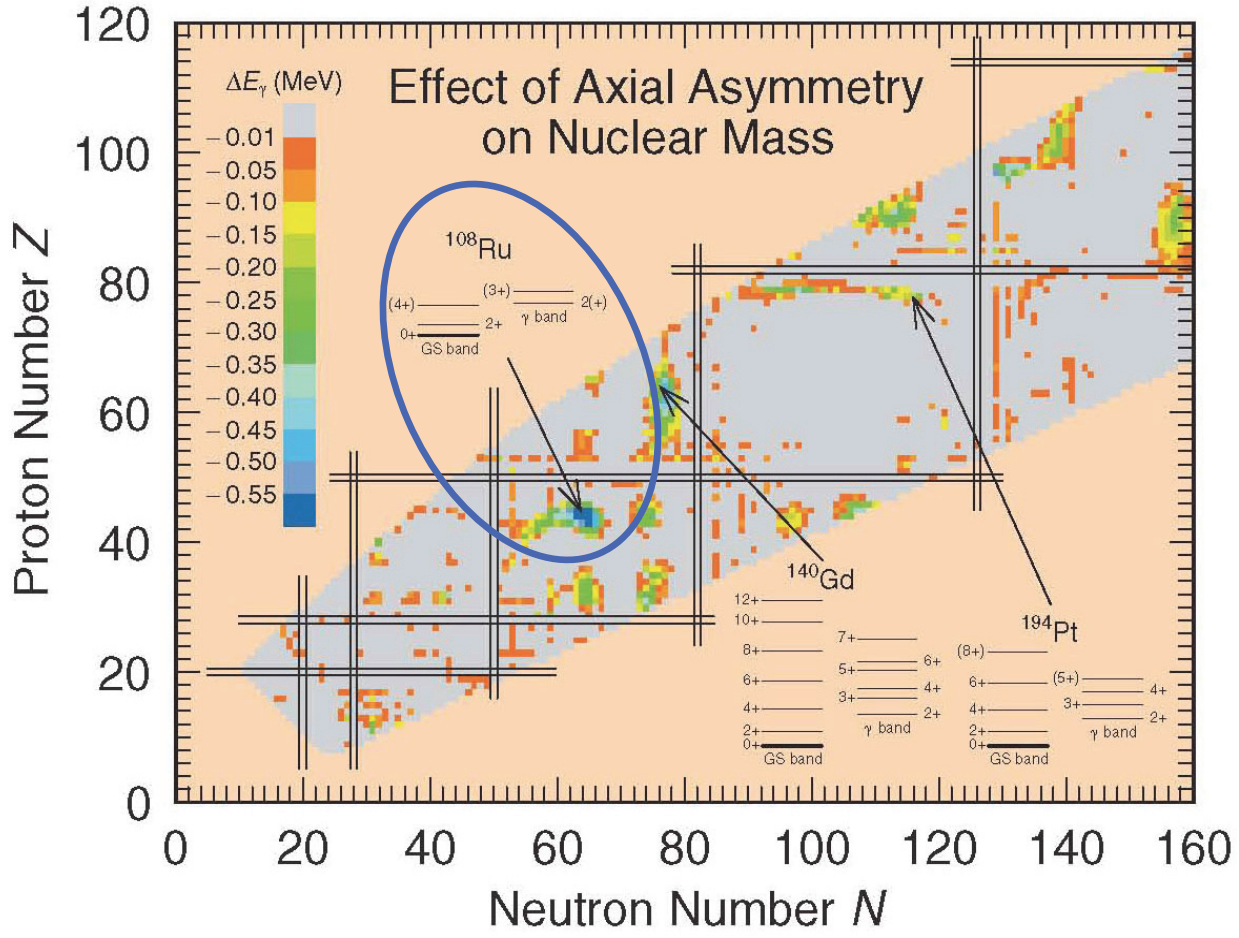

Figure 6-2: Macroscopic-microscopic model predictions showing the ground-state energy correction when axial symmetry is broken. The strongest case for triaxiality is ^{108}Ru and the surrounding neutron-rich region. This figure is from Reference [90].

Quadrupole moment vs. spin behavior (circumstantial evidence). The starting point for the present considerations is twofold. (i) Making the assumption that at low spin the nuclear shape is deformed and that collective rotation can set in. (ii) Recalling that the quadrupole moment is a function of the deformation parameter γ [see Equation (2-4)]; the downsloping trend of Q_t with spin is of interest (see Figure 5-39 and Figure 5-40). Provided that the shape elongation, expressed by β_2, does not decrease, an observed change in Q_t can be related to a change in γ. Indeed a decrease in β_2 with increasing spin is unlikely; rather a centrifugal stretching is expected do to a liquid drop behavior of

the nucleus. For example, a gradual change with spin of an initially collective prolate shape towards $\gamma=60°$, leads to a reduction in Q_t that may be observable.

Smooth band termination. This is a high-spin phenomenon that applies to rotational bands, for example, in the Sn region [93]. Starting, at low spin, with a collective prolate shape, the valence particles may successively align with the rotational axis as spin increases. Eventually all particles become aligned along this axis and then form an oblate matter distribution. In this state, the symmetry axis coincides with the rotation axis. No further angular momentum can be brought into the system for the given set of valence particles. In which case, the termination of the rotational band is reached. This process is called "smooth termination" since the energy spacing of the levels is observed to increase as spin increases; this effect is opposite to the centrifugal stretching at medium spin (decrease in level spacing as spin increases). In the process of this "smooth termination" the nuclear surface undergoes a transition, through the triaxial plane, from a collective prolate toward a single-particle oblate shape.

Wobbling bands. Nuclei with a triaxial shape can, in principle, rotate about all three principal axes. If this happens, a wider spectrum of collective rotation than usually observed occurs. Specifically, a family of three E2 bands is seen [94] [95]. All three bands are understood to be based on the same single-particle configuration. The yrast sequence represents rotation about the axis with the largest moments of inertia. The other two bands are distinguished by wobbling phonons: one phonon represents the sequence closest in excitation energy to the yrast, two phonons the sequence at the highest excitation energy. These two non-yrast sequences decay to the yrast sequence with specific electromagnetic decay properties: the sequence closest in excitation energy by $\Delta I=1$ E2 transitions and the other sequence by $\Delta I=2$ transitions. This family of bands is only seen at high spin; there the bands are typically based on a configuration other than the ground-state

configuration. The classic analog of this wobbling mode is the motion of an asymmetric top (where angular momentum is transferred between the spinning motion of the principal axes). In a quantum mechanical picture, wobbling requires phonons.

The near-yrast structure of the nuclei in the Mo-Ru region cannot be interpreted in terms of wobbling. The known transitions linking the levels of the excited and ground-state bands are predominantly of the $\Delta I=2$ and $\Delta I=0$ type, in contrast with the selective $\Delta I=1$ linking transitions associated with wobbling motion. Furthermore, the alignment properties exhibited by the excited and the ground-state bands differ significantly, while they are essentially indistinguishable in the case of wobbling. Wobbling has so far only been found in the rare-earth region.

Chiral bands. The term chirality has been applied to certain sets of degenerate bands seen in nuclear-spectroscopy high-spin work. Such bands are nearly identical $\Delta I=1$ sequences with the same parity. The term chirality is chosen by the interpretation that the bands arise from structures with different reflection symmetry or "handedness". The interpretation implies a triaxial shape and the rotation about an axis that does not coincide with a principal axis (tilted-axis cranking). Chiral bands have been reported for the light rare-earth region and the Zr-Ru region. For example, it has been suggested that the off-yrast structure of ^{110,112}Ru may contain candidates for such bands [96]. However, for γ-soft nuclei, the PES of an excited configuration and of the ground-state configuration will be different, due to the deformation driving properties of the orbitals in the former configuration and to differences in pairing. Hence, the presence of chiral bands at moderately high spin does not imply the onset of triaxiality near the ground state.

6.3 Theoretical Interpretation of the Data

The Q_t values available from experimental work and the moments of inertia are compared with the results of CRHB + LN performed by Afanasjev and Abusara; these scientists are co-authors on the paper of Reference 97. For the Q_t values, both the results from this work and the low-spin values from the literature are taken into account (see Figure 5-39 and Figure 5-40). As stated in Section 5.3, the Q_t values measured for the yrast and γ bands are similar in magnitude, but the γ-band uncertainty is large compared to the yrast band. Hence, the discussion considers only the Q_t values of the yrast band. A experimentally derived quantity that can be compared with theory is the moment of inertia (described in Section 2.3.2). A successful theory would describe both the Q_t values and the moment of inertia (e.g. $\Im^1$)in a consistent manner.

The purpose of the comparison between experiment and these theoretical calculations is to identify possible signatures of triaxiality. The best prospect, according to the discussions in Sections 5-3 and 6-2, is a possible shape change toward a triaxial shape in the ground-state bands as a function of spin. The comparison between the data and the calculations also addresses two related issues: the recent prediction of a stable triaxial ground state 98, and the predicted competition between a prolate and an oblate shape near the ground state 99 and in the ground-state band 61.

This discussion starts with the ground-state band alignment features. These are depicted in Figure 6-3 in terms of the kinematic and dynamic moments of inertia as a function of rotational frequency, a type of plot that has been discussed in Section 2.3.2. The ^{106}Mo and ^{108}Mo nuclei have essentially the same characteristics and the latter case is omitted in Figure 6-3. However, the full information on ^{108}Mo is provided in Figure 6-4.

As indicated by the shaded area in each panel of Figure 6-3, the spin range where Q_t values are now available, overlaps in part with the band-crossing region. In ^{104}Mo, for example, this region is centered around $\hbar\omega = 0.4$ MeV and $I = 12$. In all nuclei under discussion, the rise of the moments of inertia is attributed to the rotational alignment of a pair of $h_{11/2}$ neutrons [79].

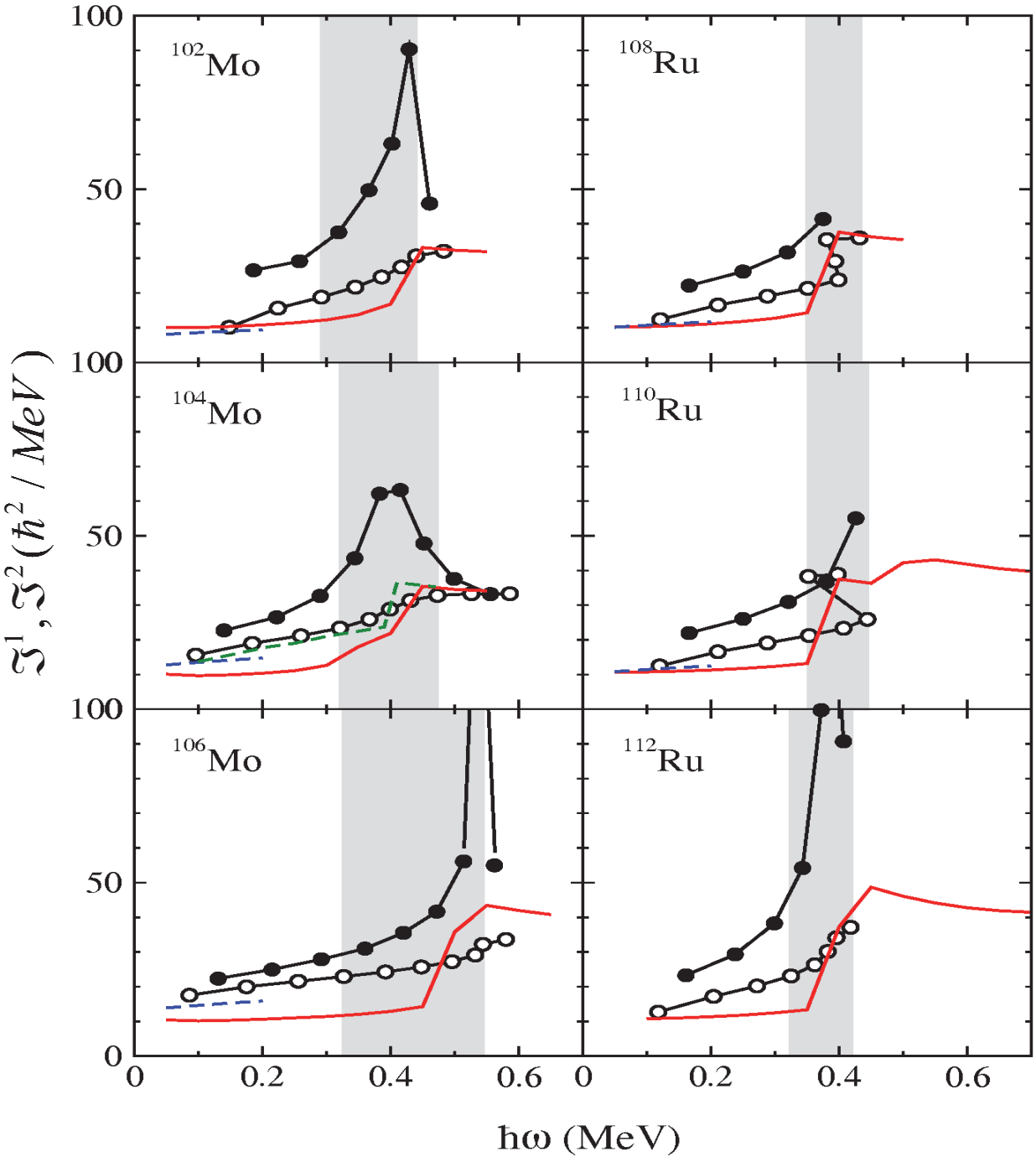

Figure 6-3: Kinematic ($\mathfrak{I}^{(1)}$, open circles) and dynamic ($\mathfrak{I}^{(2)}$, full circles) moments of inertia, as a function of rotational energy, for the yrast bands in $^{102\text{-}106}$Mo (left) and $^{108\text{-}112}$Ru (right). The data are based on the level schemes in the literature for Mo and Ru isotopes [26]. The ^{106}Mo $\mathfrak{I}^{(2)}$ moment is truncated at the highest value. The ^{108,110}Ru $\mathfrak{I}^{(2)}$ moments are truncated where the $\mathfrak{I}^{(1)}$ moments show backbends. Shaded areas represent the spin range of the presently reported Q_t values. The curves in color are the result of theoretical calculations (see text). This figure is from Reference [97].

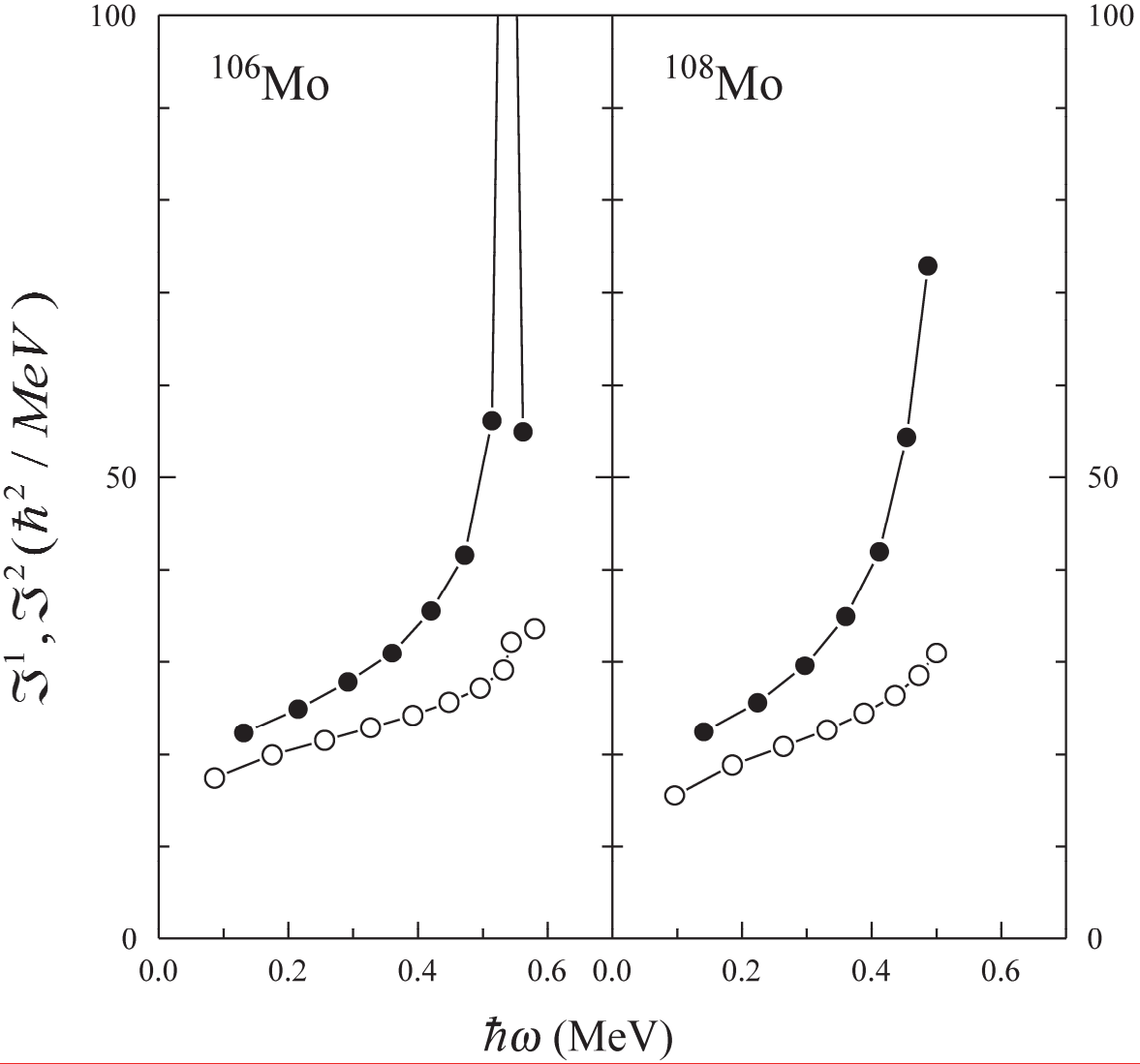

Figure 6-4: Same as Figure 6-3, but for ^{106}Mo and ^{108}Mo data only.

The results of the CRHB + LN calculations are compared with the experimental $\mathfrak{I}^{(1)}$ moments in Figure 6-3. The ground states of ^{102,104,106}Mo are calculated to be triaxial ($\gamma \sim -44°$), near-oblate ($\gamma \sim -53°$), and oblate, respectively. These solutions are energetically favored in the calculations and the corresponding $\mathfrak{I}^{(1)}$ moments are displayed as solid, red curves. Clearly, they fail

to reproduce the rise of the $\mathfrak{I}^{(1)}$ moments with frequency. The dashed, green curve for the ^{104}Mo case is the near-prolate solution, which reproduces the data.

As for the Q_t values, initial observations based on the data in Figure 5-39 and Figure 5-40 have already been made in Section 5.3. This discussion expands upon that initial framework. The Q_t values for the ground-state band decrease with increasing spin and this behavior is accentuated in the heavier isotopes. Specifically ^{102,104}Mo vs. ^{106,108}Mo and ^{108}Ru vs. ^{110,112}Ru isotopes show this trend. For example, using $8 \leq I \leq 16$, the weighted-average values for ^{110,112}Ru are respectively, 192 ± 16 efm^2 and 198 ± 26 efm^2, these are to be compared to the ^{108}Ru value of 261 ± 11 efm^2. In addition, these averages for ^{110,112}Ru are also somewhat smaller than those for ^{106,108}Mo. Indicating that the decrease in the Q_t values seems more severe in the Ru isotopes than in the available Mo nuclei. This observation suggests a dependence of $Q_t(I)$ on Z and N. It is worth noting that a reduction of the Q_t moments with increasing spin is also seen in ^{74}Kr [100] and in the rare-earth region [35]. In these nuclei, this reduction has been interpreted as being due to a γ-soft PES polarized by rotation-aligned quasiparticles inducing a triaxial shape.

In Figure 5-39 and Figure 5-40, the various solutions of the CRHB+LN calculations are shown. As said in Section 6.1.2, for these calculations the Gogny D1S force was used in the pairing channel. The code did not have constraints on the diagonal and off-diagonal elements of the quadrupole-moment tensors, Q_{22} and Q_{20}. These elements have the following relationships with Equation (6-14):

$$Q_{22} = e\sqrt{\frac{16\pi}{5}}\left\langle r^2 Y_{22}\right\rangle \tag{6-17}$$

$$Q_{20} = e\sqrt{\frac{16\pi}{5}}\left\langle r^2 Y_{20}\right\rangle. \tag{6-18}$$

As a result, the solution was restricted to local minima; i.e., Q_t and $\mathfrak{I}^{(1)}$ were calculated at the equilibrium deformations of these minima, which change with frequency. In both calculations, the NL3* parametrization of the RMF Lagrangian [101] was used.

To focus on the details in Figure 5-39 and Figure 5-40, triaxial and oblate solutions are represented by a full curve while the prolate solution is represented by a dashed curve. In these calculations, substantial shape changes take place in the associated configurations with increasing spin: the β_2 deformation increases while γ drifts towards -30°. The latter feature is pronounced in ^{104}Mo, where $\gamma \sim -30°$ is reached at $I \sim 4$ and the Q_t value rises accordingly. This prediction is in conflict with the data, including the new Q_t values, which show the opposite trend. A similar situation occurs in the Ru isotopes. Thus, the interpretation of the alignment and deformation properties of the observed bands in terms of collective motion associated with oblate and near-oblate shapes faces substantial difficulties.

The alternative is to associate the observed bands with a prolate minimum, although it is an excited one (see below). The CRHB + LN calculations indicate that, without constraining the Q_{20} and Q_{22} moments, the solution in the local prolate minimum becomes unstable when ω increases. Only in the case of ^{104}Mo is a solution obtained over a significant frequency range. In Figure 6-3, Figure 5-39, and Figure 5-40, the CRHB + LN prolate solution in ^{104}Mo, represented by dashed, green curves, provides a good description of the Q_t values for $I \leq 8$. Notably, this was also the case for the $\mathfrak{I}^{(1)}$ moment and the band-crossing frequency. The downslope of Q_t with increasing I is reproduced and is attributed to a combined decrease in β_2 and increase in γ deformation induced by rotation.

For the other nuclei, the prolate solution is only stable at the lowest ω values. The $\mathfrak{I}^{(1)}$ and Q_t values (the former is shown in Figure 6-3 as a dashed, blue line) extracted from these minima agree rather well with experiment, though in a limited range of frequency and spin. Due to this limitation, the trends in the predicted low-spin and measured high-spin Q_t values are, in the case of ^{106}Mo and ^{110}Ru, not comparable. They can, however, be viewed as complementary.

As stated earlier, the Mo and Ru nuclei under investigation are thought to be characterized by γ-soft energy surfaces and their successful description would be expected to use mean-field based models. Unfortunately, as discussed in Section 4.1 of Reference 98, no consistent picture emerges from the model calculations and different methods reach different conclusions. These calculations face two principle difficulties. First, strong shape variations with Z and N are expected that can be attributed to shell effects in the single-particle spectrum. Hence, the results depend sensitively on the adopted single-particle energies, the accuracy of which is model and parameter dependent 99 102. Second, the results of calculations strongly depend on the treatment of pairing as exemplified below.

A sample result of the triaxial RMF + BCS calculations with NL3* for ^{104}Mo, performed by Afanasjev and Abusara is shown in Figure 6-5. The PES plot illustrates the γ softness prevalent in the region. An oblate minimum and a shallow excited prolate minimum are seen. In contrast, axial RMF + BCS calculations 92 with the NL3 parametrization of the Lagrangian predict the prolate minimum to be the lowest in ^{102,104}Mo, whereas the oblate one becomes the lowest in the heavier Mo isotopes. However, CRHB + LN calculations with the NL3 parametrization suggest that the oblate minimum is lowest by 20 and 240 keV in ^{102,104}Mo, respectively.

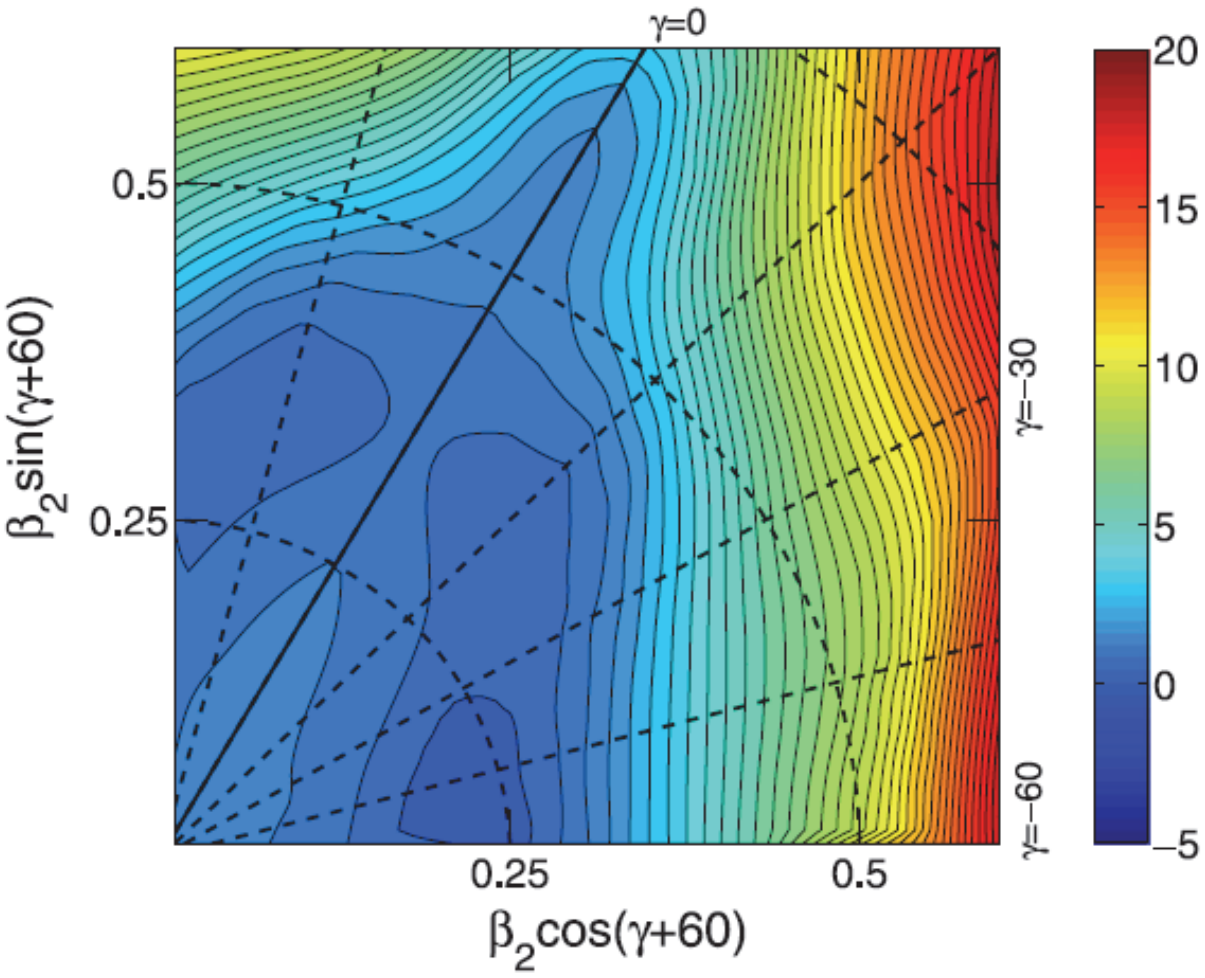

Figure 6-5: The PES for ^{104}Mo is displayed. Each contour line represents a 0.5 MeV change in energy. Collective prolate and oblate shapes are described by $\beta_2 > 0$ and $\gamma = 0^\circ$ or -60°, respectively. Notice that there are two local minima, one oblate and the other near prolate ($\gamma \sim 15^\circ$). Triaxial shapes are described by values of γ off the principal axis, for further details see the Lund Convention in Section 2.3.1. This figure is from Reference [97].

The following final comment may be in order. As stated in Reference [97], for nuclei with a very soft PES, a description on the mean-field level may not be adequate and methods beyond mean field may be required. The tensor interaction maybe important and requires the inclusion of the Fock exchange terms in the calculation [91]. Correlations related to the restoration of broken symmetries

and fluctuations of collective variables should be included for states with different shapes so that shape coexistence can be properly included [103].

Chapter 7: Summary and Outlook

The neutron-rich, even-mass $^{102-108}$Mo and $^{108-112}$Ru were studied by measuring lifetimes using the Doppler-shift attenuation method. The nuclei were produced as fission fragments of ^{252}Cf. To this end, the Gammasphere spectrometer and the Hercules fast-plastic detector array were used as experimental setup. From the information of the excited-state lifetimes, transition quadrupole moments, Q_t, were extracted. These moments were typically obtained between I=6-16ħ for the ground-state band, as well as for at least one transition in the γ-band. A byproduct of the present analysis was the determination of previously unknown γ-ray transition intensities.

The neutron-rich Mo and Ru nuclei are interesting cases for studying nuclear shape and structure effects. For a comparison with theory, the present data are combined with data at lower spin from the literature.

At moderate spin, the ground-state band Q_t values are observed to decrease relative to the low-spin values near the ground state. All nuclei under discussion have band crossings (backbendings). Below the band crossing, the data appear to be consistent with the motion associated with the rotation of a near-prolate shape. Above it, a triaxial shape may be present. This is in part supported by the relativistic mean-field model calculations of the CRHB+LN type, which have been used in this work. Other theoretical calculations predict an oblate shape or a triaxial shape with an asymmetry parameter $\gamma \sim -44°$ at low spin, but these are ruled out by the data. For ^{104}Mo, the calculations using the prolate minimum reproduce the observations, and provide some indication of a shape transition from a prolate to a triaxial shape at higher spin. The Q_t values for ^{106}Mo and ^{110,112}Ru also support this picture. However, reliable theoretical predictions cannot be made for all the nuclei studied.

Stable triaxial shapes and oblate shapes, at low spin, are hard-to-observe exotic shapes. They attract considerable attention in current nuclear-structure research (see Figure 6-2). The present work has advanced this research, particularly in the case of ^{104}Mo. In the other cases studied, γ softness, the tendency of the potential-energy surface to deviate from an axially-symmetric shape, has been tested, and to some degree verified.

Better prospects for the observing of the effects of stable triaxiality or an oblate shape on excited-state properties may be odd-mass nuclei such as $^{105\text{-}107}$Mo (odd N) or $^{105\text{-}107}$Tc (odd Z). The recent observation of an oblate shape in ^{109}Nb [104] supports this statement. The yields for these odd-mass nuclei are comparable to the even-mass nuclei studied in this work. Analyzing their lifetimes using the present data set is suggested and the work presented here provides a guide for such an endeavor.

Appendix A: Guide to Using the LINESHAPE Code

A.1 Modifying the DECHIST Routine

The DECHIST routine (see Section 4.3.3) provides an option for three methods with which to generate the stopping powers for the recoiling nucleus. They are: (1) Ward's effective charge with Ziegler's proton stopping powers, (2) Ziegler's heavy-ion stopping powers, and (3) the shell-corrected Northcliffe and Schilling stopping powers. The later was mainly used in this analysis, but a study of the so-called Stopping and Range of Ions in Matter (SRIM) by Ziegler et al. was made as well. Specifically, DECHIST was modified so the effect of the SRIM stopping powers, on the mean lifetime, could be determined.

The procedure for the code modification is documented hereafter. Notably, the LINESHAPE code must be compiled on the group's 32-bit unix machines (Mira and Orion), but the executable can then be run on the group's 64-bit unix machines (Mira1 and Orion1). There is an issue with the backwards compatibility of the gfortran compiler, which replaced the g77 compiler on the 64-bit machines.

- Run DECHIST and view the text file stopp.out (some of the DECHIST executables have the writing out of the stopping powers disabled: see /exp05/programs/DSAM/StopPowTest). Make note of the ion energies that the code uses for its stopping powers lookup table (left most column of stopp.out). Any SRIM replacement lookup table must also have values at these specific ion energies (there are 61 of them).

- Run SRIM for the case of interest. Write out the table in units of MeV/(cm^2/mg). Make sure that the ion-energy range covers the same ion-energy range as DECHIST.
- Copy the ion energy and dE/dx columns into a spreadsheet. (If the lookup table is first opened in Word the alt key can be held down to enable column selection.)
- SRIM produces an electric and nuclear stopping powers. Sum these values together to calculate the total stopping power.
- Produce a graph of stopping powers as a function of ion energy (e.g. in Excel).
- Right click on the points of the graph and select the add trendline option. A high order polynomial fit was found to produce an acceptable fit to the data. (It may be necessary to fit the low energy stopping powers with a different function than the high energy stopping powers to get a better overall fit.)
- Use the fit to interpolate the SRIM stopping powers for the specific ion energies needed by DECHIST.
- The code that needs to be modified to include the SRIM stopping powers is the STOPP subroutine of stopp.f. Open this file for editing on the Orion/Mira servers.
- After the last DO loop include the line, STP(1,2)= lowest energy new stopping power value. There will be 61 such lines, and they will end with STP(61,2) = highest energy new stopping power value. (The 2 designates that it is a stopping power for a recoil passing through the backing.)
- At the command line execute: make –f dechist.make. This makes a new executable called DECHIST. Rename this file to specify that it should only be used for a specific ion (e.g. DECHIST_SRIM106Mo).

- Run the modified DECHIST, view the new stopp.out file to check that the modification worked, and then run HISTAVER with the modified output.
- Use the modified HISTAVER velocity profiles in the LINESHAPE code and perform fits as normal.

A.2 Sample Inputs

The directory /home/ncgrp/exp05/gsfma263/post/dsam contains the bulk of the files associated with the DSAM analysis. This directory contains a subdirectory for each of the nuclei studied in this work. A list of the different extensions used and their meaning is provided below.

- *.dat → is an input file for either the DECHIST or HISTAVER routine.
- *.lis → is a human readable output file from either the DECHIST or HISTAVER routine.
- *.his → is a binary input file made by the DECHIST routine for the HISTAVER routine or the HISTAVER routine for the LINESHAPE program.
- *.dsf → called a dump file by the LINESHAPE program, it saves the setup parameters of a fit in the LINESHAPE program.
- *.spn → a file that consists of the spectrum files from each different angular bin stacked together (spectrum 5, 6, 7, 8, and 9 are 120°, 105°, 90°, 75°, and 60° respectively).
- nhist-5-15 (.f90 .par1 .par2) → are the parameter files for the post-run.sh scanning program that applies the FF and γ-ray gates and creates the angle-sorted spectra (*.spn).
- *.cmd → are command files for the Radware xmgf3 program that divide the combined *.spn file into individual *.spe files, one for each angular bin.
- *.agr → are the save files for xmgrace.
- *.out → are the output files from the LINESHAPE program, they can contain the ASCI output for the fits, the output fit parameters, or both.

Example Setup of the DECHIST Routine for ^{106}Mo [comments are in brackets]:
Run DECHIST [all the subdirectories contain the executable, copy it where it is needed]
Name of input data file (RETURN to create one) > **hit return**
Enter name of data file to be created (.dat)> **mo106**
Enter Z and A of target> **42 106**
Enter density of target> **10.28** [g/cm^3]
Enter target thickness in mg/cm^2> **0** [adaptation for fission, see Section 4.3.3]
Enter target angle (in degrees, relative to beam)> **90**
Enter Z and A of projectile> **42 106**
Beam energy (MeV)> **408** [this value must be adjusted until the correct initial FF velocity is reached]
Z and A of backing> **78 195**
Density of backing (g/cm^3)> **21.45**
Enter backing thickness in mg/cm^2> **438**
Z and A of recoil> **42 106**
The following stopping power options are available:
1 – Ward's effective charge and Ziegler's proton stopping power
2 – Ziegler's heavy-ion stopping power
3 – Shell-corrected Northcliffe & Schilling stopping power (DEFAULT)
Select one of these by entering the number corresponding to your choice
or RETURN for the default option:> **3 or hit return** [see Section A.1]
Seed (0 = random) = **0**
Enter time-step interval in picoseconds> **0.004**
Enter maximum number of time steps> **2000** [this is the maximum allowed]
Enter number of histories> **10000**

The routine now simulates the stopping for each of the histories. Open the *.lis file to view the results. Adjust beam energy in the *.dat file and rerun the DECHIST routine until the initial recoil velocity is correct for the nucleus of interest.

Example Setup of the HISTAVER Routine for ^{106}Mo [comments are in brackets]:
Run HISTAVER [all the subdirectories contain the executable, copy it where it is needed]
Name of input data file (RETURN to create one)> **hit return**
Name of file to be created> **mo106_75** [.dat file]
Target-detector distance (cm)> **25.4**
Ge detector radius (cm)> **3.55**
Theta angle (degrees)> **75.1** [see Table 4-6]
Number of Ge at that angle> **1**
Relative efficiency and phi of Ge # 1> **1 0** [efficiency is handled in the LINESHAPE program]
Enter file (.his) containing simulated histories> **mo106.his** [created by DECHIST routine]
Enter output file name> **mo106_75** [.his file for LINESHAPE program and .lis file]

The HISTAVER routine will need to be run for every theta angle that will later be included in the analysis in the LINESHAPE program. Each bin contains hundreds of the different angular combinations between the Gammasphere and Hercules detector. It is impractical to include each of those combinations, instead a single detector at the average theta for the angular bin represents the entire bin. Each bin has its own efficiency file (*.eff) to account for the relative efficiency between different bins in the LINESHAPE program.

Example Setup of the LINESHAPE Program for ^{106}Mo [comments are in brackets]:
Run LINESHAPE [all the subdirectories contain the executable, copy it where it is needed]
WHAT NEXT> setup

Number of angles = **3**
Data for angle # 1
Spectrum file = **CrunchCom654below-09.spe**
Error Spectrum = **CrunchCom654below-09.spe** [see README.pdf in ~/dsam if background is subtracted]
Number of values of theta to sum over = **1**
Velocity profile file (.HIS) = **mo106_60.his** [from HISTAVER routine]
Efficiency file (.EFF) = **bin9.eff**
Data for angle # 2
Spectrum file = **CrunchCom654below-07.spe**
Error Spectrum = **CrunchCom654below-07.spe**
Number of values of theta to sum over = **1**
Velocity profile file (.HIS) = **mo106_90.his** [from HISTAVER routine]
Efficiency file (.EFF) = **bin7.eff**
Data for angle # 3
Spectrum file = **CrunchCom654below-05.spe**
Error Spectrum = **CrunchCom654below-05.spe**
Number of values of theta to sum over = **1**
Velocity profile file (.HIS) = **mo106_120.his** [from HISTAVER routine]
Efficiency file (.EFF) = **bin5.eff**

Energy calibration intercept (MeV) = **0.0**
Energy calibration slope (MeV/ch) = **0.001**
Quadratic coefficient (MeV/ch)^2 = **0.0**
Number of levels in rotational side-feeding cascades = **5**
Dynamic moment of inertia for the side-feeding bands in MeV = **24.0** [see Section 4.3.2]
Number of transitions in cascade = **3**

Transition # 1 (starting from the bottom)
Energy of transition (MeV) = **0.6549**
Lower limit of window = **635**
Upper limit of window = **675**
Branching ratio of M1/E2 transition = **1** [means transitions are all E2s]
Side feeding intensity = **57.1** [see Table 5-3]
Initial estimate of transition Q_t = **2.5**
Will this level have independent multi-step feeding? **no**
Rotational-cascade side feeding is assumed
Initial estimate for side-feeding Q_t = **7.5** [~3x transition Q_t is a good estimate]
FWHM (in ch) of peak in level #1 angle #1 = **3.0**
Normalization of peak in level #1 angle #1 = **1.0**
FWHM (in ch) of peak in level #1 angle #2 = **3.0**
Normalization of peak in level #1 angle #2 = **1.0**
FWHM (in ch) of peak in level #1 angle #3 = **3.0**
Normalization of peak in level #1 angle #3 = **1.0**
Transition #2 (starting from the bottom) [same as transition #1 except different energy and limits]
Transition #3 (starting from the bottom) [same as transition #1 except different energy and limits]

Spin of upper level of transition 1 (in hbar) = **8**
K of band (in hbar) = **0.0** [2.0 for γ band, if the transition is between bands the Q_t will be wrong, but with the right Clebsh-Gordon coefficient the correct value can be constructed from the τ]

Window #1 [this section accounts for background peaks, use setup[/w] to avoid scrolling through all of setup again if these values need to be adjusted]
Number of regions to exclude from fit = **0**
Number of extra stopped peaks in this window = **7** [maximum of 8 can be fit per window]
Position of peak #1 (in channels) = **639.0** [if fitting a moving peak be aware that for some angles the peak height will have to be manually set to 0]
Position of peak #2 (in channels) = **641.5**
…
Position of peak #7 = **636.0**

Include efficiency correction? **yes** [this uses the bin*.eff files]
Upper Limit: Q(1) = **6** [for transition #1]
Lower Limit Q(1) = **0.1**
Upper Limit QS(1) = **11**
Lower Limit QS(1) = **0.1**
Upper Limit: Q(2) = **6** [for transition #2]
Lower Limit Q(2) = **0.1**
Upper Limit QS(2) = **11**
Lower Limit QS(2) = **0.1**
Upper Limit: Q(3) = **6** [for transition #3]
Lower Limit Q(3) = **0.1**

Upper Limit QS(3) = **11**
Lower Limit QS(3) = **0.1**

The setup is now complete. Start with the highest spin transition you can and work downward. If you need to use different angles for a different transition, create a new setup, and include one transition above the transition you are trying to measure. Fix the transition and side-feeding Q_t values of this above transition using the previous fit. This allows the direct feeding to be based upon fitted rather than modeled values.

The file README.pdf in the ~/dsam directory has a complete list of all the commands available. Some of the more commonly used ones are listed below.

- seek → basic fitting routine, use once at the start to get an initial fit.
- simplex → better fitting routine, use regularly to account for changes made.
- migrad → best fitting routine, used by minos, rarely used by itself.
- minos → χ^2 minimization routine, use this for the final fit.
- fx → brings up a list of parameters that can be fixed.
- fr → brings up a list of parameters that can be freed.
- cal → calculates the lineshapes for each angle, use periodically, the program does not always prompt you to use this if you make a change that affects it.
- setup[/w] → allows quick access to the section of the setup where background peaks can be added in each window.
- list → displays a list of the current fit parameters.
- sw → selects the window that you want to fit.
- df[/w=1,2,3] → displays the lineshape fit for the specified window.

- dump → creates a save file for the setup and fit parameters (*.dsf).
- indump → reads in a save file (remember to run cal afterwards).
- exit → exits the program

Appendix B: Table of Clebsch-Gordan Coefficients

Table B-1 shows a selection of Clebsch-Gordan coefficients relevant to this work. The left two columns of the table show stretched, intra-band E2 transitions, of the ground-state band (K=0) and the γ band (K=2), where the coefficient takes the form $\langle I_i K 20 | I_f K \rangle$. The right half of the table shows inter-band E2 transitions, where the coefficient takes the form $\langle I_i 22\text{-}2 | I_f 0 \rangle$ with $\Delta K = -2$. Recall that the angular momentum vectors must satisfy the triangle relations $I_i - I_\lambda \leq I_f$ and $I_i + I_\lambda \geq I_f$, where $I_\lambda = 2$ for an E2 transition and their projections must satisfy $K_i + \Delta K = K_f$. The Clebsch-Gordan coefficients were calculated using Stevenson's Java Clebsch-Gordan Coefficient Calculator [105] [106].

Table B-1: Clebsch-Gordan coefficients for relevant E2 transitions.

$I_i \rightarrow I_f$	$\langle I_i 020 \mid I_f 0 \rangle$		$I_i \rightarrow I_f$	$\langle I_i 220 \mid I_f 2 \rangle$		$I_i \rightarrow I_f$	$\langle I_i 22\text{-}2 \mid I_f 0 \rangle$
$2 \rightarrow 0$	0.4472		$6 \rightarrow 4$	0.4847		$6_2 \rightarrow 6_1$	0.6030
$4 \rightarrow 2$	0.5345		$7 \rightarrow 5$	0.5136		$6_2 \rightarrow 4_1$	0.3129
$6 \rightarrow 4$	0.5610		$8 \rightarrow 6$	0.5326		$4_2 \rightarrow 4_1$	0.5922
$8 \rightarrow 6$	0.5738		$9 \rightarrow 7$	0.5459		$4_2 \rightarrow 2_1$	0.3450
$10 \rightarrow 8$	0.5817		$10 \rightarrow 8$	0.5557		$2_2 \rightarrow 0_1$	0.4472
$12 \rightarrow 10$	0.5868		$11 \rightarrow 9$	0.5631			
$14 \rightarrow 12$	0.5905						
$16 \rightarrow 14$	0.5932						
$18 \rightarrow 16$	0.5953						

Appendix C: Data Structure

The raw data are structured as 32-bit words and can be represented in hexadecimal format, i.e. words comprised of four hexadecimal digits. An example is given in Figure C-1. An event in the raw data contains the data words described below. Events are separated by the ffff word, the so-called separator, highlighted in red. The digits have been swapped compared to the standard Gammasphere output format [107] (e.g. xxnn is now nnxx).

Event Header: The ten words following the ffff separator comprise the event header.

First Word: In Figure C-1, this is the word 4a80. The 4a designates the number of words in the event, in this case $4 \cdot 16^1 + a \cdot 16^0 = 74$ total words in the event. The 80 is present in every event and marks the header.

Second Word: The first two digits give the number of "clean" HPGe hits, in this case 5 such hits.

Third Word: The last two digits give the number of "dirty" HPGe hits, in this case 4 such hits. The first two digits give the number of "clean" BGO counts, in this case 7 such hits.

Fourth, Fifth, and Sixth Words: These three words output the trigger time according to the μsec clock. The clock is a 47-bit output of the master trigger module that ticks once every μs. The μsec clock time can be constructed by the following expression: (fourth word $\cdot 2^{31}$) + (fifth word $\cdot 2^{16}$) + (sixth word), in this case 377,479,811,558 μs.

Seventh Word: This word represents the TAC1 timing signal (0.25 ns/ch). It outputs the time difference between the trigger and the following μsec clock tick. The trigger time can

be determined to an accuracy of better than a ns by subtracting the TAC1 time from the μsec clock time: (μsec clock time • 1000) - (TAC1 • 0.25).

Eighth Word: This word represents the TAC2 timing signal (0.5 ns/ch). In an in-beam experiment, it represents the time difference between the pre trigger and the accelerator rf pulse. In this experiment, the signal was the time difference between the master trigger and the CsF detector. The null output in the example is typical as the CsF detector is, roughly spoken, only present in one of every fifty events.

Ninth Word: This word outputs the sum of the so-called side-channel HPGe energies.

Tenth Word: This word gives the sum of the BGO energies.

"Clean" HPGe Output: Each "clean" HPGe event contains four words. There are five "clean" HPGe events in the example.

First Word: The first two digits give the identification number for the detector hit. The last two digits encode the hit pattern. Being a "clean" event, the hit pattern records that none of the BGOs fired and only the HPGe bit is set.

Second Word: The first bit identifies if pileup occurred and the second bit identifies if the signal ranged out. These are followed by the 14-bit HPGe energy (1/3 keV/ch).

Third Word: This word encodes the 12-bit side-channel information, which leads to the angular correction for the segmented detectors.

Forth Word: This word outputs the 12-bit HPGe time (~0.56 ns/ch) relative to the trigger.

"Dirty" HPGe Output: There are four "dirty" HPGe events written out in the example. They have the same format as the "clean" HPGe output. Being a "dirty" event, the hit pattern records the BGO(s) that fired in addition to the HPGe.

"Clean" BGO Output: Each "clean" BGO event contains three words. There are seven "clean" BGO event written out in the example.

First Word: The first two digits give the identification number for the detector hit. The last two digits encodes the hit pattern. Being a "clean" BGO event, the hit pattern records that the BGO(s) fired, but the HPGe did not.

Second Word: This word outputs the 12-bit BGO time (~0.56 ns/ch) relative to the trigger.

Third Word: This word outputs the 12-bit BGO energy (3 keV/ch).

Hercules Data: The 00ff marker designates the start of external data. For this experiment, it is data from Hercules, which requires five words.

First Word: This is the header for any external data written out. The first two digits identify the number of words of external data that will follow. In the example, the header tells that four words follow. This will always be the case unless multiple FFs hit Hercules; this occurred for less than 3% of the events.

Second and Third Words: These words output the timing information from Hercules. The first two digits of the second word give the virtual station number (VSN), an id for the four 16-channel digitizers for the Hercules time signals (VSN 49-52). The third word in the example is bf74. Flipping the bytes, this reads 74bf. The 7 represents the channel number of the digitizer that has data; the channel number combined with the VSN allows the specific Hercules detector to be identified. The remaining three digits, 4bf, output the Hercules time signals.

Forth and Fifth Words: These words output the pulse-height information from Hercules. The four Hercules pulse-height digitizers have VSN 53-56.

Figure C-1: Example of the raw data written in hexadecimal representation. The leftmost column displays the location of this block within the data file. The yellow highlighting designates the event header, the light blue "clean" HPGe data, the green "dirty" HPGe data, the pink "clean" BGO data, and the dark blue Hercules data. See the text for details.

Appendix D: RIV Analysis for ^{144}Ba

D.1 Introduction

The g-factor (g) connects the spin and the magnetic moment (μ) of the nucleus, as described in Equation (D-1). The nuclear magneton is $\mu_N=3.15\cdot10^{-18}$ MeV/Gauss.

$$\vec{\mu} = \frac{g\mu_N}{\hbar}\vec{I} \tag{D-1}$$

Knowledge of the g-factor provides information about the current distribution of the nucleus. For an even-even nucleus (^{144}Ba), a change in the g-factor can indicate a change in the pairing configuration.

The recoil-in-vacuum (RIV) technique relies upon measuring the attenuation of the γ-ray angular distributions of aligned states [108]. The hyperfine interaction couples the nuclear magnetic moment to the magnetic field of the electron distribution, linking the nuclear spin to the atomic spin and causing the nucleus to precess about the resultant vector $\vec{F} = \vec{I} + \vec{J}$.

The magnetic field of the electron distribution is the result of holes in the electron shell structure with the most significant contributions coming from the inner K and L shells. The holes are the result of the FF traveling relativistically through a dense medium. The number of electrons stripped from the FF is proportional to its velocity. The distribution of the remaining electrons is kept in a state of flux from collisions with other electrons in the dense medium. This process ensures a distorted atomic configuration when the FF reaches vacuum, at which point the atomic configuration will rearrange to fill holes in the inner shells. Each atomic configuration has a lifetime

and an associated hyperfine field strength. The convolution of the average atomic configuration over the lifetime of the nuclear state provides the average hyperfine field strength perturbing the orientation of the FF.

The nuclear spin is oriented by the fission of ^{252}Cf, but when coupled to the randomly oriented atomic spin, that orientation is lost at a rate proportional to the hyperfine field strength. The loss of orientation of the nuclear spin is quantified by the attenuation coefficients G_k (k= 2, 4), they are function of lifetime of the nuclear state and the g factor. The time dependent attenuation coefficients $G_k(t)$, for a given pair of quantum numbers I and J, can be expressed as

$$G_k(t) = 1 - 2 \cdot \sum_{F>F'} \frac{(2F+1)(2F'+1)}{(2J+1)} \left\{ \begin{matrix} F & F' & k \\ I & I & J \end{matrix} \right\}^2 [1 - \cos(\omega_{FF'} t)] \qquad \text{(D-2)}$$

where $\omega_{FF'}$ is the precession frequency and it is related to the g factor through the expression

$$\omega_{FF'} = g \frac{B\mu_N}{2J} \cdot [F(F+1) - F'(F'+1)] \qquad \text{(D-3)}$$

where B is the magnetic hyperfine field at the nucleus [109].

The so-called "static model" assumes that the nuclear lifetime is short compared to the atomic lifetime [110], which implies that knowing the initial hyperfine field strength is sufficient. This has been applied empirically in the Te isotopes [111]. The hyperfine field strength is measured using "calibration" isotopes with known g factors (e.g. $^{122, 126, 130}$Te) and it is applied to the isotope of interest (e.g. ^{132}Te).

Time-dependent Monte-Carlo simulations of G_k, developed by X. Chen [112], have improved upon the "static model". The simulation randomly selects the decay time t in Equation (D-2) from

the e^{-t/τ_n} distribution, where τ_N is the nuclear lifetime. The changes in atomic configuration that the nucleus experiences before it decays are then accounted for by randomly selecting atomic decay times weighted by the distribution of the form e^{-t/τ_a}, where τ_a is the lifetime of the relevant atomic configuration. Atomic decay times continue to be selected until the simulated nucleus decays. The simulation adjusts the hyperfine field strength in Equation (D-2) for each change in atomic configuration. The lifetimes and hyperfine field strengths of the atomic configurations are based upon atomic-structure calculations from first principles using the GRASP2K code [113]. The code outputs G_k as a function of the g factor and requires atomic structure information, the lifetime of the nuclear state and the velocity of the FF as inputs. This curve is then used to translate the measured G_k into the g factor.

The angular distribution of a stretched E2 γ-ray transition is shown in Figure D-1. As discussed in Section 2.2, the spin axis may lie anywhere in a plane perpendicular to the fission axis. The E2 angular distributions of this work are constructed relative to the fission axis, this results in the averaging of all possible orientations of the spin axis about the fission axis. This has the effect of degrading the anisotropy $[W(90^\circ)/W(0^\circ)]$ of the angular distribution. The angular distribution function is defined in Section 2.3.2.

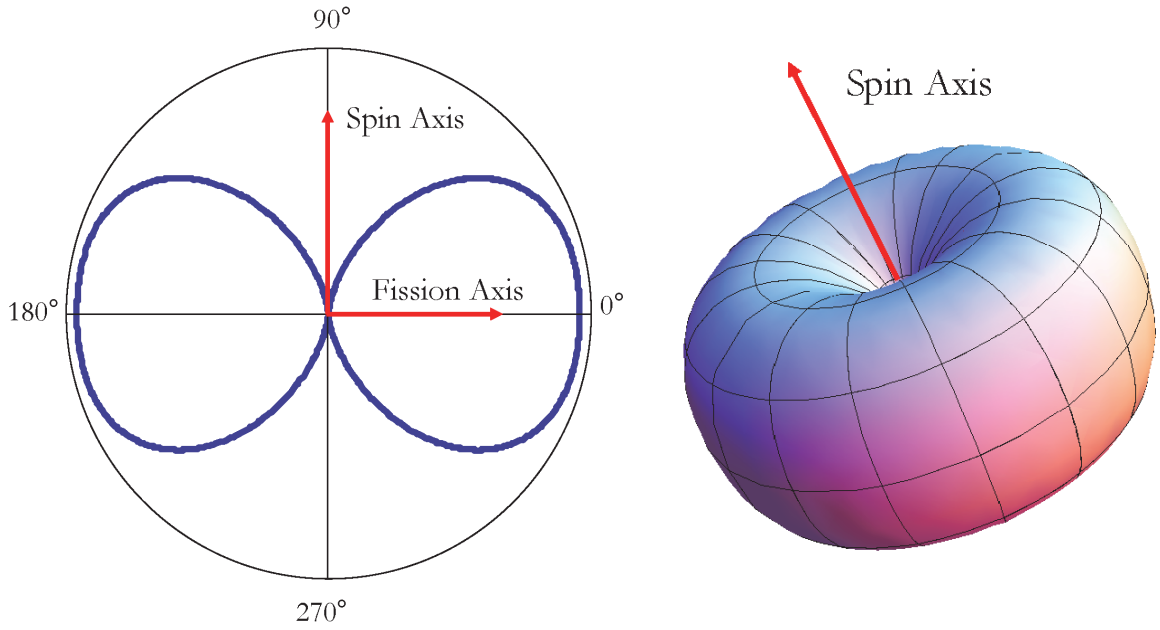

Figure D-1: The angular distribution of a stretched electric quadrupole, illustrated in 2D and 3D.

D.2 Analysis

Those details that pertain specifically to RIV are included in this section; additional information can be found in Chapter 4. The RIV method is a time-integral method, i.e. the attenuation effect is integrated over the state lifetime. The method involves measuring the angular distribution of the state of interest and its feeding transition. The angular distribution of the feeding transition is called the unattenuated distribution, while the distribution of the state itself is called the attenuated distribution. Their ratio provides a measure of the attenuation that occurred during the lifetime of the state. If there is no attenuation, and both transitions are stretched E2s, then both of these distributions will be the same.

The angular distributions are fit with the Legendre polynomial function shown in Equation (D-4). The odd terms do not contribute because the distributions are symmetric.

$$W(\xi) = A_0 + A_2 P_2(\cos\xi) + A_4 P_4(\cos\xi) \tag{D-4}$$

The G_k attenuation coefficients are measured by taking the ratio [114]

$$G_k = \frac{Q_k^{(attenuated)} A_k^{(attenuated)}}{Q_k^{(unattenuated)} A_k^{(unattenuated)}} \tag{D-5}$$

where the Q_k are the finite solid angle correction factors and the A_k are the Legendre polynomial fit parameters for the angular distribution.

It is important to either remove or account for any side-feeding contributions to the intensity of the attenuated distribution. If the cumulative lifetime of the side feeding is different than that of the direct feeding it will bias the result (e.g. if the side feeding has a short lifetime it would make the attenuated distribution appear less so). In this work, the side feeding is removed through γ-ray gating.

The general gating conditions were a LF gate in Hercules, a double gate on the γ-ray transitions, and event-by-event Doppler correction. For the unattenuated angular distribution all double gates below the feeding transition (e.g. $8^+ \rightarrow 6^+$) were included. For the attenuated angular distribution one of the gating transitions was the direct feeding transition (e.g. $8^+ \rightarrow 6^+$), the other was any transition "below" the transition out of the level of interest (e.g. "below" $6^+ \rightarrow 4^+$).

In the RIV analysis the FF are traveling along the fission axis towards Hercules. Therefore, the γ-ray transitions are sorted into, 15° wide, angular bins with respect to Ψ, the supplement of ξ used for the DSAM analysis. The bins are centered on the angles Ψ=15°, 30°, 45°, 60°, 75°, 90°, 105°, 120°, 135°, 150°, and 165°. To increase the number of data points in the Legendre polynomial fit, a second set of angular bins are created that are shifted 7.5° relative to the first set. These bins are centered on the angles Ψ=7.5°, 22.5°, 37.5°, 52.5°, 67.5°, 82.5°, 97.5°, 112.5°, 127.5°, 142.5°,

157.5°, and 172.5°. The mean bin angle can be different than the prescribed bin angle depending upon the collection of detectors included in each bin. Table 4-6 displays the simulated mean bin angles, and these angles are used when the angular distribution is fit. The peak of interest in each bin is fit with a Gaussian using the Radware software package [59]. As discussed in Section 4.3.4, moving background peaks from the partner fragment are tracked from bin to bin, and accounted for when they interfere with the peak of interest. The efficiency of each bin at the energy of the peak of interest is simulated and accounted for using the internal calibration method described in Section 4.1.3. The A_0 term of the polynomial fit [Equation (D-5)] is the average value of the fit. The counts in each bin are normalized to set A_0 equal to 1. The Legendre polynomial fit is then performed using a χ^2 minimization routine developed by Bevington [115].

The velocity of ^{144}Ba was determined by gating on the $4^+ \rightarrow 2^+$ and $2^+ \rightarrow 0^+$ transitions and projecting out the FF velocity spectrum. The peak was fit with a Gaussian to determine the centroid. The velocity for ^{144}Ba was 1.027 cm/ns.

The Au foil, included for safety (see Section 3.2), is of some concern. If the fragment recoiling into vacuum hits the Au foil before the state of interest has decayed then the atomic configuration is once again scrambled. If this happens it becomes unlikely that the hyperfine interaction can be correctly accounted for. The source holder places the Au foil 2 mm away from the ^{252}Cf, providing a 150 ps window for the g factor measurements. The measurement of the 4^+ state in ^{144}Ba, with a cumulative lifetime greater than 103 ps, was completely attenuated. Any state that does not decay before reaching the Au foil would not be accessible by this method anyway.

D.3 Results

The measured angular distributions are highlighted on the partial level scheme in Figure D-2. were measured for. The known lifetimes of the levels are also listed [118]. Figures D-3 through D-6 are the angular distributions, constructed relative to the fission axis (angle Ψ), for the $10^+ \rightarrow 8^+$, $8^+ \rightarrow 6^+$, $6^+ \rightarrow 4^+$, and $4^+ \rightarrow 2^+$ transitions of the ground-state band respectively. The Legendre polynomial fits are overlaid on each distribution. The error bars get larger as 0° and 180° are approached, this is due to fewer detectors being available at these angles. The fit parameters and the calculated attenuation coefficients and g factors for the 8^+ and 6^+ levels are in Tables D-1 and D-2. No g factor is calculated for the 4^+ level, because the angular distribution of the $4^+ \rightarrow 2^+$ transition is completely attenuated. The g factor for the 10+ level could not be measured because the lifetime is unknown. As transitions higher in the band are analyzed their lifetimes, in general, decrease as does the intensity. Shorter lifetimes mean less attenuation, which means the angular distributions of transitions higher in the band eventually become indistinguishable from each other. The Monte-Carlo simulations of G_k as a function of the g factor for the 8^+ and 6^+ levels are displayed in Figures D-7 and D-8.

The only g factor for comparison is 0.34 ±0.05 for the 2^+ level [116]. Assuming a strongly deformed nucleus, the collective rotational component of the g factor is Z/A [117]. This neglects single-particle components, but provides an estimate, $g \approx 0.39$.

Table D-1: Legendre polynomial fit parameters and finite angle correction factors.

Transition	A_2	ΔA_2	A_4	ΔA_4	Q_2	Q_4
$10^+ \rightarrow 8^+$	0.220	±0.0106	-0.211	±0.0134	0.9884	0.9505
$8^+ \rightarrow 6^+$	0.157	±0.0124	-0.0991	±0.0156	0.9876	0.9485
$6^+ \rightarrow 4^+$	0.093	±0.0053	-0.0365	±0.0069	0.9866	0.9457

Table D-2: Lifetimes [118], attenuation coefficients, and g factors for the 8^+ and 6^+ levels of ^{144}Ba.

Level	τ (ps)	Δτ	G_2	ΔG_2	G_4	ΔG_4	g	Δg	
8^+	10.3	±1.4	0.713	±0.066	0.469	±0.080	0.344	+0.179	-0.090
6^+	21.8	±2.1	0.592	±0.058	0.368	±0.090	0.242	+0.295	-0.143

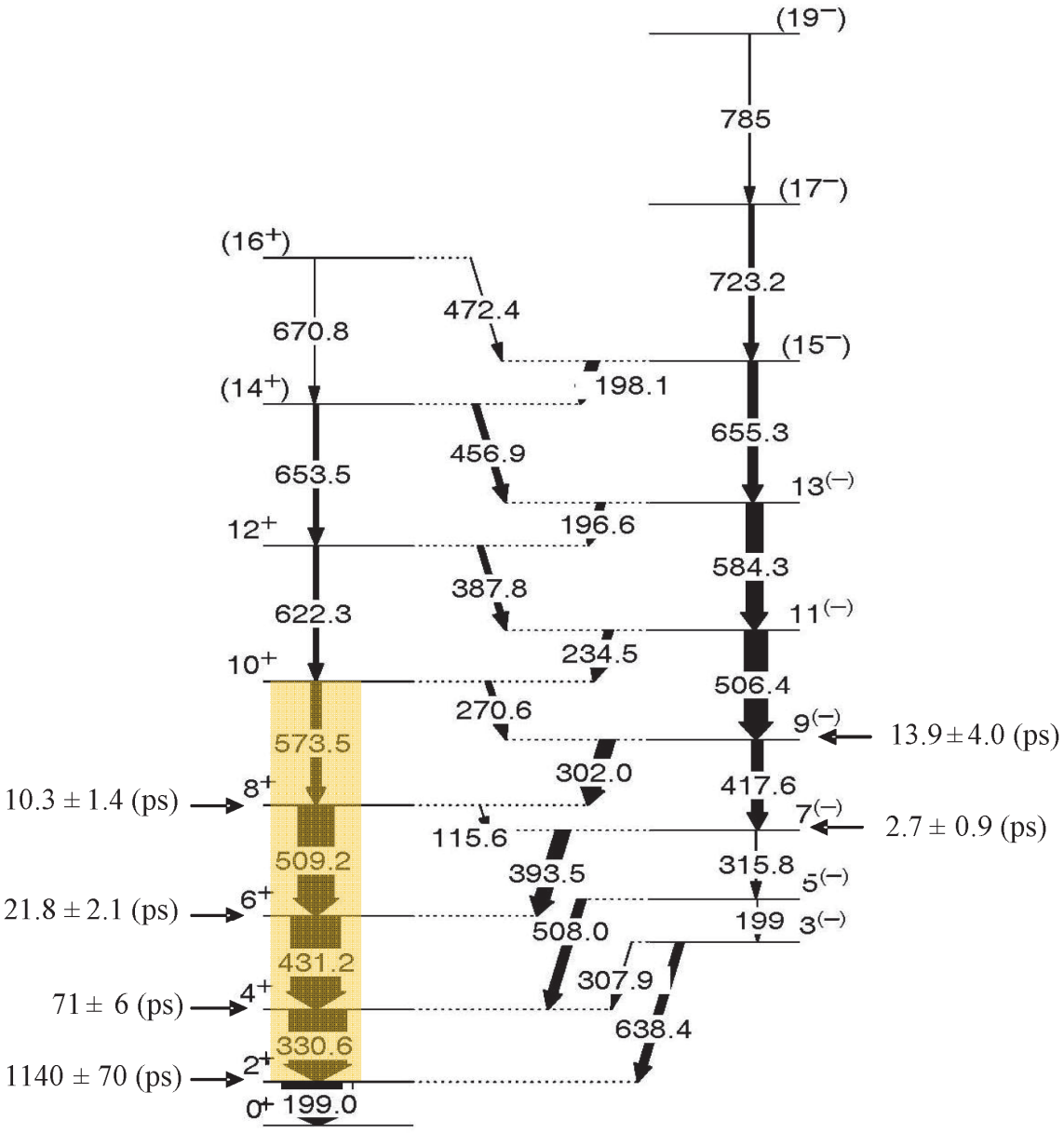

Figure D-2: Partial level scheme for ^{144}Ba with measured transitions highlighted. Known lifetimes from the literature are included [118].

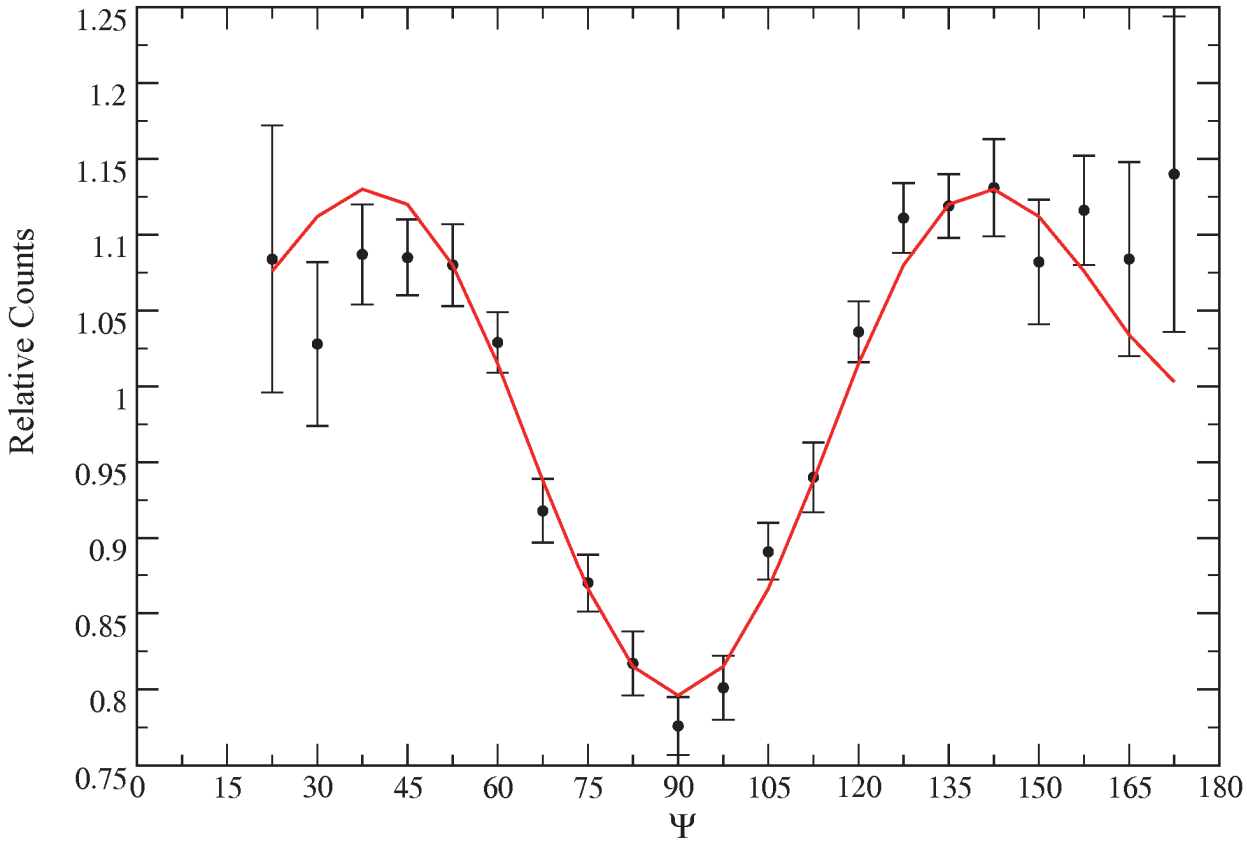

Figure D-3: The angular distribution of the $10^{+} \rightarrow 8^{+}$ transition of ^{144}Ba. The Legendre polynomial fit is overlaid on the distribution.

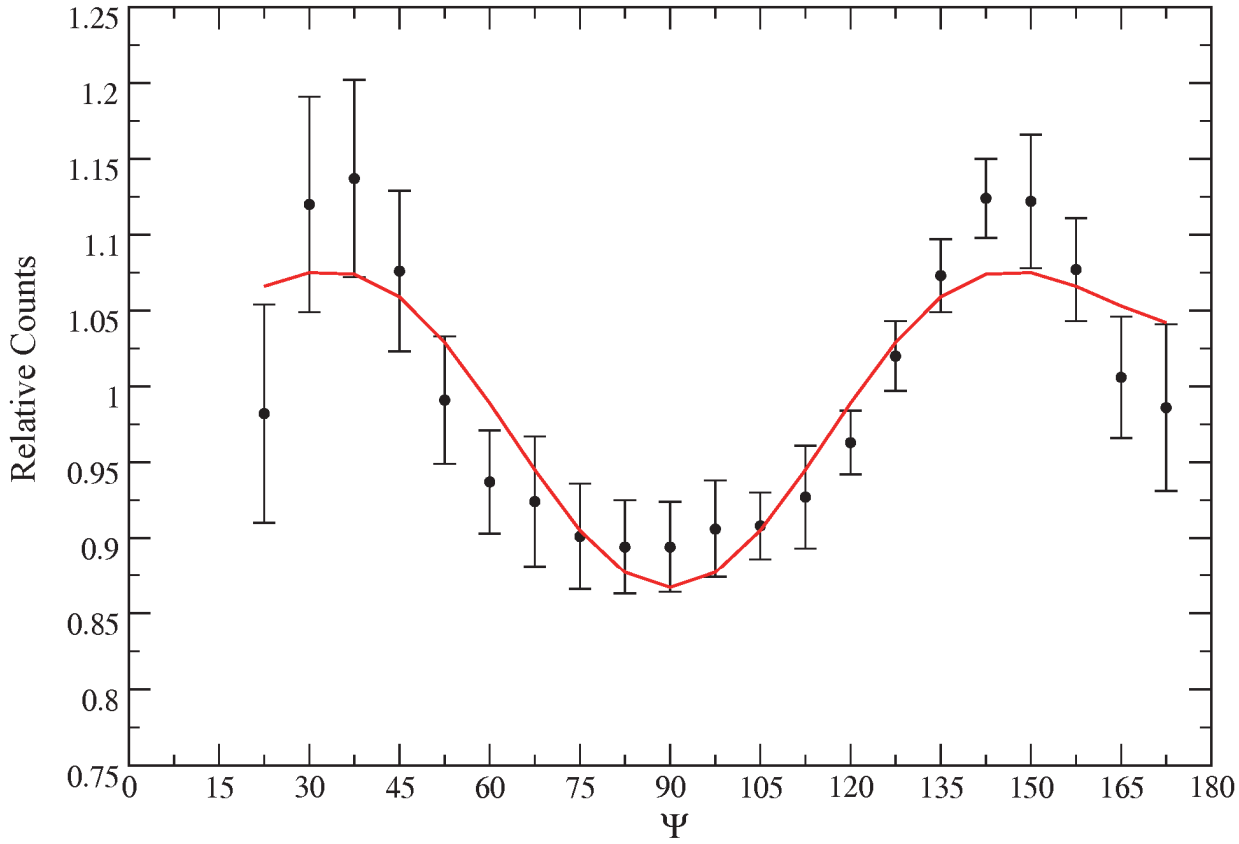

Figure D-4: The angular distribution of the $8^{+} \rightarrow 6^{+}$ transition of ^{144}Ba. The Legendre polynomial fit is overlaid on the distribution.

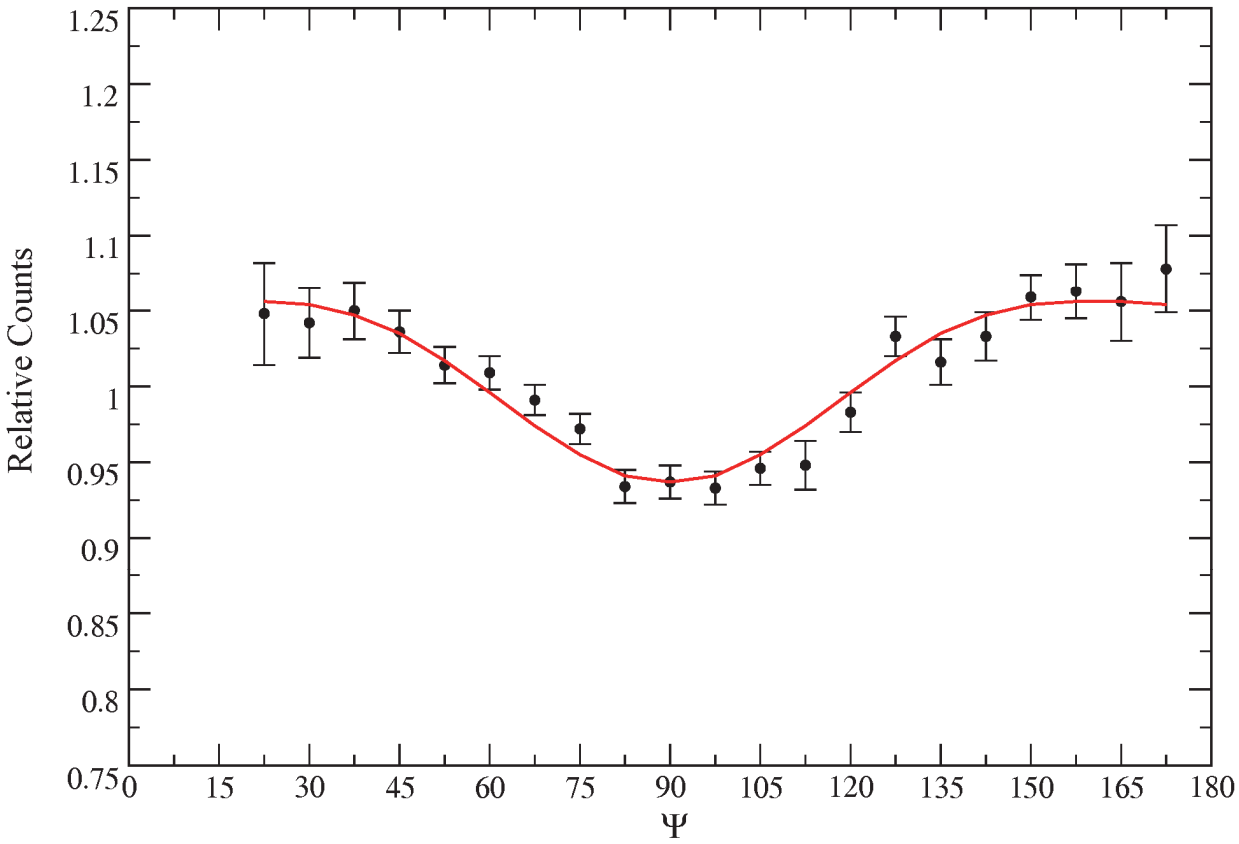

Figure D-5: The angular distribution of the $6^+ \rightarrow 4^+$ transition of ^{144}Ba. The Legendre polynomial fit is overlaid on the distribution.

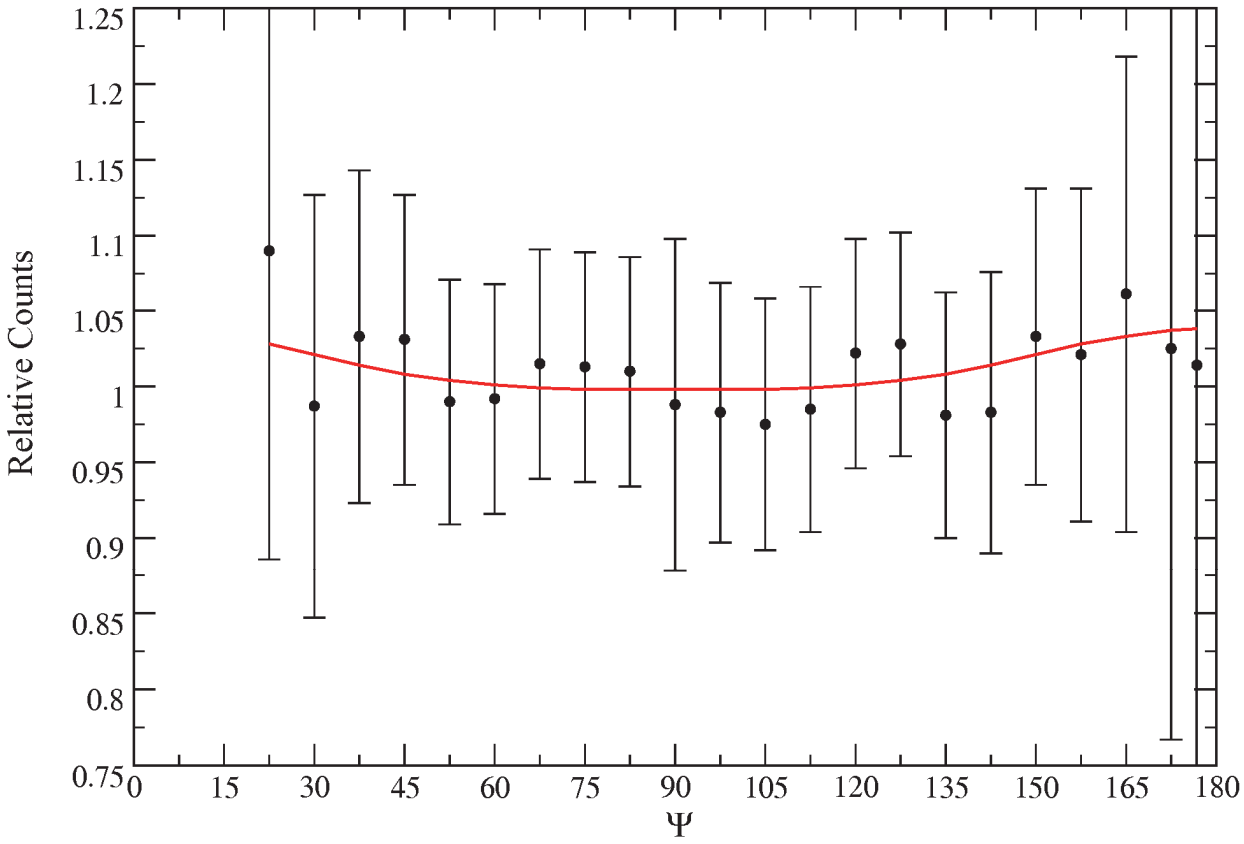

Figure D-6: The angular distribution of the $4^+ \rightarrow 2^+$ transition of ^{144}Ba. The Legendre polynomial fit is overlaid on the distribution.

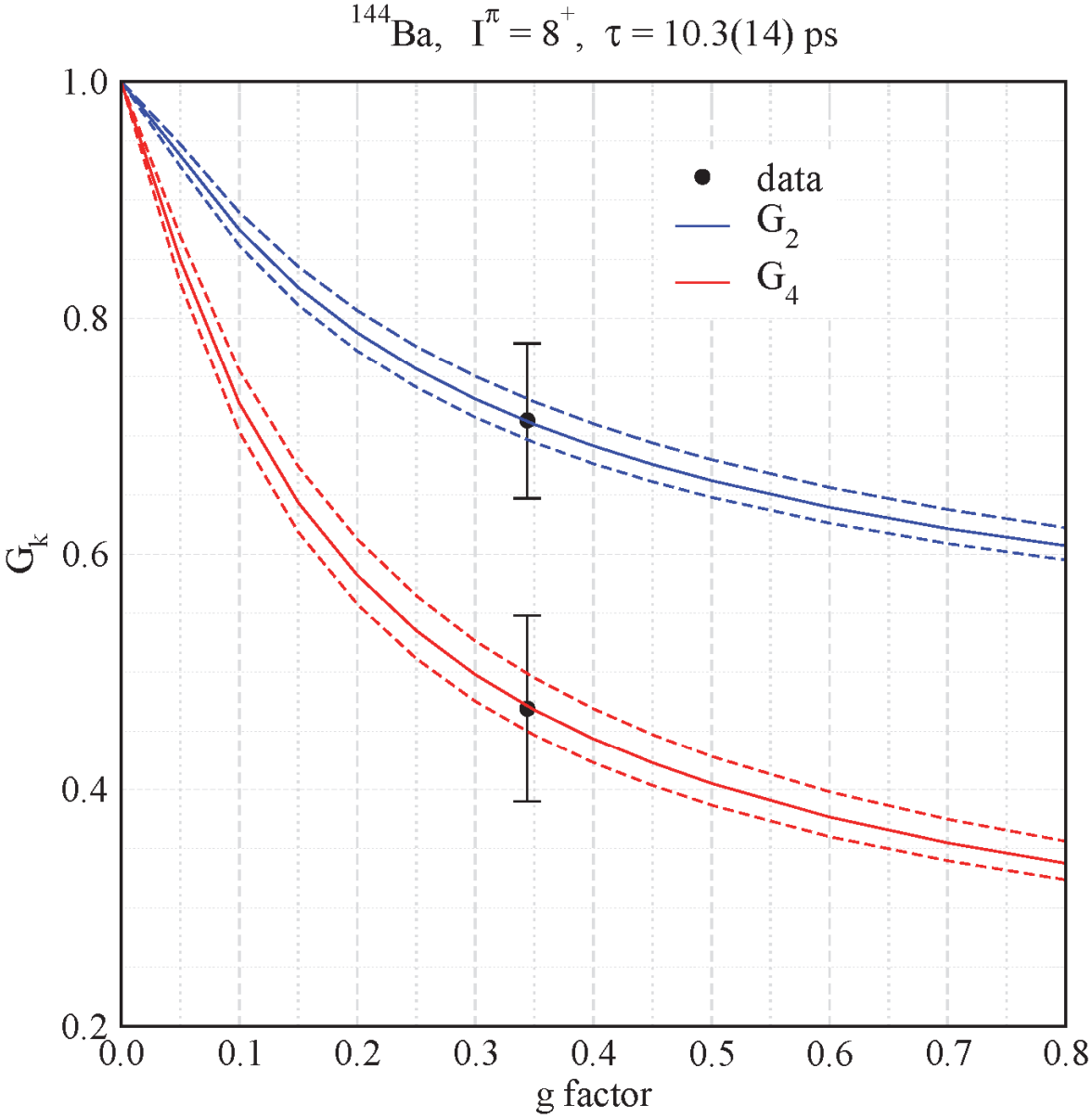

Figure D-7: Monte-Carlo simulation describing G_2 and G_4 as a function of the g factor for the 8^+ level. The data points for G_2 and G_4 are overlaid on the simulation.

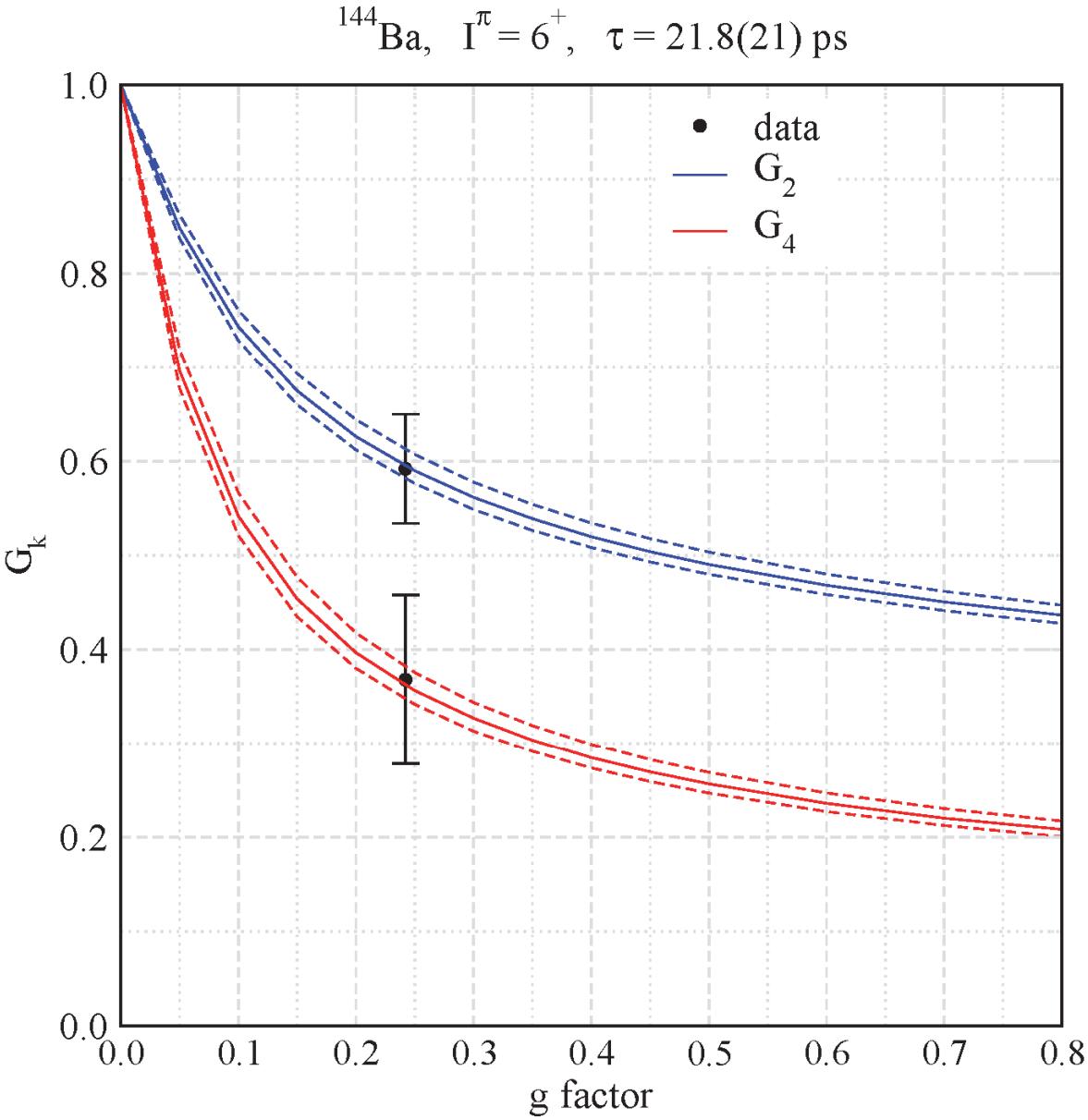

Figure D-8: Monte-Carlo simulation describing G_2 and G_4 as a function of the g factor for the 6^+ level. The data points for G_2 and G_4 are overlaid on the simulation.

D.4 Commentary

Among the FF of ^{252}Cf there is scarce g factor data available for any state other than the 2^+. This state is inaccessible in RIV so a check of the method is unavailable. The uncertainty in the

method is still too large when compared to measurements of the 2^+ level. The uncertainty on G_2 is ~9.5%, but due to the slope of the simulated G_k/g curve, the uncertainty on the g factor increases to a minimum of 25%.

Bibliography

[1] K.S. Krane, Introductory Nuclear Physics (John Wiley & Sons, New York, 1988) p. 45.

[2] W. Benenson, et al., eds. Handbook of Physics (Springer, New York 2006) p. 566.

[3] K-P. Lieb, Hyperfine Interactions 136/137 (2001) 783.

[4] A. Bohr, Nobel Lecture (1975).

[5] C.F. von Weizsäcker, Z. Phys. 96 (1935) 431.

[6] H.A. Bethe and R.F. Bacher, Rev. Mod. Phys. 8 (1936) 82.

[7] W. Loveland, D.J. Morrissey, and G.T. Seaborg, Modern Nuclear Chemistry, (Wiley, New Jersey, 2006).

[8] W. Nazarewicz and I. Ragnarsson, in Handbook of Nuclear Properties, D.N. Poenaru and W. Greiner, eds., (Clarendon Press, Oxford, 1996) p. 80.

[9] I. Ahmad and W.R. Phillips, Rep. Prog. Phys. 58 (1995) 1415.

[10] E.J. Axton and A.G. Bardell, Metrologia 21 (1985) 59

[11] J.R. Nix, and W.J. Swiatecki, Nucl. Phys. A71 (1965) 1.

[12] D.G. Sarantites, G.E. Gordon, C.D. Coryell, Phys. Rev. 138 (1965) B353.

[13] M.M. Hoffman, Phys. Rev. 133B (1964) 714.

[14] L.G. Moretto and R. P. Schmitt, Phys. Rev. C 21 (1980) 204.

[15] A.C. Wahl, Phys. Rev. C 32 (1985) 184.

[16] T.R. England and B.F. Rider, LANL Report No. LA-UR-94-3106; ENDF-349 (1993).

[17] D.L. Hill and J.A. Wheeler, Phys. Rev. 89 (1953) 1102.

[18] G. Andersson et al., Nucl. Phys. A 268 (1976) 205.

[19] F.A. Lerma, PhD Thesis, Washington University, 1999.

[20] K.J. Honkanen, F.A. Dimanian, D.G. Sarantites, S.P. Sorensen, Nucl. Instr. Meth. Phys. Res. A 257 (1987) 233.

[21] D.G. Sarantites, Introduction to the Atomic Nucleus (Lecture Notes).

[22] O.L. Pechenaya, PhD Thesis, Washington University, 2008.

[23] A.E. Stuchbery, Nucl. Phys. A 723 (2003) 69.

[24] W.G. Winn and D.G. Sarantites, Nucl. Instr. Meth. 66 (1968) 61.

[25] M.J.A. de Voigt, J. Dudek, and Z. Szymański, Rev. Mod. Phys. 55 (1983) 949.

[26] National Nuclear Data Center Website, Brookhaven National Lab. (2013) <http://www.nndc.bnl.gov/nudat2>.

[27] R.F. Casten, Nuclear Structure from a Simple Perspective, (Oxford University Press, Oxford, 1990).

[28] T. K. Alexander and J. S. Forster, in Advances in Nuclear Physics Vol. 10, M. Baranger and E. Vogt, eds., (Plenum Press, New York, 1978) p. 197.

[29] P. Ring and P. Schuck, The Nuclear Many-Body Problem, (Springer, New York, 1980).

[30] A. Bohr and B.R. Mottelson, Nuclear Structure, Vol. I (Benjamin, New York, 1969) p. 82.

[31] J.M. Blatt and V.F. Weisskopf, Theoretical Nuclear Physics, (Wiley, New York, 1952).

[32] H. Morinaga and T. Yamazaki, In-Beam Gamma-Ray Spectroscopy, (Elsevier Science Ltd., 1976), p. 70.

[33] A.Schwarzschild, Nucl, Instr. and Meth. 21 (1963) 1.

[34] P.J. Nolan and J.F. Sharpey-Schafer, Rep.Prog. Phys. 42 (1979) 1.

[35] N.R. Johnson, Prog. Part. Nucl. Phys. 28 (1992) 215.

[36] J.C. Wells and N.R. Johnson, LINESHAPE: A Computer Program for Doppler-Broadened Lineshape Analysis, ORNL Report No. 6689 (1991) p. 44.

[37] H. Bateman, Partial Differential Equations of Mathematical Physics, (Dover, New York, 1944).

[38] H. Bateman, Proc. Cambridge Phil. Soc. 15 (1910) 423.

[39] J. Lindhard, V. Nielsen, M. Scharff, and P.V. Thomsen, Mat. Fys. Medd. K. Dan Vid. Selsk. 33 (1963) 10.

[40] A.E. Blaugrund, Nucl. Phys. 88 (1966) 501.

[41] L.C. Northcliffe and R.F. Schilling, Nucl. Data Tables A7 (1970) 233.

[42] J.F. Ziegler and W.K. Chu, At. Data. Nucl. Data Tables 13 (1974) 463.

[43] J.F. Ziegler, J.P. Biersack, and M.D. Ziegler, SRIM: The Stopping and Range of Ions in Matter (Lulu Press, Morrisville, 2008) <http://www.srim.org>.

[44] D.B. Cassidy, et al., Phys. Rev. Lett. 95 (2005) 195006.

[45] F. Gao, et al., Nucl. Instr. and Meth. B 255 (2007) 286.

[46] I.-Y. Lee, et al., Nucl. Phys A 520 (1990) 641c.

[47] P.J. Nolan, F.A. Beck, and D.B. Fossan, Annu. Rev. Nucl. Part. Sci. 44 (1994) 561.

[48] Kim Blackmon, Private Communication (2001).

[49] W. Reviol, et al., Nucl. Instr. and Meth. A 541 (2005) 478.

[50] D. Desmarais, J. L. Duggan, and H. L. Adair, Am. J. Phys. 52 (1984) 234.

[51] N. Nica, Nuclear Data Sheets 106, 813 (2005)

[52] W.F. Mueller, et al., Nucl. Instr. and Meth. A 466 (2001) 492.

[53] G.J. Schmid et al., Nucl. Instr. and Meth. in Phys. Res. A 417 (1998) 95.

[54] E. Norbeck, et al., Nucl. Instr. and Meth. A 262 (1987) 564.

[55] H.W. Schmitt, W.E. Kiker, and C.W. Williams, Phys. Rev. 137 (1965) B837.

[56] I.-Y. Lee, M.A. Deleplanque, and K Vetter, Rep. Prog. Phys. 66 (2003) 1095.

[57] J.D. Leroux, et al., IEEE Nuclear Science Symposium Conference Record 3 (2003) 1723.

[58] M. Moszynski, et al., Nucl. Instr. and Meth. in Phys. Res. 205 (1983) 239.

[59] D.C. Radford, Nucl. Instrum. and Meth. 361 (1995) 297.

[60] C. Wagemans, The Nuclear Fission Process, (CRC Press, Boca Raton, 1991), p. 531.

[61] A.G. Smith, et al., Phys. Rev. C 86 (2012) 014321.

[62] D.M. Cullen, et al., Nucl. Phys. A 673 (2000) 3.

[63] J. Gascon, Nucl. Phys A513 (1990) 344.

[64] J.C. Bacelar, Phys. Rev. C 35 (1987) 1170.

[65] J.C. Bacelar, Phys. Rev. Lett. 57 (1986) 3019.

[66] W.M. Currie, Nucl. Instrum. and Meth. 73 (1969) 173.

[67] J. Lindhard, M. Scharff, and H.E. Schiott, Mat. Fys. Medd. K. Dan. Vid. Selsk. 33 (1963) 14.

[68] F. James and M. Roos, Comput. Phys. Commun. 10 (1975) 343.

[69] C.Y. Wu, et al., Phys. Rev. C 73 (2006) 034312.

[70] S. Lalkovski, et al., Phys. Rev. C 75 (2007) 014314.

[71] A. Guessous, et al., Phys. Rev. C 53 (1996) 1191.

[72] A. Guessous, et al., Phys. Rev. Lett. 75 (1995) 2280.

[73] Q.H. Lu, et al., Phys. Rev. C 52 (1995) 1348.

[74] A. Alaga et al., Mat. Fys. Medd. K. Dan. Vid. Selsk. 29, No. 9 (1955).

[75] R.F. Casten, Nuclear Structure from a Simple Perspective, (Oxford University Press, Oxford, 1990) p. 172.

[76] J.A. Shannon, et al., Phys. Lett. B 336 (1994) 136.

[77] J. Stachel, et al., Z. Phys. A 316 (1984) 105.

[78] A.V. Afanasjev, P. Ring, and J. König, Nucl. Phys. A 676 (2000) 196.

[79] J.Skalski, S. Mizutori, and W. Nazarewicz, Nucl. Phys. A 617 (1997) 282.

[80] V.M Strutinsky, Nucl. Phys. A 95 (1967) 420.

[81] V.M. Strutinsky, Nucl. Phys. A 122 (1968) 1.

[82] W.D. Myers and W.J. Swiatecki, Nucl. Phys. 81 (1966) 1.

[83] T.H.R. Skyrme, Nucl. Phys. 9 (1959) 1043.

[84] D. Gogny, Nucl. Phys. A 230 (1975) 399.

[85] W.H. Dickhoff and D. Van Neck, Many Body Theory Exposed! 2nd Ed., (World Scientific, Singapore, 2008).

[86] J. Bardeen, L.N.Cooper, and J.R. Schrieffer, Phys. Rev. 108 (1957) 1175.

[87] A. Bohr, B.R. Mottelson, and D. Pines, Phys. Rev. 110 (1958) 936.

[88] S.T. Belyaev, Mat. Fys. Medd. Dan. Vid. Selsk. 31, No. 11 (1959) 131.

[89] D. Vretenar, A.V. Afanasjev, G.A. Lalazissis, and P. Ring, Physics Reports 409 (2005) 101.

[90] P. Möller, et al., Phys. Rev. Lett. 97 (2006) 162502.

[91] Z.P. Li, et al., Phys. Rev. C 79 (2009) 054301.

92 G.A. Lalazissis, S. Raman, and P. Ring, At. Data Nucl. Data Tables 71 (1999) 1.

93 A.V. Afanasjev, D.B. Fossan, G.J. Lane, and I. Ragnarsson, Phys. Rep. 322 (1999) 1.

94 D.R. Jensen, et al., Phys. Rev. Lett. 89 (2002) 142503.

95 G.B. Hagemann and I. Hamamoto, Nucl. Phys. News 13 (2003) 20.

96 Y.X. Luo, et al., Phys. Lett. B 670 (2009) 307.

97 J.B. Snyder, et al., Phys. Lett. B 723 (2013) 61.

98 P. Möller, et al., At. Data Nucl. Data Tables 94 (2008) 758.

99 R. Rodríguez-Gúzman, P. Sarriguren, L.M. Robledo, and S. Perez-Martin, Phys. Lett. B 691 (2010) 202.

100 J.J. Valiente-Dobón, et al., Phys. Rev. Lett. 95 (2005) 232501.

101 G.A. Lalazissis, et al., Phys. Lett. B 671 (2009) 36.

102 A.V. Afanasjev and S. Shawaqfeh, Phys. Lett. B 706 (2011) 177.

103 M. Bender, P. Bonche, and P.-H. Heenen, Phys. Rev. C 74 (2006) 024312.

104 H. Watanabe, et. al., Phys. Lett. B 696 (2011) 186.

105 P.D. Stevenson, Java Clebsch-Gordon Coefficient Calculator, (University of Surrey, 2013) <http://personal.ph.surrey.ac.uk/~phs3ps/cgjava.html>.

106 P.D. Stevenson, Comp. Phys. Comm.., 147 (2002) 853.

107 Gammasphere Documentation Website, Argonne National Lab. (2012) <http://www.phy.anl.gov/gammasphere/doc/index.html> (Data Format – Data Record – Event Data).

108 A.E. Stuchbery and N.J. Stone, Phys. Rev. C 76 (2007) 034307.

109 G. Goldring, Hyperfine Interactions in Isolated Ions Vol. 5, (North-Holland, Amsterdam, 1982) p. 484.

110 A.E. Stuchbery and N.J. Stone, Phys. Rev. C 76 (2007) 034307.

111 N.J. Stone, et al., Phys. Rev. Lett. 94 (2005) 192501.

112 X. Chen, D.G. Sarantites, W. Reviol, and J. Snyder, Phys. Rev. C 87 (2013) 044305.

113 N. Stone, J. Stone, and P. Jönsson, Hyperfine Interactions 197 (2010) 29.

114 L. Grodzins, Ann. Rev. of Nucl. Science 18 (1968) 291.

115 P.R. Bevington and D.K. Robinson, Data Reduction and Error Analysis for the Physical Sciences -3rd ed., (McGraw-Hill, New York, 2003).

116 A.G. Smith, et al., Phys. Lett. B 453 (1999) 206.

117 A. Bohr and B.R. Mottelson, Nuclear Structure, Vol. II (Benjamin, New York, 1975).

118 D.C. Biswas, et al., Phys. Rev. C 71 (2005) 011301.